

Development of techniques for detection and dissolution enhancement of mineral deposits in petroleum pipelines using ultrasound.

QURESHI, M.Y.

2002

The author of this thesis retains the right to be identified as such on any occasion in which content from this thesis is referenced or re-used. The licence under which this thesis is distributed applies to the text and any original images only – re-use of any third-party content must still be cleared with the original copyright holder.

**Development of Techniques for Detection and
Dissolution Enhancement of Mineral Deposits in
Petroleum Pipelines Using Ultrasound**

Muhammad Yasser Qureshi

A thesis submitted in partial fulfilment of the requirements of The Robert Gordon
University for the degree of Doctor of Philosophy

December 2002

IMAGING SERVICES NORTH

Boston Spa, Wetherby
West Yorkshire, LS23 7BQ
www.bl.uk

**ORIGINAL COPY TIGHTLY
BOUND**

This Thesis is dedicated to my dear wife & son and my late father-in-law

Acknowledgements

First and foremost, I wish to express my sincere thanks to my supervisor Dr G.P.P Gunarathne for his unreserved and continued support, advice and encouragement throughout this project. The support also extended by Prof. N.D.Deans and Dr. A.J Miller from the School of Engineering is also gratefully appreciated. I would also like to thank Dr S.C. Elder for his advice and help with the signal processing aspects involved in the project.

The advice and guidance given by former members of the research group, Dr K.Christidis and Mr Q. Zhou is also greatly appreciated.

Special thanks must also go to the secretarial and technical staff in the school, in particular Mr J. Dickson, Mr M.Johnstone and Mr. S. Pirie for their assistance in the mechanical machining work involved in this project.

I would also like to thank the proof-readers for devoting their time to give me constructive comments on the writing of this thesis.

Finally I would like to thank my parents and my wife, for their continued moral support and patience throughout the long and testing road to the completeness of this PhD project.

Abstract

Scale formation in petroleum pipelines causes progressive flow reductions leading to large production losses and operating costs. The composition and thickness of the scale deposits vary widely but with present technology they cannot be accurately quantified or monitored. Remedial treatments such as chemical de-scaling etc are therefore largely based on guesswork, which can lead to expensive chemical wastage and production shutdowns. This project is intended to address some of the above problems using ultrasonic techniques.

Work presented in this thesis branches out into two main areas of interest namely: (a) developments concerning location of deposits from both top-side and down-hole locations and (b) developments relating to enhancement of scale removal, using ultrasound.

With regard to top-side scale detection the major challenge in this work was to develop a technique by which acoustic signatures are synthetically generated which can be used with the techniques previously developed for pipeline inspection. This required, the determination of a suitable type of transducer and the study of its radiation characteristics in developing comprehensive mathematical models for artificially generating reference echoes. The model allowed the 1st three multiple echoes (in steel objects) to be computed for given test parameters. Close agreement of the synthesised echoes with practical measurements was demonstrated with good repeatability.

An essential requirement for the detection of deposits in down-hole is the accurate alignment of the test probes with respect to the pipe-wall. In this regard a novel technique for remote alignment of the transducers was successfully formulated. It is based on identifying symmetrical properties of the signals received from the test probe itself when scanned around the correct angular position with respect to the target. However, through extensive practical measurements, it was found that an important requirement for applying this technique is to know in advance whether a particular combination of probe, target diameter and separation distance would give satisfactory angular resolution. Extensive practical examination of these factors showed that, no general conclusion can be easily drawn with respect to this requirement. Hence a mathematical model was successfully developed which would predict the suitability of given probe/target parameters.

It has been reported in previous studies that ultrasonic irradiation could greatly enhance the chemical dissolution of localised deposits during de-scaling operations. In this regard a major challenge was to improve the efficiency of power transducers, radiating into confined spaces at elevated temperatures. That required the study of radiation characteristics of ultrasonic power transducers and compensation techniques to regain loss of efficiency at elevated temperatures. Also alternative types of transducers based on flexural-horn designs were investigated and their relative merits presented.

Also significant findings related to the performance variations of ultrasonic transducers and transmission cables at elevated temperatures have been made. After examining the transducer efficiency drop with temperature a closed-loop compensation strategy was proposed for maintaining optimal performance. The matching requirements of the

cables, transmitting power from top-side to down-hole power transducers were also investigated as part of optimisation of ultrasonic power output. From this study it was found that within the temperature range of interest, the cable in itself does not require changes to the matching requirements as the environmental temperature fluctuates. However, it was noted that the transducer impedance changes rapidly with temperature and therefore a unified compensation strategy incorporating both cable and transducer impedances was proposed as a better solution.

Overall, the main objectives of the project concerning pipeline scale detection were well achieved namely (a) modelling of a suitable type of ultrasonic transducer to synthesise the reference multiple echoes to aid top-side scale detection and (b) development of a remote sensing technique for ultrasonic probe alignment in down-hole pipes. With regard to dissolution enhancement, techniques for enhancing power output of ultrasonic transducers to aid dissolution enhancement of scale deposits have been determined. Further work includes the improvements to software algorithms developed and hardware integration to achieve the expected performance of the techniques presented.

Table of Contents

	Page
1. Introduction	1
1.1 The Problem of Scale Deposits in Petroleum Pipelines	1
1.2 Current Inspection Tools and Cleaning Techniques	3
1.2.1 Review of NDT Inspection Tools	3
1.2.2 Cleaning Techniques for Scaled Pipes	5
1.3 Scale Detection and Dissolution Enhancement Using Ultrasound - A New Approach	8
1.3.1 Project Objectives	8
1.3.2 Deposit Location Techniques	9
1.3.3 Dissolution Enhancement of Scales	10
1.4 Specific Objectives of the Present Project	11
1.5 Systems Overview	13
1.5.1 Top-side System	13
1.5.2 Down-hole System	14
1.6 Structure of Thesis	16
2. Modelling and Verification of the Radiation Field of an Ultrasonic Transducer Suitable for Top-side Inspection	17
2.1 Introduction	17
2.2 Previous Work on Transducer Modelling for Inspection of Pipelines	18
2.2.1 Petroleum Pipeline Scales	18
2.2.2 Generation of Synthetic Scans	20
2.3 Approach for Synthesising Ultrasonic A-scans	21
2.4 Theoretical Modelling of a Rectangular Ultrasonic Transducer	22
2.4.1 Computation of Radiation Pressure Field	22
2.4.2 Determination of Effective Target Area	26
2.5 Experimental Verification of the Theoretical Model	27
2.5.1 Radiation Pressure Field	27
2.5.1 Effective Reflector Area	29
2.6 Results	29
2.6.1 Radiation Field Profile	29
2.6.2 Effective Reflector Area	32
2.7 Chapter Conclusions	35
3. Development of a Synthetic A-scan Technique for Top-side Pipeline Inspection	37
3.1 Introduction	37
3.2 Theoretical Modelling and Computation of Received Echoes from a Plane Target	38
3.2.1 Extension of Theoretical Models to Compute 1 st Received Echo	39

	Page	
3.2.2	Extension of Theoretical Models to Compute 2 nd and 3 rd Received Echoes	40
3.3	Modelling the Effect of Target Curvature	43
3.4	Experimental Verification of Theoretical Model for Synthesis of Received Echoes	46
3.4.1	Received Echoes from a Plane Reflector in Oil	46
3.4.2	Multiple Echoes in a Planar Steel Object	46
3.5	Results	48
3.5.1	Received Echoes from a Planar Reflector in Oil	48
3.5.2	Multiple Echoes in Steel	52
3.5.3	Reflected Echoes from Curved Surfaces - Simulated Results	55
3.6	Discussion of Results	57
3.7	Chapter Conclusions	58
4.	Development of Techniques for Positional Alignment of Ultrasonic Transducers in Down-hole Pipelines	60
4.1	Introduction	60
4.2	Problem Description	61
4.3	Background Work on Remote Alignment of Transducers	62
4.4	Proposed Approach	63
4.5	Detection of Positional Symmetry	64
4.6	Practical Examination of Detectable Limits	65
4.6.1	Experimental Arrangement	65
4.6.2	Practical Measurements on the Detectability of Transducer Positional Symmetry	66
4.7	Results	67
4.7.1	Effect of Curvature on the Angular Resolution	67
4.7.2	Effect of Distance on the Angular Resolution	69
4.7.3	Effect of Surface Roughness on the Angular Resolution	73
4.7.4	Effect of Probe Aperture on Angular Resolution	74
4.8	Theoretical Determination of Angular Resolution	76
4.8.1	Modelling the Effect of Probe/Target Orientation	77
4.8.2	Verification of Model	78
4.9	Summary of Results for Detecting the Positional Symmetry of the Probe and the Target	80
4.10	Chapter Conclusions	81
5.	Ultrasonic Power Transducers for Enhancement of Scale Dissolution	83
5.1	Introduction	83
5.2	Magnetostrictive Transducers	84
5.2.1	Equivalent Circuit	85
5.2.2	Power Transfer and Performance Efficiency	86
5.2.3	Limitations of Conventional Magnetostrictive Transducers	87

	Page	
5.3	Piezoelectric Sandwich Transducers	87
5.3.1	Construction of Transducer	88
5.3.2	Applications for Cleaning	90
5.3.3	Equivalent Circuits and Modelling of Piezoelectric Transducers	91
5.3.4	Power Transfer and Efficiency	94
5.3.5	Limitations of Piezoelectric Transducers	94
5.4	Piezoelectric Flexural-Horn Transducers	95
5.4.1	Construction of the Flexural-Horn Transducer	96
5.4.2	High Power Applications	98
5.5	Practical Evaluation of the Power Transfer Characteristics of Piezoelectric Sandwich Transducers	98
5.5.1	Transducer Efficiency from Circle Diagram	99
5.5.2	Experimental Arrangement	103
5.5.3	Circle Diagrams for Sandwich Transducer in Large Water Tank	104
5.6	Chapter Conclusions	106
6.	Techniques for Increasing the Radiation Resistance of Ultrasonic Transducers in Pipelines	107
6.1.	Introduction	107
6.2.	Transducer Efficiency Inside Pipes	108
6.3	Electrical Impedance Matching	110
6.4	Acoustic Impedance Matching	112
6.4.1	Material Choice for Acoustic Impedance Matching	114
6.4.2	Practical Evaluation of Efficiency Improvements With Acoustic Impedance Matching	115
6.4.3	Evaluation of Acoustic Impedance Matching Results	119
6.5	Design of a Flexural-Horn Transducer	120
6.6	Use of a Multiple Disk Flexural-Horn Transducer	123
6.7	Chapter Conclusions	124
7.	Optimising the Performance of Ultrasonic Power Transducers and Transmission Cables for Use in Down-hole Pipelines	126
7.1	Introduction	126
7.2	Temperature Effects on Ultrasonic Transducers	127
7.3	Variation of Transducer Parameters with Temperature	129
7.3.1	Radiation Efficiency	129
7.3.2	Study of Resonance Frequency Variation with Temperature	134
7.4	A New approach for Transducer Frequency Compensation	135
7.4.1	Implementation of Frequency Compensation	137
7.5	Optimising the Cable Performance at Elevated Temperatures by Dynamic Impedance Matching	139
7.6	Cable Requirements	140
7.7	A Coaxial Cable Model Based on the Finite Difference Method (FDM)	140
7.7.1	Summary of Existing FDM Coaxial Cable Model	141

	Page
7.7.2 Optimal Cable Matching Using the FDM Coaxial Cable Model	144
7.8 Extension of Existing Cable Models to Investigate Dynamic Impedance Matching	144
7.8.1 Approach	144
7.8.2 Calculating the Dynamic Cable Terminating Impedance (Z_T)	146
7.8.3 Results of Dynamic Impedance Matching of the Cable	148
7.9 Impedance Tracking of the Load Transducer	149
7.9.1 Transducer Impedance Variation with Temperature	150
7.9.2 Incorporating the Transducer Impedance-Temperature Profile in the Extended Cable Model	151
7.10 Chapter Conclusions	152
8. Conclusions and Future Work	154
8.1 Conclusions	154
8.1.1 Novel Techniques to Facilitate Scale Detection in Pipelines	155
8.1.2 Performance Optimisation of Power Transducers and Cables	158
8.2 Future Work	160
References	162
Bibliography	169
Publications	172
List of Publications/Oral Presentations	172
Published Papers	172
List of Key Symbols	173
Appendices	
Appendix A: Calculations and Discussions for Theoretical Models in Chapters 2 to 4	A.1
A.1: Selection of Transmitting Transducer Width	A.1
A.2: Definition of Fourier Transforms	A.3
A.3: Determining the Frequency Components for Broadband Pulse Excitation	A.4
A.4: Discussion on Experimental Factors Effecting Theoretical and Practical Comparison of Radiation Pressure Field	A.8
A.5: Calculation of B-coefficients from Relative Echo Amplitudes	A.10

Appendix B: MATLAB Software Code and Program Structures	B.1
B.1: Computation of Radiation Pressure Field from a Rectangular Transducer	B.1
B.2: Computation of Radiation Pressure Amplitude to Determine the Effective Target Area	B.5
B.3: Program Structure for Computing the 1 st - 3 rd Reflected echoes	B.9
B.4: Computation of 1 st Reflected Echo - Plane Target	B.14
B.5: Computation of 1 st Reflected Echo from a Curved Reflector	B.18
B.6: Computation of 1 st Reflected Echo from an Angled Reflector	B.20
B.7: Plotting of Circle Diagram for Efficiency of Transducers	B.21
B.8: Dynamic Impedance Matching of Cable	B.23
Appendix C: Practical Measurements for Verification of Theoretical Models in Chapters 2 - 4	C.1
C.1: Practical Measurements and Theoretical Investigation of the Sensitivity to Co-ordinate Changes for a Point Source Receiver	C.1
C.2: Practical Measurements and Theoretical Investigation of the Sensitivity to Co-ordinate Changes for a 2mm x 12mm Receiver	C.3
C.3: Practical Measurements and Simulated Results for Relative Amplitudes of Reflected Echoes (in oil)	C.4
C.4: Practical Measurements and Simulated Results for Relative Amplitudes of Reflected Echoes in Steel Block	C.6
C.5: Simulated Results for Relative Amplitudes of Reflected Echoes from a Curved Steel Target	C.8
C.6: Practical Measurements and Simulated Results for Relative Amplitudes of 1 st echo from an Angled Plane Reflector	C.9
Appendix D: Investigation of Received Echo Pulse-shapes (Chaps 2-3)	D.1
Appendix E: Data for Dynamic Impedance Matching of Cable	E.1
E.1: Simulated Tool Temperature Profile	E.1

Chapter 1

Introduction

1.1 The Problem of Scale Deposits in Petroleum Pipelines

In offshore locations pipelines remain the optimum solution for transporting large quantities of oil, gas, and water from production platforms and remote wells to onshore storage facilities over long distances. In the UK North Sea sector alone, it is estimated that some of these platforms are linked to shore by a network of some 5,600-km of offshore pipelines [1]. However, individual oil pipelines (also referred to as flowlines) may be relatively short, containing several hundred miles of pipes. The size of pipelines can vary in diameter from 2 to 60 inches; depending on the system capacity and volume to be handled [2]. Due to this large and extensive usage of pipelines they are continually monitored to ensure a 'fitness for purpose'.

During production of crude oil from an offshore well or reservoir there is often the problem of scale formation due to the mixing of injected seawater with formation water in reservoir rock formations [3]. As these mineral scales precipitate, they can adhere to pipelines causing a considerable decrease of oil flow, leading to large production losses and increased operating costs.

The most commonly found scales in offshore pipelines such as barium and strontium sulphate and calcium carbonate, are water insoluble. Figure 1.1 shows two examples of pipeline scale deposits [4].

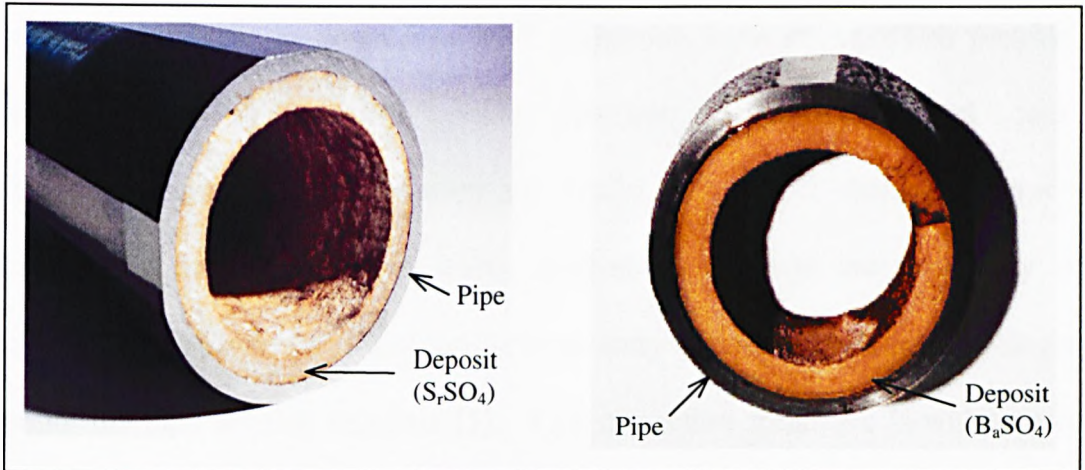


Figure 1.1: Typical scale deposits in petroleum pipelines

To prevent scale formation in the first instance, scale inhibitors (chemical based) are injected into the suspected regions of scale formations in the reservoir. Although this technique has proven effective in some offshore operations, it is expensive and difficult to monitor the effectiveness. For heavily scaled pipes de-scaling operations are required whereby expensive chemicals are pumped into the pipeline to dissolve the deposits at elevated temperatures. However, for effective remedial treatment of the deposits using chemicals, knowledge about the composition and thickness of the deposits is highly desirable, as they vary widely. This requires detailed inspection of the pipeline, e.g. using advanced non-destructive testing (NDT) and other methods based on the knowledge of formation water chemistry etc. to obtain information about the extent and composition of scales. The work presented in this thesis is concerned with detection and dissolution enhancement of scale deposits using ultrasound.

1.2 Current Inspection Tools and Cleaning Techniques

1.2.1 Review of NDT Inspection Tools

Recent developments in down-hole NDT inspection have attempted to provide the offshore pipeline industry with accurate detection and monitoring techniques for defects and flaws, such as corrosion and cracks. To detect changes in pipe-wall thickness, inspection techniques using mechanical callipers are frequently used. Typically, the inspection tool will consist of an array of pressure sensor multi-fingers to measure the pipe internal diameter [5]. This inspection technique is widely used in industry due to its good accuracy, although it does not provide a complete coverage inside the pipe. Also the hard-surfaced fingers can damage the pipe surface. A much improved measurement method for wall-thickness is based on ultrasonic techniques, giving a higher resolution and surface coverage, as well as accurate results. Ultrasonic calliper tools can give greater area coverage of the pipe compared to mechanical types and can also obtain information about the condition of the external surface of the pipe-wall as well [6].

At present, NDT based inspection in the form of in-line inspection tools (ILI) provide information about the pipe related to parameters such as, geometry and diameter measurement, bend measurement, corrosion and leak detection [7]. Figure 1.2 shows one such example of an in-line ultrasonic inspection tool that measures the internal diameter of the pipe to detect any metal loss [8].

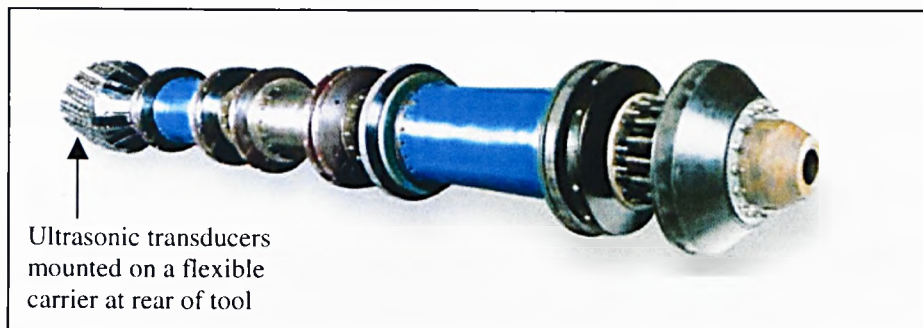


Figure 1.2: In-line ultrasonic inspection tool for corrosion detection (courtesy of PII Group Ltd)

The above tool uses an array of transducers located at the rear end to measure (a) the distance between the transducer and inner wall and (b) wall thickness. Data is then pre-processed on-board and recorded for later analysis. To interpret the data, customised software is used which maps the internal surface profile of the pipe-wall.

In the early 1980's development of pipeline inspection tools deploying ultrasonic inspection techniques were extended by means of intelligent inspection pigs [9]. These ultrasonic pigging systems provide accurate data of the metal loss in offshore pipelines with particular application for pipes with relatively large wall thicknesses.

The ultrasonic inspection pig developed by NKK is an example of this technology [10,11]. This pig is capable of inspecting over 1000 km of pipeline with high accuracy in a single run. The system measures metal loss by direct measurement of the fluid distance (distance between transducer and pipe wall) and the remaining wall thickness. Processed data regarding the wall thickness at various intervals along the pipe is then stored in a data recorder inside the main body of the pig.

As well as NDT based pipeline inspection, other methods such as visual inspection using a CCD (charge coupled device) camera have also been reported [12]. The

camera is mounted on a travelling vehicle along the pipe and is operated remotely, transmitting images via a cable. However these inspection devices can be expensive and have the disadvantage of not being able to provide quantitative measurements about the internal pipe condition, particularly with respect to pipeline deposits. Also these methods cannot be used during production, as the pipe needs to be either free of oil or filled with a clear medium like brine during inspection.

In summary, the general applications of the above type of inspection tools are mainly concerned with internal corrosion and defect monitoring (e.g. leaks, cracks). They do not provide reliable information about the type and volume of scale deposits in pipelines. It is widely acknowledged that there is a requirement for a multipurpose NDT inspection tool for accurate scale measurement and cleaning. The work presented in this thesis provides the basis of knowledge for development of such a tool. In this project, research has therefore been carried out in (a) facilitating reliable and accurate down-hole and top-side scale detection techniques and (b) methods of enhancing scale removal.

1.2.2 Cleaning Techniques for Scaled Pipes

Remedial treatments for scaled pipes involve the use of chemical de-scaling for the dissolution of the deposits or mechanical internal cleaning devices. The amount of chemicals used in chemical de-scaling is very much dependent on guesswork, as the composition and size of the scale is not known. Hence, this cleaning technique causes wastage of chemicals that are expensive and also lead to costly production shutdowns.

Furthermore, some hazardous chemicals used for cleaning can cause lasting damage to the pipelines by corrosion.

Mechanical internal cleaning devices consist mainly of pigs or high-pressure water jets. Pipeline pigs travel throughout the length of a pipeline, driven by the product flow. Utility pigs, which are used to perform this cleaning operation are available in different forms and designs (e.g. mandrel, solid casts, foam and spherical) depending on the application [7,13]. For example bi-directional pigs, the most frequently used types, are rugged and use a rigid sealing disk to aggressively scrape debris from the pipe wall. Gelled fluids can also be used with the pigs in long pipelines or where there is the possibility of the pig to become stuck due to debris build-up ahead of the cleaning pig [14]. The gels are normally used in conjunction with mechanical pigs to collect and suspend large volumes of debris ahead of the cleaning pig, therefore improving their performance. Two types of typical cleaning pigs are shown in Figs 1.3(a) and 1.3(b) [8].

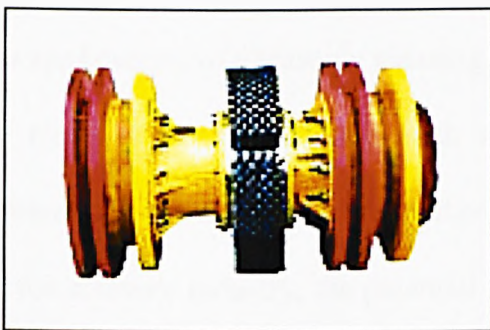


Figure 1.3(a): Circumferential brush pig



Figure 1.3(b): Bi-directional pig

Enhanced cleaning pigs are specially designed to be more aggressive than standard cleaning pigs and have been used for hard scale and wax removal from the internal pipe wall [15]. For a complete cleaning operation three types of enhanced pigs are inserted

into the pipeline: magnetic, pin wheel and brush wheel. Each type of enhanced pig gives a different level of cleaning force thus enhancing the cleaning process.

The problems associated with pigging as a de-scaling technique are that for optimum performance the type, location and volume of the substance to be removed should be known. Since different scales have different degrees of hardness, chemical resistance etc, the above information needs to be known to choose the appropriate devices or systems for de-scaling. As mentioned previously, these parameters at present, are not accurately known. Also pigs are only applicable for cleaning relatively thin layers of deposits/debris. The time required for cleaning is also quite considerable; as even for enhanced cleaning pigs several runs are required. As with chemical de-scaling there is the risk of damaging the internal pipe wall due to the abrasive mechanical cleaning action of the pig.

The Use of Ultrasound for Cleaning

The applications of ultrasonic cleaning are very widespread in industry and range from the cleaning of contaminants such as oil in fabrics to that of cleaning surgical instruments, and also in the preparation of semiconductor materials [16,17]. However, for the offshore industry, the potential of power ultrasound cleaning has not been well utilised except for some applications such as for the reduction of drill cuttings using intense ultrasonic energy [18].

It is known that ultrasonic cleaning can be far more effective and environmentally safer than many other methods. Ultrasound can also be used to accelerate chemical

processes. In these Sono-chemical processes and also in industrial cleaning applications mentioned above, the principle mechanism is considered to be due to 'cavitation' - i.e. energy released due to imploding microscopic bubbles formed by intense irradiation of ultrasound. This is a special branch of chemistry known as 'Sonochemistry' [19,20]. In the case of scale dissolution the mechanism may not be exactly the same as in sonochemistry, since it has been observed that the application of high-power ultrasound with existing chemical scale solvers could be used for the enhancement of scale dissolution at intensities below that required for cavitation [21].

1.3 Scale Detection and Dissolution Enhancement Using Ultrasound - A New Approach

In recent years a programme of research was initiated at The Robert Gordon University, to study the use of ultrasound for detection, characterisation and dissolution enhancement of scales in petroleum pipelines. This research was based on findings from an initial consultancy study that discovered the potential application of ultrasound for scale detection and cleaning [21].

1.3.1 Project Objectives

The long-term aim of the overall research project is to develop an integrated down-hole tool capable of scale detection and dissolution enhancement operations. The overall research programme in the research group identifies three main components that require study for implementation of such a tool.

These are:

- Down-hole scale deposit monitoring and characterisation in petroleum pipelines.
- Top-side (i.e. from pipe exterior) on-line monitoring of scale deposits.
- Ultrasonic scale dissolution enhancement during chemical de-scaling.

1.3.2 Deposit Location Techniques

Since scale problems occur in both top-side and sub-sea/underground pipelines, different techniques need to be developed to cater for the requirement in each case. For down-hole inspection techniques, analysis of the received echoes from a scanning transducer is applicable, whereas for top-side detection, extraction of representative features of the echoes from transducers located on the exterior pipe-wall could be used.

For **top-side** monitoring, feature extraction techniques have been successfully developed using acoustic impedance contrast analysis and frequency-domain features of acoustic signals received from a pipeline containing an unknown scale material, when insonified using high frequency broadband ultrasonic pulses [22,23]. Further work on **down-hole** scale detection and identification has been recently reported by Christidis [24-27]. In this work further extension of these techniques has also been carried out, particularly for aiding down-hole deposit location (Chapter 4).

With regard to top-side deposit detection, the approach previously developed requires the comparison of acoustic signatures from scaled and clean pipes. However, for practical implementation, the generation of reference templates for scale-free pipes in

all cases would require extensive (unlimited) data gathering, since the diameter and thickness of pipes are arbitrary. To successfully alleviate this situation extensive research in developing techniques for the generation of synthetic scans has been carried out in this project as one of the main objectives of the present study (Chapters 2-3).

1.3.3 Dissolution Enhancement of Scales

The conventional process of ultrasonic cleaning involves the use of high frequency sound waves, typically 18 to 120kHz, in a suitable liquid medium [16]. It has been widely reported that the main mechanism of ultrasonic cleaning is by means of cavitation [17]. This occurs under high intensity ultrasonic pressure variations in the liquid medium, in which microscopic bubbles implode or collapse on a hard surface. However it has been demonstrated that an effective cleaning process can take place at lower power levels, in the range of 100mW/cm^2 for the type of solvents used at temperatures in the range of $50^\circ\text{-}80^\circ\text{C}$ [21]. The present research study deals with optimising sonic radiation at these low power levels, in finite mediums such as in pipelines. The critical parameter associated with any sonic cleaning system is its efficiency. This primarily depends on the transducer design and also on the operational environment.

New Research on Dissolution Enhancement

During previous studies it was found that ultrasonic irradiation could largely enhance the scale dissolution rate, by as much as 17 times and to a lesser extent at lower power levels [16]. However, considering the cost of production shut-downs, an enhancement

of even 2 times is very significant. The actual process of dissolution enhancement is not very well known. However, it is likely that this may be due to a combination of effects such as, increased penetration of chemicals at the surface of scales, increase in diffusion or mixing of chemicals at the surface, thereby reducing saturation of reacted chemicals at the boundary layer formed at the surface of scales. To maximise the scale dissolution rate in pipelines, research into high power ultrasonic transducers and irradiation in confined spaces was required. Also, maintaining optimum power under environmental temperature variations is critical for this present application since scale de-scaling is carried out at elevated temperature zones. To address both these requirements research studies were undertaken as reported in the latter chapters of the thesis (Chapters 6 and 7).

1.4 Specific Objectives of the Present Project

The work assigned and reported in this thesis is mainly concerned with two main aspects: (a) aiding the location of deposits from both top-side and down-hole measurements and (b) ultrasonic scale dissolution enhancement. These two objectives are further described below.

a) Deposit Location

Existing techniques for deposit location from outer surfaces of pipes needed to be developed further. Hence, conducting research into techniques to facilitate the top-side deposit location process was a major objective of the present work. This required research into the development of a generalised mathematical model to represent top-

side acoustic scans as a solution to the problem of requiring acoustic reference templates. These artificially generated scans, corresponding to a given combination of transducer parameters and target layer dimensions can then be used as reference templates for feature extraction and location of deposits in scaled pipelines. This will provide an efficient and much improved top-side scale monitoring system suitable for practical use in the field.

For down-hole scale detection and monitoring, techniques previously developed under laboratory conditions require the probe to be correctly aligned with the pipe-wall [24]. This needed techniques to be developed for remote probe alignment by analysing the features of signals received from the test probe itself. This will provide critical data regarding the central alignment of the transducer for any down-hole measurements with regard to scale detection and identification.

b) Dissolution Enhancement

Unlike in the case of industrial ultrasonic cleaning, the main problems associated with transmitting high-power ultrasonic energy into confined spaces as found during the course of this project (Chapters 5 & 6) are: limited transmitting transducer surface area, silent spots due to standing waves and variable load conditions giving acoustic impedance mismatch [17, 28-29]. Hence, research into improving the radiation resistance of ultrasonic power transducers, radiating into pipes was also undertaken. That required detailed analysis of the power transfer characteristics of such transducers having a limited radiation surface area as would be the case with pipelines. Another primary requirement is to conduct research into methods of parametric stabilisation of

transducers and cables by developing a dynamic compensation strategy to optimise performance, thereby providing optimised ultrasonic irradiation in pipes during descaling operations.

It should be mentioned however that due to the very involved and diverse nature of this subject, the investigations carried out were limited to the following.

1. Development of mathematical models to synthesise the reference multiple echoes from plane and cylindrical objects for top-side deposit location.
2. Practical evaluation and theoretical modelling of a novel remote probe sensing technique using the symmetry of received signals to aid down-hole deposit location.
3. Investigation of impedance matching techniques for increasing the sonic radiation of ultrasonic transducers in pipes. Also a dynamic compensation network for a transducer-cable system operating in high temperature environments has been proposed as future development.

1.5 Systems Overview

1.5.1 Top-side System

The main components of the top-side detection system involves a high frequency (low power) transducer bonded to the outer surface of the pipe as shown in Figure 1.4.

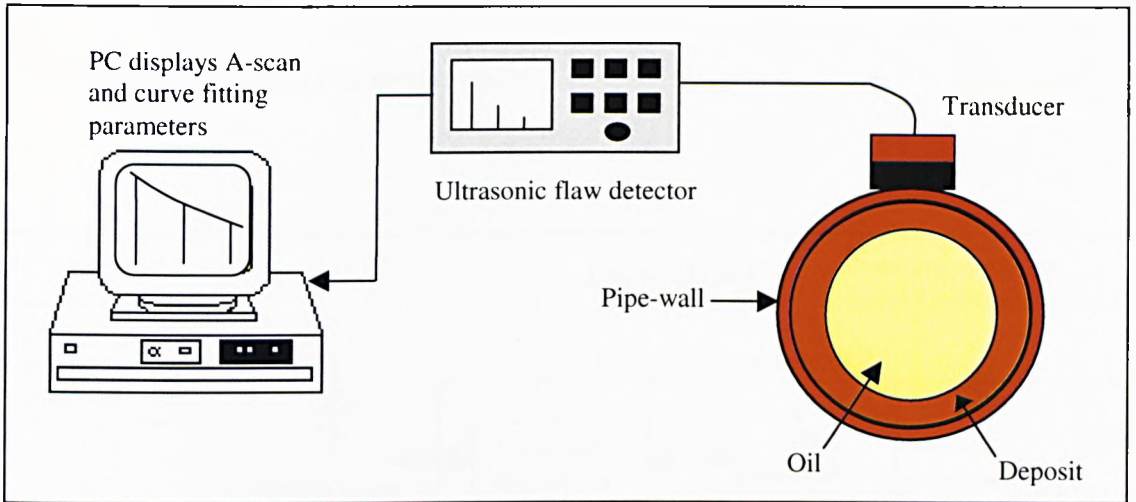


Figure 1.4: Top-side detection system

The received signals are transferred to a PC for analysis via an ultrasonic flow detector. The above system produces a series of A-scan signals, which are to be compared with stored acoustic templates. However it is practically impossible to obtain reference A-scan signals for all cases. Hence, developing a synthetic A-scan technique from given pipe and transducer parameters is one of the main areas of the present work.

1.5.2 Down-hole System

The schematic diagram in Figure 1.5 shows the main functional units of the proposed down-hole tool system. The basis for development of this system has been reported previously by Christidis [24]. It is proposed that the down-hole system will firstly operate in detection mode to identify the location of scale deposits, and then in dissolution mode using high power ultrasound to aid the dissolution of scales. A PC workstation will control the operation of the down-hole tool from the top-side end. Communication between the PC and the tool and also the power transfer from the top-side to the tool are all achieved via a single coaxial transmission line. The PC also

controls the front-end electronics of the tool and processes and displays information about any scales or dissolution operations.

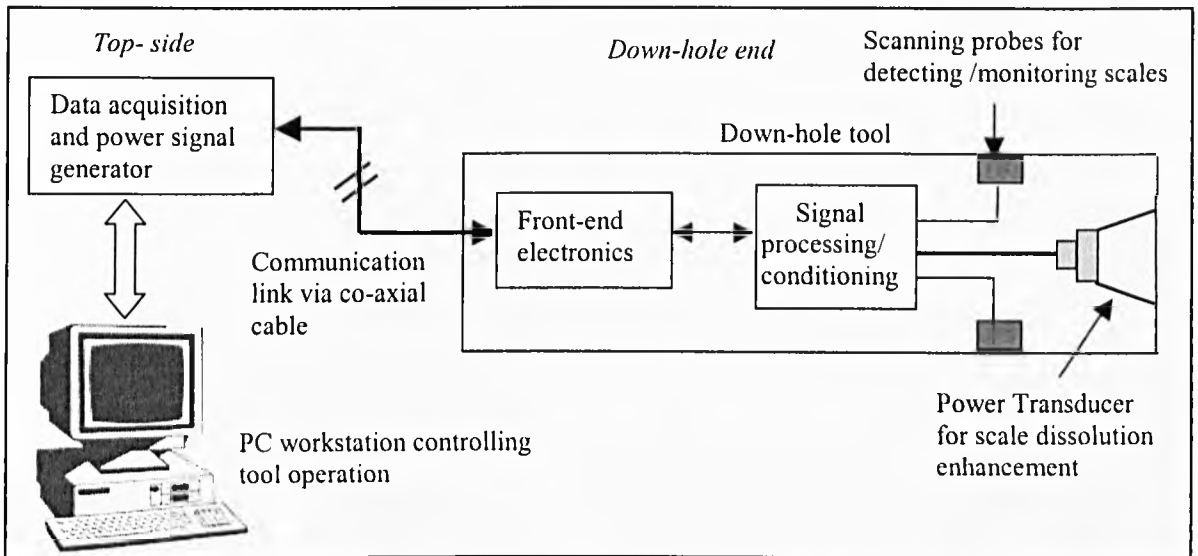


Figure 1.5: Block diagram of the proposed ultrasonic down-hole tool

Largely on the basis of distance and cost considerations, a single coaxial line has been chosen for transmitting both data and power from top-side. However this requires the transmission cable to transmit both low and high frequency signals to the tool over long distances, in some cases for several kilometres. High frequency digital signals are required for the monitoring and characterisation of scale deposits. Medium-to-low frequency (high power) drive signals are required for the power transducers when scale dissolution is required. The same transmission line also transmits low voltage control signals for the operation of the front-end electronics. All these transmission requirements are co-ordinated on a time-sharing basis.

1.6 Structure of Thesis

The thesis is divided into eight main chapters. Figure 1.6 shows the thesis layout in a flowchart form.

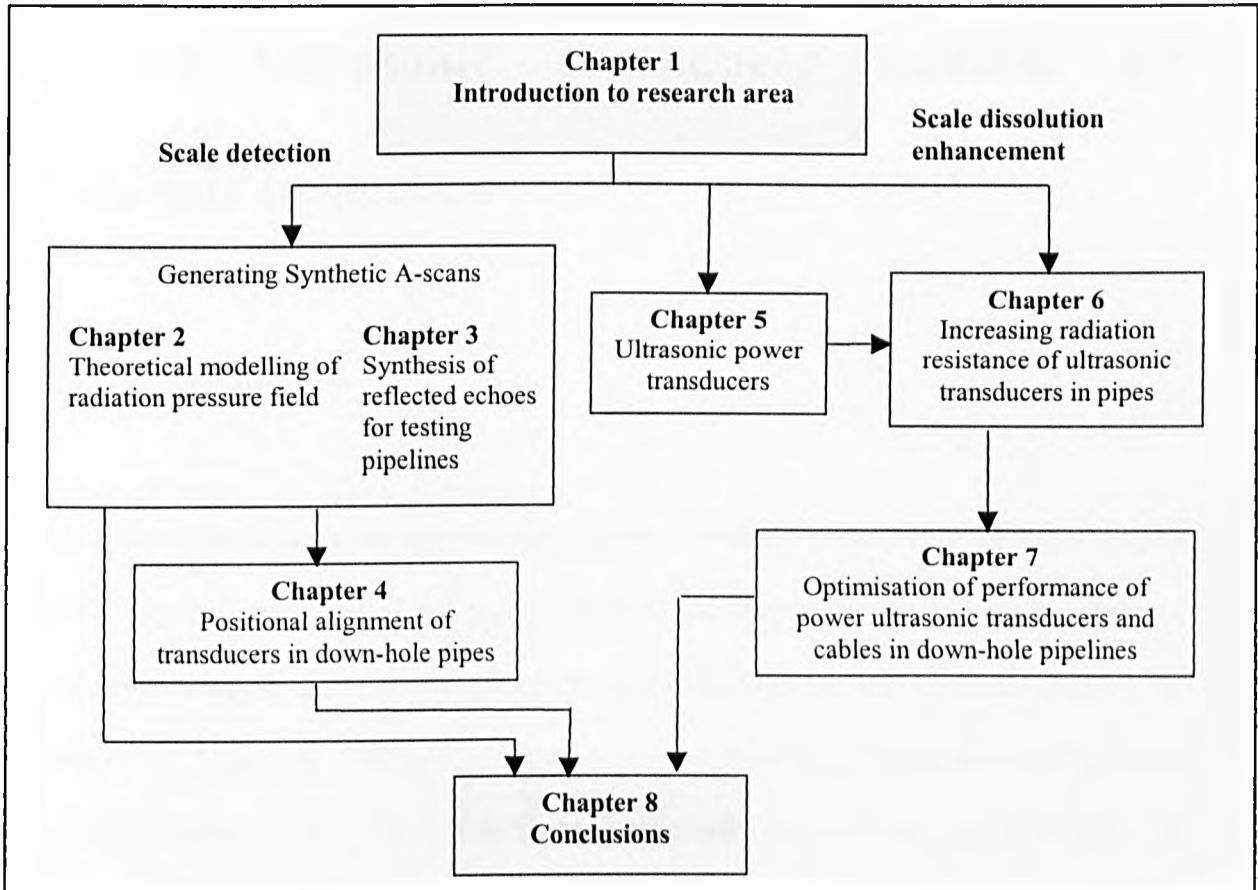


Figure 1.6: Thesis structure

Chapter 2

Modelling and Verification of the Radiation Field of an Ultrasonic Transducer Suitable for Top-side Inspection

2.1 Introduction

Apart from the needs in the present application, quantitative ultrasonic testing of targets often requires comparison of signal features of targets with respect to standard reference samples. Typical examples of these can be found in the American Society for Testing of Materials (ASTM) and the American Society of Mechanical Engineers (ASME) codes [30,31]. However, making standard reference samples to be used as acoustic templates as in the present application for top-side inspection is very difficult, since the object profiles and dimensions are unlimited. A proposed solution to this problem is to artificially generate the acoustic signatures given the dimensions of the object, target parameters, and the characteristics of the test probe.

The first step in this task was therefore to choose an appropriate transducer and to mathematically model and verify its radiation characteristics. This was an involved task and the work carried out is presented in two stages. The first stage as reported in

this chapter deals with the development and verification of a computational model simulating the radiation pattern of a narrow rectangular transducer. Having verified the model, the following chapter deals with the actual generation of synthetic A-scans.

2.2 Previous Work on Transducer Modelling for Ultrasonic Inspection of Pipelines

There is a vast amount of literature available on various modelling techniques for calculating the acoustic fields of NDT ultrasonic transducers [32-34]. However for applications where the contact surfaces are not planar, such as testing of pipelines from exterior surface, there has not been much work reported on simulating A-scans.

Some work has been reported by Birchak and Serabian [35] where an empirical solution to pulse-echo ultrasonic inspection (applicable to some cases) has been proposed. However, this solution caters for compensation of signal amplitude only, with an uncertainty of at least $\pm 2.5\text{dB}$. Also, it does not reveal changes to other important signal features, e.g. changes in frequency domain characteristics. Hence this method is not applicable for high precision work, such as testing of pipelines for scale deposits where greater accuracy and fine details are required. As such, the approach taken in this work is to construct reference signals by a process of numerical computation using fundamental properties of acoustic waves and boundary transmission characteristics.

2.2.1 Petroleum Pipeline Scales

Predicting the location of scale deposits from exterior surface of pipelines using ultrasound measurements has been demonstrated previously [22,23]. In this approach, as shown in Figures 2.1(a) and (b) the amplitude and frequency spectra of the multiple echoes generated within the pipe-wall of scaled pipes are compared with that of scale-free samples of the same dimensions.

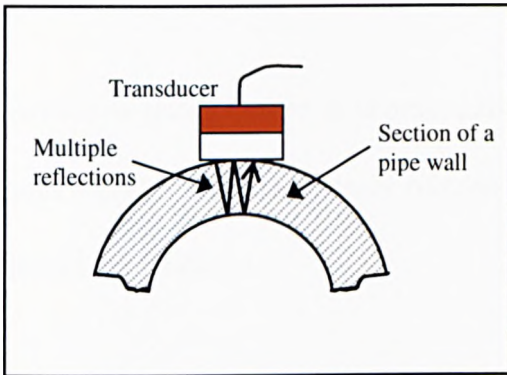


Figure 2.1(a): Clean pipe

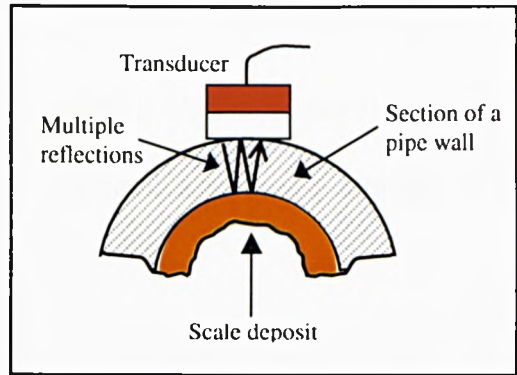


Figure 2.1(b): Pipe with a scale deposit forming

During previous work in the project, dedicated software (MSDPP) has been developed to acquire and analyse the multiple echoes produced when testing a pipe from the exterior surface [36]. Figures 2.2(a) and (b) show an example of the A-scans showing such multiple echoes received by a 5MHz broadband probe from a pipe-wall.

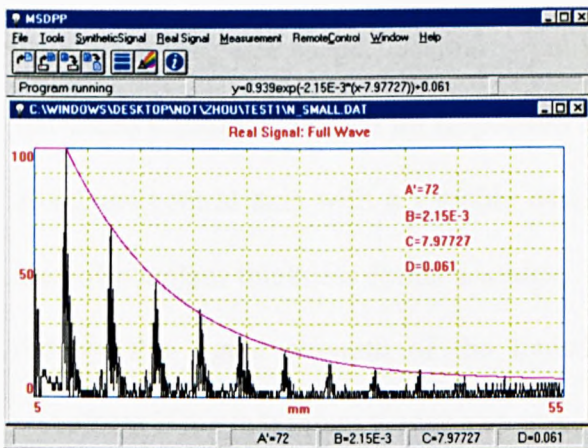


Figure 2.2(a): A-scan features of a clean pipe

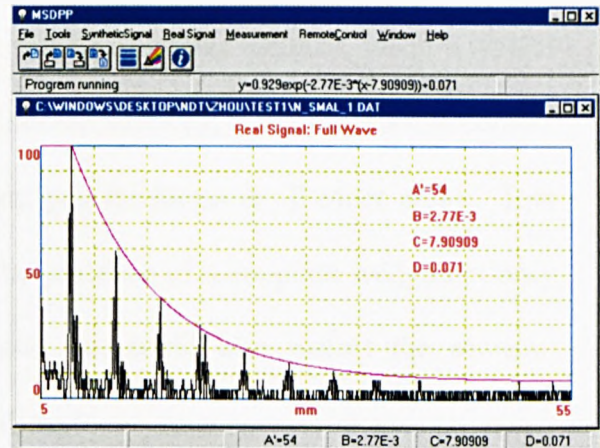


Figure 2.2(b): A-scan features of a pipe with a scale deposit forming beneath the pipe wall

The coefficients A-D as defined below generate a mathematical function of the form

$$y = A e^{-B(x-C)} + D \quad (2.1)$$

Where A is related to the first echo amplitude, B to the decay of series 1 reverberations, C to the timing of the 1st echo and D to the signal-to-noise ratio [22,23].

However as stated before, it is practically impossible to obtain the reference scans as in Figure 2.2(a) for all cases, since tubings can be manufactured to any dimensions to suit required applications.

2.2.2 Generation of Synthetic Scans

It has been previously shown that one way of simulating multiple reflections produced due to a given probe at normal incidence within a *planar*, layered material is by using boundary transmission and reflection coefficients [3,22,23]. However in the present case there are two main problems that do not allow the direct use of this method. Firstly, the contact and target surfaces are not planar, but *cylindrical* that causes changes to the pulse shape. Secondly, unlike testing of planar surfaces, when a typical flat-faced transducer is used for inspection of curved surfaces, it produces a line contact along the central axis with a variable couplant gap thickness at all other areas. This area of couplant thickness forms a *wedge*. The presence of a couplant wedge not only reduces the signal strength of the transducer, but could also distort the acoustic waveform if the maximum wedge-gap is significant.

Hence, the approach taken in this work for synthesis of acoustic signals is to develop a numerical model based on Huygens Green function [37, 38] taking into account the test object dimensions. The Huygens Green Function enables the calculation of the pressure field in a given medium due to a transmitting probe, by considering the transmitting surface of the transducer as a wavefront with an infinitely large number of point sources. The transmitting transducer selected for this work had a rectangular aperture of 2mm x 12mm with an operating frequency of 5MHz. The dimensions (2mm x 12mm) were chosen so that the maximum wedge gap is limited to within $1/10^{\text{th}}$ of the wavelength of sound in the couplant, for the maximum test surface curvature of interest (Appendix A.1).

2.3 Approach for Synthesising Ultrasonic A-scans Using Transducer and Target Parameters

In the present approach, the transmitting transducer is considered as having a large number of elementary (Huygens) sources (Fig.4) and the target area defined by a similar distribution of elementary receptors (Fig.5). The pressure field created by the transmitting sources at a given target area is obtained by numerical summation of pressure fields produced by individual sources. The received signal after reflection from the target is then computed by treating the target as a transmitter in the reverse direction. In this way, signals could be synthesised from a given set of parameters to represent echoes corresponding to reference targets. The process of signal synthesis involved the following main steps as shown in Figure 2.3.

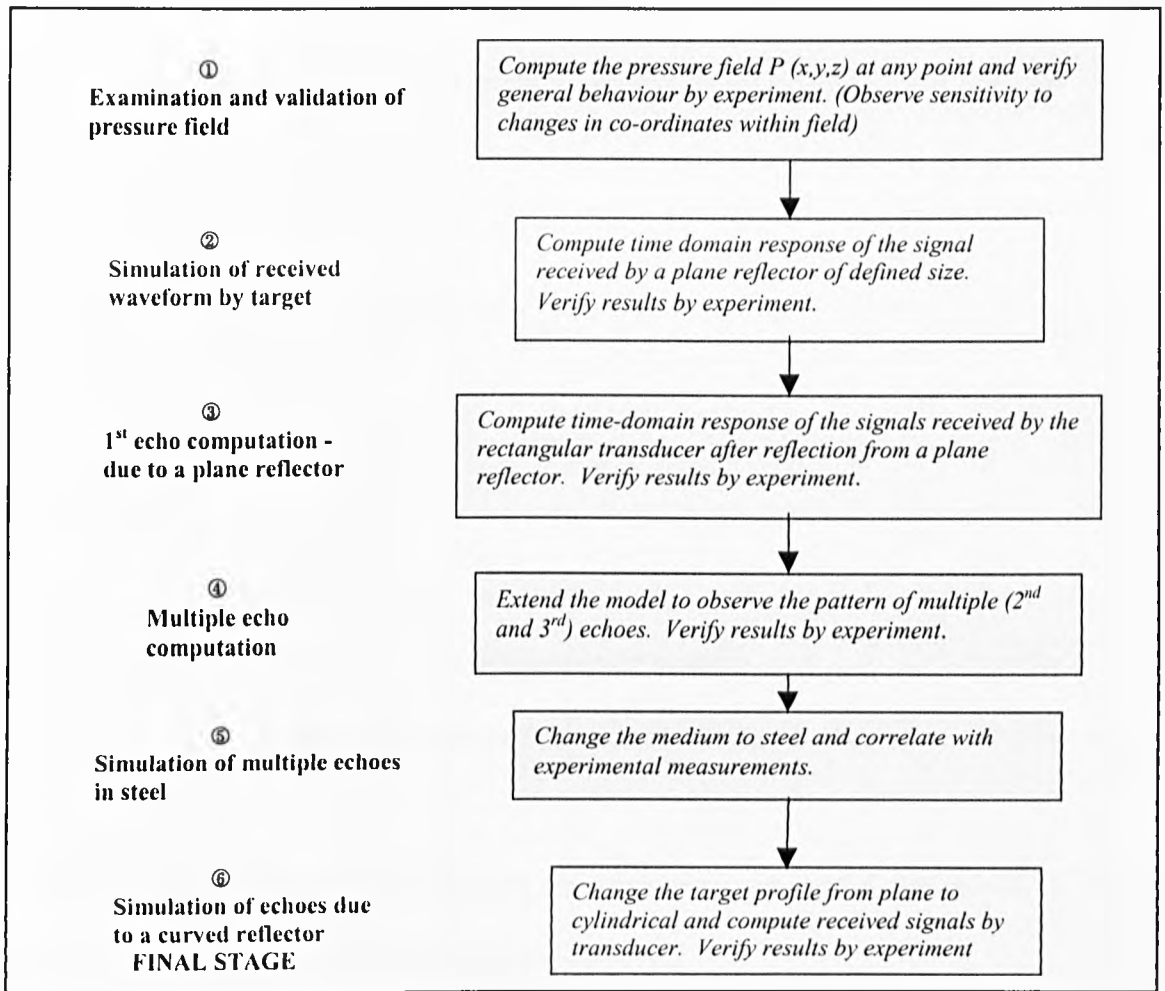


Figure 2.3: Approach for generation of acoustic signatures

This chapter presents the work carried out and results obtained on the first two main tasks, ① and ② respectively.

2.4 Theoretical Modelling of a Rectangular Ultrasonic Transducer

2.4.1 Computation of Radiation Pressure Field

A transducer of a finite size, where all points on its surface oscillate with the same amplitude and phase, can be considered as being composed of an infinite number of point sources, each radiating a spherical wave. The contribution of a small element of

the transducer surface (Δs) to the acoustic pressure P at a given point (x,y,z) for continuous emission for a single frequency, is given by Huygens Green function [37], such that

$$P(x,y,z) = A \frac{\exp(-jkr)}{r} \Delta s \quad (2.2)$$

where:

A is a constant

$k = 2\pi/\lambda$; λ is the wavelength in the medium

r = distance to the point from the elementary source

Figure 2.4 shows the geometry of a finite rectangular transducer of dimensions $(a \times b)$, representing a matrix of $(n \times m)$ elementary sources.

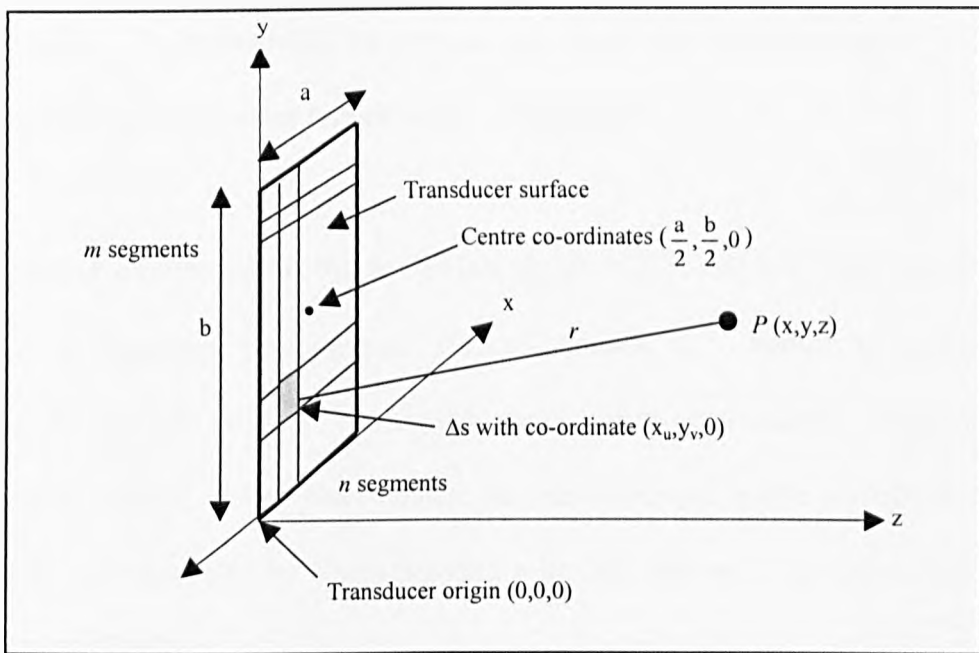


Figure 2.4: Geometry of a rectangular transducer with dimensions $(a \times b)$ and elements $(n \times m)$

To obtain a numerical solution to the pressure distribution due to a rectangular transducer, at a point $P(x,y,z)$, the pressure contributions from all the elements on the transducer surface are summed.

With reference to Figure 2.4, the pressure at point $P(x,y,z)$ due to *continuous* excitation at a single frequency can then be written as

$$P(x,y,z) = A \sum_{v=1}^m \sum_{u=1}^n \frac{\exp j\left(-\frac{2\pi}{\lambda} r\right)}{r} \Delta s \quad (2.3)$$

where

$$r = \sqrt{(x - x_u)^2 + (y - y_v)^2 + z^2}$$

$$\Delta s = \left(\frac{ab}{mn} \right)$$

and $u = 1, 2, 3 \dots n$ representing the element number in the x-direction and $v = 1, 2, 3 \dots m$ representing the element number in the y-direction.

In the present case however, the excitation signal is a broadband *pulse* containing a spectrum of frequency components. Hence, equation (2.3) should be extended to represent broadband emission. Although the number of frequency components is theoretically infinite, it has been shown that an ultrasonic pulse waveform can be adequately re-constructed by superimposing a limited number of dominant frequency components [39,40].

Using the above approach, the pressure distribution at point $P(x,y,z)$ due to a broad-band pulse excitation can then be written as

$$P_s(x,y,z) = A \sum_{v=1}^m \sum_{u=1}^n C_s \frac{\exp j\left(-\frac{2\pi f_s}{c} r\right)}{r} \Delta s \quad (2.4)$$

where C_s is the amplitude of the s^{th} frequency component (f_s) of the pulse, c is the speed of sound in the propagating medium, $s = 1,2,3,4, \dots w$; w is a finite number of dominant frequency components chosen to represent the broad-band *pulse* in the frequency domain. For the present work C_s was obtained using the frequency spectrum of a particular 5MHz broadband transducer (pages A.6/A.7). It was found by experiment that approximately 22 frequency components centred around the mean frequency covering up to the 1st minima of the spectrum was adequate to represent the pulse waveform (results shown in Appendix A.3).

To obtain the time domain pressure signal at any point in the field of the rectangular transducer, the Inverse Fast Fourier Transform (IFFT) was used (Appendix A.2). By performing an IFFT operation on the frequency spectrum produced by equation (2.4) the time domain pressure response, $P_{(t)}(x,y,z)$ was computed, such that

$$IFFT \left[P_1(x,y,z), P_2(x,y,z), P_3(x,y,z), \dots P_w(x,y,z) \right] \Rightarrow P_{(t)}(x,y,z) \quad (2.5)$$

Using this approach it was possible to examine the time-domain pressure waveform at any point in a defined target region by varying the co-ordinates as required, and the sensitivity to change in co-ordinates around a given point (x,y,z) . This latter aspect was

very useful in verifying the theoretical model by practical measurements. This is because the sensitivity to changes in co-ordinates is far more easier to assess in the present case than comparison of actual waveforms, since the latter is more sensitive to the non-ideal nature of the practical measurement system (as found during the measurement process in section 2.5).

2.4.2 Determination of Effective Target Area

The main purpose of this investigation is as follows: Firstly it is known that transmitted signals spread-out in the medium due to diffraction. Clearly, the diffracted signals received along the width of the receiver fade rapidly as the receiver width is increased. Therefore, when computing signals reflected back from a target, the *effective* target area must be known.

To determine the effective target area as required for computing reflected signals, the above mathematical model represented by eqⁿ (2.4) and (2.5) was then extended to determine the total pulse pressure amplitude over a given target area. In this way, by gradually extending the size of the target area and observing the changes in pulse shape and amplitude, the effective reflector area could be determined. Figure 2.5 shows the target area as defined by dimensions ($a_r \times b_r$), representing a matrix of ($n_r \times m_r$) elementary receptors.

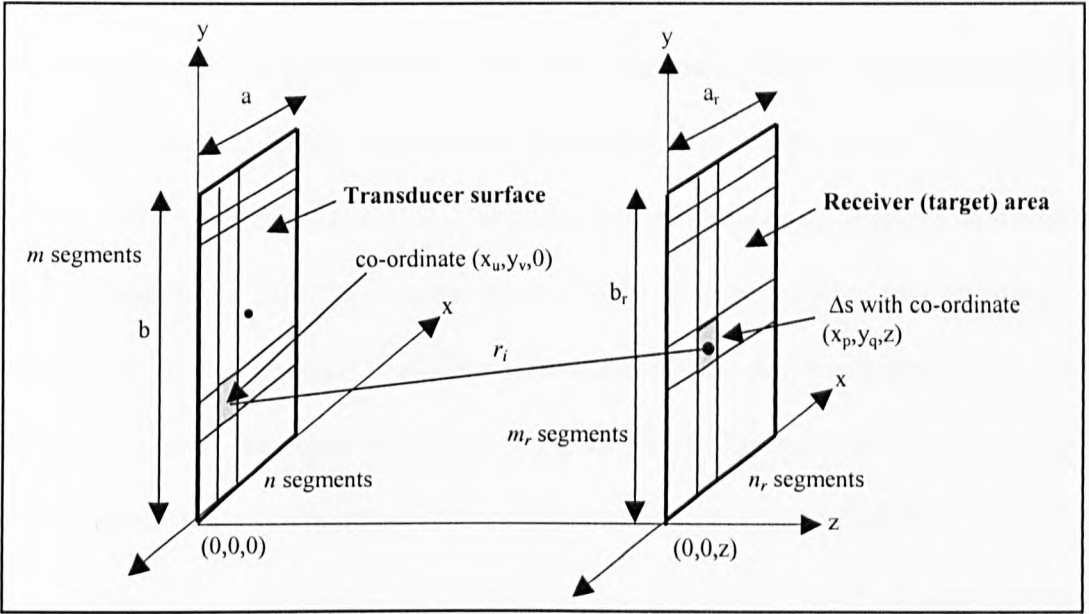


Figure 2.5: Representation of receiver (target) area with dimensions $(a_r \times b_r)$ and elements $(n_r \times m_r)$

The extended algorithm to calculate the received signal by the target as shown in Figure 2.5, would then be

$$P_{s(RI)} = A \sum_{q=1}^{m_r} \sum_{p=1}^{n_r} C_s \cdot \frac{\exp j\left(-\frac{2\pi f_s}{c} r_i\right)}{r_i} \Delta s \quad (2.6)$$

where

$$r_i = \sqrt{(x_p - x_u)^2 + (y_q - y_v)^2 + z^2}$$

and $p = 1, 2, 3 \dots n_r$ representing the target element number in the x-direction and $q = 1, 2, 3 \dots m_r$ representing the target element number in the y-direction.

2.5 Experimental Verification of the Theoretical Model

2.5.1 Radiation Pressure Field

The first step was to validate the theoretical model defining the radiation field as in eqⁿ (2.4) using practical measurements. For this purpose, a 5MHz broadband circular probe, was masked to define the required aperture (2mm x 12mm) and was placed in oil ($c = 1450$ m/s). Also, a small circular aperture was made on an identical transducer, again by masking, to form an elementary receiver*. The received signal by this point receiver was then examined at different co-ordinates in the transmitter field. The theoretical response was then computed using eqⁿ (2.4) (Appendix B.1) and compared with the practical measurements and sample results are given in section 2.6.

The transmitter and receiver transducers were mounted on adjustable metal clamps for positioning. The z-axis distance between the transmitter and receiver surfaces was varied in steps using solid separator blocks. The (x,y,z) scanning about a given point, was controlled manually using a vernier micrometer arrangement connected to the receiver transducer, with the transmitter remaining stationery. Figure 2.6 shows the practical measurement system used.

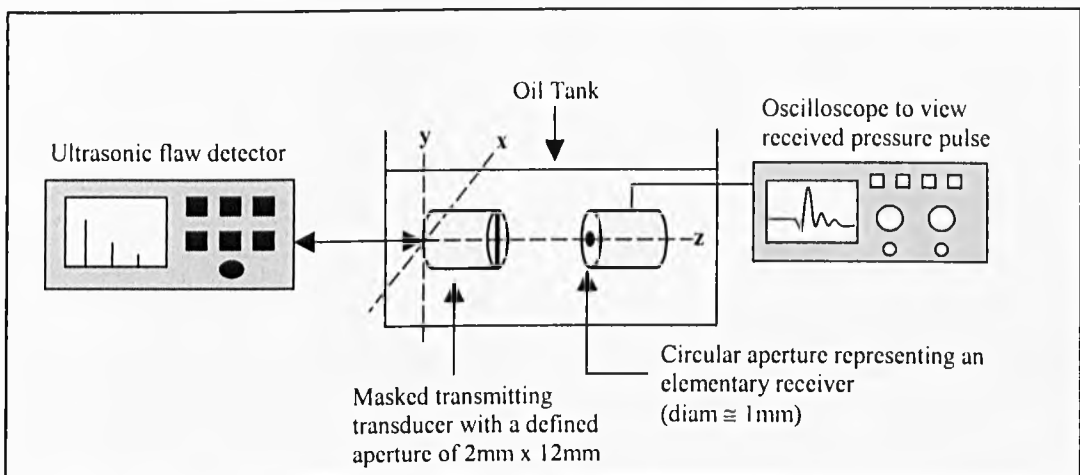


Figure 2.6: Practical measurement system for verification of simulated pressure field

* It should be mentioned that an ideal source/receiver combination cannot be obtained in this way due to the finite size, masking thickness and bandwidth limitation of the receiver. However for observing general agreement of trends between theoretical predictions and practical measurements, this arrangement was found to be adequate. Further discussion on this is included in Appendix section A.4.

2.5.2 Effective Reflector Area

The next step was to investigate the effective surface area of the reflector using both simulations (Appendix B.2) and practical measurements. For practical measurements, the same set-up in Figure 2.6 was used except that the receiver aperture was made to be rectangular, with the dimensions being gradually increased.

2.6 Results

2.6.1 Radiation Field Profile

Figure 2.7(a) shows the computed signal as received by an elemental receptor area of the target on the central axis, 13mm from the transmitting transducer. Figure 2.7(b) shows an example of the practical measurement for the same distance using the above experimental set-up. It should be mentioned that a 300 point IFFT was used for all computations by zero-padding the 22 frequency components, to effectively obtain interpolated points giving a smooth time-domain display.

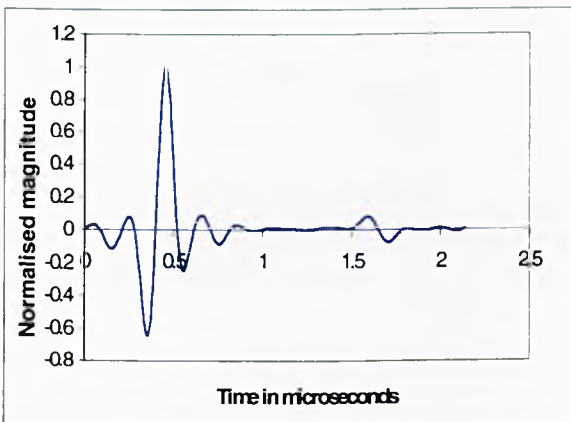


Figure 2.7(a): Simulated pulse received by a point receiver at centre using a 300 point IFFT



Figure 2.7(b): Results from practical measurement. Vertical axis = 5mV/div
Horizontal axis = 0.5 μ s/div

Although the actual pulse shapes observed were somewhat different to the computed pulse, as would be expected due to the non-ideal nature of the practical source and receiver compared to the theoretical model, the general agreement of the simulated and practical measurement can be clearly seen from Figures 2.7(a) and 2.7(b).

Experiments were then conducted to examine the general features of the pressure field, for example the sensitivity to co-ordinate changes. This was done by repeating the above computations and practical measurements for a range of co-ordinates, and also for small variations around those co-ordinates.

Tables 1(a)-(f) in Appendix C.1 shows representative results of theoretical and practical measurements for the sensitivity to co-ordinate changes, for different transmitter/receiver (z-axis) separations. Figures 2.8(a)-(f) shows these results in graphical form.

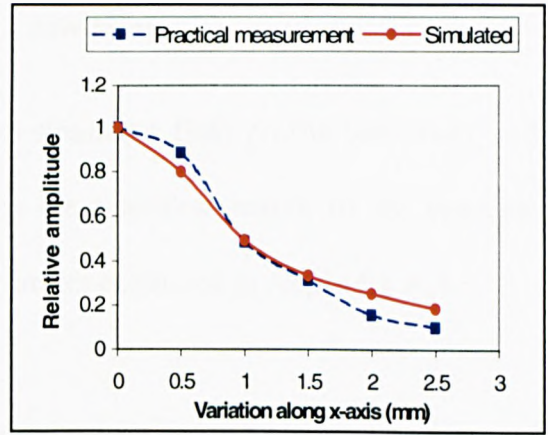
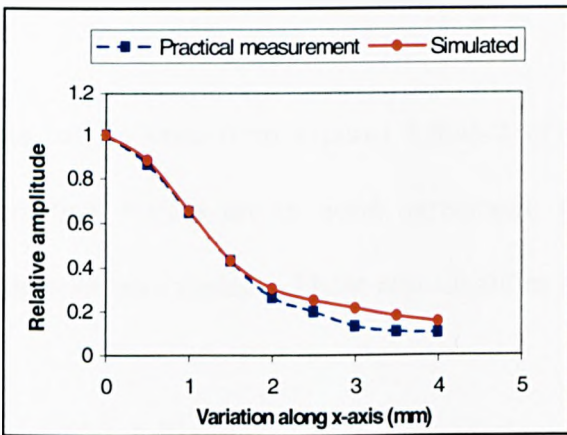


Figure 2.8(a): Pulse amplitude variation along x-axis. Starting co-ordinate (0, 0, 13mm)

Figure 2.8(b): Pulse amplitude variation along x-axis. Starting co-ordinate (0, 0, 9.12mm)

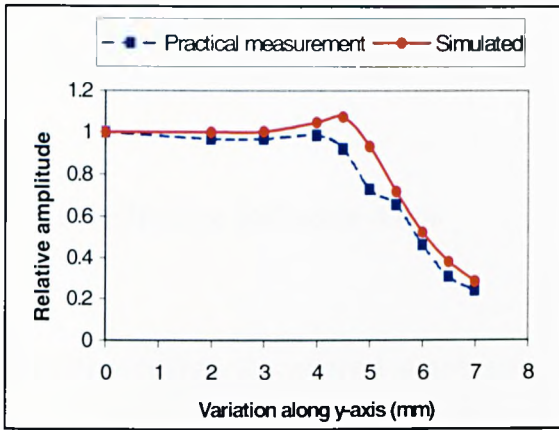


Figure 2.8(c): Pulse amplitude variation along y-axis. Starting co-ordinate (0, 0, 13mm)

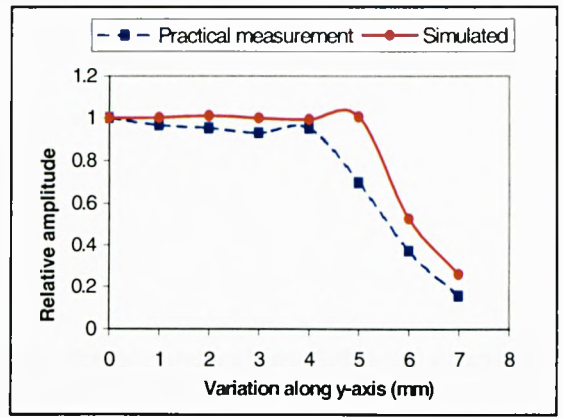


Figure 2.8(d): Pulse amplitude variation along y-axis. Starting co-ordinate (0, 0, 9.12mm)

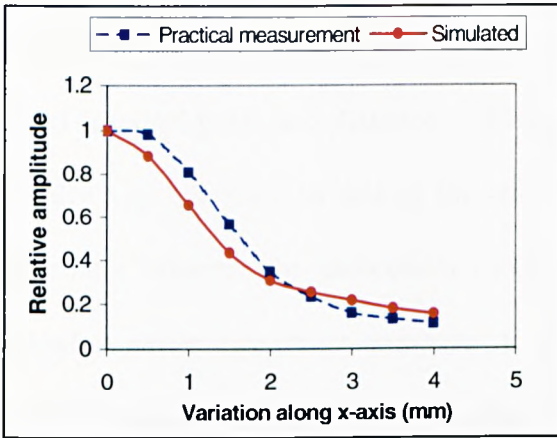


Figure 2.8(e): Pulse amplitude variation along x-axis. Starting co-ordinate (0, +1mm, 13mm)

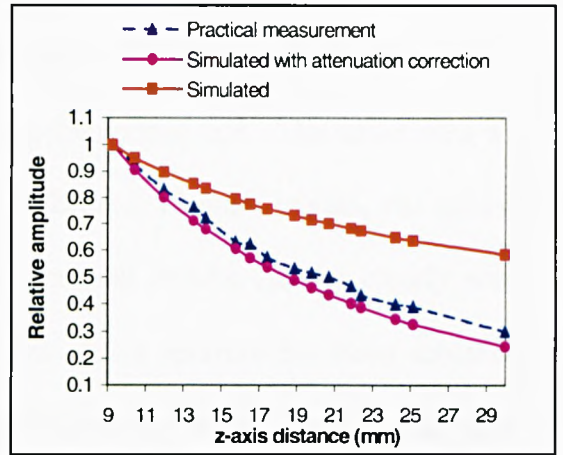


Figure 2.8(f): Pulse amplitude variation along central z-axis - attenuation correction introduced

As can be seen from Figures 2.8(a)-2.8(f), the simulated field profile sensitivity and practical results are in good agreement, given the non-ideal nature of the practical measurement system. These non-idealities are further explained in Appendix A.4.

Also the initial theoretical computations did not take into account the effect of attenuation in the medium. This was then introduced into the model (Appendix A.4, section 4). The improvement in results was very significant as can be seen from Figure 2.8(f) where the axial z-co-ordinate is varied. The improvement in the case of fixed z-

axis were not that significant, as would be expected, since there is no significant change in acoustic path length in these cases.

2.6.2 Effective Reflector Area

Having verified the general agreement between the theoretical model and practical measurements for obtaining the radiation field profile of the transducer, the next stage was to determine the *effective* reflector area, again by both theoretical and practical examination. Figures 2.9(a) and (b) show an example of the computed response and the actual received pulse at a distance of 13mm along the central axis. The target area was initially kept identical to that of the transmitter (2mm x 12mm). Again, the general agreement between the theoretical model and practical results can be clearly seen. Indeed, a closer agreement compared to the point source aperture has been achieved, since in the case of a practical point-source aperture the effects of non-idealities are much more pronounced.

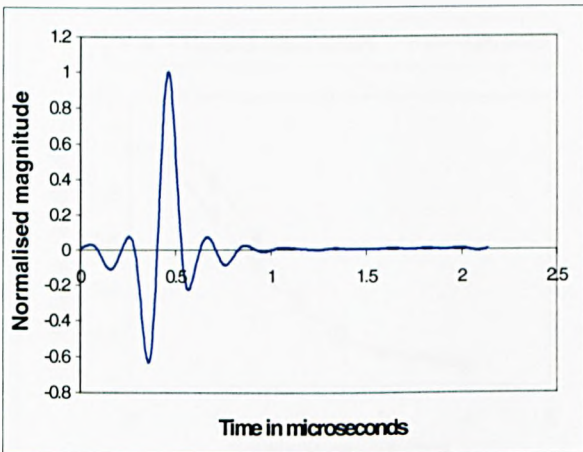


Figure 2.9(a): Simulated pulse using a 300 point IFFT **Figure 2.9(b): Measured pulse by practical measurement system. Vertical axis = 0.1V/div**
Horizontal axis = 0.5μs/div

Tests were also carried out to observe the sensitivity to co-ordinate changes as before with the rectangular receiving aperture. Figures 2.10(a) and (b) show a representative example of this at an edge point (-3mm, +2mm, 13.5mm) from the origin.

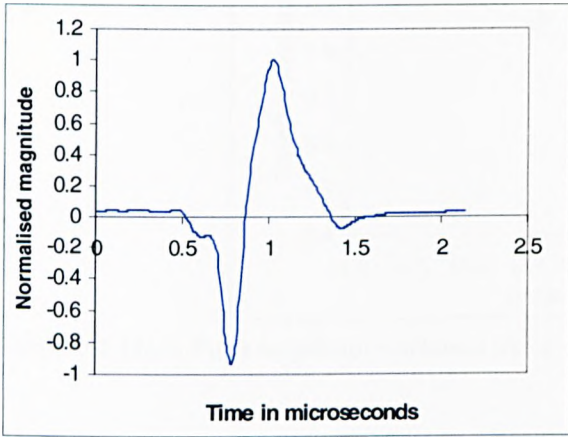


Figure 2.10(a): Simulated pulse received by defined receiver aperture at an edge point using a 300 point IFFT

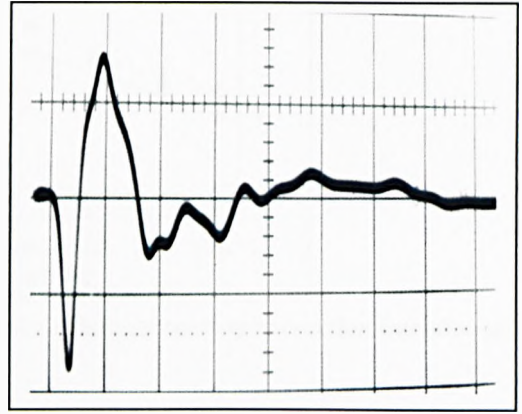


Figure 2.10(b): Measured pulse by practical measurement system.
Vert. axis = 10mV/div Horiz. axis = 0.5 μ s/div

Tables 1(a)-(c) in Appendix C.2 show representative results of theoretical and practical measurements for the sensitivity to co-ordinate changes at a z-axis distance of 13.5mm.

Figures 2.11(a)-(c) shows these results in graphical form.

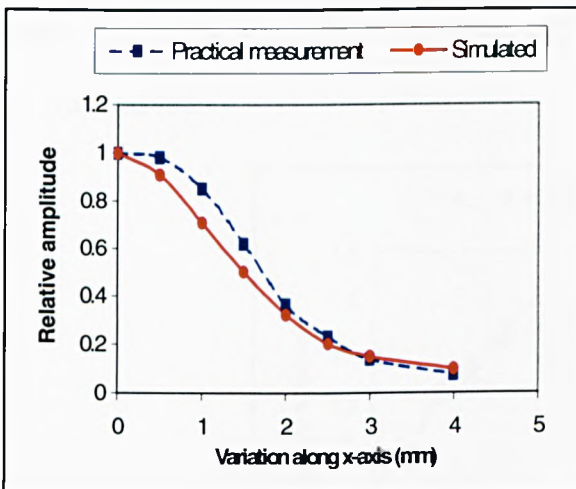


Figure 2.11(a): Pulse amplitude variation along x-axis. Starting co-ordinate (0, 0, 13.5mm)

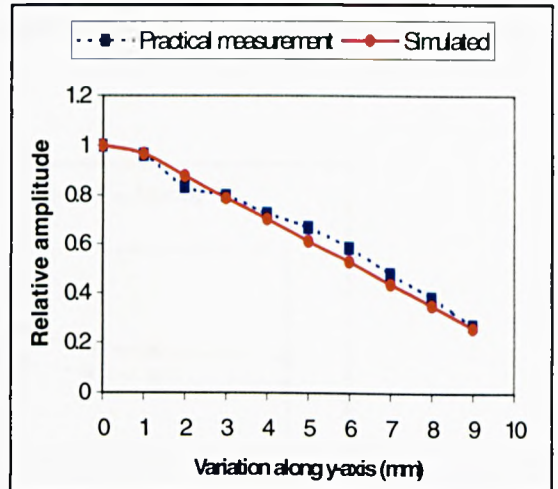


Figure 2.11(b): Pulse amplitude variation along y-axis. Starting co-ordinate (0, 0, 13.5mm)

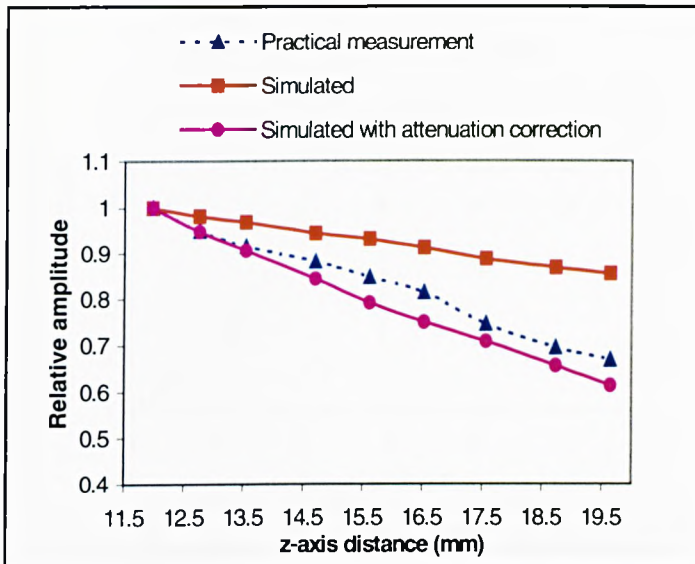


Figure 2.11(c): Pulse amplitude variation along central z-axis (attenuation correction introduced)

Having verified the model by waveform comparison and quantitative results for two different cases, namely, point source receiver aperture and a rectangular receiving aperture, the next step was to find the *effective* target area by gradually increasing the receiver aperture size, and repeating the process of computation and measurement.

The maximum transmitter/target separation used was 15mm, as this would represent a worst case requirement for the present application. The results are shown in Figures 2.12(a) and (b).

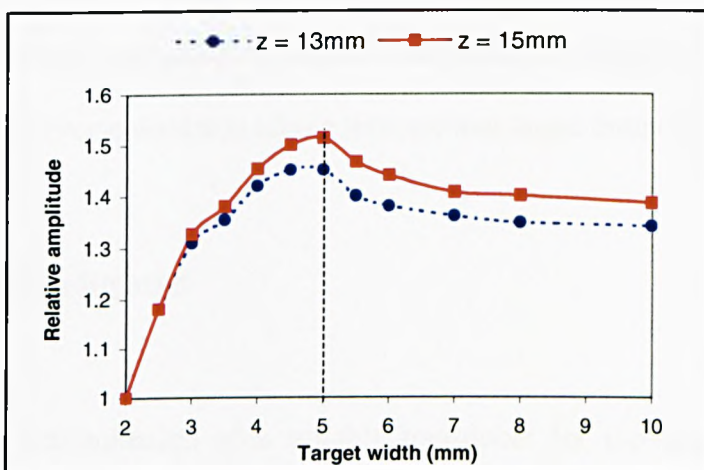


Figure 2.12(a): Simulated variation of relative pulse amplitude with target width

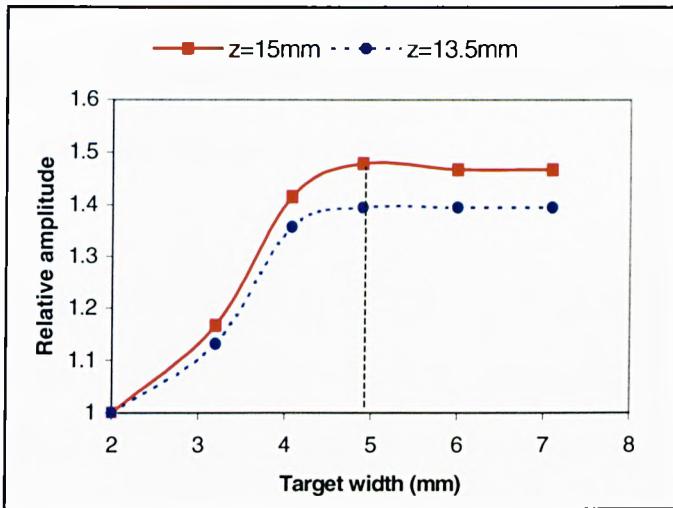


Figure 2.12(b): Practical measurement of relative pulse amplitude with target width

Although the simulated and practical results show different amplitude variations as the target width is increased, most likely due to the non-idealities of the model, both sets of data indicate that the effective target width is about 5mm. Therefore, for the present case, based on the above results, a reflector width of 5mm was considered to be adequate for the synthesis of reflected signals.

Having verified the theoretical model for synthesis of the acoustic waveforms and determining the *effective* reflector area, the next stage of this work was to generate the received echoes by the transducer after reflection from the target. This would be carried out by repeating the above computation process with the target being now considered as the transmitter in the reverse direction taking into account target boundary conditions.

2.7 Chapter Conclusions

In this chapter the determination of a suitable transducer for top-side inspection of pipelines for scale deposits and mathematical models required for representing the

radiation field from this transducer have been successfully developed and experimentally verified. Since these models gave satisfactory accuracy, no attempt was made to investigate or develop alternative models.

It is found from the above work that the use of a rectangular transducer aperture of the size in the order of 2mm x 12mm would be suitable for this purpose. The radiation field profile model was further extended to compute the received signal amplitude by a plane reflector at a given location. This allowed the determination of the effective reflector area as required for the synthesis of multiple boundary reflections, given the dimensions and other parameters of the system.

The next stage of work involves computing the received echoes by the transmitting transducer after reflection from the actual target - a cylindrical surface in the present case.

Chapter 3

Development of a Synthetic A-scan Technique for Top-side Pipeline Inspection

3.1 Introduction

Having successfully developed the necessary theoretical models for computing the radiation field of a finite width rectangular transducer, the synthesis of the signals received by the transducer is described in this chapter. The main objective is to use the synthesised echoes as the reference A-scan templates. The stages of accomplishing this objective are given below.

Stage 1

Extension of the models developed for the determination of acoustic pressure at a point, in the previous chapter, to compute echoes received from a plane reflector placed in oil (1st echo).

Stage 2

Extension of the model to compute 1st, 2nd and 3rd multiple echoes produced in oil and

then in steel, taking into account the need for enlarging the reflector area to account for diffraction spread as determined in the previous chapter.

Stage 3

After verifying the results from stages 2 and 3 with practical measurements, extension of the model towards the final objective, i.e. for the case of a cylindrical reflector, representing the outer surface of a pipe-wall.

Stage 4

Evaluation of the simulated and practical results in order to determine generalised conclusions.

3.2 Theoretical Modelling and Computation of Received Echoes from a Plane Target

In this section, the amplitudes and pulse waveforms of the received 1st - 3rd echoes after reflection from a plane reflector are modelled using the equations derived from the previous chapter. The algorithm used for computation of these echoes is shown in Figure 3.1.

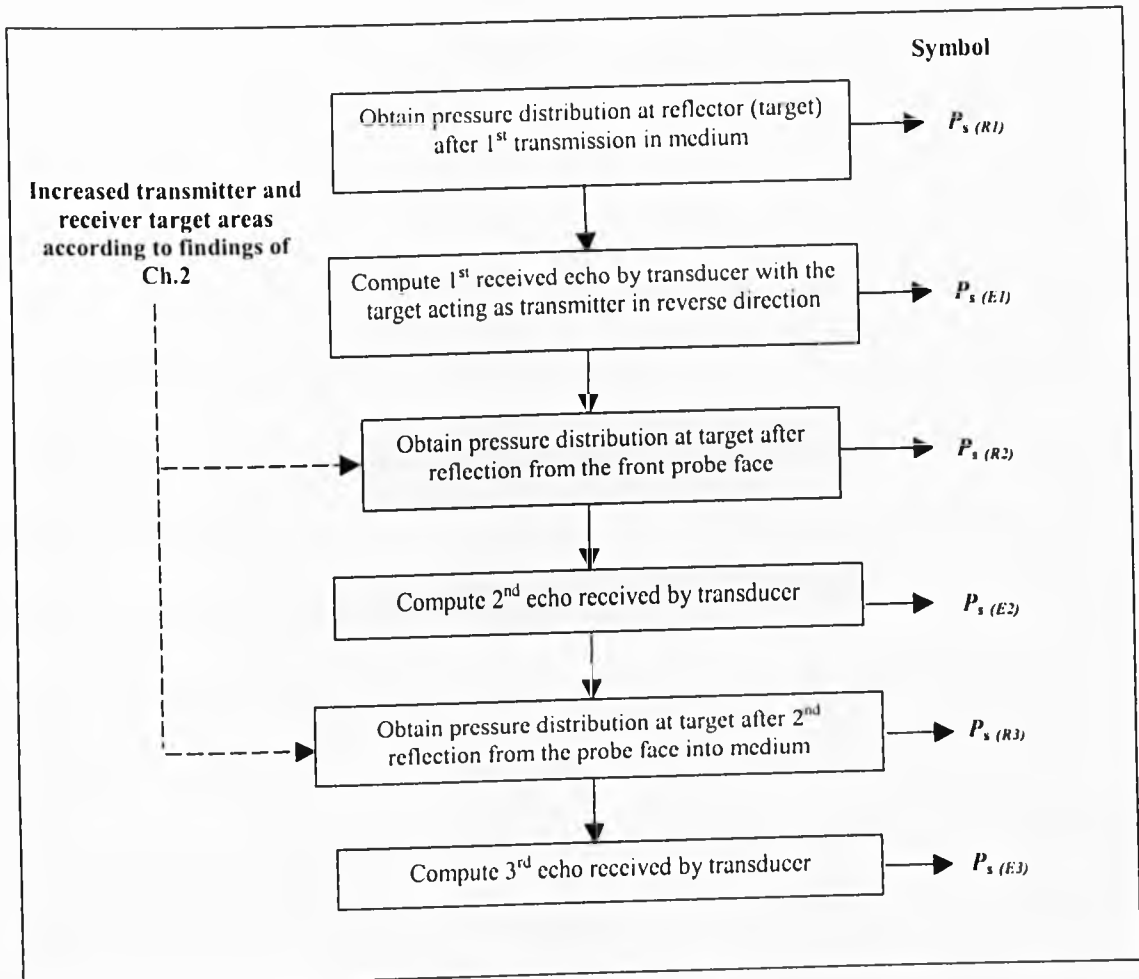


Figure 3.1: Algorithm for synthesis of received echoes

3.2.1 Extension of Theoretical Models to Compute 1st Received Echo

In the previous chapter an equation for the pressure distribution at the reflector was derived. This reflector can be considered as re-transmitting waves (incident upon it) in the reverse direction. The effective target width of the reflector (i.e. the area of the reflector, which radiates energy back to the transducer) was found to be 5mm in the previous chapter. Hence if $P_s (R1)$ (x_p, y_q, z) is the pressure amplitude at the point (x_p, y_q, z) at the reflector, then the received echo amplitude $P_s (E1)$ at the transmitting transducer after reflection from the plane target may be written as

$$P_{s(EI)} = A \sum_{v=1}^m \sum_{u=1}^n C_s |P_{s(RI)}(x_p, y_q, z)| \cdot R \cdot \left[\frac{\exp - j(\frac{2\pi f_s}{c} r_i + \phi)}{r_i} \right] \Delta s \quad (3.1)$$

where $R = (Z_1 - Z_2)/(Z_1 + Z_2)$ is the reflection coefficient at normal incidence, Z_1 and Z_2 are the acoustic impedances of the two media and $\phi = \angle P_{s(RI)}(x_p, y_q, z)$. The phase angle (ϕ) is necessarily introduced here unlike in the case of transmission (eqⁿ 2.6). This is because in the case of transmission all the elements on the transmitter assume the same phase at the instant of transmission. Whereas at the target, the phase of signals received at each point would be related to its co-ordinates in the reflector plane - hence the inclusion of the phase term (ϕ). The limits of p and q in eqⁿ (3.1) representing the target element numbers are defined as in eqⁿ (2.6). The time domain signal for the 1st echo is obtained by applying the IFFT function as shown in eqⁿ (2.5).

3.2.2 Extension of Theoretical Models to Compute 2nd and 3rd Received Echoes

In order to compute the 2nd and 3rd multiple echoes ($P_{s(E2)}$ & $P_{s(E3)}$) the above process must be repeated taking into account the need for gradual increase of the reflector/transmitter area to accommodate diffraction (as determined in Chapter 2) and respective reflection coefficients at both the transmitter and reflector boundaries.

To compute the 2nd received echo amplitude, $P_{s(E2)}$ by the transducer, the pressure amplitude at the reflector $P_{s(R2)}$ after reflection of signals from the probe face must first be obtained. The algorithm used to calculate $P_{s(R2)}$ is similar to that of eqⁿ (2.6) except for the following three important modifications.

Firstly, the amplitudes of the 1st echo pressure distribution on the surface of the transmitting transducer and its vicinity need to be introduced in to the model. Secondly, to reduce errors due to diffraction, the *effective* transmitter and reflector areas must be considered. Based on investigations in Chapter 2 the *effective* transmitter and reflector areas for computations were chosen as stated in Table 3.1, while the increased computation times were also considered.

Table 3.1: Effective transmitter and reflector areas for computing multiple echoes

Received echoes by probe	Effective transmitter area/width (mm)	Effective reflector area/width (mm)
1 st echo	2	5
2 nd echo	7	10
3 rd echo	7	10

The final change required in the model is to take into account the reflection coefficient at the transmitting transducer boundary. It should be noted with reference to Figure 3.2, there are two boundary conditions representing two different reflection coefficients i.e. - one formed by the probe and medium (width = 2mm) and the other by the immediate boundary outside the probe and medium (width = 2.5mm on either side).

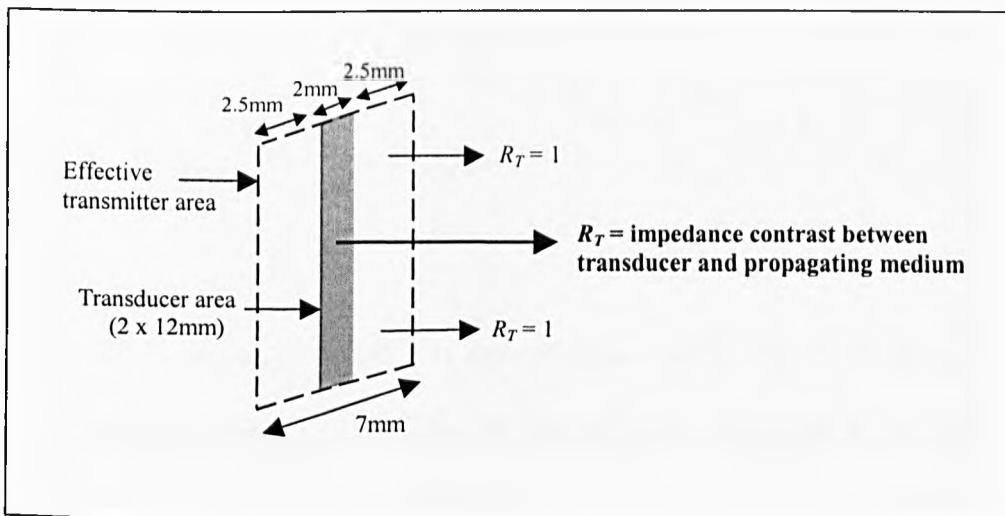


Figure 3.2: Transmitter boundary effect for 2nd and 3rd echo computation

Taking these modifications into account, the pressure amplitude at the reflector $P_{s(R2)}$ can be written as

$$P_{s(R2)} = A \sum_{q=1}^{m_r} \sum_{p=1}^{n_r} C_s \cdot |P_{s(E1)}(x_u, y_v, 0)| \cdot R_T \cdot \left[\frac{\exp - j\left(\frac{2\pi f_s}{c} r_i + \phi_{E1}\right)}{r_i} \right] \Delta s \quad (3.2)$$

where $P_{s(E1)}(x_u, y_v, 0)$ is the 1st echo pressure amplitude at the point $(x_u, y_v, 0)$ on the probe/transmitter face and $\phi_{E1} = \angle P_{s(E1)}(x_u, y_v, 0)$. The reflection coefficient at the transmitter boundary R_T can have two different values. Outside the probe contact area, the reflection coefficient $R_T = 1$ since

$$R_T = \frac{(Z_M - Z_P)}{(Z_M + Z_P)} \quad (3.3)$$

where Z_M is the acoustic impedance of the medium and Z_P is that of the probe. The probe contact area with the medium would have a different value for the reflection coefficient. Following the same approach as for the 1st echo, the 2nd echo pressure amplitude at the transducer can be written as

$$P_{s(E2)} = A \sum_{v=1}^m \sum_{u=1}^n C_s \cdot |P_{s(R2)}(x_p, y_q, z)| \cdot R \cdot \left[\frac{\exp - j\left(\frac{2\pi f_s}{c} r_i + \phi_{R2}\right)}{r_i} \right] \Delta s \quad (3.4)$$

where $\phi_{R2} = \angle P_{s(R2)}(x_p, y_q, z)$ and R is the reflection coefficient at the target/medium boundary. Using this same approach the 3rd echo pressure amplitude at the transmitting

transducer can also be computed. The pressure amplitude at the reflector $P_{s(R3)}$ can therefore be written as

$$P_{s(R3)} = A \sum_{q=1}^{m_r} \sum_{p=1}^{n_r} C_s |P_{s(E2)}(x_u, y_v, 0)| \cdot R_T \cdot \left[\frac{\exp - j\left(\frac{2\pi f_s}{c} r_i + \phi_{E2}\right)}{r_i} \right] \Delta s \quad (3.5)$$

where $\phi_{E2} = \angle P_{s(E2)}(x_u, y_v, 0)$. The 3rd multiple echo received by the transducer could be obtained from

$$P_{s(E3)} = A \sum_{v=1}^m \sum_{u=1}^n C_s |P_{s(R3)}(x_p, y_q, z)| \cdot R \cdot \left[\frac{\exp - j\left(\frac{2\pi f_s}{c} r_i + \phi_{R3}\right)}{r_i} \right] \Delta s \quad (3.6)$$

where $\phi_{R3} = \angle P_{s(R3)}(x_p, y_q, z)$.

It should be mentioned that the limits in eqⁿs (3.2)-(3.6) representing the element numbers on both transmitter (u,v) and receiver (p,q) were appropriately adjusted to represent the increased target areas, while maintaining the same element size. The numerical computations for the three received echoes $P_{s(E1)} - P_{s(E3)}$ were implemented in MATLAB. The program structure for the above algorithm is shown in detail in Appendix B.3 with sample program code in Appendix B.4. It should be mentioned that the programs shown could be made more efficient by vectorising the computed data and by avoiding the use of global function variables.

3.3 Modelling the Effect of Target Curvature

Having developed a model representing the first three received echo amplitudes after reflection from a planar surface, the next stage was to extend the model to take into consideration the target curvature. For the present application of ultrasonic testing of pipelines the reflector and contact surfaces are cylindrical. A curved reflector surface can be considered as a projection of a plane reflector with each of the elementary areas projected by an amount δ_τ as depicted in Figure 3.3 below.

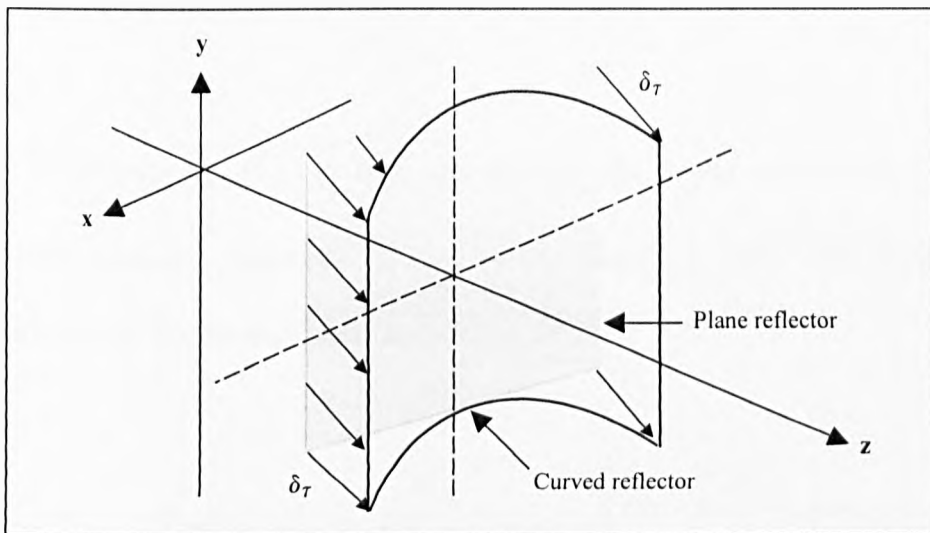


Figure 3.3: Geometry for a curved reflector represented as projected plane reflector

With reference to Figure 3.4 an expression for the projected distance δ_τ can be obtained by geometrical relations.

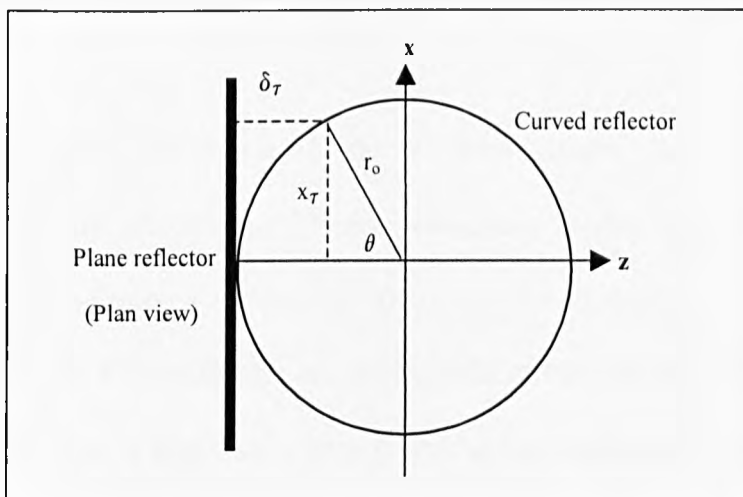


Figure 3.4: Geometrical analysis of a curved reflector to calculate δ_τ

From the above geometry the projection distance δ_τ can be obtained, such that

$$\delta_\tau = r_o \left\{ 1 - \cos \left[\sin^{-1} \left(\frac{x_\tau}{r_o} \right) \right] \right\} \quad (3.7)$$

where r_o is the radius of the curved reflector, and x_τ is the x-co-ordinate of the τ^{th} element (or point) along the x-axis.

Hence by modifying eqⁿ (3.1) to take into account the z-axis projections δ_τ , the 1st received echo pressure amplitude $P_{s(EIC)}$ by the transducer after reflection from a **cylindrical** surface can be expressed as

$$P_{s(EIC)} = A \sum_{v=1}^m \sum_{u=1}^n C_s |P_{s(RI)}[x_p, y_q, (z + \delta_\tau)]|_R \cdot \left[\frac{\exp - j \left(\frac{2\pi f_s}{c} r_i + \phi_{RIC} \right)}{r_i} \right] \Delta s \quad (3.8)$$

where $\phi_{RIC} = \angle P_{s(RI)}[x_p, y_q, (z + \delta_\tau)]$. Following the same approach by modifying eqⁿs (3.2) and (3.4)-(3.6) the 2nd and 3rd echoes could be obtained.

The theoretical model developed in the previous chapter has been significantly extended to obtain the 1st, 2nd and 3rd received echoes by the transmitting transducer from both planar and curved reflectors. This was one of the main objectives of the present study. In the following section, comparison of the simulated echoes, and more importantly their relative amplitudes with practical measurements, are discussed. The propagation medium was initially chosen to be oil with the transducer used in pulse-

echo mode. After completing the initial measurements, the medium was then changed to steel with the transducer in direct contact with the test object.

3.4 Experimental Verification of Theoretical Model for Synthesis of Received Echoes

3.4.1 Received Echoes from a Plane Reflector in Oil

The first step was to validate the extended theoretical model for received echoes from a plane reflector placed in oil. To measure the pulse waveforms and relative amplitudes of the first three received echoes a similar arrangement as in section 2.5.1 was used. The same masked 5MHz broadband circular probe was used with the plane steel target placed in oil. The received echoes were then recorded for comparison with the computed response using the aforementioned model. The measurements were repeated for z-axis co-ordinates of 18,13 and 6.5mm respectively. Figure 3.5 shows the practical measurement system used for this purpose.

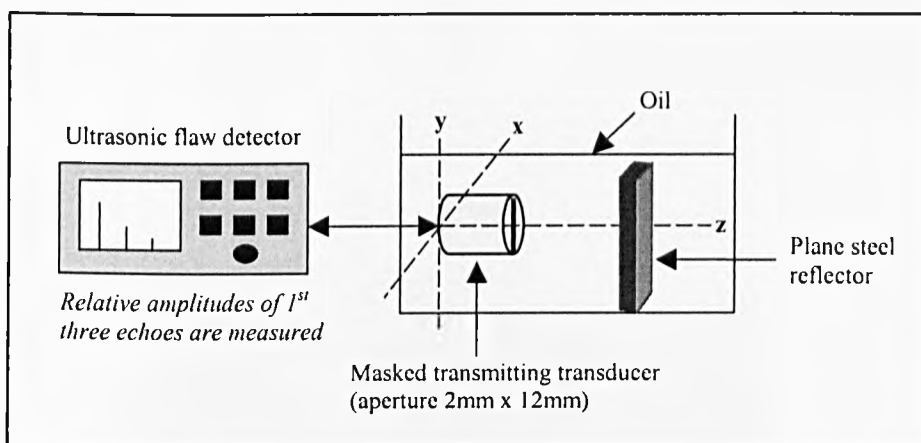


Figure 3.5: Practical measurement system for verification of received echoes by a plane reflector

3.4.2 Multiple Echoes in a Planar Steel Object

The next step was to examine the multiple echoes generated in a steel block having a flat contact surface. This represents a closer situation to the actual application of this work for testing pipelines. For the measurement of received signals by the transducer, the contact area of the above circular transducer was limited to the specified aperture of 2mm x 12mm. This was achieved by leaving a 'strip' section on a block of steel by machining with the strip dimensions equal to the dimensions of this aperture as shown in Figures 3.6(a) and (b). The height of the strip was kept to about $\sim 0.1\text{mm}$ (i.e. $\ll \lambda$). The surface of this strip was manually polished to achieve a good acoustic contact.

The steel block was then placed in oil as shown in Figure 3.7 and the received echoes by the transducer were observed and measured for various thicknesses between 5-10mm.

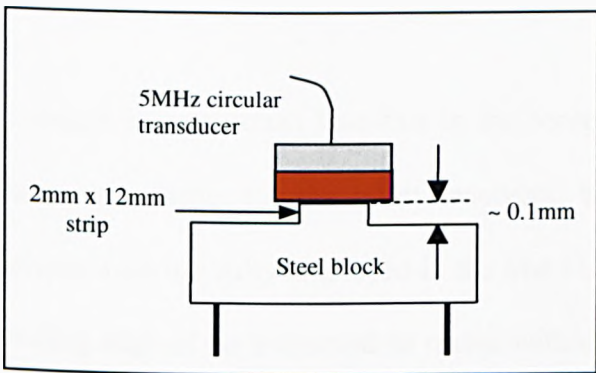


Figure 3.6(a): Schematic of experimental arrangement (steel block)

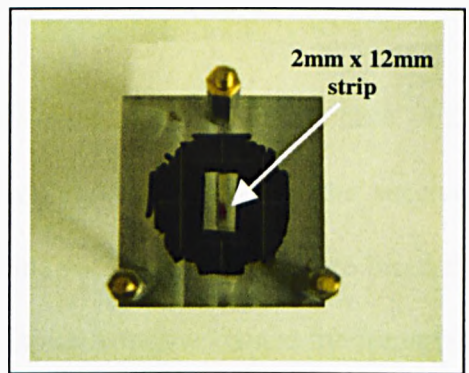


Figure 3.6(b): Actual steel block with 2mm x 12mm strip in centre

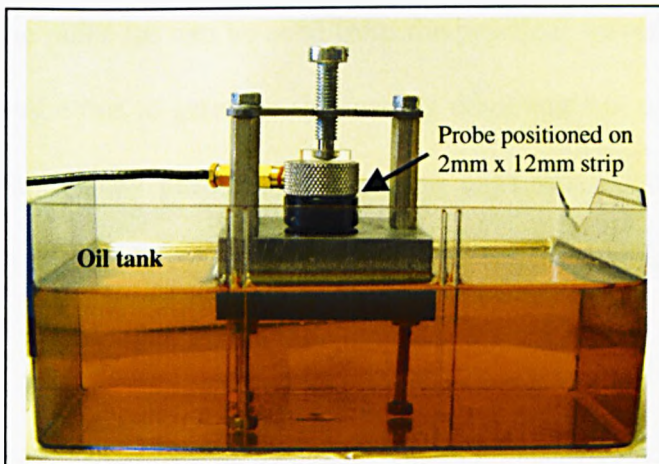


Figure 3.7: Experimental arrangement

3.5 Results

Using the various experimental configurations described in the previous section the next stage of work involved the comparison of simulated results with corresponding practical measurements for received echoes by the narrow rectangular transducer.

3.5.1 Received Echoes from a Planar Reflector in Oil

Pulse waveforms

Figures 3.8(a) and (b) show the normalised computed and measured pulse waveforms for the 1st echo reflected from the plane steel reflector at a distance of 13mm in oil.

It should be mentioned here that in the computation process, unlike in the case of the pulse waveforms for the point receivers, the complete waveform for the received echoes were not fully displayed in the MATLAB window. Indeed it only produced the trailing edge of the pulse and its image within the display window. Since the important aspect in this work is the peak-to-peak pulse amplitude which is determined by the trailing edge of the pulse (as can be seen from the practical waveforms) it was decided that further investigations to generate the leading edge was not essential at this stage. Therefore only for display purposes, the leading edge was considered as the mirror image of the trailing edge to represent the computed pulse, although clearly that would not be the correct waveshape.

However, further tests were carried out and the cause of the problem was identified, as described in Appendix D.

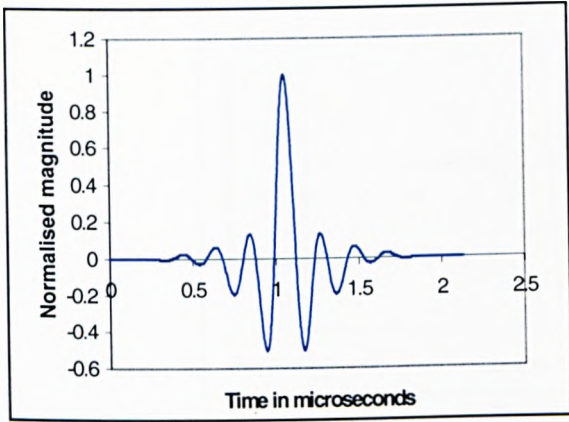


Figure 3.8(a): Simulated 1st echo after reflection from a plane target ($z=13\text{mm}$)

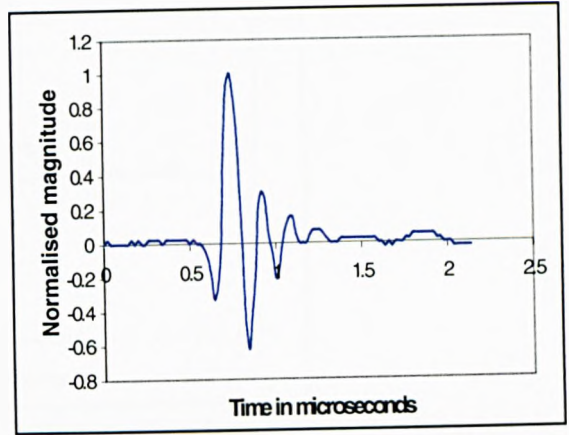


Figure 3.8(b): Practical measurement of 1st echo after reflection from a plane steel reflector in oil ($z = 13\text{mm}$)

Further results of the reflected echoes are shown in Figure 3.9(a) where the simulated 2nd and 3rd reflected echoes are computed at distance of $z = 13\text{mm}$. It should be noted that the relative amplitudes of these echoes have been normalised to the peak value of the 1st reflected echo.

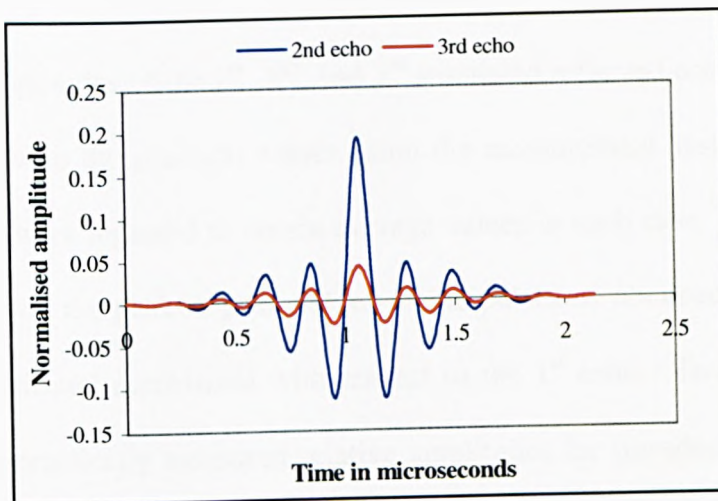


Figure 3.9(a): Simulated 2nd and 3rd reflected echoes from a plane steel reflector in oil ($z=13\text{mm}$) (Amplitudes are normalised with respect to 1st echo of Fig 3.8(a)). Signals superimposed for comparison

Figure 3.9(b) shows the measured 2nd and 3rd reflected echo pulses for further comparison with the computed response.

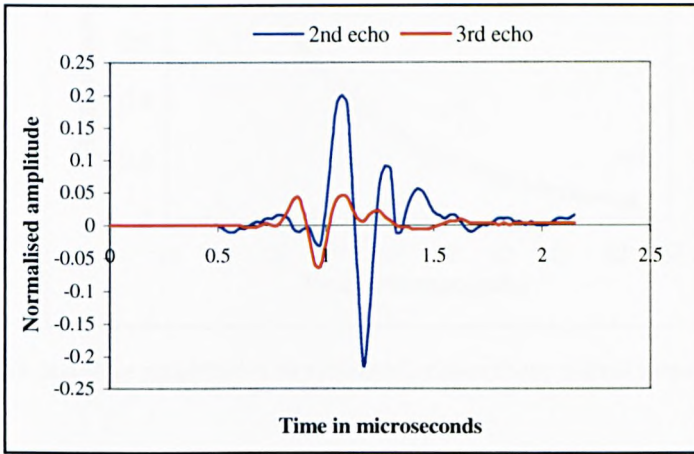


Figure 3.9(b): Practical measurement of 2nd and 3rd reflected echoes from a plane steel target in oil ($z=13\text{mm}$) (Amplitudes are normalised with respect to 1st echo of Fig 3.8(b)). Signals superimposed for comparison

It can be observed from the received echo pulses in Figures 3.8, 3.9(a) and (b) above, that the leading edges of the simulated pulses are different to the practical signals for the reasons described in Appendix D.

Relative peak amplitudes of reflected echoes

The relative amplitudes of the 1st, 2nd, and 3rd simulated reflected echoes were obtained and compared with the practical values using the measurement system of Figure 3.5. Measurements were repeated to obtain average values in each case. In the case of the simulated echoes, the peak-to-peak values of the pulses as obtained by the 300-point IFFT were used, and normalised with respect to the 1st echo. Two examples of the simulated and practically measured relative amplitudes for transducer/target distances of 13 and 18mm are shown in Figures 3.10(a) and (b). The actual data used for these plots is listed in Appendix C.3.

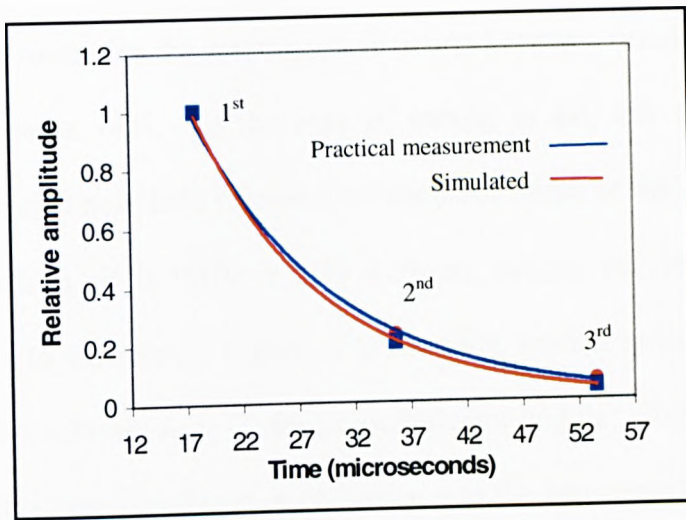


Figure 3.10(a): Relative amplitudes of reflected echoes from a steel target in oil ($z=13\text{mm}$)

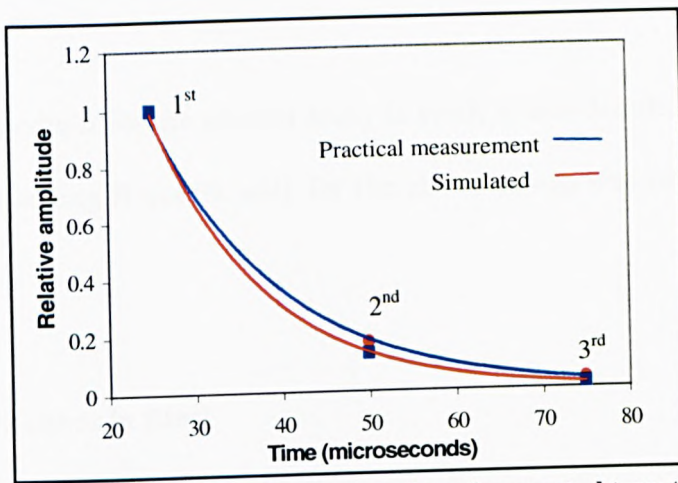


Figure 3.10(b): Relative amplitudes of reflected echoes from a steel target in oil ($z=18\text{mm}$)

As can be seen from Figures 3.10(a) and (b) there is agreement between simulated and practical results for the decay of the reflected echoes. The decay constant, known as the B-coefficient as defined in eqⁿ (2.1) (Chapter 2) was calculated for the above sets of data using the method described in Appendix A.5. The results of the B-coefficient calculations are shown in Table 3.2

Table 3.2: B-coefficients from relative reflected echoes from a planar reflector in oil

z-axis distance (mm)	B-coefficient from simulated echoes	B-coefficient from practical measurements	% deviation
13	-121	-111	8.3
18	-110	-94.5	14.1

For the above two examples the worst-case deviation between simulated and practical measurements is about 14%. In the case of testing in oil, this deviation may be attributed to significant near-field ripples since the pulse width of the probe is finite and also the wavelength in oil at 5MHz is only 0.29mm, making the fractional positional errors with respect to wavelength higher. For example, typical measurement accuracy for (x,y,z) axes is $\pm 0.25\text{mm}$ and $\sim 2^\circ$ for probe/reflector angular alignment. As can be seen these errors are very significant in comparison to the wavelength in oil. Thus, the positional errors of the probe in the experimental set-up became very significant.

Since the actual medium for the present study is steel, it was decided that further work to improve the matching B-coefficients for the above set-up was not necessary at this stage.

3.5.2 Multiple Echoes in Steel

The theoretical model was then modified to obtain the 1st three reflected echoes in the steel block of Figure 3.6. The sound velocity was changed to 5960 m/s and the reflection coefficient was re-calculated at the transmitter boundary as shown by Figure 3.2, with $Z_M = 47$ Rayls. For completeness, an attenuation figure was also added into the model ($\alpha = 2.47$ Np/m at 5MHz) [41]. The z-axis distance in the model now represents the thickness of the steel sample. Finally, the value of the scaling constant 'A' was appropriately selected to be 10^3 for transmission into steel.

Pulse waveforms

Figure 3.11(a) shows the simulated pulse waveforms for the received echoes using the modified model, in steel, for a thickness of 10mm. The measured 1st received echo using the experimental set-up in Figure 3.7 was also obtained as shown in Figure 3.11(b). The difference in leading edges of the pulse is still visible, but as stated before, it is the peak amplitudes that are of main interest here rather than the pulse shape.

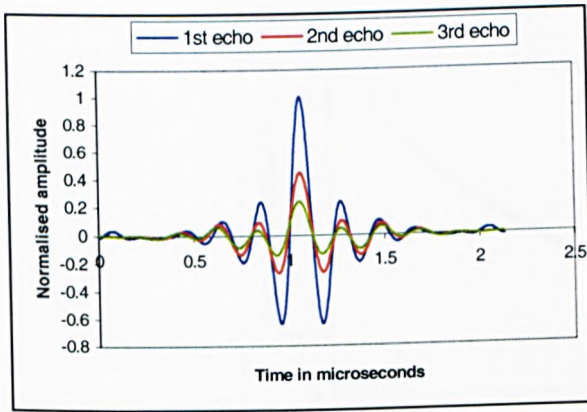


Figure 3.11(a): Simulated reflected echoes in steel (z=10mm) (waveforms superimposed)

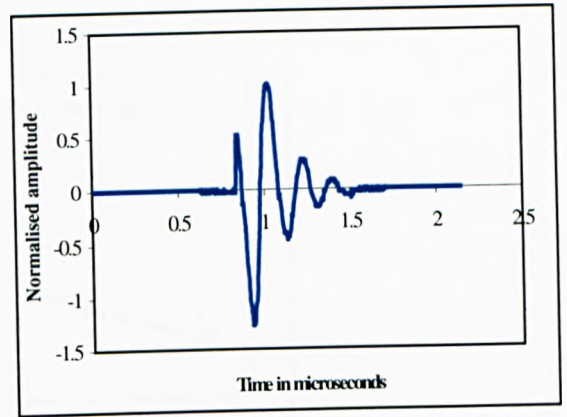
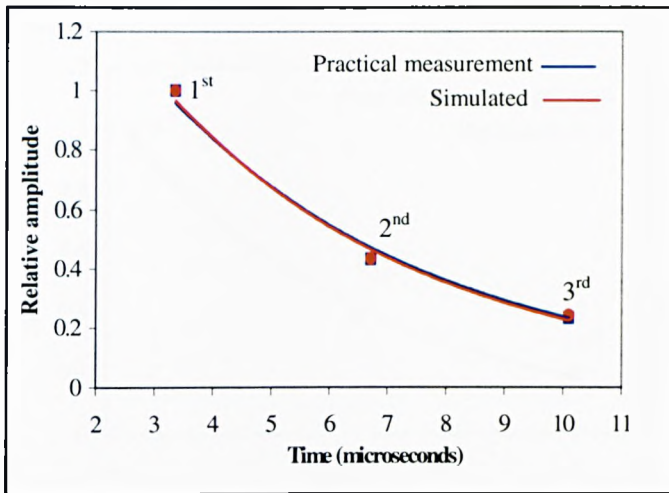


Figure 3.11(b): Practical measurement of 1st reflected echo in steel (z=10mm)

Relative peak amplitudes

The next step was to obtain the relative echo amplitudes in steel from simulated and measured data. In this regard, echo (averaged) measurements for thicknesses 10, 7.5, 6.5 and 5mm of the steel block were carried out using the aforementioned method. These thicknesses were chosen as they mostly represent the thicknesses of actual pipe-walls. The comparison of these results with the simulated data is shown in Figures 3.13(a) to (d). The actual data used for these plots is listed in Appendix C.4.



**Figure 3.13(a): Relative echo amplitudes in steel block ($z=10\text{mm}$)
Max. deviation from mean = 3.6%**

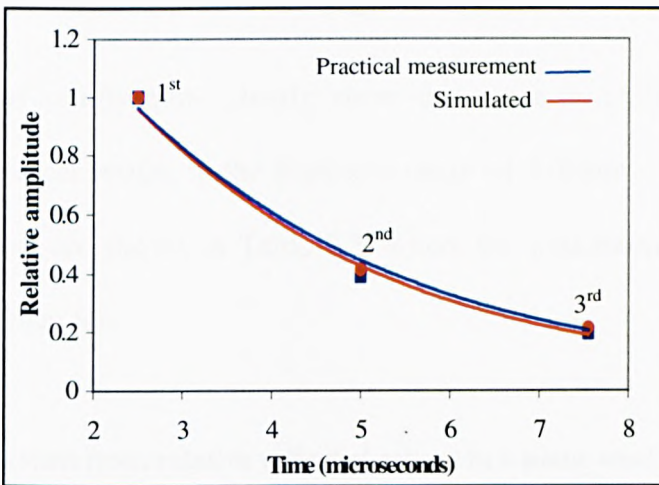


**Figure 3.13(b): Relative echo amplitudes in steel block ($z=7.5\text{mm}$)
Max. deviation from mean = 8.4%**

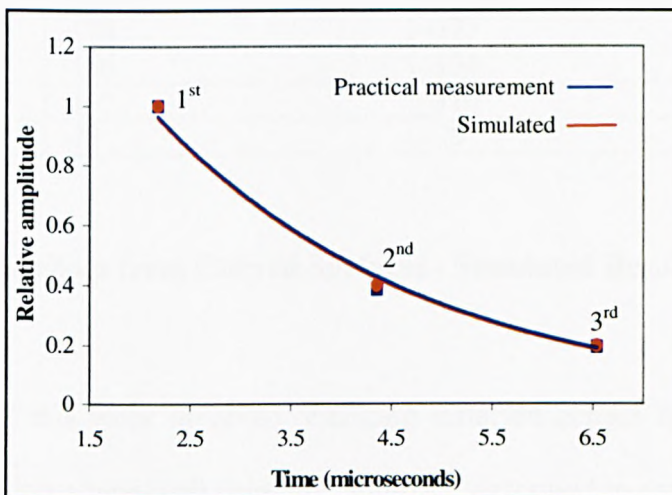


**Figure 3.13(c): Relative echo amplitudes in steel block ($z=6.5\text{mm}$)
Max. deviation from mean = 3%**

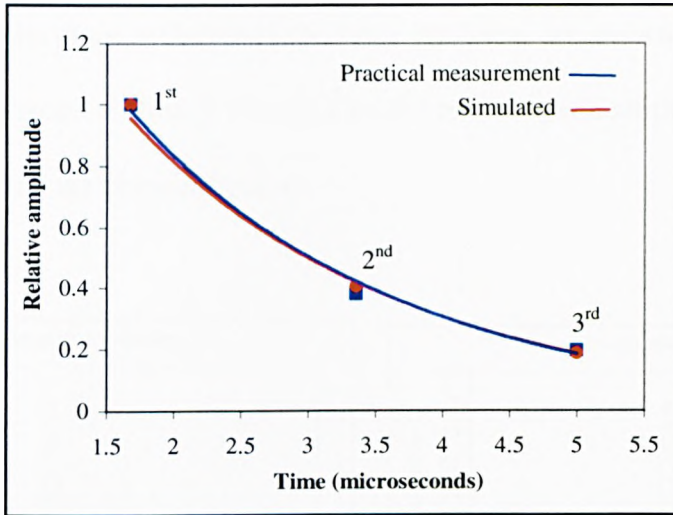


**Figure 3.13(d): Relative echo amplitudes in steel block (z=5mm)
Max. deviation from mean= 6.1%**

The above sets of results quite clearly show that there is excellent agreement of simulated and practical results in the thickness range of 5-10mm. The corresponding B-coefficient values are shown in Table 3.3, where the maximum deviation between values is no more than 6%.

Table 3.3: B-coefficients from relative reflected echoes in a plane steel block immersed in oil

z-axis distance (mm) (i.e. thickness)	B-coefficient from simulated echoes	B-coefficient from practical measurements	% deviation
5	-178	-173	2.8
6.5	-136	-134	1.5
7.5	-117	-110	6
10	-78	-75	3.8

3.5.3 Reflected Echoes from Curved Surfaces - Simulated Results

The final stage of this work involved obtaining reflected echoes from a curved steel reflector representing a pipe-wall using the approach described in section 3.3. This was carried out for two curved reflectors with diameters 12.5cm and 5.4cm, both of 5mm

thickness. The results of the simulation (Appendix B.5) for the 5.4cm diameter reflector and also the plane reflector of the same thickness are shown in Figures 3.14(a) and (b) for comparison. Figure 3.14(c) shows the relative peak amplitudes for both the curved reflectors and the plane reflector.

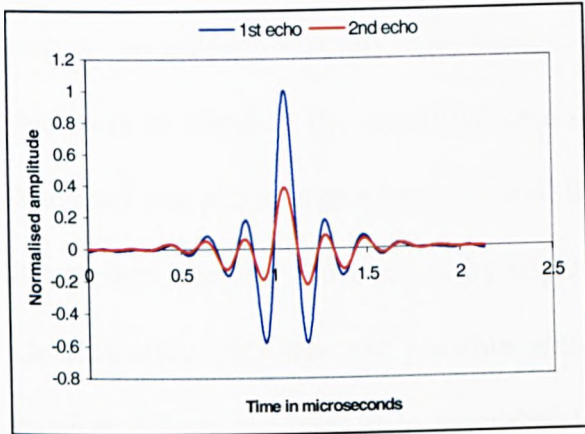


Figure 3.14(a): Simulated reflected echoes from a curved target- diameter =5.4cm, thickness=5mm

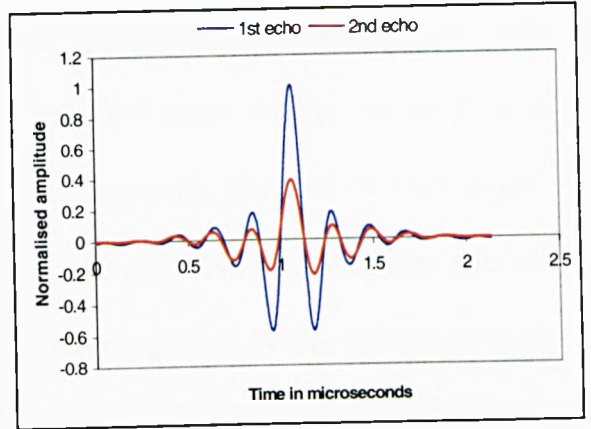


Figure 3.14(b): Simulated reflected echoes from a plane target- thickness=5mm

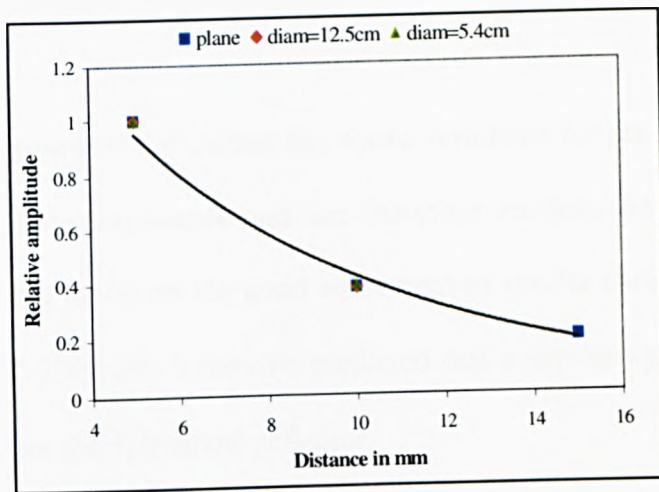


Figure 3.14(c): Relative amplitudes of reflected echoes from plane and curved reflectors ($z=5\text{mm}$)

From Figures 3.14(a) to (c) it is observed that in this case, the effect of target curvature seems to have little effect on the pulse waveforms and therefore on relative echo amplitudes. In fact, Figure 3.14(c) shows that the relative amplitudes of the 2nd reflected echo are almost inseparable when plotted on the same graph as the plane

reflector (Appendix C.5 shows the actual values of relative echo amplitudes for the curved reflectors).

If this was the case for other thicknesses and curvatures within this required range as well, then the synthesised reference echoes may be obtained from respective plane targets. In order to test this hypothesis, the above procedure was repeated for a wall thickness of 10mm. The simulated results (1st and 2nd echo) for the curved (5.4cm diameter) and plane targets again showed that they are nearly identical (< 1% change). It was then necessary to confirm by experiment whether these findings were correct. Unfortunately, this was not possible within the time period as the procedure now requires a 2mm x 12mm strip broad-band transducer with a response similar to that used in the simulation to be constructed, whereas for the previous experiments, it was appropriate to use a standard commercial probe.

Hence, due to these practical difficulties the above simulated results were unable to be verified by practical measurements and are therefore recommended for immediate future work. However based on the good agreement of results obtained for the plane reflector in Figures 3.13(a)-(d), it may be predicted that a similar agreement of results would likely follow for the cylindrical reflector.

3.6 Discussion of Results

Pulse Shape

When the actual response of the probe is used in a model, as was the case in this work,

it should be possible to compute the received echoes from a given target that would closely represent the practically measured pulse. However this was not achieved for the leading part of the computed waveform as described in section 3.5.1. The problem of pulse shape reconstruction was later analysed and identified as shown in the findings of Appendix D.

Pulse Amplitude

A good general agreement of results was found when only the relative echo amplitudes were compared. Although in oil there were significant differences in results, probably due to the large wavelength, in steel repeatable results were obtained. In a plane steel object the model can predict the relative 1st, 2nd and 3rd echo amplitudes and also the B-coefficients with a good accuracy. Although the results obtained are only for thicknesses in the range 5-10mm, it is sufficient for the present investigation, as pipe-wall thicknesses are usually within this range.

In relation to the curved reflector the results from simulated data indicate that the effect of target curvature may not be significant in the present application. This may be due to the smaller width of the transducer (2mm) and the short target distances (5-10mm) involved.

3.7 Chapter Conclusions

A method for artificially generating acoustic reference signals for ultrasonic measurements has been described. In this regard, a comprehensive theoretical model

was developed based on a finite width rectangular transducer, suitable for the present application.

The 1st three reflected echoes from planar surfaces in both oil and steel were generated, and in both cases a good general agreement with practical results was achieved. Although the pulse shapes were somewhat different in all cases, the amplitude of synthetic echoes was in good agreement with the practical results, with a worst case error of less than 9% and the resulting B-coefficients within an accuracy of 6%. In the case of a cylindrical target, simulations show that there is very little difference in echo amplitudes for the curvatures and wall thicknesses used. However, this needs to be confirmed by experiment, which was not feasible at this time.

Some of the work presented in this chapter (and results from Chapter 2) has been published in the Proceedings of the IEEE Instrumentation & Measurement Technology Conference, 2002 [42].

Chapter 4

Development of Techniques for Positional Alignment of Ultrasonic Transducers in Down-hole Pipelines

4.1 Introduction

Having satisfied the main objectives with respect to location of deposits from top-side, the next step was to develop techniques to aid detection of deposits from within pipelines.

A critical requirement of the down-hole deposit location techniques previously developed is the accurate alignment of the ultrasonic transducers within the pipeline [43]. The probe must be radially aligned with the curved target before the signals are acquired and analysed for the presence of scales. This chapter presents a study on the development of a technique for remote transducer alignment by analysing the waveform features of the signals received by the transducer from the internal pipe-wall.

In pulse-echo ultrasonic measurements, it is known that when a reflecting surface is not orientated normal to the axis of the source transducer the received signals are

significantly changed in terms of amplitude and waveform shape. Thus, it was anticipated that monitoring the shape and amplitude of the waveform could be used to determine the angular positional accuracy of the transducer within the pipeline.

4.2 Problem Description

As mentioned before, previous work carried out on down-hole monitoring for scale deposits did not incorporate a method for ascertaining the positional symmetry of the transducer with respect to the target. In the absence of a method for determining the positional symmetry of the transducer, its placement at any point within the pipe is arbitrary as seen from Figures 4.1(a) and (b).

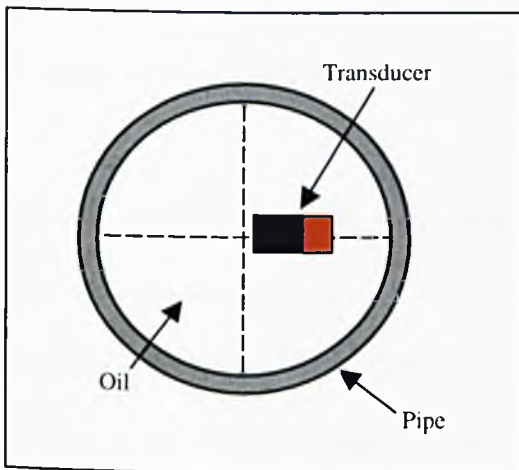


Figure 4.1(a): Transducer in correct alignment with pipe-wall

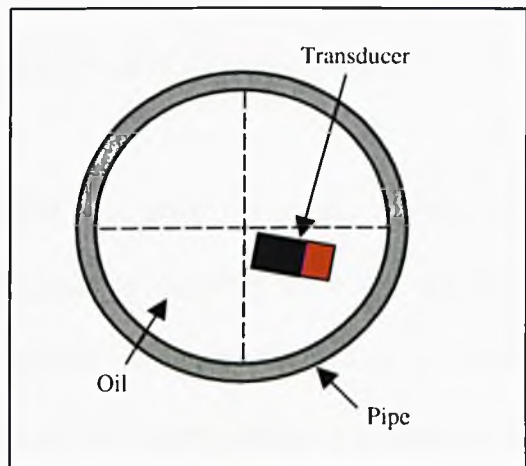


Figure 4.1(b): Transducer out of alignment

As a result the amplitude and pulse shapes of the received echo signals will be incorrect for the detection and characterisation of deposits [43]. Therefore it was decided to investigate a method for predicting the alignment of this probe with respect to the pipe-wall based on examining the return echo signals. The data thus received by the top-side acquisition system in Figure 1.4 may then be used to align the transducer position

by appropriately mounting the transducer system on a motorised head on the tool. The sequence of operation would be that the transducer is scanned a few degrees on either side while the signals are being monitored at the top-side computer. Once the computer detects the best alignment, the signals corresponding to that alignment would be used for the detection of deposits according to the techniques previously developed.

4.3 Background Work on Remote Alignment of Transducers

The problem of misalignment between transmitter and reflector is also encountered in other applications such as ultrasonic ranging. This can lead to large errors in the distance measurement as a result of angular misalignment between the normals of the transmitting and receiving surfaces [44]. Hence the development of a suitable practical technique would also be beneficial for applications beyond the present objectives.

Pederson and Orofino [45, 46] have modelled the effect of target angular mis-orientation on the spectrum of the received signal by deriving an Angle-dependent Spectral Distortion (ASD) function. The method employs the use of an *image* transducer i.e. a mirror-image representation of the actual source transducer, thus eliminating the reflecting interface. However the ASD function is transducer specific and the work published so far only deals with a planar reflector, whereas in the present case the reflector is cylindrical. Also the effect of target angular orientation on the actual pulse waveforms of the received echoes is not explicitly reported.

For applications of pulse-echo measurements inside fluid-filled pipes, some work has been reported by Stanke et al [47] re-emphasising the effects of the amplitude of

received waveforms due to transducer misalignment. However this work only gives results for the lateral displacement of the transducer with respect to the pipe, and not for the actual angular rotation. A lateral displacement would mean an associated change in target position in addition to a pure angular displacement. The approach taken in the present study is to use the symmetrical nature of received signals about the central alignment of the transducer to obtain its angular position with respect to the target. The work reported here is mainly based on a practical study, but this is followed by theoretical justification using a computer simulation of a representative example.

4.4 Proposed Approach

The signals received from the target yield the maximum amplitude at normal alignment. However, note that the signal at central alignment is not symmetrical in practice, as this would depend on the actual response of the probe. However, if the transducer is misaligned, the waveshape and amplitudes of the received signal will differ as illustrated in Figure 4.2, but with waveshapes practically identical at equal angles on either side of central alignment.

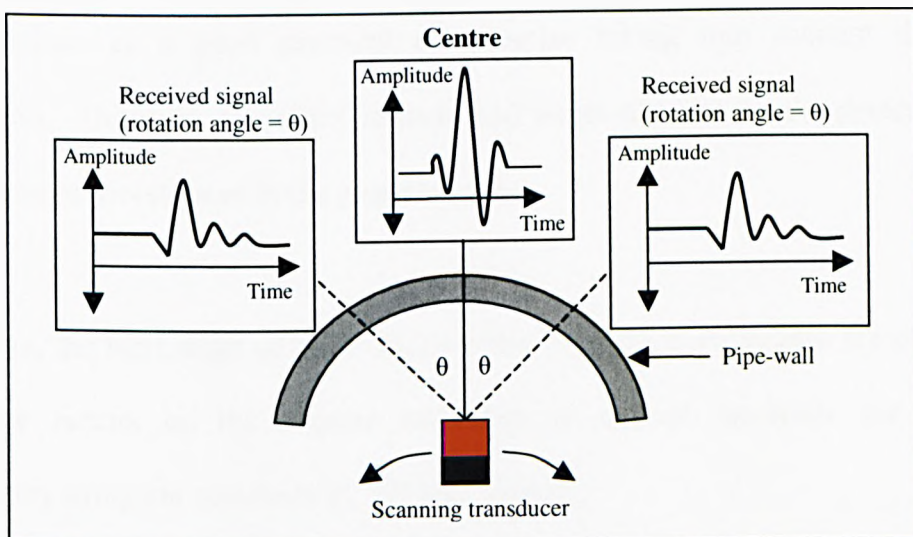


Figure 4.2: Detecting the symmetry of received signals from a scanning transducer inside a pipe

There are two properties of interest here - optimal wave shape and maximum amplitude of signals. It can be understood that if the angular displacement about the central position is equal, as shown in Figure 4.2, then the waveforms on either side would be identical. However, the amplitude of the signals will be less than that at the normal. It is found by experiment that the latter property is much easier and accurate to use in the present application since amplitude changes are easier to monitor than waveshape changes.

4.5 Detection of Positional Symmetry

To detect the symmetry of received signals from the scanning transducer, the detectable limits of the system need to be defined, i.e. the rotation angle that gives a detectable change in signal amplitude with the equipment used. In a practical situation, there are also the effects due to other factors such as pipe diameter, surface roughness and distance between transducer and target. In the present application the transducer/target separation distance has been fixed at 6.5mm from previous work [43]. This separation distance of 6.5mm has been chosen for down-hole measurements during previous investigations as a good practical compromise taking into account dimensional constraints. However, the effect of increased target distance on the detectable limits has also been investigated in the present study.

Therefore, the next stage of the work involved a practical study into the effect of the definable factors on the angular resolution at normal incidence for transducer positioning using the symmetry of reflected signals.

4.6 Practical Examination of Detectable Limits

4.6.1 Experimental Arrangement

The basic configuration used for the experimental investigation of the detectable limits of the transducer positional symmetry is shown in Figure 4.3. A rotatable arm was used to manually adjust the angle of rotation of a 5MHz broadband transducer, immersed in oil. The rotation angle was measured on a graduated scale to an accuracy within 0.5° . Pulse waveforms received by a digital flaw detector were transferred to a PC.

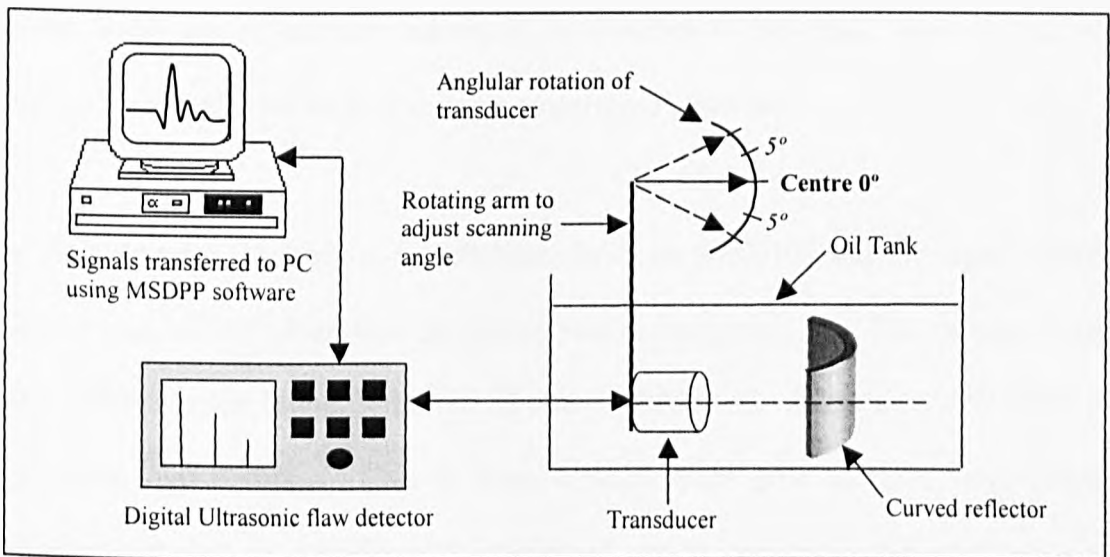


Figure 4.3: Experimental configuration to investigate detectable limits for transducer positional symmetry

Using the above measurement set-up the detectability of symmetry from the 1st received echo pulse was observed for three curved reflectors and a plane target at distances in the range of 6.5 to 20.5mm. In the first stage of experiments the diameter of the circular transducer used was 12.7mm. The experiments were also repeated using

a 2mm x 12mm masked aperture on the same probe with a view to simulating and verifying the validity of the technique used.

The results of this investigation are shown in the following section, with a discussion of the main findings.

4.6.2 Practical Measurements on the Detectability of Transducer Positional Symmetry

As mentioned before, the detectable changes in amplitude were used to obtain the angular resolution. For each reflector, initially kept at a distance of 6.5mm, the peak-to-peak amplitude of the received signal, as function of the angle from normal, was acquired and transferred to the PC using customised software.

The flaw detector used was a Krautkramer-Branson (USD10) and the signal transfer software was MSDPP developed previously within the group [34]. The transducer used was a 5MHz circular broadband probe (Aerotech CA211A). All targets were made out aluminium pipe sections. This is because aluminium pipe sections were already available and also no significant departure of results would be expected since the impedance contrasts in both cases (i.e. steel/oil and aluminium/oil) are very high. The surface roughness parameter R_a , for the samples used were in the range of 0.22-0.25 μm , where R_a is the arithmetic mean of the absolute deviation of the roughness profile from the mean line of the surface. The type of oil used for the propagating medium was Multigrade motor oil (20W/50).

The results were plotted and from the graphs the rotation angle which gave a detectable change in signal amplitude was identified. Using the same approach, the angular resolution at other distances was obtained.

The results are reported in the following order.

- Effect of curvature
- Effect of distance
- Effect of surface roughness
- Effect of changes in probe aperture

4.7 Results

4.7.1 Effect of Curvature on the Angular Resolution near Normal Incidence

The reflected 1st echo signals from a curved reflector of diameter 8.8cm and a plane reflector, both kept at distances of 6.5mm from the probe in oil are shown below in Figures 4.4(a) and (b), for a few probe rotation angles from the centre. The probe used was a 5MHz broadband type with an aperture of 12mm (diameter).

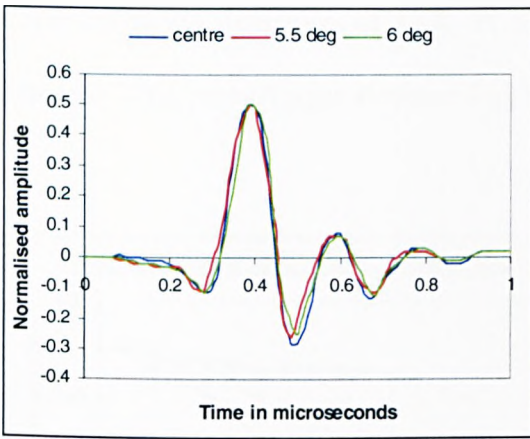


Figure 4.4(a): Reflected 1st echo signals from a cylindrical reflector of 8.8cm diameter target/probe separation = 6.5mm

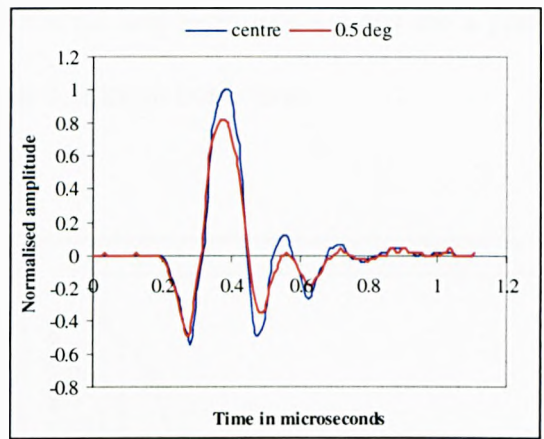


Figure 4.4(b): Reflected 1st echo signals from a plane reflector target/probe separation = 6.5mm

As can be seen from Figure 4.4 (a) a change in peak-to-peak signal amplitude at a probe rotation angle of about 5.5° can be detected with the equipment used (8-bit resolution) representing a signal drop of 2-3 % approx. Although visibly small, in the case of Figure 4.4(a) the changes shown were consistently observed during experiments. Since the measurement is to be ultimately performed by automatic signal measurement and not by ‘visual’ comparisons, it should be possible to monitor changes of this magnitude. For example, if only the quantisation accuracy is considered during signal digitisation (8-bit resolution), the quantisation error for Figure 4.4(a) is approximated as $(0.8/256) \times 100 = 0.3\%$. However the minimum difference between amplitudes in Figure 4.4(a) is in the range of 2-3%, well above the limits of the quantisation error.

In the case of the plane target, a much greater change in amplitude at a much lower rotation angle ($<0.5^\circ$) was observed.

The next step involved measuring the rotation angles that produce a detectable change in signal amplitude for different curvatures. Examples of this are shown in Figure

4.5(a) for target diameters of 13.4, 11.6 and 8.8cm, and in Figure 4.5 (b) for a plane reflector. The probe/target distance was kept at 6.5mm in both cases.

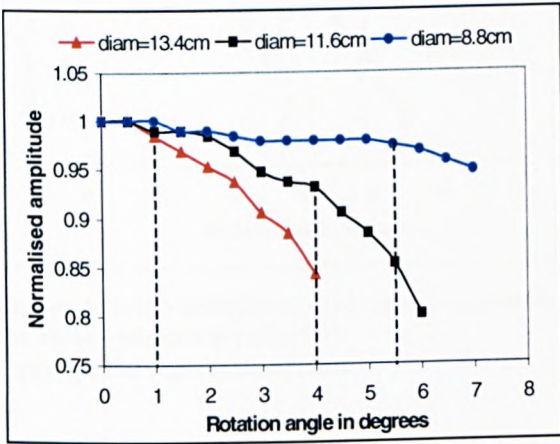


Figure 4.5(a): Variation of echo signal amplitude for three cylindrical reflectors target/probe separation=6.5mm

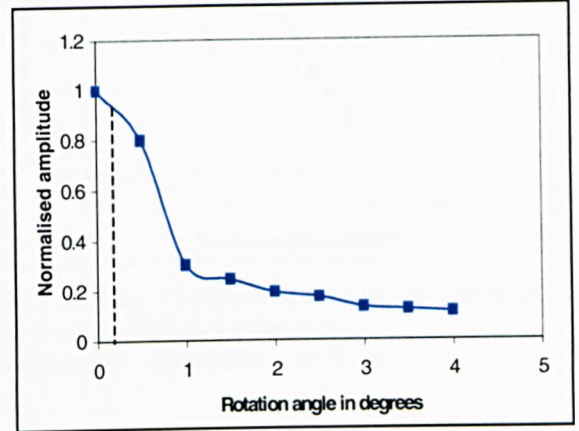


Figure 4.5(b): Variation of echo signal amplitude for a plane reflector target/probe separation=6.5mm

For cylindrical reflectors, Figure 4.5(a) shows that as the pipe diameter increases the angular resolution also increases, i.e. rate of amplitude drop increases. The smallest resolvable angle for the 8.8cm diameter reflector is about 5.5° while that for the 13.4cm diameter reflector is less than 1° . For a plane reflecting surface it is noticeable from Figure 4.5 (b) that the angular resolution is much lower, probably in the range of 0.25° . A discussion on these results is presented in section 4.9.

4.7.2 Effect of Distance on the Angular Resolution near Normal Incidence

The next stage of measurements was concerned with the investigation of the effect of distance between probe/target on the angular resolution. Figures 4.6(a) and (b) show results for the three curved reflectors used above at distances of 15mm and 20.5mm respectively from the probe.

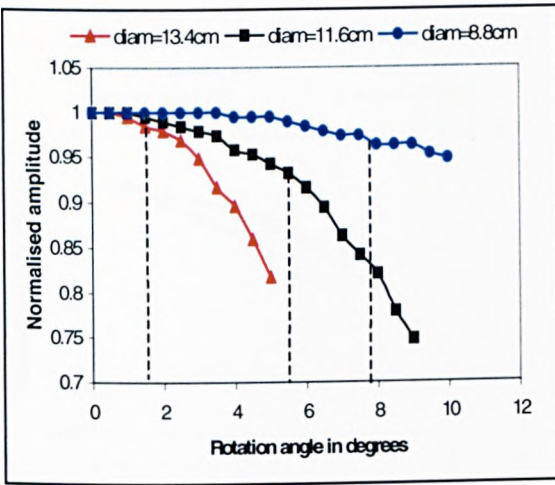


Figure 4.6(a): Variation of echo signal amplitude for three cylindrical reflectors target/probe separation=15mm

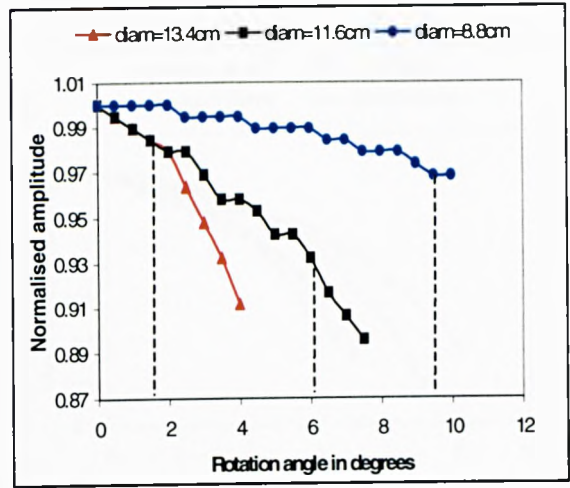


Figure 4.6(b): Variation of echo signal amplitude for three cylindrical reflectors target/probe separation = 20.5mm

From these measurements it can be observed that as the distance increases the detectable angular resolution at normal incidence also increases for the respective curved reflectors. It is also seen from Figures 4.6(a) and (b) that the increase in detectable angular resolution shows the same pattern with the respective diameters for the above two cases, showing an increase in resolution with increase in diameter. However, this is not a general conclusion since other factors such as the probe aperture could play a significant role as discussed later in the chapter.

Further measurements were then carried out for two of the cylindrical targets (diameter 13.4cm and 11.6cm) for various target/probe distances and the results showed the same trend, as can be see from Figures 4.7(a) and (b) i.e. resolution increases with distance and diameter.

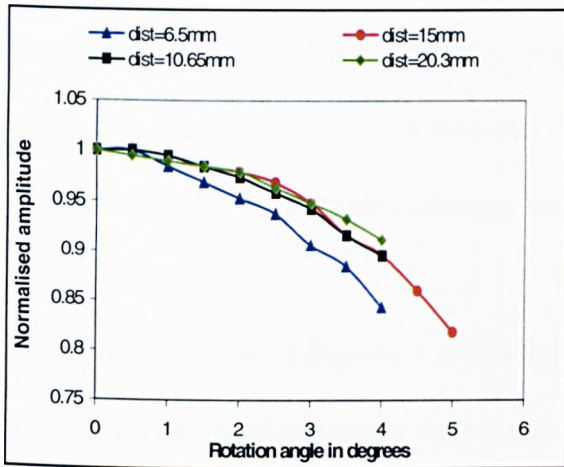


Figure 4.7(a): Variation of echo signal amplitude with distance for a cylindrical reflector of 13.4cm diameter

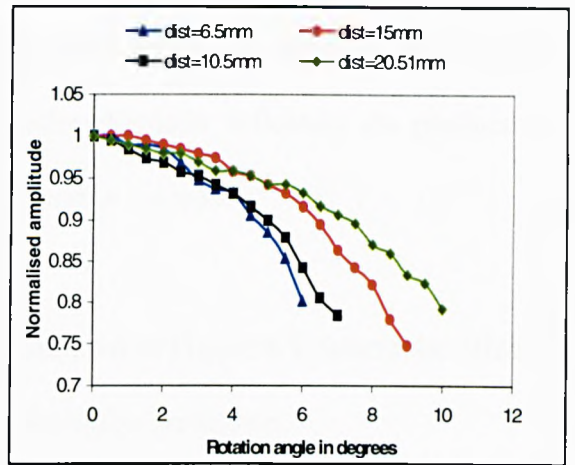


Figure 4.7(b): Variation of echo signal amplitude with distance for a cylindrical reflector of 11.6cm diameter

Tests as in Figure 4.7 were then repeated with a plane reflector and the results are shown in Figure 4.8.

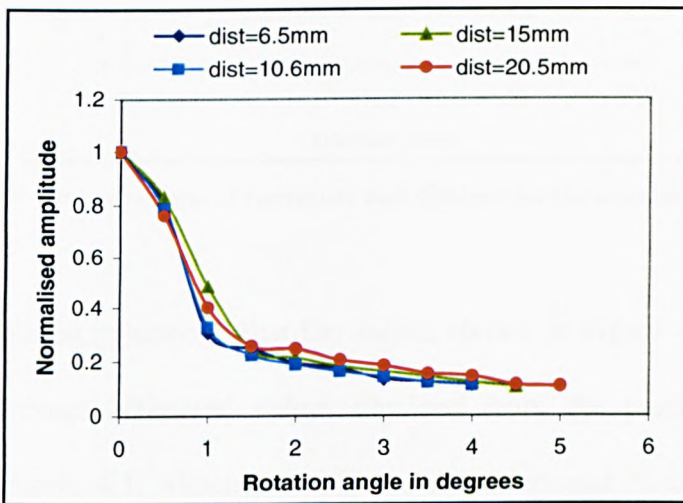


Figure 4.8: Variation of echo signal amplitude with distance for a plane reflector

Another observation that could be made from Figures 4.6 and 4.7 was that for large diameter reflectors the rate of amplitude drop or ‘steepness’ of the curves with distance was less than that for smaller diameters. For the plane reflector in Figure 4.8 it is observed that there is virtually no change in the angular resolution with distance within

the above range. Therefore this indicates that the larger the diameter of the reflector, the higher the detectability of angular resolution and lesser the effect of distance on changes to the detectability. Conversely, smaller diameter reflectors do produce a distinct change in the angular resolution as the distance increases.

The above results as in Figures 4.6 to 4.8 are combined in Figure 4.9, where the effects of target curvature and distance on the angular resolution are shown.

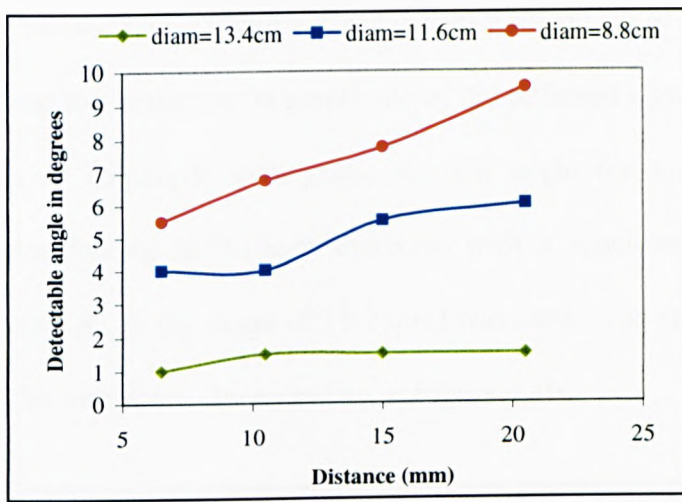


Figure 4.9: Overall effects of curvature and distance on the angular resolution

However, it should be mentioned that the values shown in Figure 4.9 for the angular resolution are average estimated values obtained from the practical measurement system used in Figure 4.3, within the range of diameters and distances stated. This system has non-idealities such as limited 8-bit resolution. There are also small errors associated with the angular rotation movement of the probe as only a manual method was used within an accuracy of $\pm 0.5^\circ$. A better system would give better resolutions than that was achieved in this work. This is feasible since the system used only had a modest set of specifications. However, as the original aim of this study was to develop

a technique for detecting the probe alignment, the above set-up was found to be adequate to demonstrate the method.

4.7.3 Effect of Surface Roughness on the Angular Resolution near Normal

Incidence

In the case of detection of scale deposits in down-hole pipelines an important factor that needs to be considered is the surface roughness of the target - scales in this case. The reflection of waves from a rough surface causes a distortion of the wave-front due to scattering leading to a reduction in amplitude of the reflected signals. To investigate this the variation of amplitude with probe rotation angle for a smooth and rough surface, a reflector having an 11.6cm diameter with a machined surface (surface roughness parameter, R_a , in the range of 17-25 μm) was used. The probe separation was kept at 6.5mm. The results are shown below in Figure 4.10.

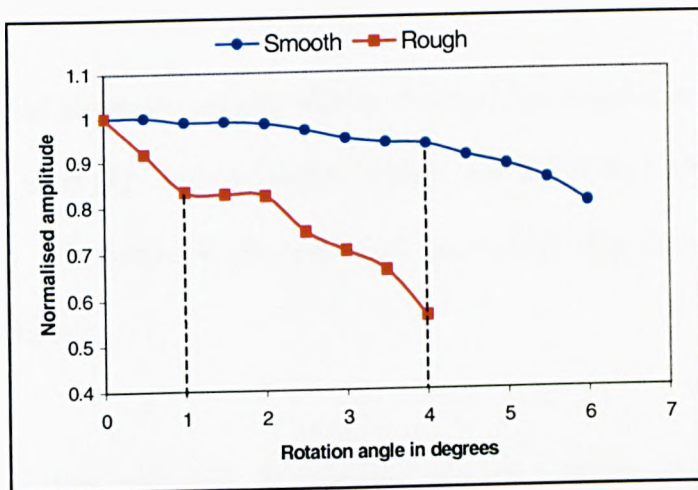


Figure 4.10: Effect of surface roughness on the echo signal amplitude for a 11.6cm diameter reflector (probe separation = 6.5mm)

As can be seen from Figure 4.10, the effect of surface roughness is to increase the sensitivity to angular alignment in this case. However, the dependence on surface

roughness needs to be examined in more detail e.g. by repeating experiments with samples of different degree of roughness to make any general conclusions. Nonetheless, the above results indicate that the technique described is relevant to the present application, where the targets are not smooth.

4.7.4 Effect of Probe Aperture on Angular Resolution near Normal Incidence

The measurements carried out thus far were using a single circular probe of 5MHz with a 12.7mm diameter. A smaller probe aperture increases the beam divergence of a transducer. This has the effect of increasing the width of the central energy lobe of the transducer [48]. Hence a smaller aperture probe may reduce the detectable angular resolution for targets with large diameters or for plane targets, but could be favourable in the case of smaller diameter cylindrical targets. Therefore, it was decided to investigate the effect of changes in the probe aperture size on angular resolution.

Figures 4.11(a) and (b) show sample results obtained for angular resolutions with the probe previously used (12.7mm diameter, 5MHz) and those for a smaller probe (7mm diameter, 5MHz). The reflector diameter used was 8.8cm, and the tests were repeated for two target distances.

Similar tests were then performed for a plane reflector with the target/probe distances kept same (6.5mm and 10.6mm as before). The results are shown in Figure 4.12 (a) and (b).

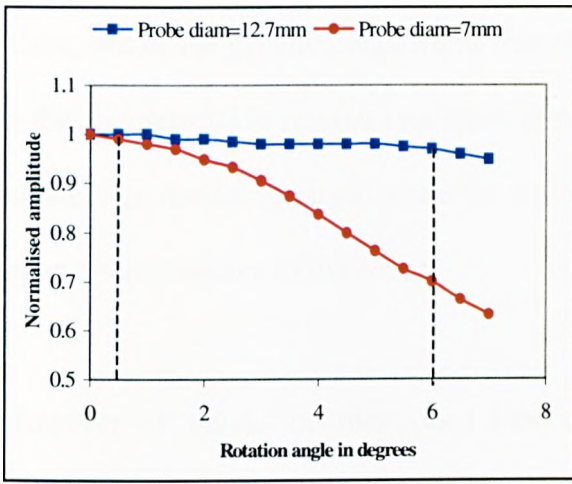


Figure 4.11(a): Angular resolution measurements - reflector diameter = 8.8cm target/probe separation=6.5mm

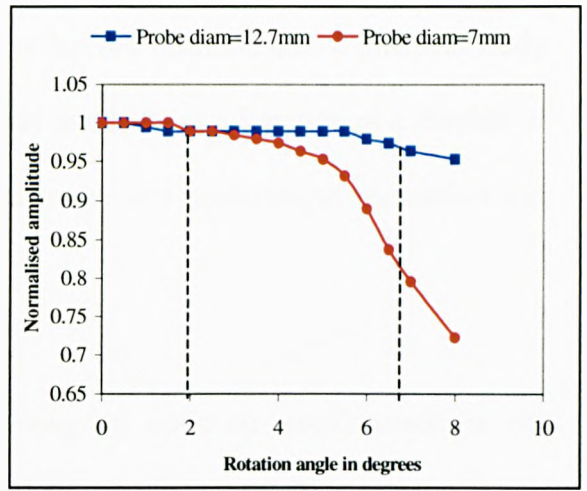


Figure 4.11(b): Angular resolution measurements- reflector diameter = 8.8cm target/probe separation = 10.6mm

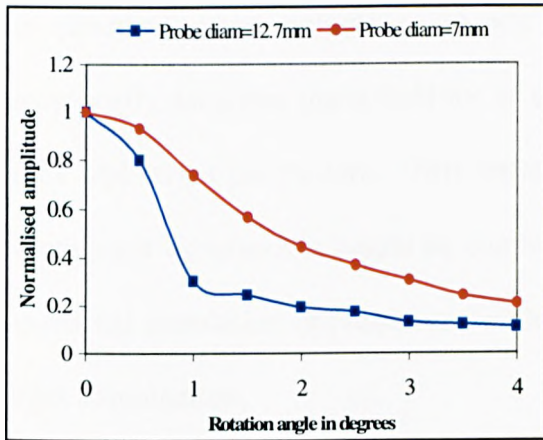


Figure 4.12(a): Angular resolution measurements from a plane reflector target/probe separation = 6.5mm

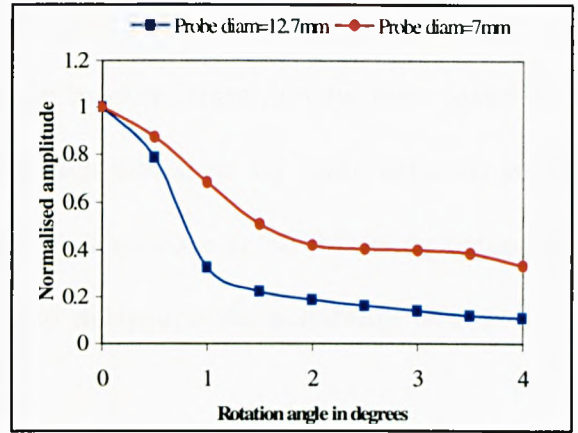


Figure 4.12(b): Angular resolution measurements from a plane reflector target/probe separation = 10.6mm

In the case of small diameter targets, the results in Figures 4.11(a) and (b) indicate that the use of the smaller probe gives better detectability of the angular resolution under the conditions specified. Whereas for the plane target, it was the opposite case as shown in Figures 4.12(a) and (b). Hence for the intermediate curvatures, it is not possible to know what would be the best option using a straight set of rules.

Thus, one of the general conclusions that can be derived from the above practical study is that the detectable angular resolution at normal incidence is a function of a number of parameters including target diameter, probe diameter and probe/target separation and other characteristics of the probe.

However, it should be mentioned that obtaining an optimum combination is not necessary for the present application as long as the angular positioning of the probe is adequately accurate e.g. within $\sim \pm 3^\circ$. In order to ascertain whether a particular combination would be satisfactory, two options could be used. One option is to carry out practical measurements as shown above or the second option could be to theoretically ascertain the suitability of a probe by simulation, having been given the probe and target parameters. This latter approach would be far more efficient since carrying out experiments would be cumbersome. Therefore in the following section, a theoretical simulation approach is developed to determine the suitability of a probe-target combination.

4.8 Theoretical Determination of Angular Resolution

The results shown so far give a useful indication as to the variability of the detection of symmetry due to physical parameters such as probe/target distance, probe aperture and pipe diameter. However, to understand the causes of the changes in the detectability due to these factors, a theoretical model is desirable. The model could also be used to predict the suitability of a probe aperture and probe/target distance corresponding to a given pipe diameter.

It should be mentioned at this stage, that the simulation was carried out using a 5MHz strip-line transducer, since that has been modelled previously. Modelling a circular probe was thought to be unnecessary since the basic idea was to show the feasibility of the simulation approach, and that developing a new model for a circular aperture would be excessively time consuming within the constraints of the present work. This is because the circular aperture has to be represented in a different way, e.g. by a finite summation of rectangular apertures or using a finite number of sectors within the circular aperture. Also, a plane target was chosen as this gave the highest sensitivity in the practical study, although accommodating a cylindrical target would be possible when required.

4.8.1 Modelling the Effect of Probe/Target Orientation

The model previously developed in Chapter 3 for the strip-line transducer was extended to compute the 1st received echo from a plane target in oil at ‘oblique’ incidence relative to the probe at a given axial distance. The angular reflector can be considered as a projection of a plane reflector with each of the elementary areas projected by an amount (δ_R) as shown in Figure 4.13.

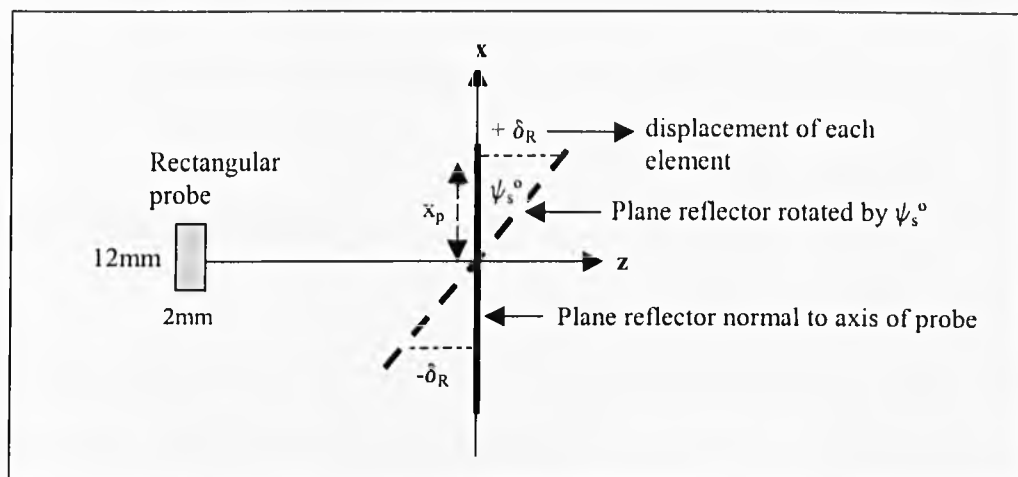


Figure 4.13: Angular orientation of a plane reflector in the x-z plane

From the geometry in Figure 4.13 the projection distance δ_R due to a reflector at an oblique incidence can be derived such that

$$|\delta_R| = x_p \tan \psi_s \quad (4.1)$$

where x_p is x-co-ordinate of the p^{th} element (or point) along the x-axis and ψ_s is the relative angular rotation of the reflector with respect to the probe (Note that δ_R could be either positive or negative depending on the co-ordinate position at the reflector).

Hence if $P_{s(RIA)}(x_p, y_q, z)$ is the pressure amplitude at the point (x_p, y_q, z) at the reflector then the 1st echo pressure amplitude $P_{s(EIA)}$ after reflection from the **angled** plane reflector can be expressed as

$$P_{s(EIA)} = A \sum_{v=1}^m \sum_{u=1}^n C_s \left| P_{s(RIA)}[x_p, y_q, (z + \delta_R)] \right| \cdot R \cdot \left[\frac{\exp - j \left(\frac{2\pi f_s}{c} r_i + \phi_A \right)}{r_i} \right] \Delta s \quad (4.2)$$

where $R = (Z_1 - Z_2)/(Z_1 + Z_2)$ is the reflection coefficient, Z_1 and Z_2 are the acoustic impedances of the two media, and $\phi_A = \angle P_{s(RIA)}(x_p, y_q, z)$. The other symbols and limits in eqⁿ (4.2) are as defined in sections 2.4.1 and 2.4.2.

4.8.2 Verification of Model

The 1st echo amplitude after reflection from a plane steel angled reflector was computed for various rotation angles at a distance of $z = 6.5\text{mm}$ (Appendix B.6). Also,

the practical variation of detectability was obtained using the measurement system of Figure 4.3, but with the circular probe replaced by the 2x12mm rectangular transducer obtained by masking a 12.7mm circular probe. A plane steel reflector was used instead of a curved one. The computed and practical results of the relative amplitude variation with probe rotation angles along the long axis (y-axis) of the transducer as shown in Figure 4.14 with the actual data in Appendix C.6.

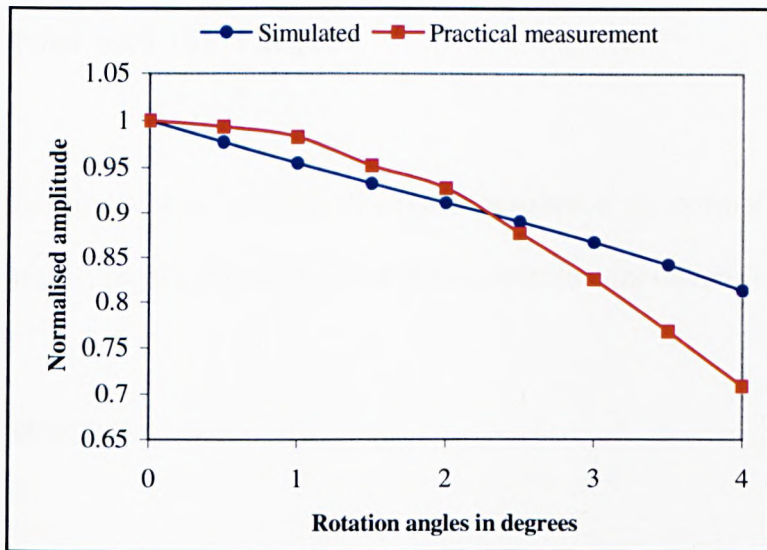


Figure 4.14: Relative amplitude variations for a plane target in oil probe/target separation = 6.5mm

From the above results it can be seen that there is reasonable agreement between the simulated and practical variations on the detectability of angular alignment. The maximum deviation in the range of 0-3° is approximately 5% representing adequate correlation of results. However at greater angles the deviation between results increases, possibly due to the non-idealities of the masked probe as discussed in Appendix A.4.

Therefore, these results show that it is very much feasible to model the probe angular movement with respect to the target to determine the suitability of a particular probe-target/distance combination for the present application. Although the results shown here are only for a plane reflector at a fixed distance the approach may be used to model other probe aperture/ target combinations.

4.9 Summary of Results for Detecting the Positional Symmetry of the Probe and the Target

Having observed the general patterns of angular resolution (at normal incidence) for the detection of positional symmetry of the probe, certain conclusions can be drawn.

Larger diameter targets

- Detectable angular resolution is higher
- Little change in resolution with distance

Smaller diameter targets

- Detectable angular resolution is lower
- Highest reduction in detectable angular resolution with increasing distance

Plane targets

- Highest detectable angular resolution

- Lowest or negligible change of resolution with distance

Surface roughness

- Uniformly rough surfaces give better detectability in terms of angular resolution measurements

The ambiguous effect of target curvature and distance on the angular resolution is very likely due to the nature of focussing effects of return energy from the target, captured by the finite size of the transducer. A significant finding in this work was that it is theoretically possible to determine the suitability of a probe aperture for a given target and distance combination without having to test this using a practical arrangement. This would also provide a useful tool not just for the present application, but for general NDT inspection requiring remote alignment of ultrasonic probes.

4.10 Chapter Conclusions

For the present application of down-hole scale deposit monitoring, an important aspect of measurement is the central alignment of the scanning probe with respect to the pipe internal-wall. In this regard, a novel NDT technique that allows the angular alignment of the transducer using the amplitude of received echoes has been developed.

It was found that the detectability of angular resolution depends on probe/target parameters and their separation. Hence, in order to determine whether a particular combination is suitable, a simulation technique has also been developed. This

technique was also verified by practical measurements for the case of a plane reflector and a strip-line transducer with good agreement of results.

Chapter 5

Ultrasonic Power Transducers for Enhancement of Scale Dissolution

5.1 Introduction

Having completed the project objectives concerning scale detection using high frequency, low power ultrasound, this part of the thesis presents the work carried out on dissolution enhancement using high power ultrasound.

The use of ultrasound for high power applications such as cleaning requires a detailed study of the power transfer capabilities of the ultrasonic transducers in the environment in which they are to be used. For the present application of cleaning inside pipelines, there are obvious dimensional constraints of the transducers, particularly the size of the radiating surface. In addition, the transducer must be able to deliver maximum power output under all environmental conditions (e.g. high and varying temperature conditions) in confined spaces.

In this chapter, three types of high power ultrasonic transducers are evaluated for suitability for this demanding application. The transducer characteristics and their

merits for high power applications are discussed along with relevant equivalent circuits, where appropriate. The power transfer capability of the piezoelectric transducer radiating into liquid media is then evaluated in detail, with the aid of experimental measurements. To determine the transducer efficiency the technique of circle plots was used, as this was a relatively simple and convenient method.

5.2 Magnetostrictive Transducers

This class of transducers work on the principle of the magnetostrictive effect, discovered by Joule in the early 1840s [49,50]. To produce ultrasonic waves by this effect, an alternating magnetic field is created by passing a high-frequency oscillating current at ultrasonic frequencies through a coil, surrounding the transducer material (e.g. nickel rod). As shown in Figure 5.1 this field induces mechanical vibrations in the rod, which is coupled to the surface to be vibrated (e.g. plate or diaphragm, through an epoxy bond) [51].

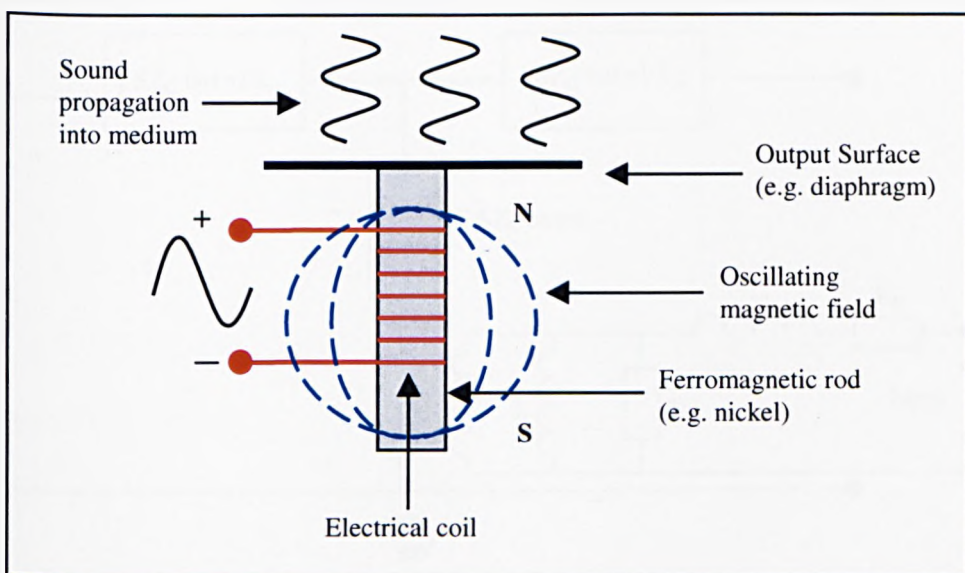


Figure 5.1: Principle of magnetostrictive transducer

The most common type of transducer design is the Zero-spaced magnetostrictive transducer [17]. In this type of transducer, laminated nickel strips are attached tightly together with the electrical coil placed over the nickel stack. This stack is then silver brazed directly to the output diaphragm, creating a solid metallic joint. This results in a far more efficient assembly compared to the design of Figure 5.1 as there is better coupling of the diaphragm to the transducer.

5.2.1 Equivalent Circuit

The derivation of the equivalent circuit for the magnetostrictive transducer is based on a transmission line model. However, there are energy losses that arise in the transducer namely hysteresis and eddy current losses. Hence, for an accurate electrical representation of the transducer, both these losses must be represented. A complete equivalent circuit for the magnetostrictive transducer including these losses is shown in Figure 5.2 [52].

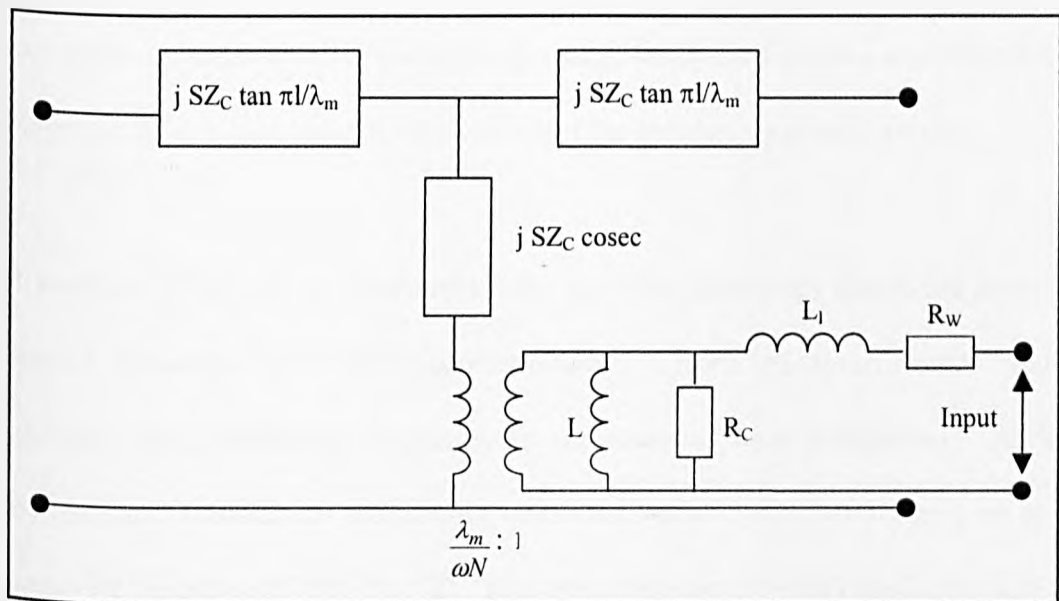


Figure 5.2: Equivalent circuit for a magnetostrictive transducer (with losses)

In the above, L represents the winding inductance of the core, R_w its resistance. L_l is the leakage inductance and R_c represents the core losses. Z_c is the acoustic impedance of the core and S and l the cross-sectional area and magnetic path length, respectively. N is the number of turns of the transducer winding, ω the angular frequency and λ_m is the magnetostriction constant.

5.2.2 Power Transfer and Performance Efficiency

Due to the relative physical size and inherent mass of conventional magnetostrictive transducers (e.g nickel based) compared to piezoelectric types, they can drive more power into a medium compared to other power transducers [17]. They are also durable and less sensitive to load-changes. Ultrasonic systems with magnetostrictive transducers with power outputs as much as 6kW (at 20kHz) are now available with new transducer materials such as some alloys of iron, known as giant magnetostrictive materials (GMMs) e.g. Terfenol-D [53, 54]. In these types of transducers the Terfenol-D material (usually in rods) is put inside the magnetic coil. The Terfenol-D grows and shrinks under magnetostriction undergoing a large amount of strain i.e. deformation as the magnetic field is generated around the coil thus generating greater power.

The transducer efficiency is dependent on the operating frequency due to the previously mentioned hysteresis and eddy current losses. Both of these losses increase considerably with increasing frequency in the form of heat dissipation. As such, magnetostrictive transducers are usually restricted below 20kHz to achieve an overall efficiency of the order of 70% [51,52]. However, they do provide consistent long-term

performance, as there are no significant drifts of physical parameters of the transducer over time.

5.2.3 Limitations of Conventional Magnetostrictive Transducers

Although they can deliver a lot of power, the main disadvantage of conventional magnetostrictive transducers for high power applications is low efficiency compared to piezoelectric transducers, particularly at high frequencies [51, 20]. They are also much more bulkier and heavier than other high power transducers e.g. piezoelectric types, and are also more expensive. Size limitations can make them difficult to use in confined spaces, such as in pipelines.

However new types of magnetostrictive materials such as Terfenol-D, are replacing older actuators and are available in much smaller sizes and different forms due to their higher energy density. They also exhibit a much higher saturating strain and energy density (14000-25000 J/m³) compared with PZT (930 J/m³) and Nickel (30 J/m³) given their giant magnetostriction property [55]. However the cost of Terfenol-D transducers can be a major drawback compared with other common transducer materials such as PZT or nickel alloys due to higher machining costs [56].

5.3 Piezoelectric Sandwich Transducers

The vast majority of modern transducers for cleaning operations utilise the piezoelectric effect [49,50,57]. These types of transducers convert electrical energy directly into mechanical energy coupling into the loading medium. These transducers are easy to use and offer good power transfer performance.

There is a wide range of materials that demonstrate the piezoelectric effect (e.g. crystals such as quartz, tourmaline, barium titanate and Rochelle salt). Some of these materials such as quartz are not a good choice for high power applications due to their low efficiency and the difficulty of machining. Other materials such as barium titanate can be unstable [58]. However, today's power transducers use piezoelectric ceramic materials that are stronger, more efficient and versatile. They can also be manufactured in many different shapes or sizes at a relatively small cost. The most common ceramic material for high power transducers is lead zirconate-titanate (PZT) that can also withstand high levels of mechanical stress [59].

5.3.1 Construction of Transducer

Transducers used in modern ultrasonic cleaning systems are based upon the prestressed piezoelectric sandwich transducer [60]. For cleaning operations, usually a low operating frequency (20-100kHz) is preferred but transducers having sufficiently large radiating surface areas are required. It would be difficult and expensive to manufacture large sizes and thicknesses of crystals to satisfy both these requirements. To overcome this problem the sandwich transducer is used that consists of a number of piezoelectric elements (ceramics) bolted between two metal end masses [49,50,61]. The basic construction of the sandwich transducer is shown in Figure 5.3.

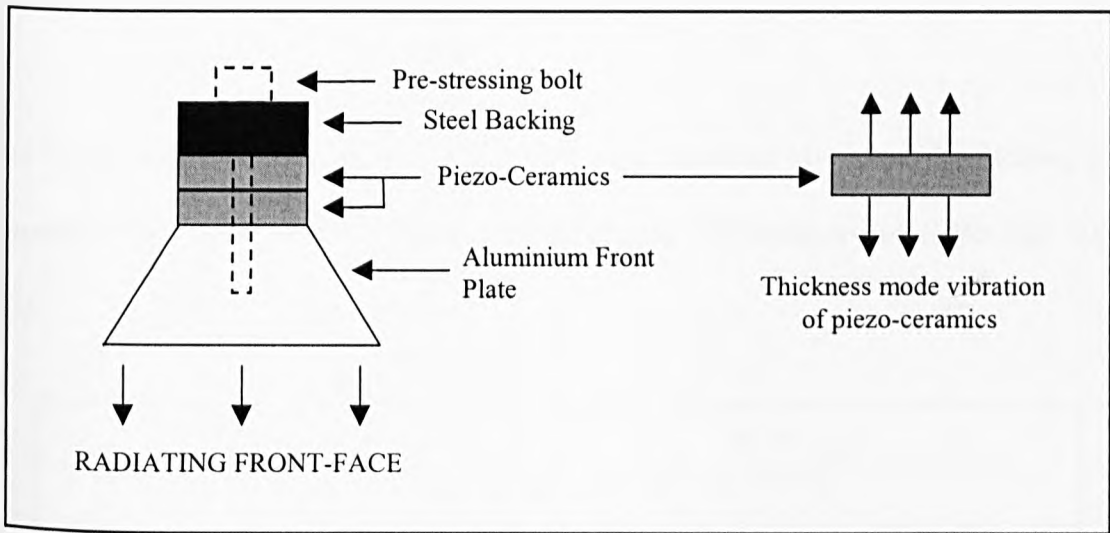


Figure 5.3: A sandwich transducer arrangement with thickness mode vibration

By varying the length of the front and back metal blocks different resonance frequencies are attainable. For optimal efficiency the piezo-ceramics should be positioned at the displacement amplitude node (i.e. point of maximum stress) in the assembly. Furthermore, all the contacting surfaces in the assembly should be flat and smooth to within a few microns (particularly between ceramics) for optimal performance. Both of these design aspects of the transducer have also been reported by Shuyu and Fucheng [62] by theoretical modelling and experiment. The assembly is pre-stressed using a clamping mechanism so that the whole assembly vibrates as one resonant mass. The piezoceramic crystals used in the transducers have a much higher thickness mode resonance frequency than that of the assembly as a whole, e.g. a 20kHz sandwich transducer may have 100kHz piezoelectric elements. By pre-stressing the assembly the resonance frequency of the complete transducer assembly is lowered.

5.3.2 Applications for Cleaning

The configuration of the sandwich transducer when used for low intensity cleaning in a laboratory-type tank would be as shown in Figure 5.4 (courtesy of S.Berliner III's [63]).

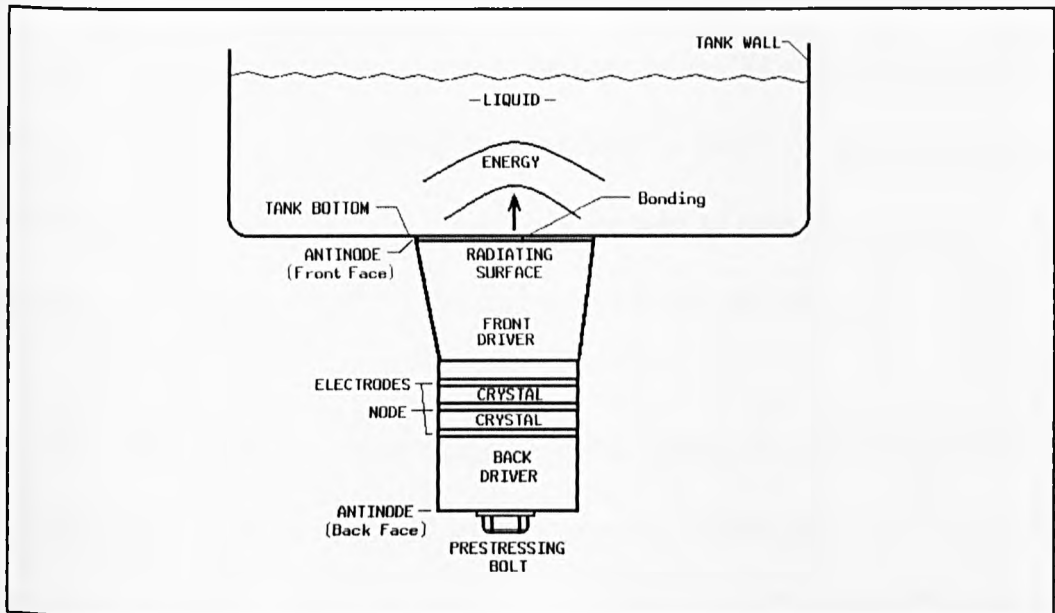


Figure 5.4: Configuration of sandwich transducer for industrial cleaning in a tank

The transducer is bonded to the bottom or side-wall of the tank, which acts as a diaphragm. When energised, the displacement in the crystals causes the diaphragm to vibrate, which in turn causes a pressure wave to be transmitted through the liquid into the tank. For the present application it was thought that a similar configuration could also be used to perform cleaning in a confined area, (e.g. in pipelines) except that no diaphragm could be attached and hence the front face of the transducer would form the contact vibrating surface in the medium. Also in the present application, the acoustic load would not be constant.

5.3.3 Equivalent Circuits and Modelling of Piezoelectric Transducers

To study the performance of the piezoelectric transducer under different load conditions, and to evaluate the power transfer capabilities an electrical equivalent circuit is required. To accurately represent the transducer in this way, the dielectric, piezoelectric and mechanical properties of the transducer material must be known along with information about the dimensions of the transducer. The most common of these equivalent circuits for the piezoelectric transducer is based on either the Mason or KLM model described below. The derivations and uses of both these models to predict performance parameters of the transducers have been well documented by Silk [64].

In the Mason model the acoustical elements of the transducer, such as load impedance and particle velocity are represented by their electrical equivalents using transmission line analogy. An ideal transformer links the mechanical and electrical properties of the piezo-ceramic material. The Mason model has found applications in transducer design and also matching networks for maximum power transfer [65, 66]. In both cases, there is a fairly close agreement between theory and experiment, highlighting the accuracy of the model.

An improvement to the Mason model was developed by Krimholtz, Leedom and Matthaei, now known as the KLM model. The equivalent circuit represents the piezoelectric element as a finite acoustic transmission line, with the electrical circuit coupled at the mid-point of the transmission line. The main advantage of this model is that multiple front layers can be easily added as transmission line sections, for the optimum design of ultrasonic transducers [67].

Derived from both the Mason and KLM transducer models is the lumped parameter equivalent circuit. Similar to both the previous models, this type of equivalent circuit is also based on an electrical transmission line. At the two ends of the transmission line are the load impedances of the two media in contact with the surface of the transducer. In this equivalent circuit all the parameters associated with the transducer (acoustic and electrical parameters) are grouped together into the three main impedance components. This equivalent circuit for a transducer with a flat disc of piezoelectric material of thickness L , is shown in Figure 5.5 [61]. In the present case the transducer is narrow-band and with appropriate constants, this circuit may be used as a narrow-band representation.

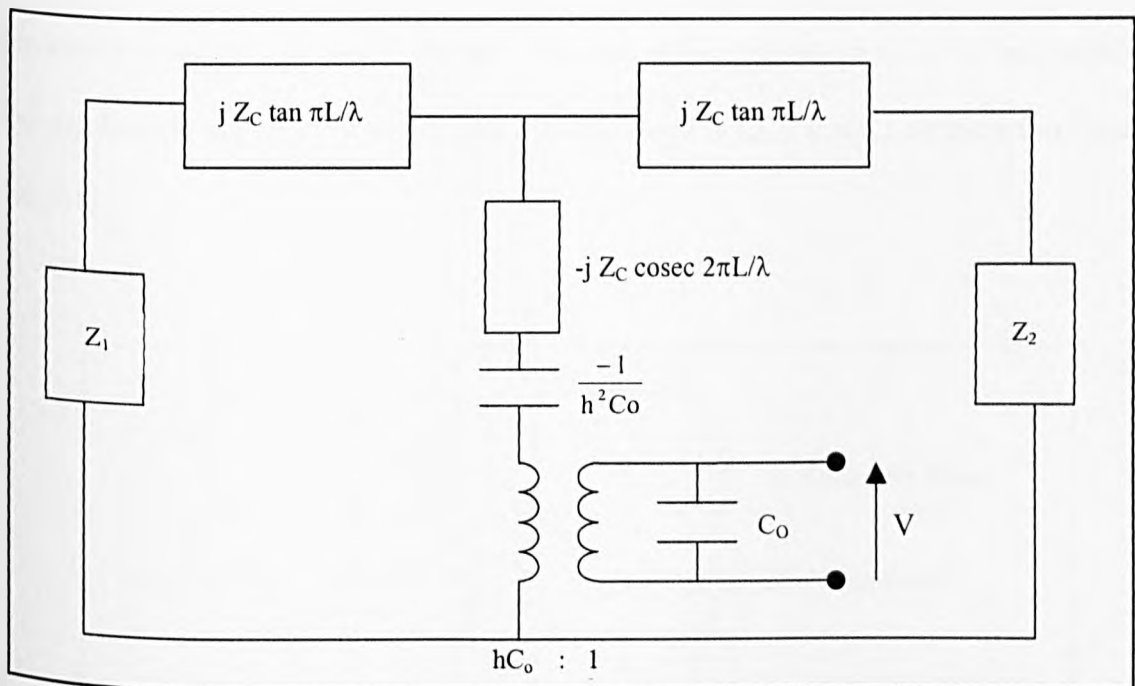


Figure 5.5: The lumped parameter equivalent circuit for a piezoelectric transducer

where Z_1 and Z_2 represent the impedances of the two media in contact with the transducer (e.g. air and water), C_0 is the static capacitance of the piezoelectric material, h is the piezoelectric constant defined as $1/d_{33}$ (where d_{33} represents the direction of the

field and strain) [59] , V is the applied voltage to the transducer, Z_C is the acoustic impedance of the piezoelectric disc and λ is the wavelength.

The acoustic power output in Watts (at resonance) of the transducer when radiating into a medium with acoustic impedance Z_2 is given by:

$$W_o = \frac{4h^2 C_o V^2 Z_2}{(Z_1 + Z_2)^2} \tag{5.1}$$

For most common analyses the above circuit model can be simplified. This circuit is derived from the circuit of Figure 5.6 but is only valid at frequencies at and near the resonance frequency of the transducer. The derivation procedure involves representing the mechanical elements of the transducer into a series LCR circuit as shown in Figure 5.6 [61].

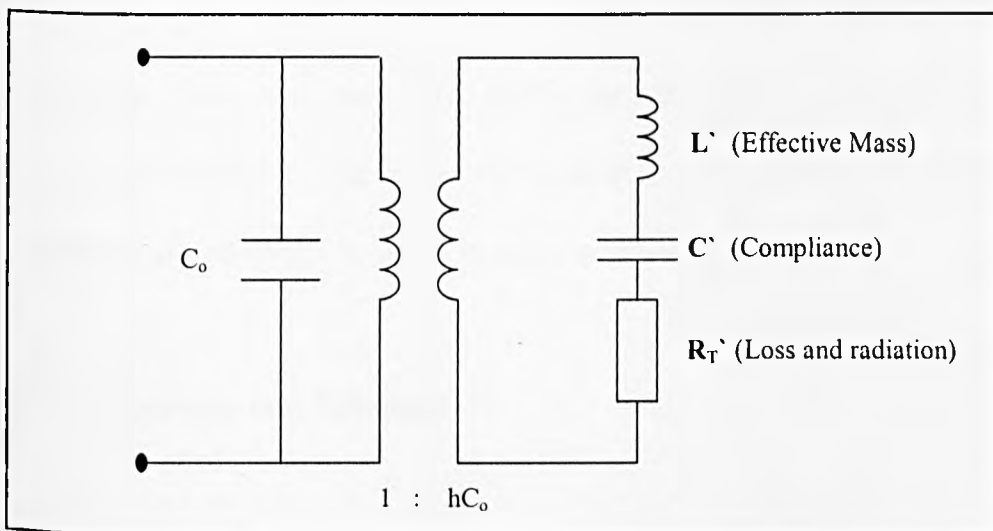


Figure 5.6: Equivalent circuit of a piezoelectric transducer near resonance

The transformer section represents the electrical equivalent of the transducer. The term hC_o represents the force generated due to the applied voltage to the transducer.

However for purely electrical analysis, it is common to simplify the above circuit further to a simple LCR circuit in parallel with C_o as shown in Figure 5.7 [57, 68]. This circuit is extensively made use of in the present study, to evaluate the power transfer characteristics of the piezoelectric transducer. (Note that the numerical values of L , C , and R in Figure 5.7 are not the same as in the circuit of Figure 5.6).

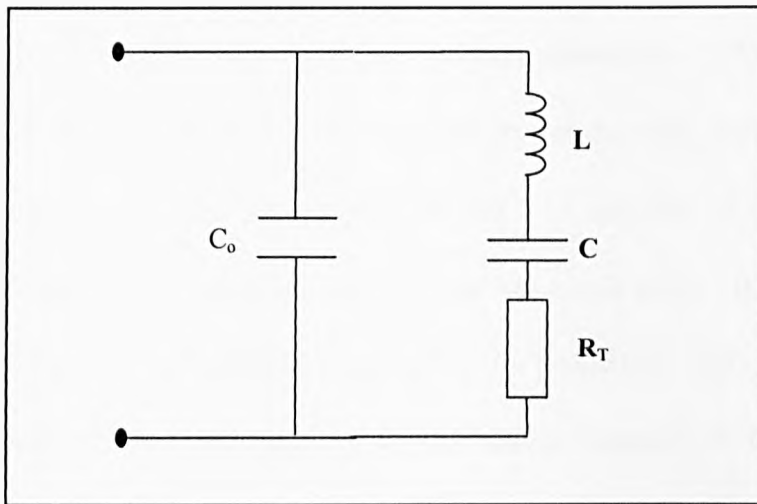


Figure 5.7: Further simplified equivalent circuit of a piezoelectric transducer near resonance

It is also important to note that the resistance R_T , consists of two resistive components: R_L and R_R . The losses of the transducer are represented by R_L , which should be as small as possible. The power transmitted by the transducer into a medium depends on R_R - the radiation resistance. The higher the value of R_R , the more power is dissipated into the medium, which results in higher transducer efficiency.

5.3.4 Power Transfer and Efficiency

Sandwich transducers can have efficiencies in excess of 90% and power outputs up to 1kW. Typically the maximum peak to peak displacement of the transducer front face at 20kHz can be of the order of 10-20 μ m (continuous excitation) [60]. Although this power output is considerably less compared to magnetostrictive transducers, sandwich

transducers are much smaller and inexpensive to assemble which makes them desirable for the present application.

5.3.5 Limitations of Piezoelectric Transducers

Although the piezoelectric sandwich transducer is a popular choice for high power ultrasonic applications, there are some performance drawbacks. The most common problem is that over time, the performance of the crystal degrades resulting in a lesser amplitude displacement to the front plate [17, 20]. In addition, if the transducer is continually exposed to high temperatures (i.e. near the Curie point - the temperature at which the crystal permanently loses its piezoelectric properties) then the piezoelectric effect is considerably reduced, leading to permanent damage of the piezoelectric element [59]. The effects of temperature below the Curie point on the sandwich transducer assembly is to change its resonance conditions thus reducing its efficiency and hence power output. Hence, this creates a potential drawback for the present application inside high temperature environments, and therefore optimising the performances by means of compensation techniques need to be developed, as presented later in Chapter 8.

5.4 Piezoelectric Flexural-Horn transducers

Another transducer design consisting of the piezoelectric sandwich type driver coupled to a flexural vibrating radiating plate has also been used for high power applications. To further enhance the power, the output is increased using an acoustic horn connected between the piezoelectric elements and the flexing plate, which acts as a vibration

amplifier [69, 70]. The horn is preferably made from titanium alloy or aluminium which transfers high amplitude vibrations to the thin radiating plate, where the flexing movement of this plate generates flexural waves (anti-symmetrical mode of Lamb waves) into the propagating medium. This concept of coupling acoustic horns to ultrasonic transducers originates from the classical loudspeaker design, where the object of the horn is to reduce the acoustic impedance mismatch between the vibrating diaphragm of the loudspeaker and the surrounding air [71].

5.4.1 Construction of the Flexural-Horn transducer

This same principle of the loudspeaker horn can be extended to the flexural vibrating transducer, except that the high vibrational energy is now focussed onto a small end point and coupled to a front plate. This concept has been applied in the design of a high power transducer for use in gases by Gallego-Juarez et al. [72], using a solid stepped horn assembly. The longitudinal vibrations generated by the piezoelectric elements in a sandwich configuration are amplified by this steel horn, which drives a large radiating plate at its centre. The extensive area of this metal plate increases the radiation resistance of the transducer and offers good prospects for impedance matching with the radiating medium. The basic design of this transducer is shown below in Figure 5.8.

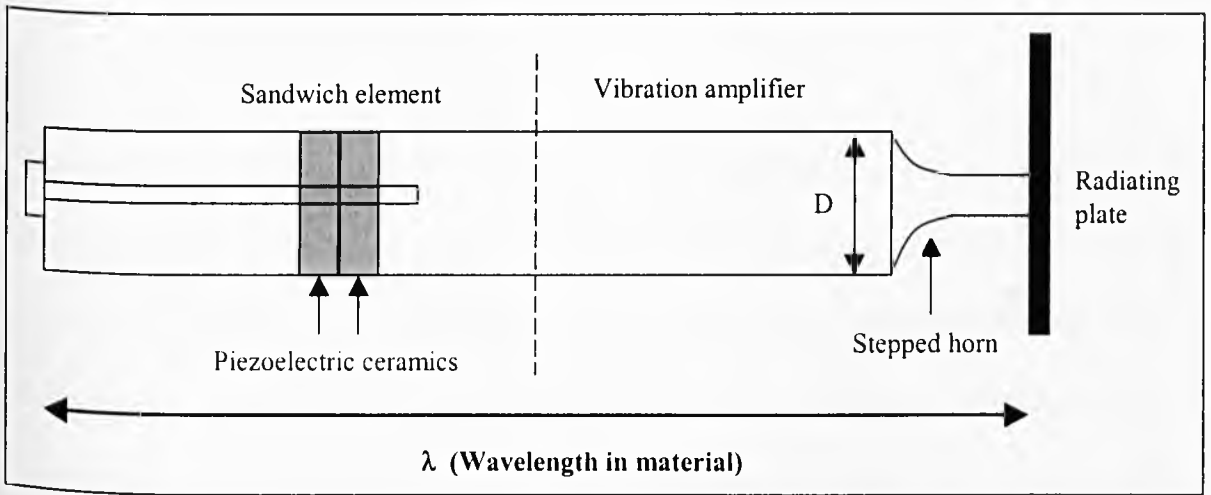


Figure 5.8: Construction of a Flexural-Horn transducer

For maximum vibration amplification by the stepped horn, the diameter 'D', in Figure 5.8, should be made much larger than that at the tip of the horn. For further performance enhancement the front plate can be 'stepped' on either sides of the nodal circle regions to obtain a directivity pattern equivalent to that of a theoretical piston. If it is 'stepped' by a height of $\lambda/2$, where λ is the wavelength of the propagation medium (i.e. water or air) then all the flexural vibration waves will leave the plate *in-phase*, resulting in a more coherent radiation pattern as illustrated in Figure 5.9 [70, 72].

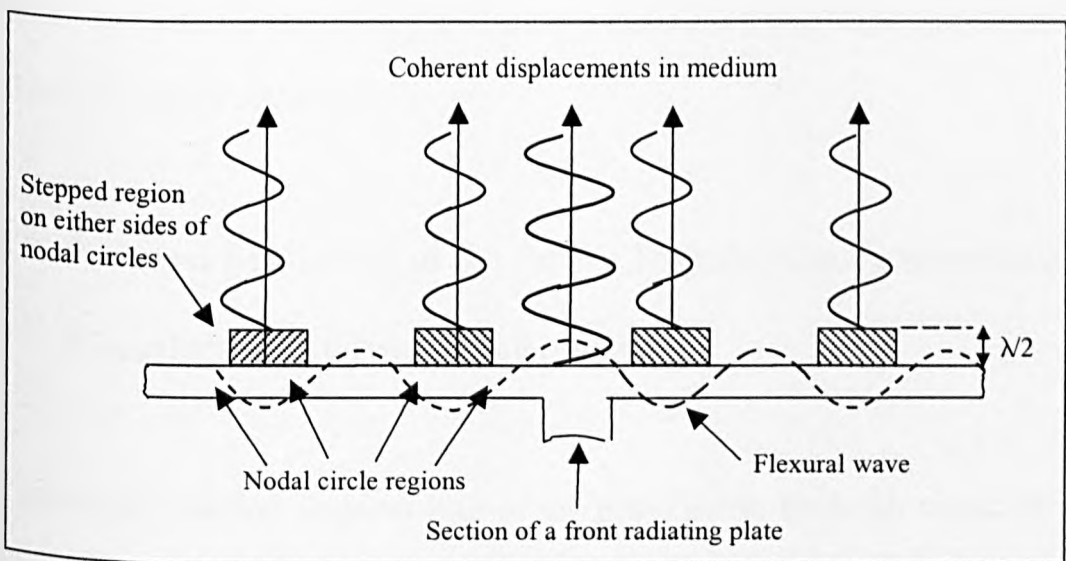


Figure 5.9: Side-end view of a stepped radiating plate

5.4.2 High Power Applications

The flexural-horn transducer has found successful applications ranging from ultrasonic plastic welding to the medical field for renal lithotripsy treatment [73, 74]. In these respective applications it is the high amplitude vibrations generated at the tip of the horn that is used in delicate operations. Coupling a large radiating stepped plate to the horn, with a diameter up to 70cm, has reported efficiency figures in the region of 80% and power capacities above 1kW [75]. These transducers have been used for industrial applications in liquid such as de-foaming and textile cleaning.

For the present application of high power radiation for cleaning inside pipelines of finite dimensions, the above type of transducer would not be directly suitable due to obvious size constraints of the vibrating front plate. However, based on literature reviewed [70, 72-75], the power performance of flexural-horn transducers could be superior to using a conventional sandwich transducer. Therefore, further investigation regarding the possibilities of the flexural-horn transducer having a limited size of radiating surface (e.g. up to 20cm in diameter) was carried out. This aspect is studied further in Chapter 6 of the thesis.

5.5 Practical Evaluation of the Power Transfer Characteristics of Piezoelectric Sandwich Transducers

To assess the radiation characteristics of the piezoelectric sandwich transducer in a liquid medium, experiments were carried out using the circle diagram technique to measure both the efficiency and radiation resistance. This required deriving necessary

power transfer and efficiency equations from the transducer admittance plots as discussed below.

5.5.1 Transducer Efficiency from Circle Diagram

Referring to Figure 5.7 the input complex impedance of the sandwich transducer can be written as $Z_s = R_s \pm jX_s$, where R_s and X_s denote the resistance and reactance as functions of frequency. This variation near the resonance frequency of the transducer yields a circle plot in the impedance plane [61]. However, in practice it is the complex admittance of the transducer, $Y = G \pm jB$ that is plotted (susceptance v. conductance) as a function of the frequency. To obtain the power transfer parameters (radiation resistance and efficiency) for the piezoelectric transducer the following two steps were therefore required:

- 1) Practical measurements to obtain the transducer admittance at frequencies around resonance.
- 2) Plotting and derivation of necessary efficiency parameters from the resultant circle plot.

Practical Measurements to Obtain Transducer Admittance - Approach

To obtain the input admittance of the transducer by practical measurements the basic circuit shown in Figure 5.10 was used.

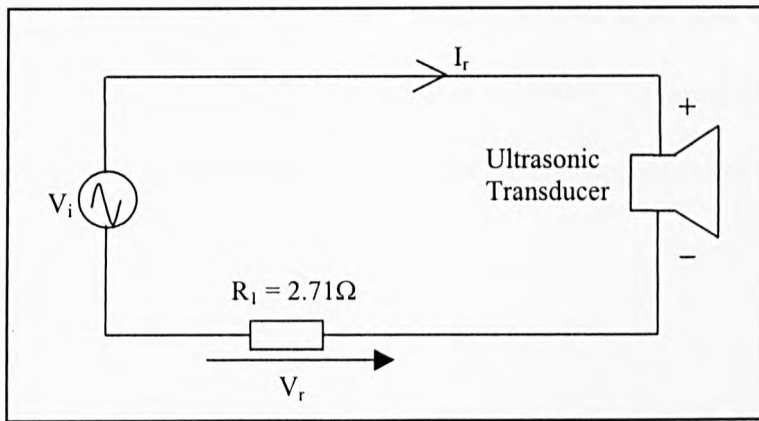


Figure 5.10: Measurement of transducer impedance for circle diagram

The voltage V_i is kept constant e.g. 8V pk-pk. The voltage across the small resistor R_1 , is measured (both magnitude and phase, w.r.t V_i) as the frequency is changed gradually around the resonant frequency of the transducer. By calculating the current I_r , the input (complex) impedance as seen by the transducer (V_i/I_r) is obtained at each frequency around resonance. Hence, the admittance $Y = G + jB$ (in siemens), can be obtained at any frequency. A MATLAB program (Appendix B.7) was written to perform this admittance calculation and for plotting the resultant locus (i.e. circle) diagram.

Obtaining Power Transfer Parameters from the Circle Diagram

Referring back to the simplified equivalent circuit of Figure 5.7, the total transducer admittance can be written as

$$Y = G + jB = \frac{1}{R_T + j(\omega L - \frac{1}{\omega C})} + j\omega C_o \quad (5.2)$$

where R_T , L , C , and C_o are the equivalent circuit components, and ω represents the frequency in radians/second. It can be shown that the above equation (5.2) represents a circle in the complex admittance plane [76]. The G and B components can be extracted from

$$\left[G - \frac{1}{2R_T} \right]^2 + B^2 = \left[\frac{1}{2R_T} \right]^2 \quad (5.3)$$

which describes a circle with radius $1/2R_T$, centred on the point $G = D_C + 1/2R_T$, $B = B_o$.

The circle plots for the piezoelectric transducer when radiating into air (assuming there is no significant radiation into air) and a liquid load can be represented in the admittance plane as shown in Figure 5.11.

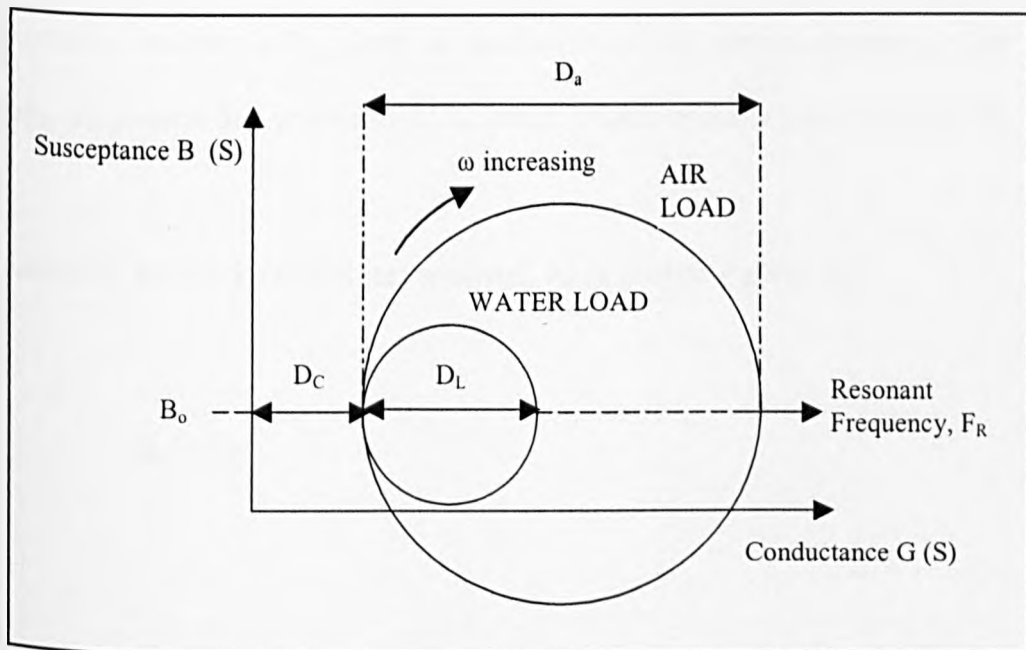


Figure 5.11: Power transfer parameters - circle diagram in the admittance plane

In the above diagram D_a and D_L represent the circle diameters when the transducer is radiating into air and water respectively and B_o is the susceptance at the resonance frequency, F_R . From equation (5.3) the diameter of the loaded circle plot can be expressed as

$$D_L = \frac{1}{R_T} \quad (5.4)$$

where $R_T = R_R + R_L$ (i.e. radiation + loss resistance). Since transmission into air is negligible, the loss (R_L) and radiation resistance (R_R) can be expressed as:

$$R_L = \frac{1}{D_a} \quad (5.5)$$

$$R_R = \frac{1}{D_L} - R_L \quad (5.6)$$

The radiation resistance R_R gives an indication of the power transfer to the liquid medium. In general this value should be much greater than the loss resistance R_L .

The dielectric loss of the transducer material, R_d is similarly given by

$$R_d = \frac{1}{D_c} \quad (5.7)$$

The centres of both the loaded and unloaded circles also coincide at a susceptance B_o .

From this susceptance value the static capacitance of the transducer can be calculated,

since

$$C_o = \frac{B_o}{\omega_R} \quad (5.8)$$

Finally, the transducer efficiency as a **numerical index** is given by the ratios of the

unloaded and loaded circle diameters:

$$\eta = \frac{D_a}{D_L} \quad (5.9)$$

5.5.2 Experimental Arrangement

To find the power transfer characteristics of a typical piezoelectric transducer, a sandwich transducer with a resonance frequency of 80kHz was used for initial experiments. These experiments should give an indication of the efficiency for these types of transducers. Initially an 'infinite' medium was chosen to eliminate the complications due to reflections and standing waves.

The transducer was mounted inside a plastic holder to ensure only the front surface can radiate into a medium and was placed inside a large water tank as shown in Figure 5.12. The assembly was slightly angled to minimise any reflections from the floor of the tank.

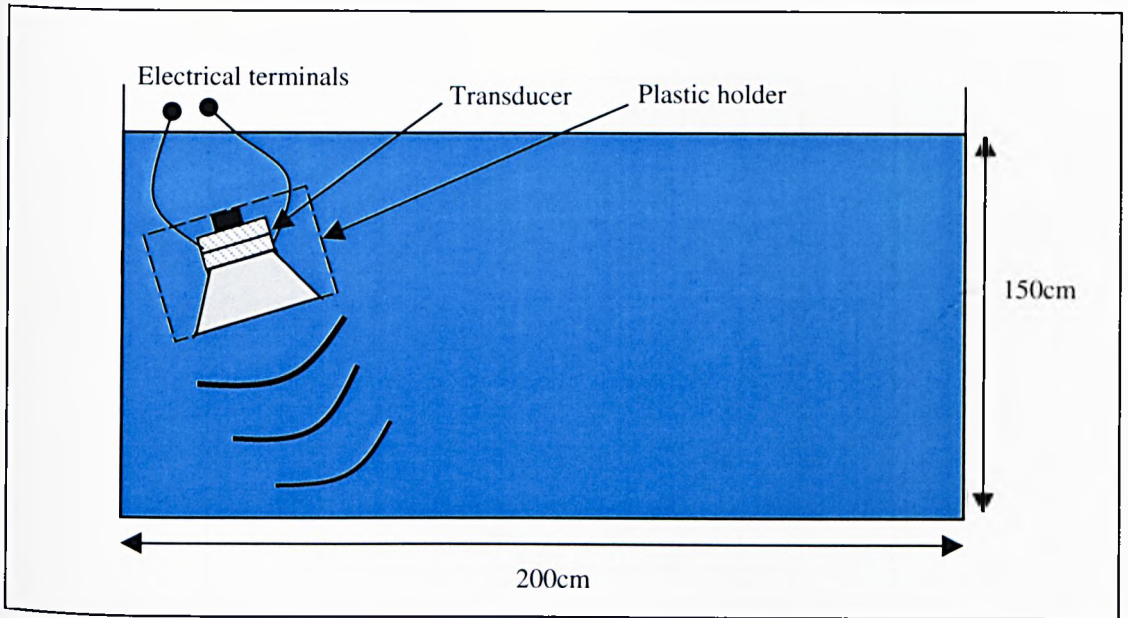


Figure 5.12: Sandwich transducer radiating in a large water tank (side end view)

5.5.3 Circle diagrams for sandwich transducer in large water tank

To determine the transducer efficiency the circle plots for the transducer radiating firstly into air, and then in water, was required. Examples of the circle plots obtained after practical measurements (computed using MATLAB program B.7) are shown in Figures 5.13 and 5.14. In both plots a best-fit circle was obtained manually.

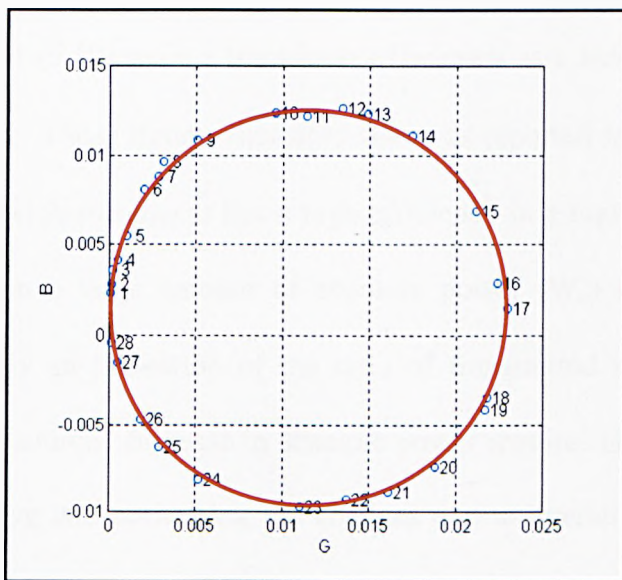


Figure 5.13: Circle diagram for transducer radiating into air

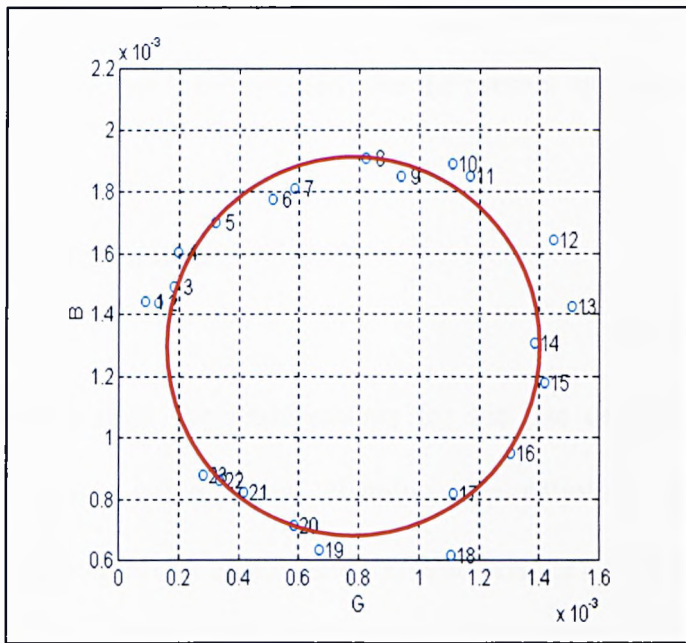


Figure 5.14: Circle plot for transducer radiating into a large water tank - 'infinite medium'

From Figure 5.13, the measured diameter $D_a = 0.0223$ S approx. and the loss resistance $R_L = 44.5\Omega$ using equation (5.5). The static capacitance C_o was calculated to be 2.586nF using equation (5.9). This was also measured separately and found to be close to the above value (2.53nF). The efficiency of the transducer was then evaluated.

From Figure 5.14 the diameter of the loaded circle $D_L = 1.242$ mS approx. Applying equations (5.6) and (5.10) gave a transducer efficiency as a numerical index of 17.95 with $R_R = 760.7\Omega$. These figures therefore show, as reported in the literature that the piezoelectric sandwich transducer has a high efficiency in a liquid medium. However, this does not mean a large amount of absolute power (W_o) is transferred into the medium but simply an indication of the ratio of transmitted acoustic power to that absorbed from the source. Increase in absolute power requires electrical and acoustical impedance matching and optimising the changes due to operating conditions. Hence

these aspects including the effect of the radiating environment on the efficiency, for example inside a pipe requires further study for the present application.

5.6 Chapter Conclusions

For the present application the requirements for the use of high power ultrasound transducers differ from conventional cleaning applications. In this regard, the applicability, design and power performance characteristics of the three most common types of power transducers have been reviewed and discussed.

Magnetostrictive transducers can drive high levels of power (up to 6kW) into liquid mediums. However, their size and their low efficiency make them less desirable for applications in confined areas. Most commonly, the piezoelectric sandwich transducer is used for low frequency cleaning operations. These types of transducers demonstrate efficiencies in the region of 90% in water loads, as has been shown by the experimental data. However, their radiation characteristics in pipes need to be further investigated.

Flexural-horn transducers offer higher levels of vibrations from the front disk using the sandwich transducer construction. The radiating surface has been reported to be quite large for successful designs, but their performance with a smaller radiation area also requires further investigations. These will be discussed in the next chapter.

Chapter 6

Techniques for Increasing the Radiation Resistance of Ultrasonic Transducers in Pipelines

6.1 Introduction

A critical requirement of the transducer system for the present application of scale dissolution enhancement in pipelines is that it must deliver maximum power into the radiating medium. In the previous chapter, the radiation characteristics of the piezoelectric sandwich transducer in an infinite medium (water) were discussed. The transducer efficiency and radiation resistance were obtained when radiating into a large water tank.

In this chapter, electrical and acoustic impedance matching to increase both the above power transfer parameters for the sandwich type transducer, radiating within confined spaces are investigated. The use of flexural-horn transducers to increase the power transfer performance of the sandwich transducer structure, as reported in Chapter 5, is also investigated further. A prototype design of the horn transducer was also tested. A possible development of this type of transducer, with multiple radiating disks for improved power output is then proposed.

6.2 Transducer Efficiency Inside Pipes

In the previous chapter, the efficiency of the piezoelectric sandwich transducer in a large water tank was obtained using the circle diagram technique. However, it is the radiation characteristics of the transducer inside pipelines, which is of interest in the present study. Initial measurements in a water filled straight plastic tube (180cm in length), gave excessive reflections, making it difficult to obtain an accurate circle plot [77]. An extended S-shaped plastic tube as shown in Figure 6.1 was then used for further experiments to assess the radiation efficiency of the sandwich transducer in water. The transducer was placed inside a plastic holder which only allows the front face to come in contact with the medium inside the pipe. The inlet and outlet valves are for circulating heated water into the pipe section when necessary. This pipe section also represents the practical situation, as scale deposits are more likely to be located in pipe bends and bottlenecks.

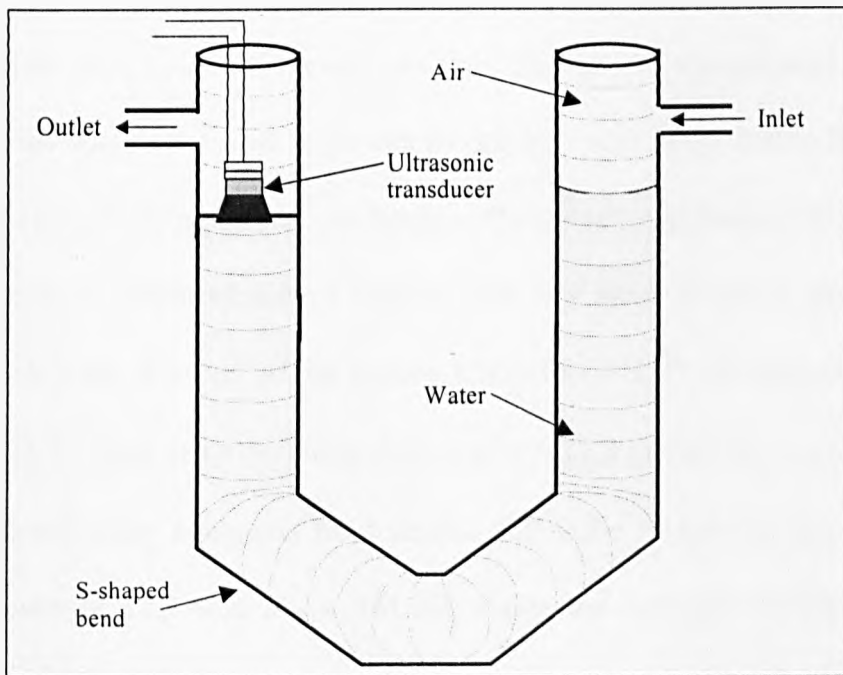


Figure 6.1: Extended S-shaped plastic pipe section used to assess radiation of power transducer (Dimensions: Total length = 4.3m approx., Diameter = 14cm)

The circle plot for the sandwich transducer radiating into the above pipe section was then obtained using the method described in 5.5.1. The best-fit circle plot achievable, after repeating several measurements is shown in Figure 6.2.

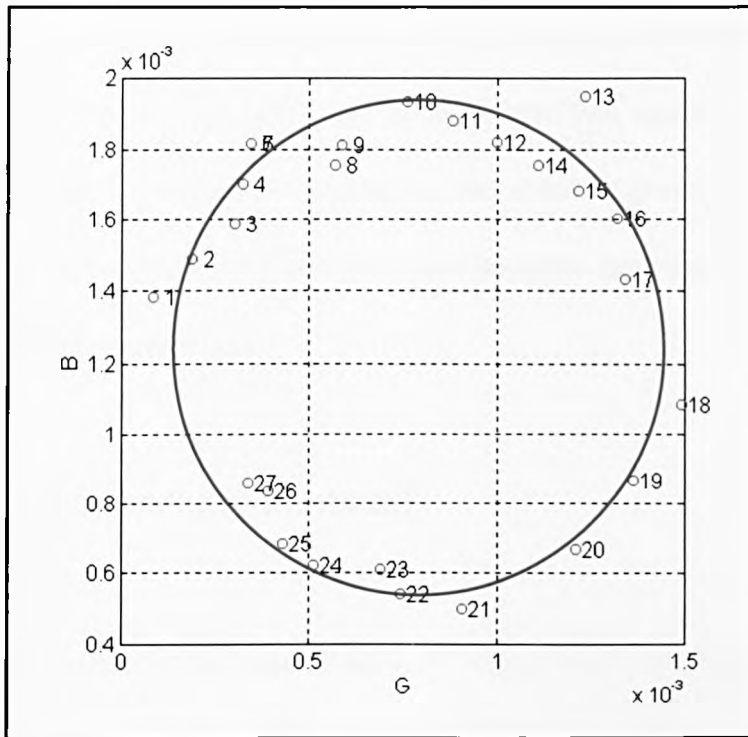


Figure 6.2: Circle diagram for transducer radiating into water in extended S-tube

The circle plots were not well shaped (unlike in the case of transmission into infinite medium). This was later found to be due to acoustic reflections within the structure, representing changes in impedance conditions. The presence of these reflections makes it very difficult to obtain efficiency figures with any great accuracy and reliability. From Figure 6.2 the diameter of the best-fit circle $D_{Li} = 1.29$ mS approx. Recalling from section 5.5.3, that in air the circle diameter $D_a = 22.3$ mS and $R_L = 44.5\Omega$, then by applying the efficiency equations from section 5.5.1, the transducer has a numerical index efficiency of 17.3 with $R_R = 733.1\Omega$, inside the extended S-shaped tube. It should also be mentioned that the estimates of transducer efficiency have an uncertainty of approx. ± 0.3 in terms of the numerical index figure, due to the scattering

of points in the circle plot. It can therefore be seen that the power transfer efficiency has been decreased compared to the case when radiating into infinite media (section 5.5.3).

Having assessed the radiation characteristics of a typical piezoelectric power transducer in infinite and finite media, the next stage of work involved research into methods of increasing the radiation resistance to increase the absolute power output. For this purpose, techniques for optimising electrical and acoustic impedance matching under the present constraints were studied.

6.3 Electrical Impedance Matching

This method of maximising the transmission of power from the electrical source into the transducer, involves matching the generator source impedance (typically 50Ω) to the transducer impedance using a matching transformer [78, 79]. The transformer is designed so that the inductance of the secondary winding tunes out C_o (static capacitance) at the series resonant frequency of the transducer, ideally diverting all the signal current into the load. This also improves the power factor of the transducer. The basic principle of electrical impedance matching is shown in Figure 6.3. The transducer circuit as shown in Figure 5.7 has been further simplified because near the resonance frequency, the series inductive and capacitive reactances cancel each other, leaving the resistive component R_T as the load.

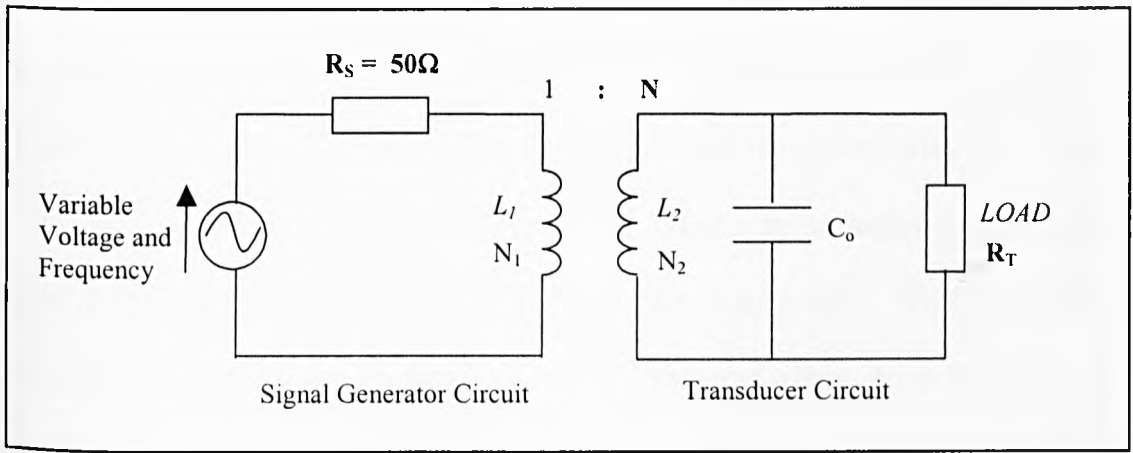


Figure 6.3: Electrical impedance matching using a power transformer

The value of L_2 at the resonance frequency ω_R , is calculated from

$$L_2 = \frac{1}{\omega_R^2 C_0} \quad (6.1)$$

Since $L_2 = N_2^2/S$ where S is the reluctance of the former, the number of turns N_2 can be calculated. Assuming ideal properties, the number of turns of the primary winding (N_1) is calculated from the transformer turns ratio, $N = N_2/N_1$. However, the reflected impedance on the secondary is $R_T = N^2 R_S$, with

$$N = \frac{N_2}{N_1} = \sqrt{\frac{R_T}{R_S}} \quad (6.2)$$

This allows the number of turns required in the primary winding for matched conditions to be calculated.

Electrical impedance matching has been successful in applications such as underwater acoustics and medical transducers for increasing power transfer [65-67]. However for our present application this matching technique presents two main constraints. Firstly, in down-hole pipelines temperature gradients effect the transducer performance, resulting in the load impedance also changing significantly with temperature. Secondly, the parameters of the transmission cable providing drive signals to the transducer over extended distances can also change with temperature. Thus, an automatic impedance matching network, which tracks the cable and transducer impedance may be required to effectively match the generator impedance to the transducer impedance for the present application. Work on these areas under dynamic impedance matching is reported in Chapter 8.

6.4 Acoustic Impedance Matching

The front radiating face of the sandwich construction transducer is usually made from aluminium which has an acoustic impedance of 17.3 Rayls. For the present application, the transmission medium is water (similar impedance to oil) with an acoustic impedance of 1.48 Rayls. This is a very high impedance contrast, which allows only about 30% of energy to be transmitted into the medium. Hence, even with the resonant matching conditions considerably less ultrasonic power will be transmitted from the transducer into water unless a good acoustic match between the two media is established.

One way of achieving this objective is to use a matching layer/plate between the transducer radiating surface and the radiating medium. The transmission will be at a

maximum if this matching layer has an impedance equal to the 'Geometric Mean' of the two mediums, and has a thickness equal to $\lambda/4$ (λ being the wavelength within the material of the layer at resonance) [80, 81]. An alternative option is double layer matching, which can give further increases in transducer efficiency and bandwidth, but is not considered here due to the constructional and operational difficulties [78]. The arrangement of the single matching layer with respect to the transducer is shown in Figure 6.4.

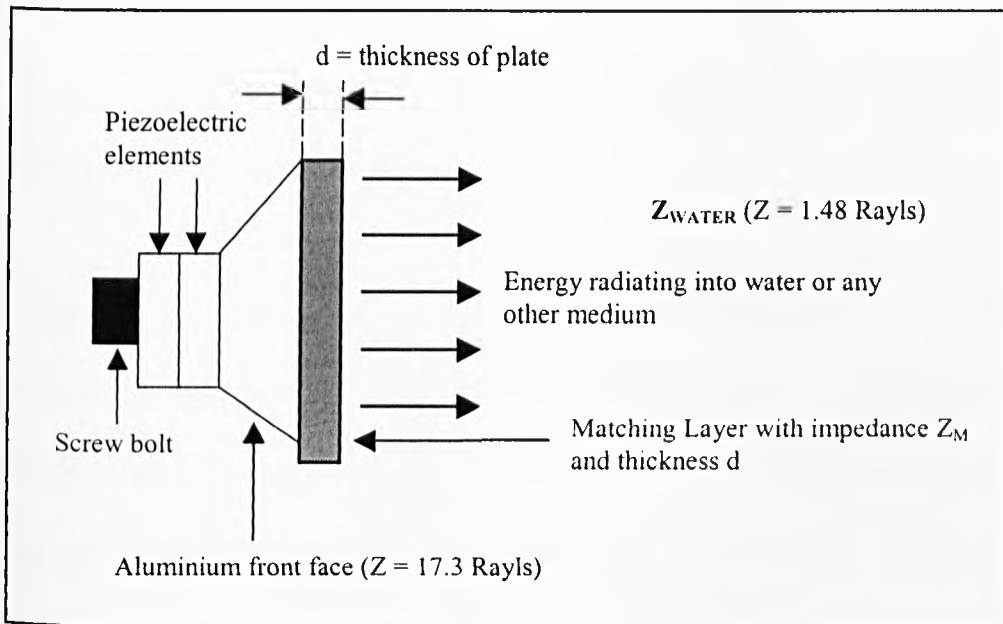


Figure 6.4: Acoustic Impedance Matching

For the present case, the required impedance Z_M of the matching layer can be given as

$$Z_M = \sqrt{Z_{\text{Water}} \cdot Z_{\text{Alum}}} \quad (6.3)$$

Hence for the present application,

$$\begin{aligned} Z_M &= \sqrt{1.48 \times 17.3} \\ &= 5.060 \text{ Rayls} \end{aligned}$$

Another important aspect, apart from meeting the impedance criteria, is that the chosen material should have very low attenuation. Otherwise the benefits of acoustic matching can easily be outweighed by the power transfer loss due to attenuation.

It is quite difficult to obtain materials with low attenuation and an acoustic impedance of 5 Rayls. Perspex/Plexiglass ($Z = 3.2$) and Teflon ($Z = 3$) are widely used materials that have an acoustic impedance close to the desired value with low attenuation values. More often, composites of materials are used for matching layers with low impedance, e.g. fibreglass with epoxy and aluminium powder in araldite. These can be difficult to make due to bonding imperfections.

In addition to the importance of the matching layer impedance for maximum transmission, the thickness, 'd' must also be carefully chosen. It has been widely reported in related literature that this thickness should be $\lambda/4$, to improve both the efficiency and bandwidth of PZT disc transducers [66, 82-84]. However, for a transducer that is slightly under matched (e.g. Z_M less than the geometric mean) as would be the case in practice, it has been reported that the optimum thickness could be nearer $\lambda/4.44$ [81]. Both these thickness dimensions were investigated for efficiency improvement for the present transducer, radiating into water.

6.4.1 Material Choice for Acoustic Impedance Matching

After investigating many possible materials that could be used for the matching plate, two were finally chosen. These were Perspex and a fibreglass/resin composite. Perspex was used because it has an acoustic impedance close to the required value of 5

Rayls. It is also readily available and easy to machine for different thickness dimensions. A fibreglass/resin composite was also constructed for matching because it has a very low attenuation compared to plastics and the bulk impedance could be closely adjusted to the required value. Table 6.1 shows the properties of both matching materials as measured, along with the thicknesses that were used for the sandwich transducer (centre frequency 80kHz). Only one thickness of fibreglass was used due to constructional difficulties.

Table 6.1: Material Properties for Acoustic Impedance Matching

Material	Velocity (m/s)	Impedance (Rayls)	λ (mm)	$\lambda/2$ (mm)	$\lambda/4$ (mm)	$\lambda/4.44$ (mm)
Perspex	2680	3.2	33.5	16.75	8.39	7.5
Fibreglass*	3942	8	49.3	-	12	-

* All parameters obtained by actual measurements using a 13mm thick sample

6.4.2 Practical Evaluation of Efficiency Improvements with Acoustic Impedance Matching

To evaluate the effectiveness of acoustic impedance matching with the materials in Table 6.1, all experiments were initially performed in the large water tank. The transducer configuration was kept the same as that shown in Figure 5.12. The respective matching plates were screwed onto the front face of the plastic transducer holder (coupled with lubricant oil) to achieve a good acoustic contact. The circle plots were used to obtain the efficiency parameters as described in the previous chapter.

Measurements in Large Water Tank

In order to eliminate complexities due to reflections, the large water tank was initially used for evaluating efficiency improvements. The results showed that the highest increase in efficiency with the perspex plate occurred when the thickness was $\lambda/4.44$ (7.55mm). However, overall the best matching material was the fibreglass plate as shown in Figure 6.5.

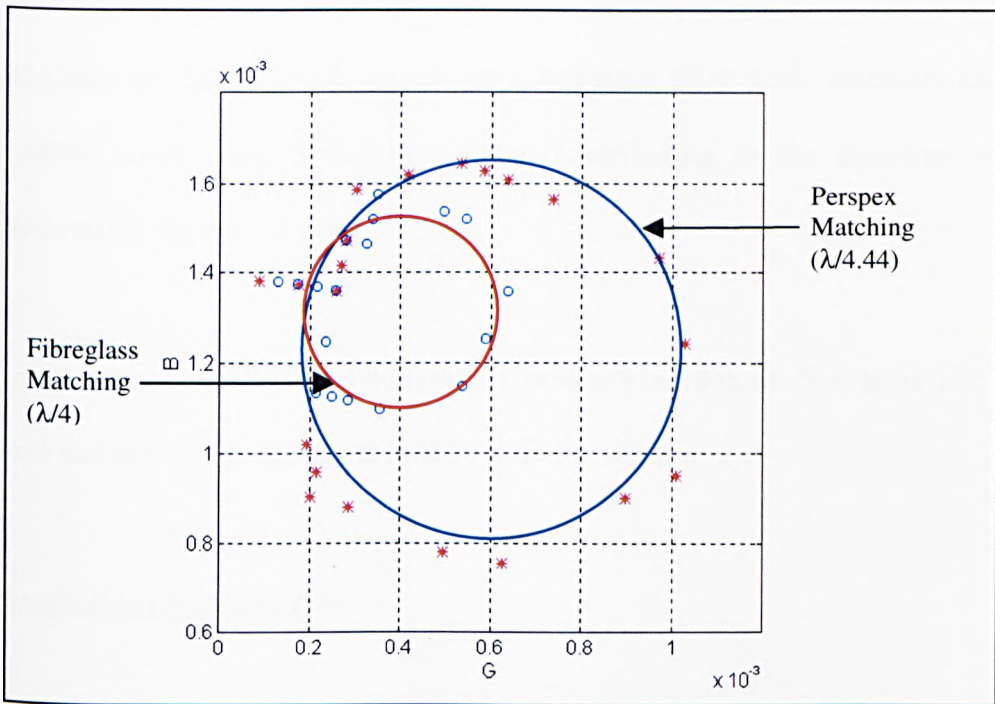


Figure 6.5: Efficiency improvements with Fibreglass and Perspex ($\lambda/4.44$) matching plates in water

The power transfer improvement can be seen more clearly when the radiation resistance (R_R) is considered. These parameters of the transducer with the perspex and fibreglass matching plates are summarised in Table 6.2 below.

Table 6.2: Summary of power transfer parameters with Perspex and Fibreglass matching in large water tank

Material	Thickness (mm)	Circle Diameter (S)	Efficiency (numerical index)	R_R (Ω)
NONE	-	1.24	17.9	760.7
Perspex	16.75, $\lambda/2$	1.1	21.2	883.7
Perspex	8.4, $\lambda/4$	0.98	22.8	977.8
Perspex	7.55, $\lambda/4.44$	0.85	26.4	1137.6
Fibreglass	12, $\lambda/4$	0.44	50.9	2238.6

Theoretically, $\lambda/2$ matching should give no improvement, although some marginal improvements are seen from the above results. However, it may be possible that the conical shape of the sandwich transducer's radiating front plate assembly may have some effect when using a matching plate, contributing to the discrepancy in the expected results for the $\lambda/2$ case.

Experiments were then repeated with the transducer placed in the S-shaped tube (finite medium) and the results are given in the following section.

Measurements in S-shaped tube

Due to difficulties encountered with excessive reflections in the S-tube, measurements were restricted to the $\lambda/2$ (16.75mm) and $\lambda/4$ (8.4mm) perspex matching plates only. The largest increase in efficiency was found to be with the quarter wave matching plate as shown in the circle plot of Figure 6.6.

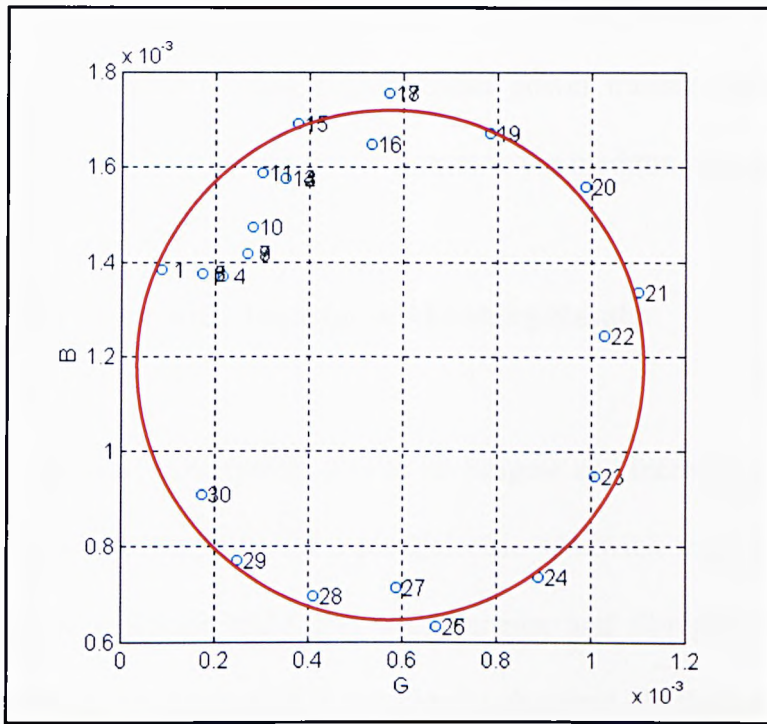


Figure 6.6: Circle diagram for 80kHz sandwich transducer with $\lambda/4$ perspex plate radiating into water inside a pipe

Although reflections prevented an accurate circle to be drawn, the performance improvements could be seen from Table 6.3 for the case of perspex matching. The experiments could not be performed with fibreglass matching transmitting into the S-tube due to the very high level of reflections.

Table 6.3: Summary of power transfer parameters with Perspex matching in S-tube

Thickness (mm)	Circle Diameter (S)	Efficiency (numerical index)	R_R (Ω)
NO MATCHING	1.29	17.3	733
16.75, $\lambda/2$	1.15	19.4	825
8.4, $\lambda/4$	1.08	20.6	879

Given the experimental inaccuracies in the case of the S-tube measurements, it can be seen (in comparison with Table 6.2) that the results for matching with perspex favourably compare with measurements made in the infinite medium. The fact that

excessive reflections was found coming from bends within the pipe also supports the finding that matching with fibreglass gives better power transfer performance, since reflections are normally larger when power output in the medium increases.

6.4.3 Evaluation of Acoustic Impedance Matching Results

The aim of this series of experiments was to investigate any increase of efficiency and radiation resistance representative for a piezoelectric sandwich transducer. Using the acoustic impedance matching technique with Perspex and fibreglass, an increase in efficiency and radiation resistance (R_R) was clearly observed. In the extended S-shaped tube, problems with reflections caused large inaccuracies in the circle plots (Table 6.3). However, when these results were compared with those obtained in the water tank (Table 6.2), there was general agreement. This indicates that the extended S-tube test-rig can be used to produce circle diagrams with a reasonable accuracy, as well as representing closer similarity to the actual operating environment. The slight differences in circle diameters could be due to errors in the best-fit circle plots taken in the S-tube, because of reflections. However for accurate and repeatable efficiency measurements the water tank presented a better environment.

Table 6.2 also shows that the $\lambda/4$ fibreglass matching plate provides the a higher increase in transducer efficiency and radiation resistance. Although there is some scattering of points in the circle plot even in the case of water tank measurements, (probably due to bonding imperfections in the matching layer) a reasonable circle could be drawn as shown in Figure 6.5. With fibreglass matching, the transducer efficiency (in terms of numerical index) has more than doubled (50.9) with an even greater

increase of the radiation resistance R_R (2238.6Ω). The resultant power output improvement in this way may also be expressed in dBs as

$$10 \cdot \log_{10} \frac{W_2}{W_1} = 10 \cdot \log_{10} \left[\frac{R_L + R_{R(\text{Matched})}}{R_L + R_{R(\text{Unmatched})}} \right] \quad (6.4)$$

$$10 \log_{10} \left[\frac{44.48 \Omega + 2238.6 \Omega}{44.48 \Omega + 760.7 \Omega} \right] = 4.5 \text{ dB}$$

where W_2 and W_1 are the acoustic power outputs for the matched and unmatched conditions respectively. This therefore represents a significant increase in the power transmission of the transducer into water using a quarter wave fibreglass matching plate. The next section examines possible alternative methods to further increase power transmission using flexural-horn transducers.

6.5 Design of a Flexural-horn Transducer

The theory and operation of flexural-horn transducers was discussed in Chapter 5. The transducer design basically consists of a piezoelectric sandwich driver coupled to an acoustic horn. The end of the horn is attached to a thin radiating disk that produces high amplitude flexural vibrations into the radiating medium. The various applications of this high power transducer with a large radiating surface have also been discussed in Chapter 5. However to evaluate the suitability of the flexural-horn transducer for the present application, a design was prototyped using a scaled-down version of a

published design [72]. The dimensions and operating frequency of the flexural-horn transducer are as follows.

The diameter of the front plate was restricted to 80mm as this would be about the maximum diameter permissible in the present application. The material for the transducer assembly was chosen to be stainless steel for immunity against chemical attack/reactions etc. The transducer resonant frequency was selected as 40kHz as this would be a typical frequency for high-power cleaning operations. The total length of the transducer was made equal to one wavelength in stainless steel i.e. $\lambda=143.5\text{mm}$. The crystals that were used were 5mm thick (each) with a natural frequency of 400kHz approx. The complete assembly was bolted together tightly, and the front disk (1mm thick) was screwed into the centre of a stepped horn. To obtain a high vibration amplification, the tip diameter of this horn was made to be as small as possible (in this case 5mm because of practical limitations). Before assembly both the crystal surfaces and adjacent steel pieces were thoroughly polished to achieve good mechanical contacts. The prototype design of this transducer is shown in Figure 6.7

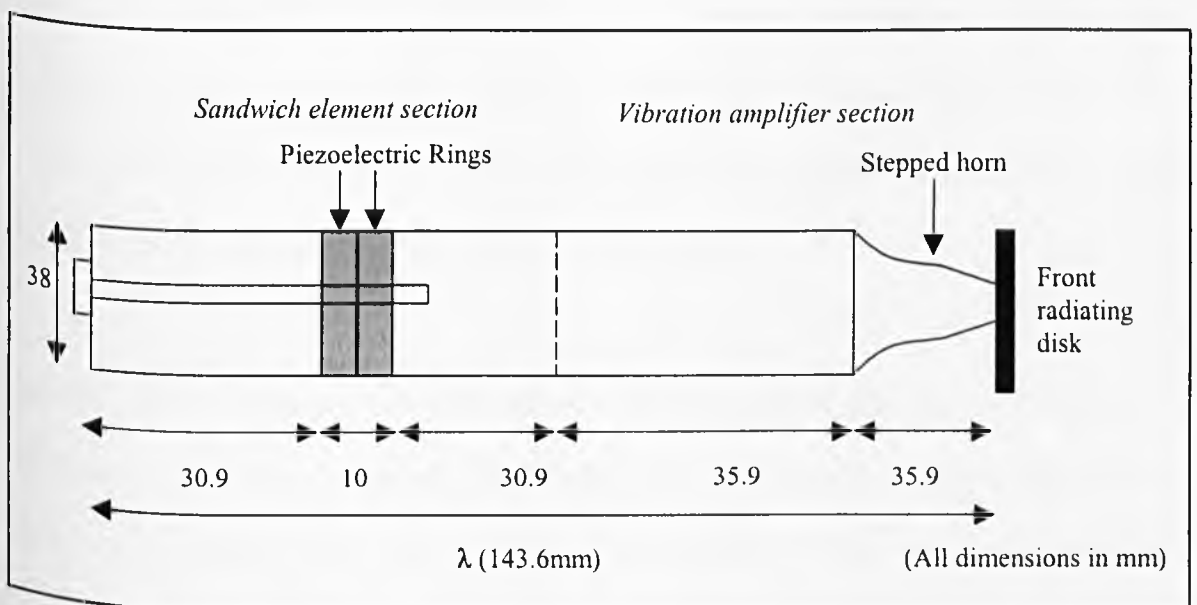


Figure 6.7: Flexural-horn transducer prototype design

To obtain a total transducer length of one wavelength the vibration amplifier section consisting the stepped horn as in Figure 6.7, was made to a length of $\lambda/2$ (i.e. 71.8mm approx.). Similarly the length of the sandwich element section was also made equal to $\lambda/2$, taking into account the thickness of the piezoelectric rings.

To verify if the transducer assembly was operating as expected, the transducer was energised using a RF power amplifier with a voltage of 150V approx. Nodal circles were appearing on the surface when a sawdust type powder was placed on the surface. However the resonant frequency was not at 40kHz as expected from the dimensional calculations. In fact, it appeared to be nearer 80kHz. After analysis and further experimentation, it was concluded that there are two main reasons why this was the case.

Firstly, the piezoelectric crystals have a much higher natural frequency of oscillation than the desired frequency of the assembly. When these crystals are put into an assembly as in Figure 6.7, the combined mass effect gives a much lower resonating frequency. In fact, this is the basis of design for sandwich transducers. It is however difficult to control the resonance frequency when there several factors influencing performance, such as flatness of mating surfaces of the assembly (to within a few μm) the state of the electrodes and the level of pre-stressing.

Secondly, the mechanical coupling between the piezoelectric elements and the rest of the structure is also very critical. A common method is to use epoxy-resin bonding for this purpose although this would reduce power capability to some extent. In addition,

if there is significant surface roughness present between the piezoelectric element and the steel interface, this mechanical coupling will become poor.

The transducer initially showed satisfactory performance with nodal circles being detected but the performance rapidly degenerated. Many attempts were made by re-polishing and re-assembling the transducer but the same inconsistency of performance was observed. It became apparent that the mechanical coupling deteriorated with evidence of erosion at crystal/metal interfaces, indicating inadequate surface flatness and finish. Hence these construction difficulties did not permit the design to be effective as expected. Also the radiating surface being limited to 80mm is another drawback as far as power output is concerned.

6.6 Use of a Multiple Disk Flexural-horn Transducer

Since the diameter of the radiating surface cannot be increased for the present application, consideration was given to the development of a new type of transducer containing multiple disks on a central drive spindle, as shown in Figure 6.8 [21].

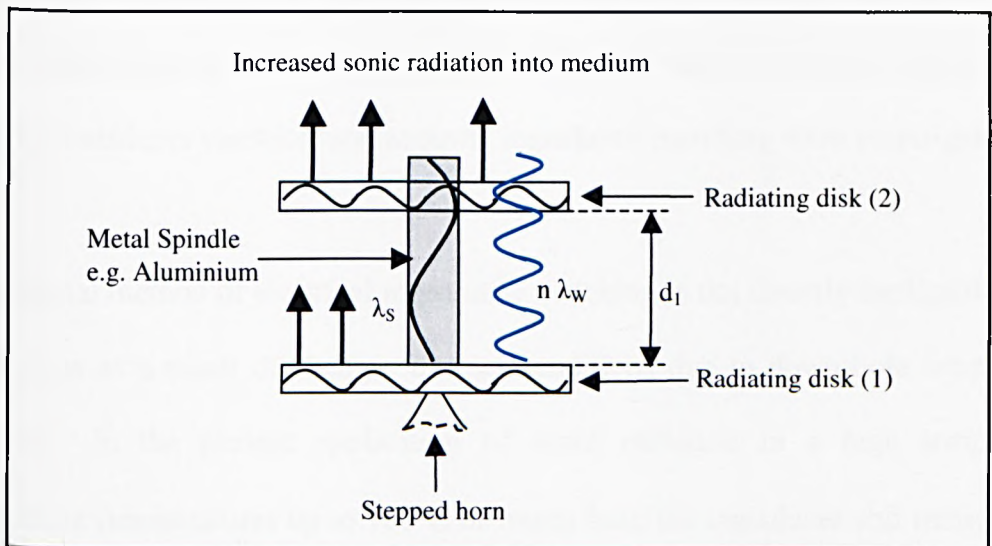


Figure 6.8: Design concept for a multiple disk flexural-horn transducer

The basic hypothesis here is that individual disks are separated appropriately so that the separation (d_1) is equal to an integer multiple of the wavelength in water (λ_w), while at the same time equal to one wavelength in the material of the spindle (λ_s) so that

$$\lambda_s = n \lambda_w \quad n = 1, 2, 3, \dots \quad (6.5)$$

In this way the radiation energy from all disks should be coherently superimposed to give greater radiation efficiency.

Again, a proper evaluation of the above approach was unable to be carried out due to constructional difficulties, particularly with regard to polishing and bonding.

6.7 Chapter Conclusions

The requirement for scale dissolution enhancement is that the cleaning transducer should transmit as much power as possible into the radiating medium. Techniques to increase the radiation efficiency of the piezoelectric sandwich transducer inside the limited space of a pipe have been evaluated. To increase the power transfer of the sandwich transducer electrical and acoustic impedance matching were investigated.

Conventional method of electrical impedance matching is not directly applicable in the present case as a result of changes in load conditions due to down-hole temperature gradients. In the present application of sonic radiation in a high temperature environment (temperatures up to 100°C or more) both the transducer and transmission

cable impedance may vary with temperature. This aspect of temperature on matching is discussed in Chapter 8.

The method of acoustic impedance matching was then performed with the transducer radiating into water. Perspex and Fibreglass matching plates were used because they represented an acoustic impedance close to the geometric mean of water and aluminium (transducer front face) with good results. Overall, it was observed that the greatest increase in transducer efficiency (numerical index from 17.98 to 50.91), occurred when the $\lambda/4$ fibreglass plate was used.

To further increase the power transfer of the sandwich transducer, a flexural-horn design was investigated, but the constructional difficulties did not permit practical measurements and evaluation of performance. A novel approach to increase power radiation in confined spaces using a multiple-disk horn transducer, has been proposed. In this regard further work needs to be carried out.

Chapter 7

Optimising the Performance of Ultrasonic Power Transducers and Transmission Cables for Use in Down-hole Pipelines

7.1 Introduction

For the present application, the transducers are required to operate over long distances under wide temperature ranges, which causes their electromechanical properties to change and the resonance condition to drift, causing loss of efficiency. The conventional method of regaining loss of efficiency is to dynamically maintain the transducer drive voltage and current waveforms in phase. However, this approach may not be ideal in the present case since the acoustic load could be rapidly changing due to the generation of unpredictable acoustic reflections and due to pipe bends etc. Hence the method proposed here is to actually monitor the amplitude of vibration of the transducers and use this to optimise the drive conditions.

Furthermore, the transmission cables intended for connecting the top-side drive system and the ultrasonic power tools in the down-hole pipeline undergo various temperature zones, thus changing their transmission characteristics. This could further reduce

ultrasonic power generated at the tool-end. This chapter presents the investigations carried out and some general conclusions drawn in addressing both these problems concerning transducers and cables.

7.2 Temperature Effects on Ultrasonic Transducers

High temperatures can cause constructional changes in the transducer assembly, effecting the mechanical pre-stressing and bonding between elements. This also has the effect of shifting the resonance frequency of the transducer, causing a decrease in efficiency with increasing temperature. Some methods of compensating for such variations have been reported in literature for transducers used in ultrasonic ranging, based on pulse-echo measurements [85, 86]. However, for the piezoelectric sandwich transducers, the effects of resonance frequency drift when subjected to high temperatures reaching 100° C or more are not particularly well known.

Previous work in the area of frequency control for ultrasonic transducers has tended to focus on the measurement of phase between the current and voltage waveforms applied to the transducer. This technique makes use of control circuits based on a Phase Locked Loop (PLL) device where the voltage across, and the current through the transducer are brought in phase. This method of compensation has been adequate for ultrasonic transducers operating in gases for high power industrial applications, and for some ultrasonic sensors used in low-power, high sensitivity applications e.g. to measure the liquid concentration [86-89].

However, for the present application of transducers radiating into pipes, it was observed from previous measurements of transducer efficiency (section 6.2) that the above stated condition of phase coherence can not be always maintained. This could be due to the reflections within the pipe section as observed before and due to the formation of microscopic air bubbles on the surface of the transducer. The problem of air bubbles forming was confirmed by experiment. In this regard, it was found that when a d.c voltage of approx. 0.7V was applied between the aluminium front face of the transducer and the medium (water), the formation of air bubbles was apparently suppressed due to opposing electrode potentials. However this method was not practicable as slight variations in voltages or temperature caused worsening results. Applying soap to the front face of the transducer was also tried but only provided protection against air bubbles for a few minutes. Because of these problems a different approach was therefore required to provide automatic frequency control for the ultrasonic transducer used for the present application.

The importance of providing temperature compensation to the insonifying power transducer for the present study has been highlighted in previous studies by Gunarathne [21] from scale dissolution enhancement measurements. A rapid decline in the performance of the transducers used became apparent, particularly around 60-70°C approximately, well below their Curie temperature. Further investigations revealed that the centre frequency of the transducer drifts considerably requiring frequency tracking compensation to minimise decline in power output of the transducer. Also, another problem observed in the case of transmission into confined spaces, such as in pipelines was the generation of static nodes, i.e. 'silent spots' due to standing waves. To address both these requirements, a novel technique based on sensing the actual power output

from the transducer while introducing a degree of frequency modulation was investigated. Therefore, to achieve this objective, a systematic study to obtain the transducer drift characteristics and to determine the parameters of the control and modulation system was required.

7.3 Variation of Transducer Parameters with Temperature

The two most critical parameters that vary with temperature, causing a reduction of the power output are the radiation efficiency and resonance frequency. In order to gain a quantitative understanding the variation of these parameters for an 80kHz sandwich transducer were studied.

7.3.1 Radiation Efficiency

To study the variation of the radiation efficiency of the piezoelectric sandwich transducer in water, the extended S-shaped plastic tube was initially used. The required temperatures were achieved using a heated water circulation system ensuring the complete pipe section was at a uniform temperature. A temperature sensor was attached to the transducer to measure its temperature. The transducer was immersed in a column of oil (20w/50 Multigrade motor oil). Since the acoustic impedance of the two media (oil and water) are similar, this enabled a method of eliminating the formation of gas bubbles without losing the acoustic continuity of the load. The complete experimental configuration is shown below in Figure 7.1.

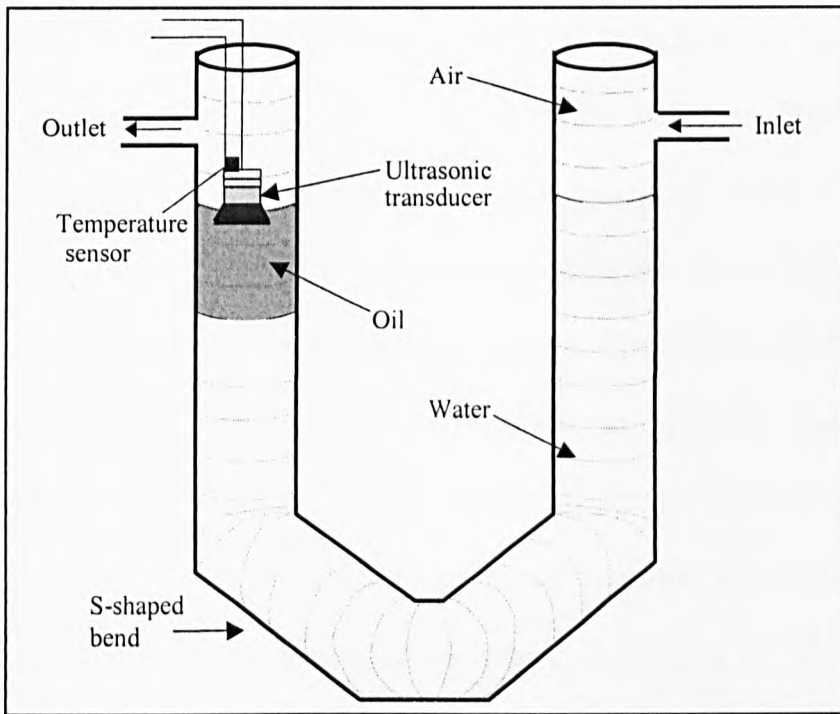


Figure 7.1: Test-rig for transducer efficiency measurement with temperature

The circle plots were used to measure the transducer efficiency at different temperatures. From the measurements made, the general trend of the transducer efficiency with temperature was observed as shown in Figure 7.2.

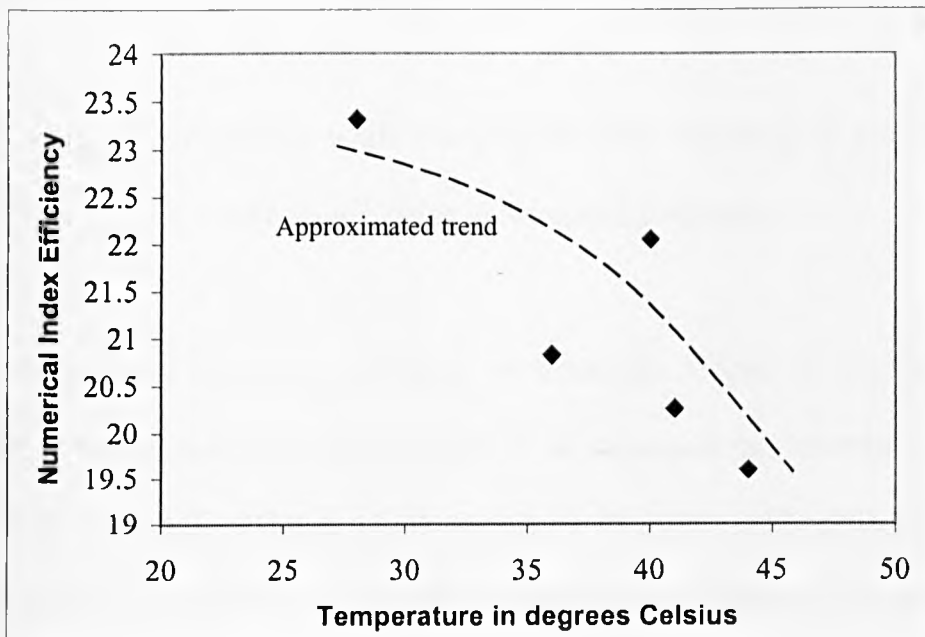


Figure 7.2: Sandwich transducer efficiency with temperature in S-shaped tube (Transducer fully dipped in oil)

The scattering of points highlights the problem of reflections in the plastic pipe, causing large inaccuracies in the circle plots. It can be seen from Figure 7.2 that the maximum change of the numerical index efficiency (using eqⁿ (5.9)) is approximately 3.72. The worst case uncertainty in these measurements was found to be approx. ± 1.2 (in terms of the numerical index of efficiency figure). Therefore to study the variation of the transducer performance with temperature an approach based on direct measurement of vibration amplitude was attempted. In this approach, an elemental (small) wide-band probe bonded to the back-side of the power transducer, was used to detect the actual physical vibration of the transducer. This in effect detects the resonance condition of the transducer under variable load conditions.

The pick-up voltage (a measure of vibration) was measured within the temperature range of 30-85°C. This was separately carried out under two conditions.

1. Varying the temperature while the drive frequency was kept constant at a value equal to the resonance frequency at room temperature (25°C).
2. Varying the temperature while changing the drive frequency to give maximum vibrations - i.e. tracking the change in resonance frequency.

The latter condition represents the basis of automatic frequency tracking of the transducer to deliver maximum power output at all temperatures. In order to quantify the limits of frequency tracking, measurements of frequency drifts with temperature were carried out. The measurement process is illustrated in Figures 7.3(a) and (b).

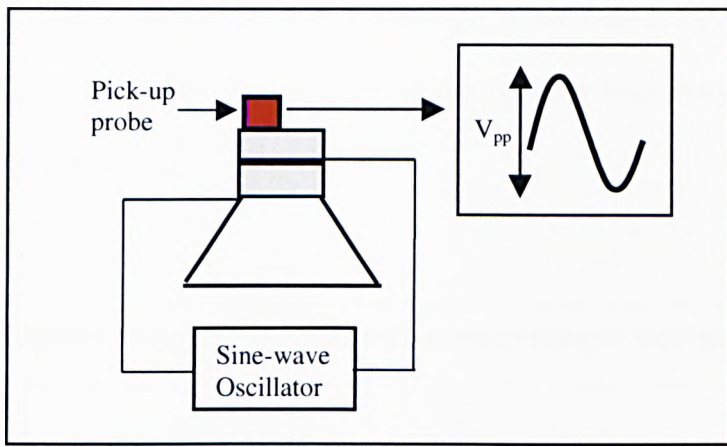


Figure 7.3(a): Measurement of pick-up probe voltage

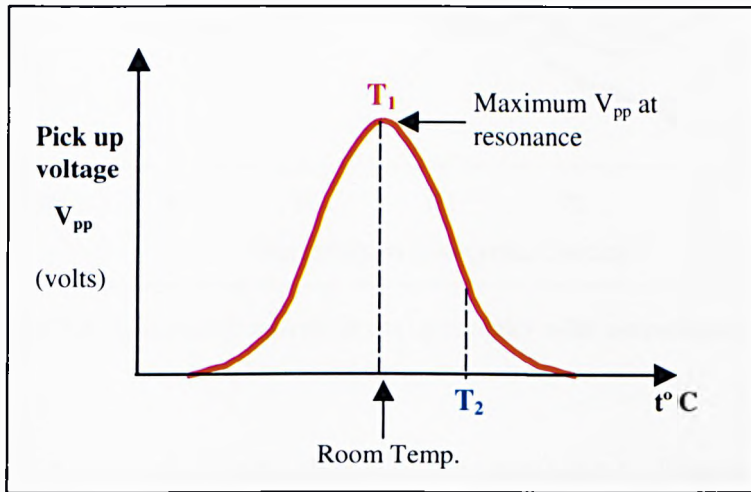


Figure 7.3(b): Variation of V_{pp} with temperature

As shown in Figure 7.3a, the sandwich transducer is manually driven at its resonance by observing the maximum pick up signal V_{pp} from the pick up probe. With reference to Figure 7.3b, corresponding to any temperature, V_{pp} will have a maximum value at resonance. However as temperature increases to T_2 say, then due to changes in the transducer assembly, the resonance vibration level reduces resulting in a lower pick-up voltage. The pick up voltage measured in this way, for the 80kHz sandwich transducer, is shown in Figure 7.4.

Curve (a) shows the variation of pick-up voltage if no frequency adjustments were made, while curve (b) shows the variation if the optimal frequency setting for each temperature was maintained.

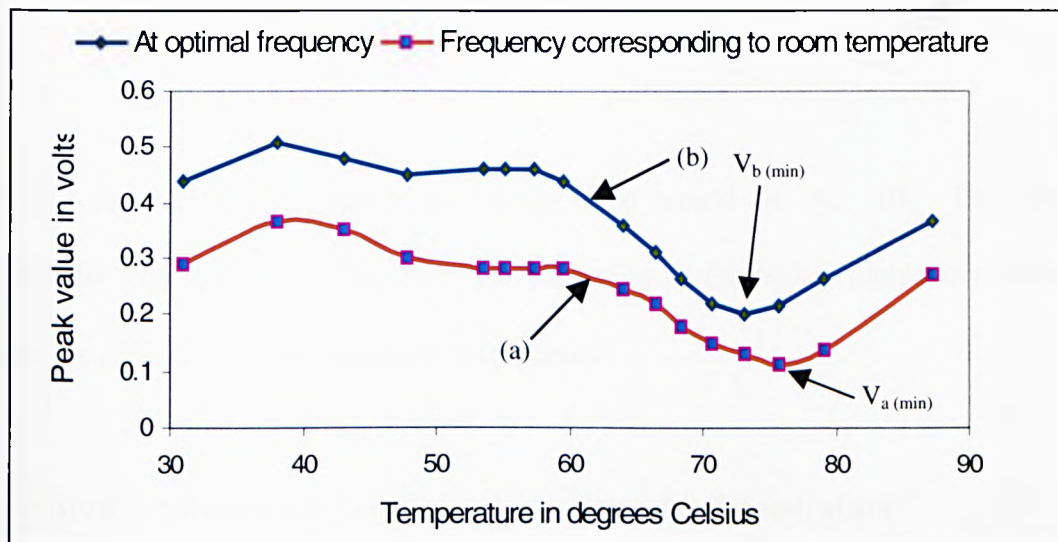


Figure 7.4: Transducer vibration characteristics with temperature in air

From Figure 7.4 it is observed that after 60°C the transducer vibration decreases quite severely, resulting in a drop of the power output. This temperature region coincides with that reported from earlier work, where the performance of sandwich power transducers started to decline [21]. The experiments were repeated and it was found that the results were repeatable. It is evident from these results that the transducer impedance is also changing considerably with temperature.

The effect of not maintaining any frequency compensation is also clearly seen, by comparing curves (a) and (b) in Fig 7.4. Although the vibration level decreases for both fixed and optimal frequency settings, a significant improvement in power output may be gained with frequency compensation. Since $(V_{pp})^2$ is proportional to power output, the power drop in the 70-80°C range may be expressed in dBs as

$$20 \log_{10} \left(\frac{V_{a(\min)}}{V_{b(\min)}} \right) \quad (7.1)$$

$$20 \log_{10} \left(\frac{0.115}{0.2} \right) = -4.8 \text{ dB}$$

Similarly for the 50-60°C range, the power drop would be -4.3 dB. This clearly justifies the requirement for frequency compensation of the power transducer to regain some of its efficiency loss at elevated temperatures.

7.3.2 Study of Resonance Frequency Variation with Temperature

In order to formulate a strategy for compensating against the drift in resonance frequency, the transducer temperature/frequency characteristics must be known. However, such data was not available within the required temperature range from the manufacturers. Thus, measurements were initially conducted in the test rig of Figure 7.2, with the 80kHz sandwich transducer. However as was the case for the efficiency measurements, excessive reflections made it difficult to measure the resonance frequency of the transducer with any great accuracy and repeatability. To overcome this problem the resonance frequency drift with temperature was measured with the transducer radiating in air, on the assumption that such drifts are closely similar irrespective of the load medium. The results of these measurements are shown in Figure 7.5.

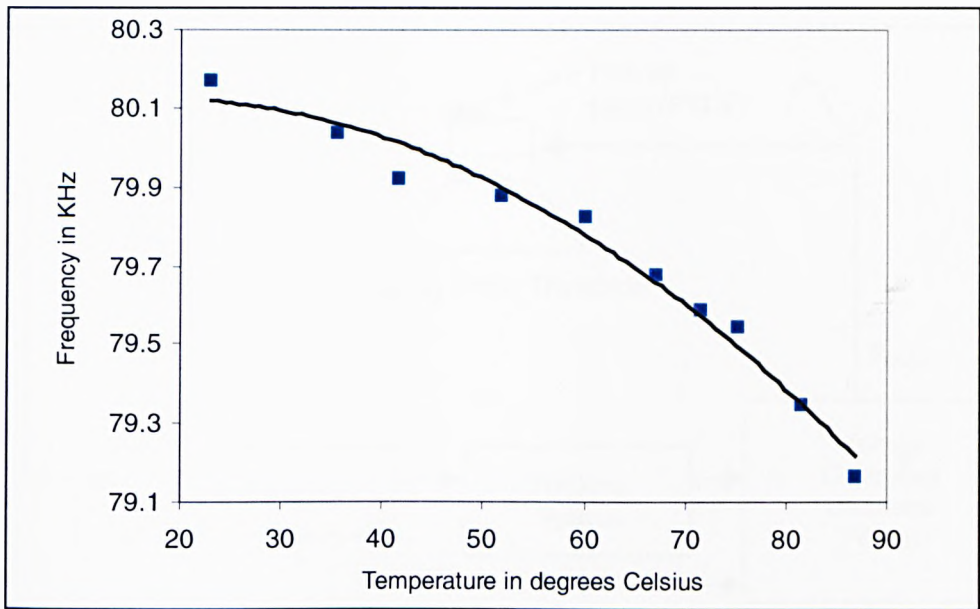


Figure 7.5: Resonance frequency variation with temperature (radiation in air)

From the above measurements, it can be stated that the series resonance frequency decreases with increasing temperature with a maximum departure of 1kHz from 20-85°C. Therefore, to stabilise the transducer efficiency at elevated temperatures, an important requirement in the present application is to monitor the output conditions in order to dynamically adjust the source frequency at all temperatures within the operating range.

7.4 A New Approach for Transducer Frequency Compensation

For optimum efficiency, and therefore maximum power transfer into the radiating medium, a system is required that continually corrects the resonance frequency of the transducer according to its frequency/temperature characteristic, as shown in Figure 7.5. For the present application in confined spaces, it is also important to provide a degree of frequency modulation to avoid static nodes. One approach proposed to achieve this is shown in Figure 7.6.

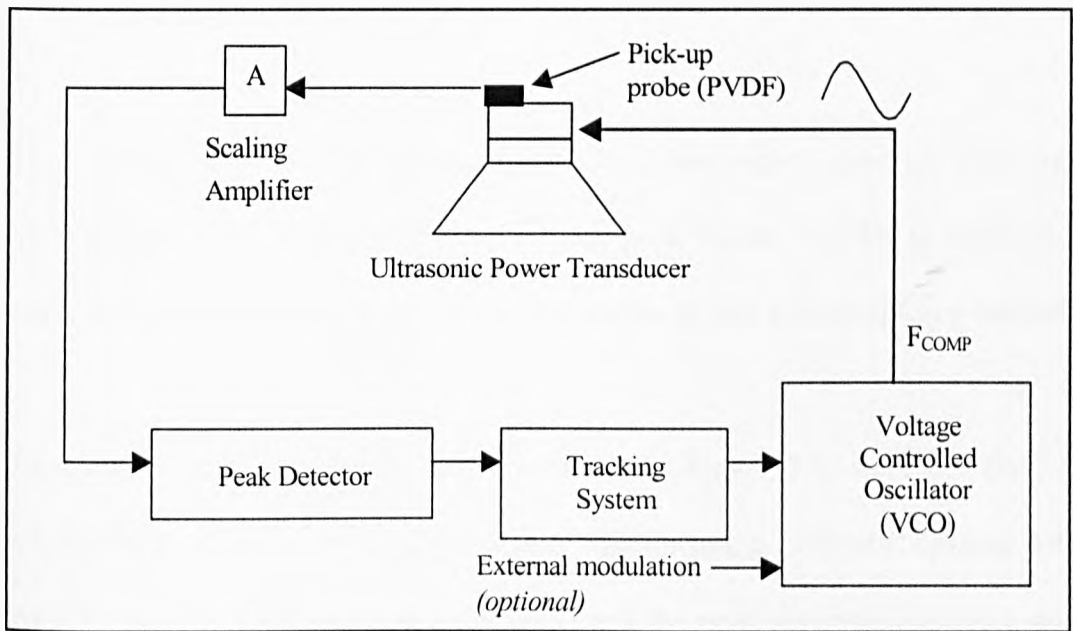


Figure 7.6: Block diagram of resonance frequency compensation system

The design for the above compensation system is based on the signal picked up from the wideband (PVDF) probe bonded to the power transducer to detect the level of actual physical vibration. The probe produces a maximum signal when the power transducer is driven at its resonance frequency. The output of this probe is appropriately scaled before the peak signal value is detected. The detected peak signal is then presented to a tracking system, whose function is to appropriately alter the input voltage presented to a voltage controlled oscillator (VCO) which changes its output frequency in a manner that produces the maximum vibration of the power transducer. A degree of frequency modulation (or chirp) may also be introduced at this stage in one of many ways, for example, by appropriately adjusting the delays within the system or using a separate input to the VCO. It should also be mentioned that since ultrasonic power is transmitted from top-side, the control electronics should also be at the top-side except for the pick up probe mounted on the power transducer.

7.4.1 Implementation of Frequency Compensation

The intended operation of the tracking system was to compare previous peak signal amplitudes of the pick-up probe with the current peak values in order to generate the appropriate correction signals to the VCO, to maintain closed-loop frequency control.

All the components of the closed-loop system as in Figure 7.6, were designed and tested separately. The scaling amplifier was designed using a CA3140E op-amp with a gain of 3.3. The amplifier gain was selected so that the peak detector receives a signal level of $\sim 1V$ at the resonance frequency of 80kHz (at room temperature). The peak detector was also built using op-amps. The tracking system consisted of a Sample and Hold device with a sampling time of 2 sec approx. After comparing the peak amplitudes through the use of a differential amplifier, the output from the tracking system is then fed to a VCO to generate the required drive frequency. The waveform generator used as the VCO had an output frequency range of 0.01Hz-100kHz. A schematic of the tracking system and VCO circuit is shown in Figures 7.7(a) and (b).

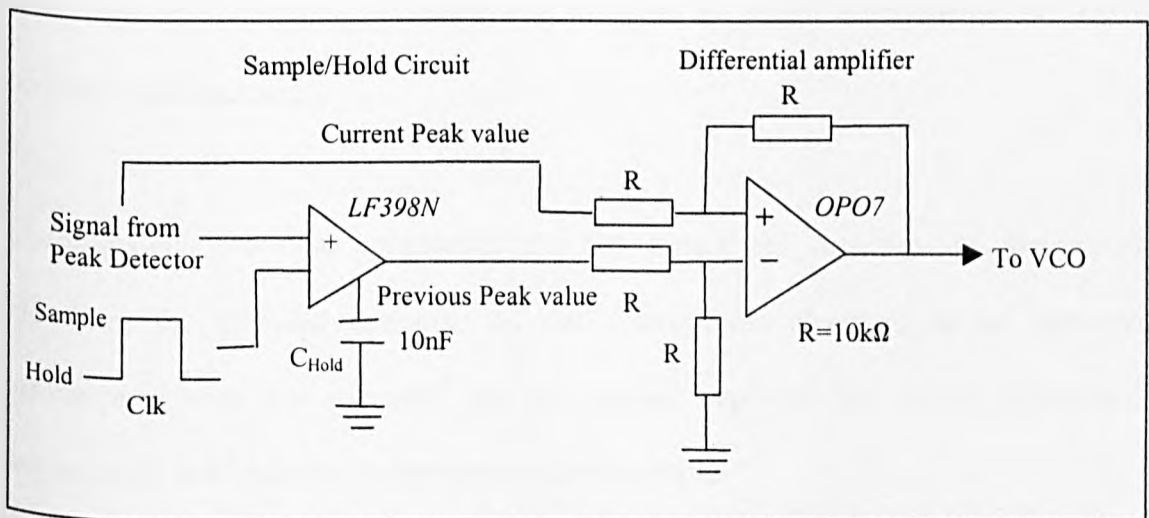


Figure 7.7(a): Tracking System Concept

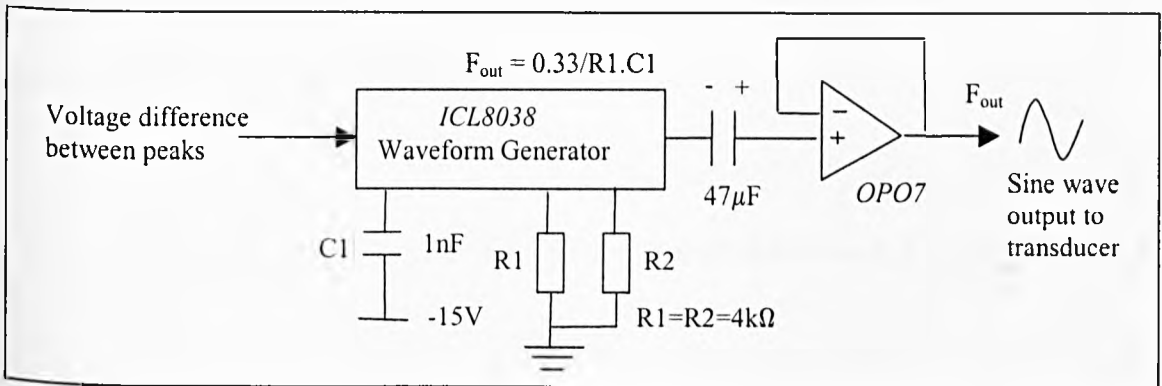


Figure 7.7(b): Frequency Control Schematic for transducer frequency compensation

In Figure 7.7(b) the frequency of the waveform generator is a direct function of the DC input voltage. The values of the external timing resistors R1 and R2 were chosen to select the required frequency modulation range (F_{out}).

In the closed-loop form however, the analogue tracking system did not function as expected. Several attempts to rectify this did not improve the situation, perhaps due to difficulties of satisfying input/output transfer requirements with the devices used. Hence, it was thought that a better way to achieve this would be to implement this digitally, e.g. using a microcontroller. This latter approach will have the added advantage of eliminating problems due to drifts in circuit components etc. of the original tracking design.

Unfortunately, the time constraints did not permit the re-design of the system. However, the intended operation of the system was observed in an open-loop arrangement with the automatic tracking system replaced by manual adjustments according to the frequency/temperature characteristics.

The next stage of the project was to study the effect of temperature on transmission cables as presented in the following sections.

7.5 Optimising the Cable Performance at Elevated Temperatures by Dynamic Impedance Matching

The proposed down-hole tool system is broadly composed of a single co-axial cable connected to the power transducer (load) over long distances. It should be mentioned here that the choice of a single cable for transfer of drive signals, power and data was chosen previously on the basis of cost and thermal dissipation requirements at the tool-end. Having already studied some of the temperature effects on the transducer, the following sections investigate the effects of temperature gradients on the matching requirements of the cable itself with the view to deliver maximum power to the load during de-scaling operations.

A static mathematical model previously developed can be used to analyse the cable parameters subjected to temperature variations [90]. Using this model the optimum matching conditions for the present application have also been recommended [91]. However as the cable passes through various temperature zones the matching conditions also change. The main objective of this work was therefore to investigate dynamic impedance matching requirements of the cable and also the impedance variation of the load transducer by extension of existing models.

7.6 Cable Requirements

There are three main transmission requirements on the co-axial cable providing signal transmission from topside locations to the front-end electronics at the down-hole tool end. Firstly, the cable is required to carry high power sinusoidal drive signals in the frequency range 20kHz - 120kHz (supplied by a 200V rms. generator) for the ultrasonic power transducers used for de-scaling operations. High frequency digital signals up to 10MHz are also to be received from the tool as required for down-hole imaging, scale deposit monitoring and characterisation. Finally, DC power transmission is required for the operation of the tool electronics. To provide three sets of transmission lines to cater for each requirement would be expensive and not feasible due to the large distances involved (up to 3km). Therefore, a single transmission line operating on a time-shared basis was proposed as a better solution for the present application.

7.7 A Coaxial Cable Model based on the Finite Difference Method (FDM)

To cater for the above transmission requirements a comprehensive mathematical model based on the primary parameters of the coaxial cable has been previously developed by Christidis [90]. This model takes into account the effects of both temperature and frequency on the cable parameters. A finite difference method is used to model the effect of temperature differentials on a small section of the cable, where the unit length of this section is very much less than the electrical wavelength (λ) at the signal frequency on the cable. The model was then used to investigate different matching

conditions that provide maximum power transfer to the load. In the following section the main equations and relationships of this model are discussed, with particular emphasis on the terminating impedance Z_T , with the view to extend it towards dynamic matching.

7.7.1 Summary of Existing FDM Coaxial Cable Model

The primary parameters of a coaxial cable are denoted as R, L, C, G; where R is the resistance, L is the inductance, C is the capacitance, and G is the conductance, per unit length under given operational conditions. The temperature and frequency effects have been introduced in to the primary constants R, L, C, G through dependent parameters to form the following relationships [90]

$$R(t) = \left[\frac{1}{\pi r_i^2 - \pi(r_i - \delta_{(t)})^2} + \frac{1}{\pi r_s^2 - \pi(r_s - \delta_{(t)})^2} \right] l \cdot \rho(t) \quad (7.2)$$

$$L(t) = (R(t)/\omega) + [\mu_{(t)} \ln(r_o/r_i) / 2\pi] \quad (7.3)$$

$$C(t) = 2\pi\epsilon_{(t)} / \ln(r_o/r_i) \quad (7.4)$$

$$G(t) = \omega C(t) \psi \quad (7.5)$$

Where, $\rho(t)$ = conductor resistivity at $t^\circ\text{C}$, l = cable length, r_s = outer conductor external radius, r_i = inner conductor radius, r_o = outer conductor internal radius, δ = skin depth, $\epsilon(t)$ = permittivity of the insulation material at $t^\circ\text{C}$, $\mu(t)$ = permeability of the

insulation material at $t^\circ C$, $\psi = \tan\theta_L$, $\theta_L =$ loss angle and $\omega =$ angular frequency. The basic schematic of the transmission cable system in this model is shown in Figure 7.8.

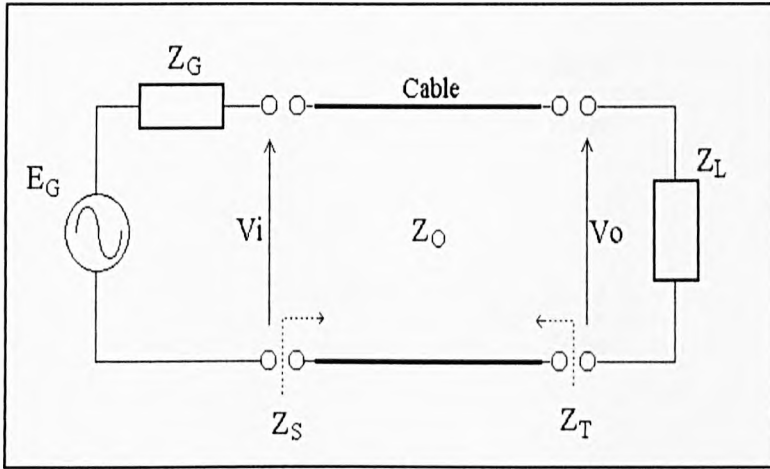


Figure 7.8: Schematic of a transmission system

Z_S is the impedance as seen at the input of the cable, Z_T is the impedance as seen at the output of the cable, Z_o is the cable characteristic impedance and Z_L is the load impedance. Z_G is the generator impedance at the topside, typically 50Ω . These respective impedances are calculated in the model using standard relationships for the secondary parameters of the cable i.e. propagation coefficient (γ) attenuation coefficient (α) phase constant (β) and the characteristic impedance (Z_o).

The characteristic impedance Z_o of the cable may be written as:

$$Z_o = \sqrt{\frac{RG + \omega^2 LC}{G^2 + \omega^2 C^2} + j \frac{\omega(LG - RC)}{G^2 + \omega^2 C^2}} \quad (7.6)$$

The impedances Z_S and Z_T are obtained as functions of the temperature and frequency and are related such that $Z_S = f(Z_o, Z_L)$ and $Z_T = f(Z_o, Z_G)$. To calculate Z_S and Z_T the following equations are used

$$Z_S = Z_o \frac{(Z_L + Z_o)e^\gamma + (Z_L - Z_o)e^{-\gamma}}{(Z_L + Z_o)e^\gamma - (Z_L - Z_o)e^{-\gamma}} \quad (7.7)$$

$$Z_T = Z_o \frac{(Z_G + Z_o)e^\gamma + (Z_G - Z_o)e^{-\gamma}}{(Z_G + Z_o)e^\gamma - (Z_G - Z_o)e^{-\gamma}} \quad (7.8)$$

For dynamic impedance matching of the cable at various temperature zones, it is the output impedance, Z_T that is of importance. Since the cable primary parameters are temperature dependent, Z_T will change along the length of the cable if the temperature varies.

The complete cable system is considered to be a cascade of a finite number of small segments, where the length of a segment is chosen to be small enough, so that the temperature over that segment could be regarded as practically constant. However, in down-hole conditions, the entire length of the cable can be subjected to non-uniform temperature gradients.

For calculation of impedances Z_S and Z_T , the primary cable parameters are defined in an array of $4 \times n$ elements, where n represents the number of segments in the finite element model as

$$\begin{bmatrix} R_1 & R_2 & \dots & R_n \\ L_1 & L_2 & \dots & L_n \\ C_1 & C_2 & \dots & C_n \\ G_1 & G_2 & \dots & G_n \end{bmatrix}$$

So for each different temperature section, updated coefficients would be generated which may be represented as elements of a matrix of the form [91]

$$\begin{bmatrix} R_1(T_1) & R_2(T_2) & \dots & R_n(T_n) \\ L_1(T_1) & L_2(T_2) & \dots & L_n(T_n) \\ C_1(T_1) & C_2(T_2) & \dots & C_n(T_n) \\ G_1(T_1) & G_2(T_2) & \dots & G_n(T_n) \end{bmatrix}$$

The above array is also referred to as the *transmission cable matrix* in further sections of the chapter.

7.7.2 Optimal Cable Matching Using the FDM Coaxial Cable Model

Using the above model and verification by experiments it has been found that a good matching condition for maximum power delivery to the load, within the low to medium frequency range, occurs when Z_L is equal to the conjugate of Z_T [91]. However, as the cable is subjected to temperature variations while travelling along the pipe this Z_T value will change with temperature, indicating that some form of dynamic compensation may be needed.

7.8 Extension of Existing Cable Models to Investigate Dynamic Impedance Matching

7.8.1 Approach

The approach taken to investigate whether dynamically matching the cable impedance gives any improvement in power delivered to the load was to firstly examine the changes to the cable itself as it is subjected to various temperature zones between 0°-100°C. The existing FDM coaxial cable model was appropriately modified and extended to specify the cable terminating impedance Z_T within varying temperature zones along the cable mimicking its passage into the pipe. A schematic of the dynamic impedance matching process as the transducer system advances into a pipeline is shown in Figure 7.9.

As the cable advances into a pipeline, the termination impedance may be dynamically calculated as required to provide optimal power transfer. In this way, an automatic tap-changing compensation network may be used to present the updated impedance to the terminating end of the cable.

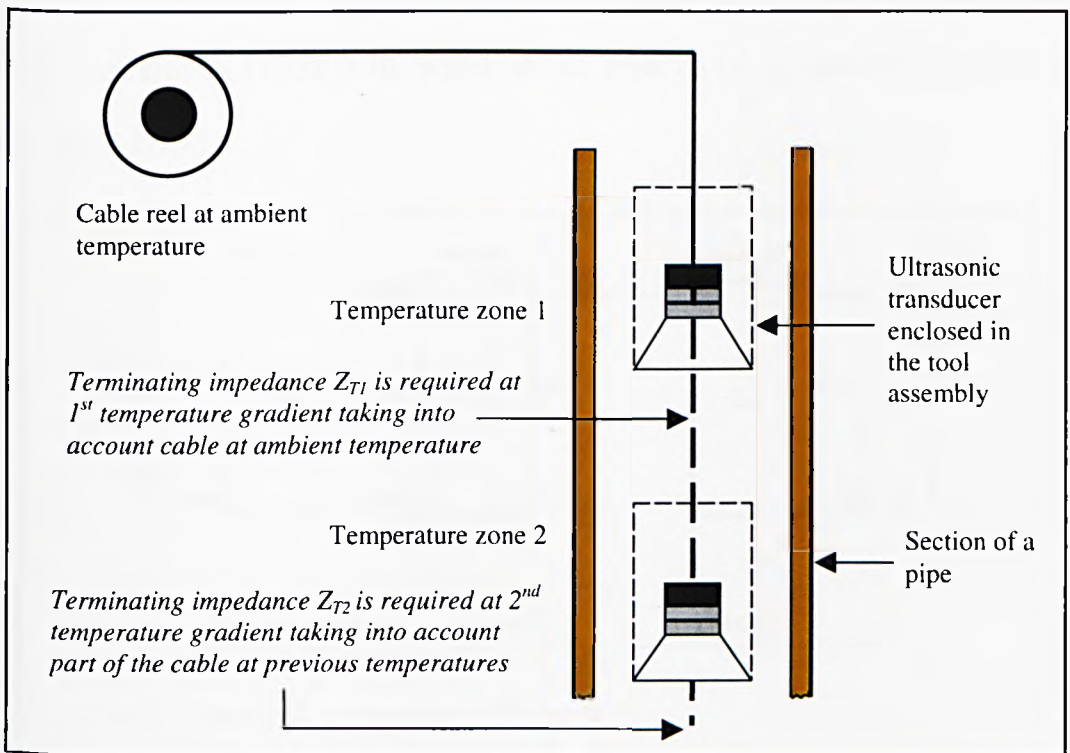


Figure 7.9: Method of dynamic impedance matching of cable

7.8.2 Calculating the Dynamic Cable Terminating Impedance (Z_T)

A file was created for test purposes that simulated a typical temperature profile of the tool. When the on-board sensors detect a temperature change, the measured temperature is stored in this file. For initial tests ten 'dummy' temperature values were created in this file to create a slightly non-linear temperature profile (Appendix E.1). When a length of cable advances through these 'dummy' temperature zones, the terminating impedance Z_T is calculated. An 'incremental length' is initially defined in the extended model, e.g. 5m. This is the length interval at which the temperature is logged by the down-hole tool, and also the point at which the *transmission cable matrix* is updated, allowing Z_T to be dynamically computed.

To calculate Z_T at a particular temperature zone all the primary parameters, Z_o and the Z_T values for the length of the cable at previous temperatures need to be re-calculated. This is illustrated in Figure 7.10, which shows how Z_T is calculated iteratively using equations (7.2-7.8).

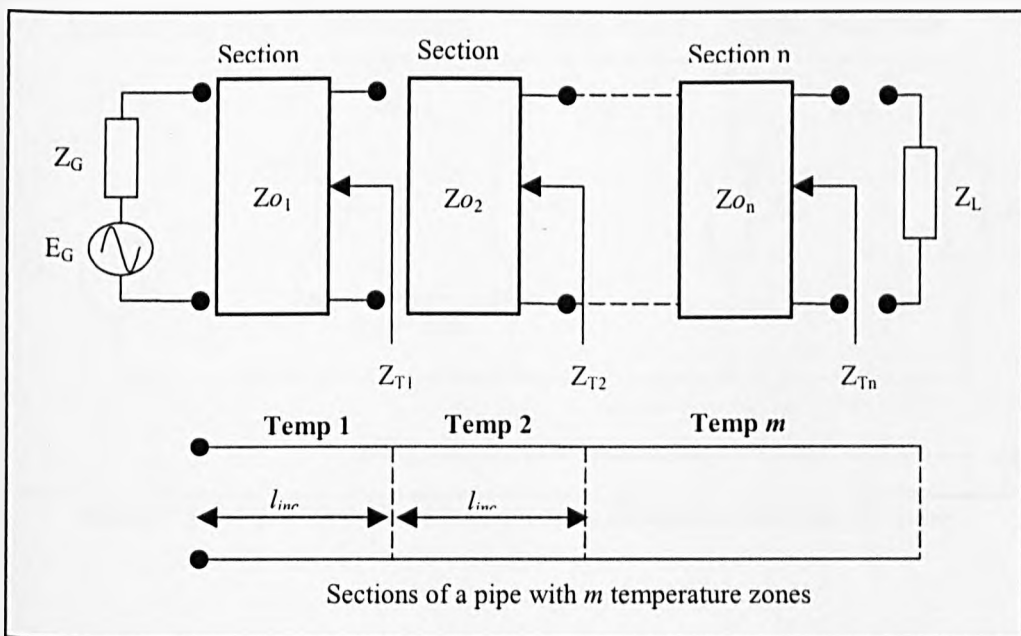


Figure 7.10: Calculation of output impedance (Z_T) for the entire cable divided into n finite sections

This calculation process continues until the tool reaches its final destination, thus ensuring that the model is always updated when a new temperature zone is detected after the specified incremental length. In Figure 7.10, l_{inc} represents the incremental length in the model. This length is chosen small enough so that the temperature across that section is considered uniform.

The main algorithm of the extended model to dynamically calculate the cable output impedance Z_T is best explained with a practical example of a cable entering and travelling through a pipeline section.

Consider a 100m cable connected to an ultrasonic transducer in a down-hole tool. When the complete system is lowered into the pipeline and the increment length set to 10m say, as shown in Figure 7.11, then after every 10m interval the cable output impedance Z_T is computed.

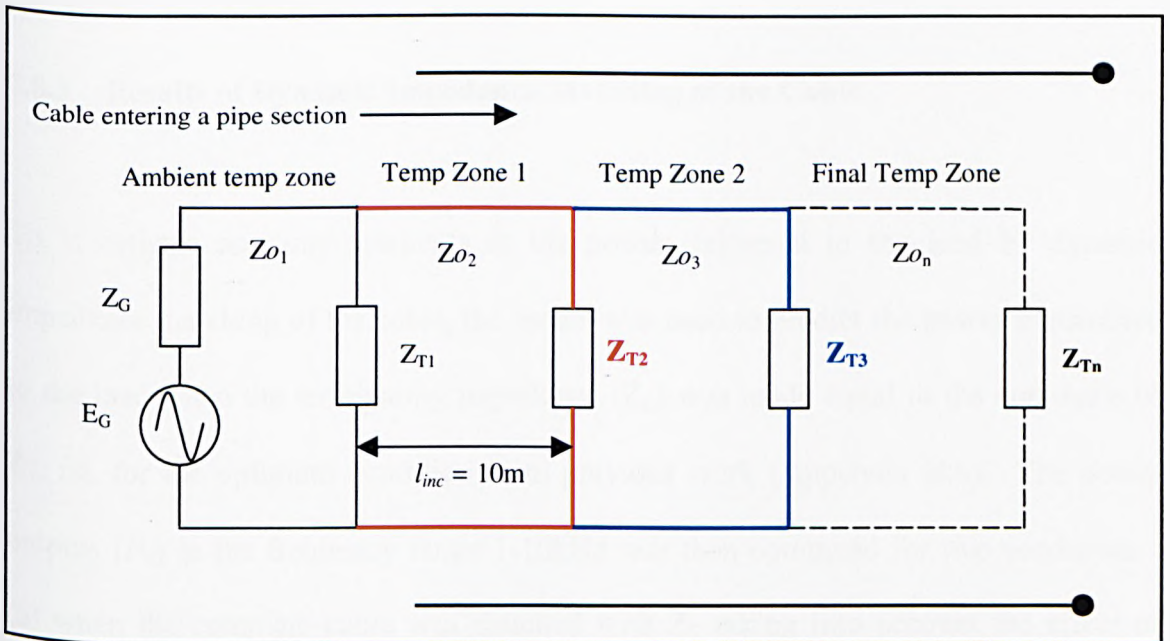


Figure 7.11: A practical example of dynamic impedance matching the cable

As the above cable enters and travels along the pipe section during de-scaling operations, the model calculates the respective terminating impedances at different temperature zones using the following relationships, with the corresponding cable lengths such that,

$$\begin{aligned}
 Z_{T1} &= f(Z_G, Z_{O1}) && 100m \text{ at ambient temperature} \\
 Z_{T2} &= f(Z_{T1}, Z_{O2}) && 90m \text{ at ambient temperature, } 10m \text{ at Temp Zone 2} \\
 Z_{T3} &= f(Z_{T2}, Z_{O3}) && 80m \text{ at ambient temperature, } 10m \text{ at Temp Zones 2 \& 3} \\
 \dots & && \dots \\
 \dots & && \dots \\
 Z_{Tn} &= f(Z_{T(n-1)}, Z_{O_n}) && 10m \text{ at all temperature zones (including ambient temp)}
 \end{aligned}$$

Note that a minimum cable length equal to the incremental length always remains outside the pipe.

7.8.3 Results of Dynamic Impedance Matching of the Cable

To investigate any improvements in the power delivered to the load by dynamic impedance matching of the cable, the model was used to predict the power transmitted to the load when the terminating impedance (Z_L) was made equal to the conjugate of Z_T , i.e. for the optimum condition from previous work (Appendix B.8). The power outputs (P_o) in the frequency range 1-10kHz was then computed for two conditions - (a) when the complete cable was matched with Z_T taking into account the effect of temperature on the cable at 100°C and (b) when the complete cable was assumed to be at ambient temperature (25°C) using eqⁿ (8.8).

$$P_o = |V_o| |I_o| \cos(\angle I_o - \angle V_o) \quad (8.8)$$

where, V_o is the output voltage and I_o the output current of the cable.

These two conditions represents the worst case situation if no dynamic matching was to be performed, while the temperature of the cable was raised to 100°C. The simulation results indicated that by correctly matching the cable, the power output to the load increases only marginally - by 4.5% approx. at the worst case (20Khz).

Based on these findings, it was concluded that there seems to be little advantage in dynamically matching the cable alone. However, the impedance of the load i.e. the power transducer changes considerably with temperature as evident from work presented earlier in the chapter. Hence it is the dynamic matching of this impedance that is important in the present application since the cable impedance change within the required temperature range is only marginal as found from the above investigation.

7.9 Impedance Tracking of the Load Transducer

In section 7.3.2 it has been shown that the resonance frequency of the sandwich power transducer drifts with temperature. The transducer impedance (as seen at the input terminals) will also change with temperature due to electromechanical changes in the transducer assembly. Further work was therefore required to obtain the transducer impedance-temperature profile by practical measurement, and also to incorporate the measurements in the model using a look-up table approach. Although this part of the

work was unable to be completed due to time limitations, the proposed approach is presented in the following sections.

7.9.1 Transducer Impedance Variation with Temperature

To measure the impedance variation of the sandwich transducer with temperature the circuit shown in Figure 7.12 could be used. In fact the same method described in section 5.5.1 to obtain the transducer admittance could be used to obtain the complex transducer impedance. However, the drive frequency of the transducer must be manually adjusted at each temperature to obtain the impedance at the resonance condition. Alternatively, an automatic impedance bridge may be used if that was available.

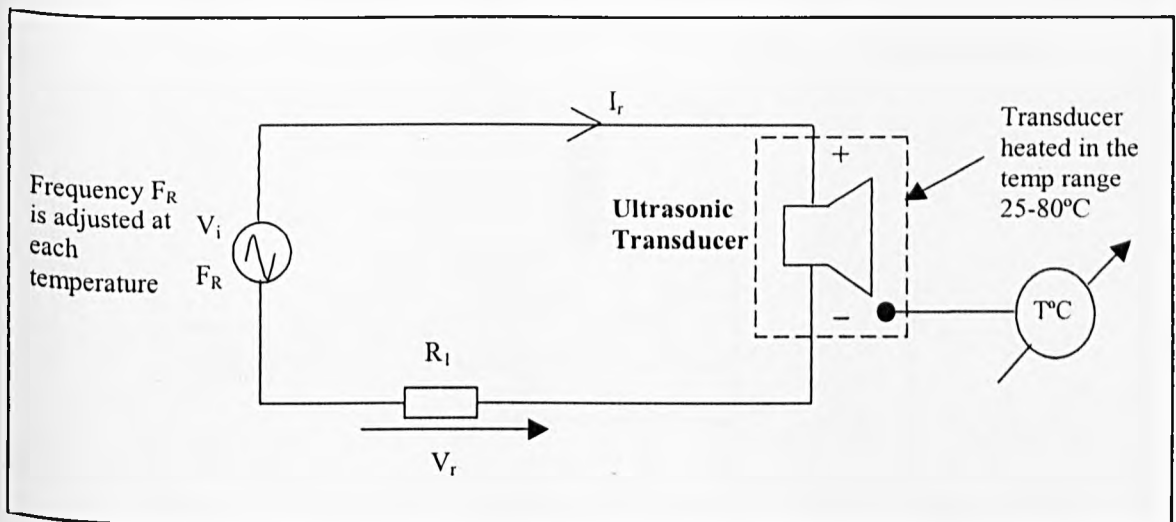


Figure 7.12: Measurement of transducer impedance with temperature

By measuring the voltage V_r (magnitude and phase w.r.t V_i) at each temperature at resonance, the input current I_r can be calculated. The input complex impedance Z_{TT} as seen by the source would then be equal to V_i/I_r which can be determined at every temperature setting.

7.9.2 Incorporating the Transducer Impedance-Temperature Profile in the Extended Cable Model

The extended cable model with dynamic impedance matching must specify the load terminating impedance, taking into account both cable and transducer variations with temperature. In this respect, a method of achieving this aim could be to use a look-up table approach as shown in Fig 7.13, in which the transducer impedance-temperature profile is stored in a file.

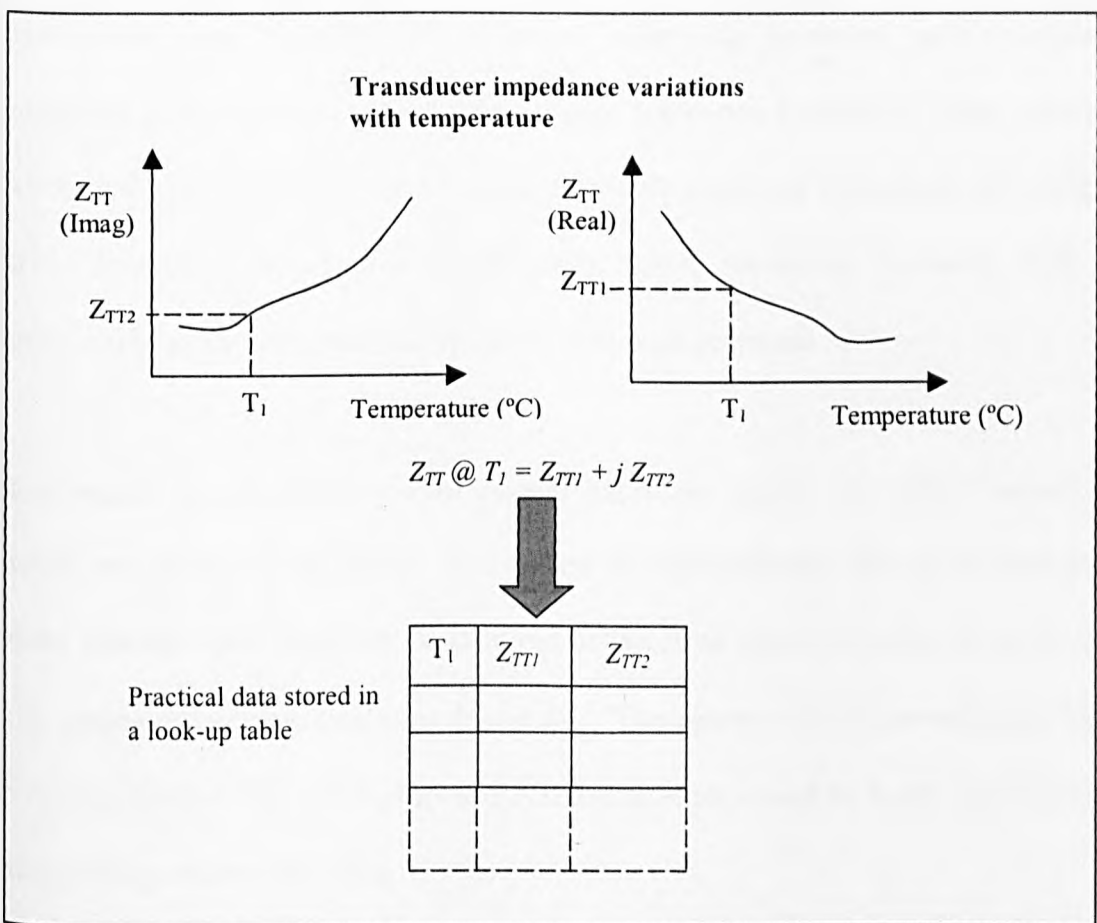


Figure 7.13: Look-up table approach to take into consideration transducer impedance variations with temperature

When an actual temperature is read from the tool-end, the system would look for the nearest temperature/impedance entry in the look-up table to determine the appropriate termination impedance. This may then be used to activate an automatic matching

network e.g. an electromechanical or electronic tap changing network. This matching network would terminate the cable at any given temperature zone with the dynamic impedance composed of Z_T (cable parameters) and Z_{TT} (transducer).

7.10 Chapter Conclusions

In this chapter the effect of elevated temperatures on ultrasonic sandwich transducers and cables for high power applications has been studied. It was found from practical measurements, that the transducer radiation efficiency decreases with increasing temperature, partly due to the shift of the series resonance frequency. This variation was practically demonstrated for a typical ultrasonic sandwich transducer operating at 80kHz. In order to regain loss of efficiency due to resonance frequency drift, an automatic frequency compensation technique has been proposed.

In this regard, an electronic control system based on sensing the actual transducer vibration was designed and tested. The system operated appropriately in an open-loop manner, although the closed-loop system did not work as expected due to the problems of the analogue tracking electronic hardware. The results of this investigation have also been published [92]. It is proposed that this scheme would be better implemented digitally using a microcontroller.

In the latter part of the chapter, the effect of dynamically matching a coaxial cable for optimum power delivery to the load (transducer in this case) in down-hole pipelines was also investigated. In this regard, a previously developed cable model was extended to dynamically calculate the terminating impedances as the cable passes through the

temperature zones. However it was found by simulation in section 7.8.3 that matching the cable alone gives no significant increase in the power delivered to the load.

The transducer impedance also changes with temperature. Therefore the model must take into account both cable and transducer impedances when specifying the terminating impedance of the complete system. A method for implementing this using a look-up table has been proposed as future work.

A part of the work in this chapter has also been presented at the 1st IEE International Seminar and Exhibition on On-line Monitoring Techniques, June 1999, Aberdeen, UK [93].

Chapter 8

Conclusions and Future Work

8.1 Conclusions

In this project a wide range of ultrasonic techniques for scale detection and dissolution enhancement have been investigated and developed. The main achievements of this project together with recommendations for further work are summarised in the rest of this final chapter.

As mentioned in the beginning of the thesis this project covered two main but, almost diverse research areas. The first area of work presented in the thesis highlighted the successful development of ultrasonic inspection techniques to facilitate top-side and down-hole deposit location (Chaps 2-4). This involved detailed mathematical modelling for synthesising and simulating the nature of ultrasonic echoes within pipeline walls during testing, and experimental verification of the models.

The second part of the thesis investigated techniques for optimising power output of sandwich ultrasonic transducers which are intended to operate efficiently in confined spaces such as pipelines (Chaps 5-6). That required investigation into methods of improving radiation resistance of transducers used and a comprehensive study on the

effects of temperature on performance. This was followed by a proposal of compensation strategies for optimising performance of power transducers during de-scaling operations (Chap 7).

8.1.1 Novel Techniques to Facilitate Scale Detection in Pipelines

Top-side applications

A major problem with the techniques previously developed for the detection of scale deposits in pipelines was the need for “virtually unlimited” reference samples. This problem was successfully addressed by developing a novel technique for synthesising the reference echoes using modelling and numerical computation.

The above required the development of a numerical computational model representing transmission and reception of ultrasound in steel and oil, using “Huygen’s Green function”. It also required the determination of an appropriate size and shape of an ultrasonic transducer suitable for the application of testing pipelines for scales from the top-side surface. From the results of this investigation it is proposed that a 2mm x 12mm, 5MHz broadband transducer be used for this purpose.

The model developed caters for the synthesis of the 1st three multiple echoes, given the transducer characteristics and the required dimension of the pipe-wall. It was observed that there was a noticeable difference between the leading edges of the synthesised and practical wave shapes, most likely due to the imperfections of both theoretical model and practical measurement system. However, this is of little importance in the present

case since the requirement is for the comparison of echo amplitudes and not the exact wave shapes.

Initially the model was tested with planar targets. When using the relative 'peak' amplitudes of multiple echoes, an extremely good correlation of results was obtained for plane steel targets. In fact, the signal decay (B) values only showed a worst case error of about 6% for the wall thickness range of 5-10mm. Extension of the model for cylindrical targets was then accomplished. It was interesting to note from the results that, for the dimensions of the pipe-walls considered and the size of the transducer aperture used, there was only a slight difference in relative echo amplitudes (less than 1%) between planar targets and the cylindrical targets of the same thickness. If this was the case, for all pipe dimensions of interest, then echoes may be generated using the computationally less intensive plane target model. However, this requires further series of comparative study between the results from the two models and practical verification for a range of target dimensions. That was not possible at the time and therefore recommended as further work.

Thus, the achievements on this major objective of the project concerning top-side detection of scales is summarised as follows.

- Development of a computational model for the synthesis of multiple echoes in steel planar targets.
- Extension of the model to accommodate for cylindrical targets, such as pipelines.

- Determination of an appropriate size and type of a transducer suitable for top-side applications.

Although the work described above is mainly related to the inspection of pipelines, the underlying principles could be extended for general applications in Non-destructive Testing (NDT) and measurement, e.g. identifying disbonds or laminates.

Down-hole applications

An important requirement for the detection and characterisation of down-hole pipeline deposits previously developed was the remote alignment of ultrasonic transducers to an accuracy of $\pm 3^\circ$. Hence, developing a technique to achieve this was another main objective of the present work. In this regard, a novel sensing technique of using the “off-axis” amplitude profile of the signals received from the test probe itself was successfully developed.

The methodology of evaluating the detectability of this technique initially involved a thorough practical study. However, it was found from this study that the detectability (i.e. angular resolution near normal) is dependent on three factors for a given probe, namely: probe aperture, target curvature and probe/target separation. It was also found that no general rule for a suitable combination of parameters could be derived from such practical measurements. Hence, a theoretical model was developed. A significant finding from this theoretical approach was that by modelling the probe/target orientation the detectability of signal symmetry could be predicted with good accuracy. This was demonstrated by using a 5MHz strip-line transducer for angular resolution

measurements, where the error was no more than 5% in the specified range. The model may be extended for any other aperture, and in this way, the suitability of a particular combination of aperture/distance and pipe diameter can be ascertained computationally rather than by laborious experimentation.

Testing this sensing technique using a feedback-controlled motorised system is recommended as future work.

8.1.2 Performance Optimisation of Power Transducers and Cables

This aspect of the project involved three main areas of study. The first aspect dealt with the improvement of radiation efficiency by acoustic impedance matching. The focus of the second aspect was to quantitatively determine the degree of efficiency loss under the range of operating temperatures and hence to formulate a strategy for minimising power loss. The third aspect was intended to investigate the effect of temperature on transmission cables connecting the down-hole transducers and top-side drive and data acquisition systems. Research into the possible need for dynamic impedance matching, as the transducer/cable system advances into the pipeline through different temperature zones was also carried out.

The findings of these investigations are summarised below.

A quarter-wave matching plate made of fibreglass matrix in epoxy, with an acoustic impedance of 8 Rayls provided a good means of acoustic impedance matching, with an acoustic power output improvement of about 4.5 dB.

The power output of transducers decreases considerably as temperature increases from 20°- 85° C. For sandwich transducers of the type used, resonance frequency changes by about 1kHz within the above temperature range. If not dynamically adjusted this would result in a drop of output by -4.8 dBs approximately around 70° C, where this range actually coincides with the temperature at which chemical de-scaling operations are mostly carried out. In the 50°-60° range, the power drop was also significant amounting to -4.3 dB.

In order to address the power drop due to drift in transducer resonance frequency a closed-loop automatic frequency compensation system based on sensing the actual transducer vibration has been proposed as a new method for correcting the transducer drive frequency at all temperatures. The individual control blocks of this system have been independently tested for correct operation but closed-loop system integration was only partly achieved due to time constraints. The main problem encountered was the analogue tracking block not functioning as expected. It is proposed that a better implementation of the complete scheme would be to use a microcontroller system.

Losses due to change in cable characteristics with temperature in the 20°- 100° C range were negligible, and therefore did not require dynamic compensation of the cable termination impedance alone. However, based on observations, the transducer impedance may change considerably requiring impedance matching in a dynamic manner, if the power performance degradation was to be kept to a minimum.

Overall, the main project objectives concerning scale detection have been successfully achieved. The critical factors affecting performance of transducers and cables for

intended use in de-scaling operations, have also been determined with a view to enhance their performance.

8.2 Future Work

There are certain aspects of the work presented in this thesis that need to be continued forward. These are identified in the following sections.

With regard to top-side scale detection, the computational efficiency of synthetic A-scans can be improved for faster execution. The theoretical models developed for this purpose were implemented using MATLAB due to the ease of programming. However, MATLAB is generally not recommended for computationally intensive work of this nature due to the relatively slow execution times. Therefore, a faster computational method would be the use of object orientated C++ programming. Alternatively MATCOM may be used to convert the existing MATLAB source codes into C++.

Another useful aspect of future work would be the development of a feedback controlled motorised system for remote probe alignment. This again could be implemented using a microcontroller system with the signals displayed on a PC. It would then be possible to acquire the signals from the probe itself and to use those signals with the sensing technique developed, to best align the probe with respect to the pipe wall. This could be easily carried out under laboratory conditions to verify the accuracy of probe alignment.

The implementation of transducer frequency tracking and the dynamic impedance matching of the transducers and cables along the methods proposed in this thesis are also recommended as future work. It is proposed that the same microcontroller as above may be used to achieve this operation concurrently. The hardware elements for frequency compensation can be interfaced directly to the microcontroller. Dynamic impedance matching of the cable/transducer system may then be implemented by software routines using the proposed look-up table approach.

References

- [1] The Pipeline Industries Guild: 'Pipelines: All you wanted to know', 1994, p.27. (Authors undisclosed), ISBN 095172862X
- [2] Kennedy, J.L.: 'Oil and Gas Pipeline Fundamentals', 2nd Edition, PenWell Publishing Company, 1993, pp. 54-55.
- [3] Keatch R.W and Gunarathne G.P.P: 'Novel techniques for quantification and enhancement of chemical dissolution of oil field mineral scale deposits', 8th *International Oil Field Chemical Symposium*, Geilo, Norway, March 2-5, 1997
- [4] Gunarathne G.P.P: 'Novel techniques for monitoring and enhancing dissolution of mineral deposits in petroleum pipelines', *Ultrasonics*, Vol. 34, No 2-5, 1996, pp. 411-419.
- [5] Read Well Services Ltd, UK: <http://www.read-well.co.uk/mfctool.htm>
- [6] Newton, K and Saunderson, D.H: 'NDT Research for the Oil and Gas Industry', *The British Journal of Non-destructive Testing*, Vol. 43, No. 3, March 1992, pp. 123-8
- [7] Pigging Products and Services Association, 1996-98
<http://www.piggingassnpps.com/about/htm>
- [8] PII Group Ltd
<http://www.piigroup.com/>
- [9] de Raad, J.A: 'Various methods of ultrasonic pipeline inspection: free-swimming and cable operated tools', *Pipes and Pipelines International*, Vol. 34, No.2, April 1989, pp.17-25.
- [10] Kobayashi, M and Minato,H et al.: 'NKK ultrasonic pipeline inspection pig', *NKK Technical Review*, No. 80, 1999, pp. 46-50
- [11] NKK Corporation 2000
<http://www.nkk.co.jp/en/products/engineering/pipeline-inspection/6-proiect.htm>
- [12] Fujiwara, S: 'Development of an in-pipe inspection vehicle', *Materials Evaluation*, Vol. 53, No. 5, May 1995, pp. 566-569.
- [13] StarTrak Pigging Technologies, 1996: http://www.starpig.com/Modern_pigs.htm
- [14] Tiratsoo, J.N.H: 'Pipeline Pigging Technology', 2nd Edition, Gulf Publishing Company and Scientific Surveys Ltd, 1992, pp243-249.
- [15] Kershaw, C.F: 'Enhanced cleaning pigs remove deposits from internal pipe wall', *Pipe Line & Gas Industry*, Jan 1998, pp. 65-69
- [16] Hal Horning 1996: <http://www.pond.com/~hhorning/dp/ultra.html>

- [17] Blue Wave Ultrasonics Inc, 1999: <http://www.bluewaveinc.com/reprint.htm>
- [18] Expro Group: www.exprogroup.com/pdfs/explorer/techandtech.pdf
- [19] Blackstone ~ NEY Ultrasonics: <http://www.blackstone-ney.com/fu-page6.php3>
<http://www.blackstone-ney.com/fu-page7.php3>
- [20] Hunicke R.L: 'Industrial applications of high power ultrasound for chemical reactions', *Ultrasonics*, Vol.28, September 1990, pp.291-294
- [21] Gunarathne, G.P.P: 'Detection and Quantification of Scale Deposits in Petroleum Pipelines', *Confidential Consultant Reports*, Aug 1994, School of Electronic and Electrical Engineering, The Robert Gordon University, Aberdeen, UK.
- [22] Gunarathne, G.P.P: 'Novel Techniques for Monitoring and Enhancing Dissolution of Mineral Deposits in Petroleum Pipelines', *Proceedings of Offshore Europe 1995*, 5-8 September, 1995, Aberdeen, UK, pp.507-522
- [23] Gunarathne, G.P.P; Q. Zhou, and K. Christidis: 'Ultrasonic Feature Extraction Techniques for Characterisation and Quantification of Scales in Petroleum Pipelines', *Proceedings of the IEEE Ultrasonics Symposium*, Japan (Sendai), Vol.1, October 1998, pp.859-864.
- [24] Christidis, K: 'Characterisation and Monitoring of Mineral Deposits in Down-hole Petroleum Pipelines', *D.Phil Thesis*, The Robert Gordon University, Aberdeen, UK, Oct 2000.
- [25] Gunarathne, G.P.P and Christidis, K: 'Material Characterisation *in situ* Using Ultrasound Measurements', *IEEE Transactions on Instrumentation and Measurement*, Vol.51, No.2, April 2002, pp.368-373
- [26] Gunarathne, G.P.P and Christidis, K: 'Measurement of Surface Texture Using Ultrasound', *IEEE Transactions on Instrumentation and Measurement*, Vol.50, No.5, October 2001, pp.1144-1147
- [27] Christidis, K and Gunarathne, G.P.P: 'Effect of Temperature on Ultrasound Measurements', *IEEE Transactions on Instrumentation and Measurement*, Paper under Review.
- [28] MP InterConsulting <http://mpi.powerultrasonics.com/mmm-technology.html> (2002)
- [29] Soniclean Pty Ltd <http://www.soniclean.com.au/techno.htm> 1998-2002
- [30] ASTM Recommended Practices A388-71, A418-64(69), E114-74 and E164-74, *1975 Annual Book of ASTM standards*, Parts 4 and 11, Philadelphia: American Society of Testing and Materials, 1975.

- [31] ASME Section III, 'Nuclear Power Plant Components' and Section V, 'Nondestructive Examination', (See SA388, SE114 and IX-3432.1.) New York: American Society of Mechanical Engineers, 1971.
- [32] Stephanishen, P.R: 'Transient Radiation from Pistons in an Infinite Planar Baffle' *Journal of the Acoustical Society of America*, Vol.49 No.5 (Part 2), 1971, pp1629-1638.
- [33] KielcZynski, P; Paejewski, W et al: 'Finite Element Method (FEM) and Impulse Response Method (IRM) analysis of circular and rectangular transducers', *Proceedings of the 1995 IEEE Ultrasonics Symposium*, 7-10th Nov, Seattle, WA, U.S.A, Vol.1 pp.693-696.
- [34] Kuehnicke, E and Voelz, U: 'Transient Wave Field Calculation for Ultrasonic Transducers Using Integral Transform Methods', *Acoustical Imaging*, 13-16th April 1997, Boston, U.SA, Vol.23, pp.343-8
- [35] Birchak, J.R and S. Serabian: 'Calibration of Ultrasonic Systems for Inspection from Curved Surfaces', *Materials Evaluation*, Vol.36, No.1, Jan 1978, pp.39-44.
- [36] Internal Reports by Q.Zhou (1999) and P.Bonin (1996), The Robert Gordon University, School of Engineering, Aberdeen, U.K.
- [37] Marini, J and J. Rivenez: 'Acoustical fields from rectangular ultrasonic transducers for non-destructive testing and medical diagnosis', *Ultrasonics*, No.12, November 1974, pp.251-256.
- [38] Archer-Hall, J.A and Gee, D: 'A single integral computer method for axisymmetric transducers with various boundary conditions', *NDT International*, June 1980, pp.95-101.
- [39] El Amrani, et al: 'Numerical computation of the acoustic field passing through a plane interface: Application of new phased array transducers', *Ultrasonics International Conference Proceedings*, Vienna, Austria, 6-8 July 1993, pp.197-200.
- [40] Christidis, K: 'Characterisation and Monitoring of Mineral Deposits in Down-hole Petroleum Pipelines', *D.Phil thesis*, The Robert Gordon University, Aberdeen, UK, Oct 2000. pp.60-61
- [41] Kaye, G.W.C and Laby T.H: 'Tables of Physical and Chemical Constants and some Mathematical Functions', 15th Edistion, Longman Group Limited, 1986, pp.73-76.
- [42] Gunarathne, G.P.P and Qureshi, Y: 'Development of a Synthetic A-scan Technique for Ultrasonic Testing of Pipelines', *Proceedings of the IEEE Instrumentation & Measurement Technology Conference*, 21-23rd May 2002, Anchorage, AK, USA, Vol.1, pp.547-552

- [43] Christidis, K: 'Characterisation and Monitoring of Mineral Deposits in Down-hole Petroleum Pipelines', *D.Phil Thesis*, The Robert Gordon University, Aberdeen, UK, Oct 2000. pp.55-163
- [44] Lamancusa, J.S and Figueora, J.F: 'Ranging errors caused by angular misalignment between ultrasonic transducer pairs', *Journal of the Acoustical Society of America*, Vol.87, No.3 March 1990, pp1327-1335
- [45] Orofino, D.P and Pedersen, P.C: 'Angle-dependent spectral distortion for an infinite planar fluid-fluid interface', *Journal of the Acoustical Society of America*, Vol.92, No.5, November 1992, pp.2883-2899
- [46] Pedersen, P.C and Orofino, D.P: 'Modeling of Received Signals from Finite Reflectors in Pulse-Echo Ultrasound', *IEEE Ultrasonics Symposium*, Cannes, France, Nov 1-4, 1994, Vol. 2, Part 2 of 3, pp1177-1181.
- [47] Stanke, F.E; Randall, C and D'Angelo, R: 'Experimental verification of a mathematical model for internal ultrasonic inspection of pipes', *Journal of the Acoustical Society of America*, Vol.88, No.1, July 1990, pp 525-534
- [48] Birks, A.S and Green R.E Jr.: 'Nondestructive Testing Handbook - Second Edition', Volume 7: Ultrasonic Testing, American Society for Nondestructive Testing, 1991, pp. 52-54
- [49] Brown, B and Goodman, J.E: 'High Intensity Ultrasonics: Industrial Applications', D.Van Nostrand Company Inc., 1965, pp.75-90.
- [50] Blitz, J: 'Fundamentals of Ultrasonics', Butterworths (London) 1963, pp. 62
- [51] CAE Ultrasonics: <http://www.caeultrasonics.com/fu-page10.php3>
- [52] Gooberman, G.L: 'Ultrasonics: Theory and Application', English Universities Press Ltd, 1968, pp.87-92
- [53] ETREMA Products Inc. <http://www.etrema-usa.com/terfenol/index.asp>
- [54] Stillesjo, F; Engdahl, G. et al: 'Dynamic Simulation and Performance Study of Magnetostrictive Transducers for Ultrasonic Applications', *Proceedings of the SPIE - The International Society for Optiact Engineering*, Vol.3992, 2000, pp.594-602
- [55] http://users.bigpond.net.au/cam/meir1/meir1.htm#_Toc11035716300037
Major Engineering and Investigation Report 1: Magnetostrictive Actuator Design for Micro-Mechatronic Devices, Mcwilliam, C
- [56] Priv.Comm ETREMA Products, Inc. (22/4/03)
- [57] Kocis, S & Figura, Z: 'Ultrasonic Measurements and Technologies', Chapman and Hall, 1996, pp.39-46.

- [58] CAE Ultrasonics: <http://www.caeultrasonics.com/fu-page11.php3>
- [59] Morgan Metroc Limited, 'Piezoelectric Ceramics **Data Book for Designers**', Transducer Products Division
- [60] Perkins, J.P: 'Power Ultrasonic Equipment: Practice and Application', *Sonic Systems-Technical Paper*, <http://sonicsystems.co.uk/sonic.htm>
- [61] Gooberman, G.L: 'Ultrasonics: Theory and Application', English Universities Press Ltd, 1968, pp.52-83
- [62] Shuyu, L & Fucheng Z: 'Study of vibrational characteristics for piezoelectric sandwich transducers', *Ultrasonics*, Vol.32, No.1, January 1994, pp.39-42
- [63] S.Berliner III's Ultrasonic Cleaning Page, Feb 2001
<http://home.att.net/~berliner-ultrasonics/us-clean.html>
- [64] Silk, M.G: 'Ultrasonic Transducers for Nondestructive Testing', Adam Hilger Ltd, 1984, pp. 28-41.
- [65] Coates, R & Mathams, R.F: 'Design of matching networks for acoustic transducers', *Ultrasonics*, Vol.26, March 1988, pp.59-64
- [66] Souquet, J. et al: 'Design of Low-Loss Wide-Band Ultrasonic Transducers for Noninvasive Medical Application', *IEEE Transactions on Sonics and Ultrasonics*, Vol.SU-26, No.2, March 1979, pp.75-81
- [67] Van Kervel, S.J.H & Thijssen, J.M: 'A calculation scheme for the optimum design of ultrasonic transducers', *Ultrasonics*, May 1983, pp.134-140.
- [68] Redwood, M: 'Experiments with the Electrical Analog of a Piezoelectric Transducer', *The Journal of the Acoustical Society of America*, Vol.36, No.10, October 1964, pp.1872-1880.
- [69] Cherek, B and Kielec, D: Optimization of a Sandwich Driver Structure using Finite Element Analysis, *IEEE International Ultrasonics Symposium Proceedings*, Japan, October 1998, Vol.2 pp.1011-1014.
- [70] Barone, A and Gallego-Juarez, J.A: Flexural Vibrating Free-edge Plates with Stepped Thicknesses for Generating High Directional Ultrasonic Radiation, *The Journal of the Acoustical Society of America*, 1971, Vol. 51, No 3 (Pt 2), pp. 953-959.
- [71] Briggs, G.A: 'Loudspeakers', 5th Edition, Wharfedale Wireless Works Ltd, 1963, pp.220-222.
- [72] Gallego-Juarez, J.A: 'An ultrasonic transducer for high-Power applications in gases', *Ultrasonics*, November 1978, No 6, pp. 267-271.

- [73] Watanabe, Y and Mori, E: 'A study on a new flexural-mode transducer-solid horn system and its application to ultrasonic plastics welding', *Ultrasonics* Vol.34, No 2-5, June 1996, pp. 235-238.
- [74] Muhlen, S.S: 'Design of an Optimized High-Power Ultrasonic Transducer', IEEE Ultrasonics Symposium Proceedings, Dec 1990, Honolulu (USA), Vol. 3, pp. 1631-1634.
- [75] Gallego-Juarez, J.A: 'New Technologies in High-Power Ultrasonic Industrial Applications', IEEE Ultrasonics Symposium Proceedings, Nov 1994, Cannes (France), Vol.3, pp. 1343-1352.
- [76] Neustadt, H et al. 'Computer derivation of equivalent-circuit RLC values for an ultrasonic transducer from measured values of the transducer's driving-point impedance', *NDT International*, Vol. 17, No. 6, December 1984, pp. 343-348
- [77] Christidis, K: 'Monitoring scale deposits in petroleum pipelines', *Monthly Progress Report*, Jan-Feb 1998, The Robert Gordon University, Aberdeen, UK.
- [78] Blitz, J: 'Fundamentals of Ultrasonics', Butterworths (London) 1963, pp. 52
- [79] Heuter, T.F and Bolt, R.H: 'Sonics: Techniques for the Use of Sound and Ultrasound in Engineering and Science', John Wiley & Sons, Inc, 1955, pp.104-105.
- [80] Cracknell, A.P: 'Ultrasonics', Wykeham Publications (London) Ltd, 1980, pp.71-73.
- [81] Draheim, M.R and Wenwu, C: 'Finite Element and Experimental Study of Impedance Matching Layer Optimization', *SPIE* Vol.3037, pp 135-139.
- [82] de Belleval, J.F and Lecuru, D: 'Improvement of Ultrasonic Transducers by Using a Multilayer Front Face', *1978 IEEE Ultrasonics Symposium Proceedings*, pp 122-125.
- [83] Persson, H.W and Hertz, C.H: 'Acoustic Impedance Matching of Medical Ultrasound Transducers', *Ultrasonics*, No 23, March 1985, pp. 83-89.
- [84] Silk, M.G: 'Predictions of the effect of some constructional variables on the performance of ultrasonic transducers', *Ultrasonics*, January 1983, pp. 27-33.
- [85] Martin, J.M. et al, 'Ultrasonic ranging gets thermal correction', *Sensor Review*, Vol.9, No 3, July 1989, pp153-155.
- [86] Freire Bastos, T. et al, 'Ultrasonic signal variations caused by thermal disturbances', *Sensors and Actuators A*, Vol 44, No 2, August 1994, pp 131-135.

- [87] Ramos-Fernandez, A. Montoya-Vitini, F. and Gallego-Juarez. J.A: 'Automatic system for dynamic control of resonance in high power and high Q ultrasonic transducers', *Ultrasonics*, Vol. 23, July 1985, pp151-156.
- [88] Ikeda, K: 'Ultrasonic Liquid-Concentration Sensor with Temperature Compensation, Proceedings of the 1998 IEEE International Frequency Control Symposium', Pasadena, CA, U.S.A, 27-29 May 1998, pp 652-659.
- [89] Ishikawa, J. Mizutani, Y. et al: 'High-Frequency Drive-Power and Frequency Control for Ultrasonic Transducer Operating at 3MHz', IEEE Industry Applications Society, 32nd Annual Meeting, New Orleans, Louisiana, U.S.A, October 5-9 1997, pp 900-905.
- [90] Christidis, K: 'Characterisation and Monitoring of Mineral Deposits in Down-hole Petroleum Pipelines', *D.Phil Thesis*, The Robert Gordon University, Aberdeen, UK, Oct 2000. pp.9-42
- [91] Gunarathne, G.P.P. Christidis, K. Qureshi, Y. Miller, A.J. and Deans, N.D.: 'Analysis and Optimisation of Transmission Characteristics of Cables for Down-hole Tools and Data Acquisition Systems', *Proceedings of the IEE Instrumentation & Measurements Technology Conference*, May 1999, Venice, Italy, pp. 86-92.
- [92] Qureshi, Y; Gunarathne, G.P.P and Christidis, K: 'Compensation of High Power Ultrasonic Transducers for Optimum Power Transmission', NDT 2000, *The 39th Annual Conference of The British Institute of Non-Destructive Testing*, Buxton, UK, 12-14th September 2000, pp. 69-74.
- [93] Y.Qureshi, G.P.P Gunarathne and K.Christidis: 'Dynamic Impedance Matching of Transmission Cables for Down-hole Tools', *1st IEE International Seminar and Exhibition on On-line Monitoring Techniques for the Offshore Industry*, Aberdeen, 2nd June 1999, pp.11/1-11/4.

Bibliography

Chapter 1

Elsevier Advanced Technology: 'Valves, Piping and Pipelines Handbook, 2nd Edition, Elsevier Science Ltd, 1995, pp. 426-439.

Kraus, P et al McClain R: ' "Near" real time scale deposition measurement making advances' *Offshore (incorporating the Oilman)*, Vol.59, No.5, May 1999, pp.92-178.

Cross, Newbold O. : 'Global Condition-Scanning of Pipe', *11th World Conference on Nondestructive Testing (Through the eyes of an eagle)*, Las Vegas, USA, 1985, pp.1240-1245

Agothoven van, R and de Raad, J.A: Ultrasonic inspection of risers - a simple and affordable alternative to self-contained pigging', *Insight*, Vol.43, No.6, June 2001, pp.399-403.

Bindal, V.N; Jain S.K et al: 'Use of High Power Ultrasonics in the Benefication of Coal Fines', *Indian Journal of Technology*, Vol.26, June 1988, pp.275-277

Chapters 2-3

Elmore, W.C and Heald, M.A: 'Physics of Waves', Dover Publications, Inc, 1969, pp. 347-350.

Kinsler, L.E; Frey, A.R et al: 'Fundamentals of Acoustics', 3rd Edition, John Wiley & Sons, 1982, pp163-175

D'hooge, J; Nuyts, Johan et al: 'The calculation of the transient near and far field of a baffled piston using low sampling frequencies', *Journal of the Acoustical Society of America*, Vol.102, Part 1, pp.78-86.

Freedman, A: 'Sound Field of a Rectangular Piston', *Journal of the Acoustical Society of America*, Vol.32, No 2, pp.197-209.

Reibold, R and Kazys R: 'Radiation of a rectangular strip-like focussing transducer Part 1 harmonic excitation', *Ultrasonics*, Vol.30 No.1, 1992, pp. 49-55.

Reibold, R and Kazys R: 'Radiation of a rectangular strip-like focussing transducer Part 2 transient excitation', *Ultrasonics*, Vol.30 No.1, 1992, pp. 56-59.

Ifeachor, E.C and Jervis, B. W: 'Digital Signal Processing: A Practical Approach'. Addison Wesley Publishers Ltd, 1993, Chapters 1-2.

Goodyear, C.C: 'Signals and Information', London Butterworths, 1971, Chapter 2.

MATLAB Basic Reference Guide, The Mathworks, Inc, August 1992

Chapter 5

Shuyu, L: 'Study on the multifrequency Langevin ultrasonic transducer', *Ultrasonics*, Vol.33, No.6, Jan 1995, pp.445-448.

Dubus, B et al: 'Analysis of mechanical limitations of high power piezoelectric transducers using finite element modelling', *Ultrasonics*, Vol.29, May 1991, pp.201-207.

Nicholson, N.C and McDicken, W.N: 'A comparison of coupling horns for waveguides used in medical ultrasonics', *Ultrasonics*, Vol.34, 1996, pp.747-755.

Welsby, V.G: 'The design of flexural-mode transducers', *Ultrasonics International Conference Proceedings*, Imperial College, London, UK, 24-26 March 1975, pp257-260.

Lin, S and Zhang, F: 'Measurement of ultrasonic power and electro-acoustic efficiency of high power transducers', *Ultrasonics*, Vol.37, No.8, Jan 2000, pp.549-554.

Chapter 6

Collie, D.A.L and Player, M.A: 'Extended computer method for predicting the transient response of ultrasonic NDT probes', *Ultrasonics*, Vol.27, May 1989, pp141-149

Lamberti, N; Caliano, G. et al: 'A new Approach for the Design of Ultrasono-Therapy Transducers', *IEEE Transactions on Ultrasonics, Ferroelectrics and Frequency Control*, Vol.44, No.1 Jan 1997, pp. 77-84.

Turo, A; Salazaar, J. et al: 'Performance improvement of ultrasonic therapy equipment by modifying the classical transducer design', *IEE Proceedings of Science, Measurement and Technology*, Vol.146, No.2 March 1999, pp.107-112

Guang-Ping, Z; Cheng, Cun-Di et al: 'A new High Power Ultrasonic Rod Cone Radiator for Cleaning the Inner Wall of a Long Thin Pipe', *Chinese Science Bulletin*, (English Version) Vol.38, No.13, July 1993, pp.1075-1078

Chap 7

Arnold, F.J and Muhlen, S.S.: 'The resonance frequencies on mechanically pre-stressed ultrasonic piezotransducers', *Ultrasonics*, Vol.39 No.1 Jan 2001, pp.1-5.

Mortimer, B; du Bruyn, T. et al: 'High power resonant tracking amplifier using admittance locking', *Ultrasonics*, Vol.39, No.4, June 2001, pp.257-261.

Houghton, R.B et al: 'Ultrasound Power Generating System with Sampled-Data Frequency Control', United States Patent, Patent Number: 4,966,131, 30th Oct 1990.

Berthelsen, G: 'Communication Cables in the Offshore Environment', *Electrical Communication*, 1st Quarter, 1994, pp.60-65

Sun, Y and Fidler, J.K: 'Design method for impedance matching networks', *IEE Proceedings of Circuits, Devices and Systems*, Vol.143, No.4, August 1996, pp.186-194.

Publications

List of Publications

- [1] Gunarathne, G.P.P. Christidis, K. Qureshi, Y. Miller, A.J. and Deans, N.D.: 'Analysis and Optimisation of Transmission Characteristics of Cables for Down-hole Tools and Data Acquisition Systems', *Proceedings of the IEEE Instrumentation & Measurement Technology Conference*, May 1999, Venice, Italy, pp 86-92.
- [2] Y.Qureshi, G.P.P Gunarathne and K.Christidis: 'Dynamic Impedance Matching of Transmission Cables for Down-hole Tools', Poster Paper at the 1st IEE International Seminar and Exhibition on On-line Monitoring Techniques for the Offshore Industry, Aberdeen, 2nd June 1999, pp.11/1-11/4.
- [3] Y.Qureshi, G.P.P. Gunarathne and K.Christidis: 'Compensation of High Power Ultrasonic Transducers for Optimum Power Transmission', NDT 2000, *The 39th Annual Conference of The British Institute of Non-Destructive Testing*, Buxton, UK, 12-14th September 2000, pp. 69-74.
- [4] G.P.P Gunarathne and Y.Qureshi: 'Development of a Synthetic A-scan Technique for Ultrasonic Testing of Pipelines', *Proceedings of the IEEE Instrumentation & Measurement Technology Conference*, 21-23rd May 2002, Anchorage, AK, USA, Vol.1, pp.547-552
- [5] G.P.P Gunarathne and Y.Qureshi: 'Development of a Synthetic A-scan Technique for Ultrasonic Testing of Pipelines', *Paper submitted to the IEEE Transactions on Instrumentation and Measurement*, (Oct 2002).
- [6] G.P.P Gunarathne and Y.Qureshi: 'A Novel Technique for Dynamic Alignment of Ultrasonic Transducers in Real-time Non-destructive Testing'. *Proceedings of the IEEE Instrumentation & Measurement Technology Conference 20-22nd May 2003*, Vail, Col, USA, Vol.2, pp.1137-1142

Oral Presentations

- [1] Paper presented at The 39th Annual Conference of The British Institute of Non-Destructive Testing, Buxton, UK, 12-14th September 2000
- [2] Y.Qureshi and G.P.P Gunarathne: 'Detection and Dissolution Enhancement of Mineral Scale Deposits in Petroleum Pipelines using Ultrasonic NDT', *Scottish Marine Group (SMG) Spring Meeting*, University of Aberdeen, 27th February 2002

Published Papers

Analysis and Optimisation of Transmission Characteristics of Cables for Down-hole Tools and Data Acquisition Systems

G.P.P. Gunarathne, K. Christidis, Y. Qureshi, A.J. Miller, N.D. Deans

School of Electronic and Electrical Engineering, The Robert Gordon University, Aberdeen, AB10 1FR, UK.

Abstract

This paper examines the conditions required to optimise transmission of mixed signals (analogue, digital and power) for down-hole tools and data acquisition systems, when using coaxial cables. The performance of the cables was analysed using a finite element model. A special feature of the model is that it implicitly introduces the effects of temperature differentials to which the cable may be exposed through the primary constants of the cable, where, the temperature dependency of each constant is either known, or practically established. Using this model, various matching options were investigated and verified by experiments. From these investigations, it is found that within the low-to-medium frequency range (1kHz-100kHz) conventional method of matching (termination impedance equal to nominal characteristic impedance at high frequency) does not yield optimal performance. It is proposed that better matching conditions could be achieved as predicted by the model.

1. Introduction

Cables used for down-hole tools are often required to carry different types of signals e.g. digital, analogue and power transmission[1]. However the duplication of transmission lines to cater for each requirement may be prohibitively expensive or may not be feasible at all. Also, temperature gradients between topside and down-hole locations may be very large, e.g. in excess of 200°C, affecting the transmission parameters and hence the performance of the cables. Some work has been reported on the analysis of cables for down-hole applications, but their scope is limited to specific applications under restricted conditions, such as for very low frequency, high frequency or low power applications[2] [3]. These models are also limited to instances where the temperature along the transmission line is assumed to be constant, or increasing gradually, as the depth increases;

conditions which are not adequately satisfied in many situations.

The main objective of this work is to investigate the optimal conditions for transmission of different signals as above, using a single co-axial line, taking into account temperature and frequency effects. The study is based on the requirements for a new ultrasonic down-hole tool, where the cable is to carry high power sinusoidal drive signals in the frequency range 10Khz - 80Khz (supplied by a 200V rms generator), digital signals up to 10Mhz for imaging applications, and DC power transmission for operation of the tool and data acquisition boards.

2. Analogue transmission

A comprehensive mathematical model, based on finite element analysis has been developed. The primary constants of the transmission line (co-axial cable) are denoted as R_c , L , C , G ; where, R_c is the resistance, L is the inductance, C is the capacitance, and G is the conductance, per unit length under given operational conditions. Although not explicitly shown here, the temperature and frequency effects have been introduced in to the primary constants R_c , L , C , G through dependent parameters to form the following relationships:

$$R_{c(t)} = \left[\frac{1}{\pi r_i^2 - \pi(r_i - \delta)^2} + \frac{1}{\pi r_s^2 - \pi(r_s - \delta)^2} \right] l \cdot \rho(t) \quad (1)$$

$$L_{(t)} = (R_{c(t)} / \omega) + [\mu_{(t)} \ln(r_o/r_i) / 2\pi] \quad (2)$$

$$C_{(t)} = 2\pi\epsilon_{(t)} / \ln(r_o/r_i) \quad (3)$$

$$G_{(t)} = \omega C_{(t)} \psi \quad (4)$$

where, $\rho(t)$ = conductor resistivity at t° C, l = cable length, r_s = outer conductor external radius, r_i = inner conductor radius, r_o = outer conductor internal radius, δ = skin depth, $\epsilon(t)$ = permittivity of the insulation material at

$\mu(t) = \text{permeability of the insulation material at } t^\circ \text{C,}$
 $\psi = \tan \theta, \theta = \text{loss angle.}$

In this way, the combined effect of temperature and frequency was taken into account unlike in the case of conventional models [1] [2]. Also, typical simplifying assumptions made in the conventional models were not used, such as low or high frequency limits, as they lead to significant errors in the transition region, which happens to be the area of interest in the present work. Figure 1 shows the basic schematic of the system,

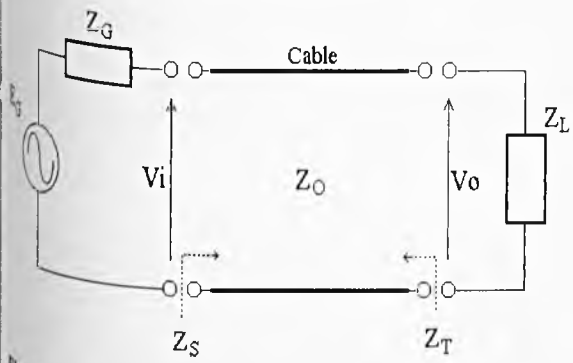


Figure 1. Schematic of a transmission system

where Z_S is the impedance as seen at the input of the cable, Z_T is the impedance as seen at the output of the cable, and Z_0 is the cable characteristic impedance.

The characteristic impedance Z_0 of the cable may be written as:

$$Z_0 = \sqrt{\frac{R + j\omega L}{G + j\omega C}} = \sqrt{\frac{RG + \omega^2 LC}{G^2 + \omega^2 C^2} + j \frac{\omega(LG - RC)}{G^2 + \omega^2 C^2}} \quad (5)$$

Since, $Z_S = f(Z_0, Z_L)$ and $Z_T = f(Z_0, Z_G)$

Z_S and Z_T may then be derived.

For analysis, the cable is considered to be a cascade of a finite number of small segments as shown below, where the length of a segment is chosen to be small enough, so that the temperature over that segment could be regarded as practically constant.

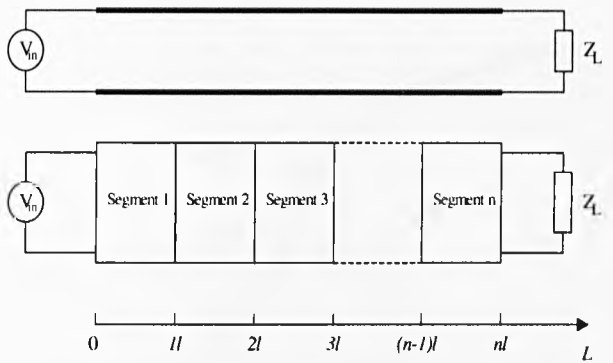


Figure 2. A long coaxial cable divided into n small sections.

Using the above model, the primary parameters were then defined as an array of $4 \times n$ elements, where n representing the number of segments in the finite element model. The temperature effect for each segment is introduced into each primary constant to generate a new $4 \times n$ array of the form as shown below.

$$\begin{bmatrix} R_{c1} & R_{c2} & \dots & R_{cn} \\ L_1 & L_2 & \dots & L_n \\ C_1 & C_2 & \dots & C_n \\ G_1 & G_2 & \dots & G_n \end{bmatrix} f \begin{pmatrix} T_1 \\ T_2 \\ \vdots \\ T_n \end{pmatrix} \Rightarrow \begin{bmatrix} R_{c1}(T_1) & R_{c2}(T_2) & \dots & R_{cn}(T_n) \\ L_1(T_1) & L_2(T_2) & \dots & L_n(T_n) \\ C_1(T_1) & C_2(T_2) & \dots & C_n(T_n) \\ G_1(T_1) & G_2(T_2) & \dots & G_n(T_n) \end{bmatrix}$$

From the above, the attenuation coefficient α and the phase constant β for each segment were computed to obtain a second array of $2 \times n$ elements as shown below.

$$\begin{bmatrix} R_{c1}(T_1) & R_{c2}(T_2) & \dots & R_{cn}(T_n) \\ L_1(T_1) & L_2(T_2) & \dots & L_n(T_n) \\ C_1(T_1) & C_2(T_2) & \dots & C_n(T_n) \\ G_1(T_1) & G_2(T_2) & \dots & G_n(T_n) \end{bmatrix} \Rightarrow \begin{bmatrix} \alpha_1 & \alpha_2 & \dots & \alpha_n \\ \beta_1 & \beta_2 & \dots & \beta_n \end{bmatrix}$$

Where,

$$\alpha = \{ \frac{1}{2} [(R^2 + \omega^2 L^2)(G^2 + \omega^2 C^2)]^{1/2} + \frac{1}{2} (RG - \omega^2 LC) \}^{1/2} \quad (6)$$

$$\beta = \{ \frac{1}{2} [(R^2 + \omega^2 L^2)(G^2 + \omega^2 C^2)]^{1/2} - \frac{1}{2} (RG - \omega^2 LC) \}^{1/2} \quad (7)$$

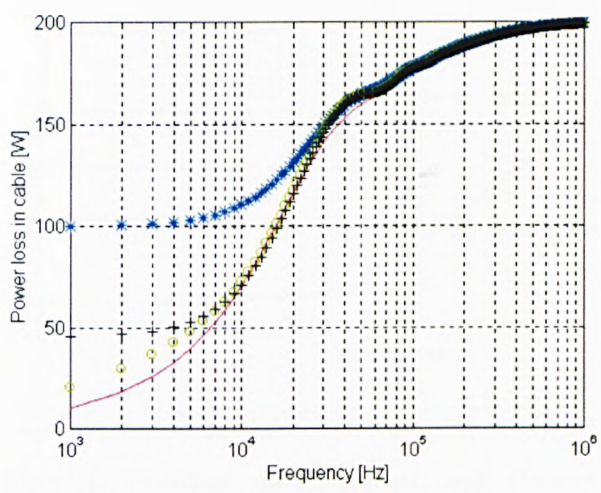
The propagation coefficient $\gamma_N(T)$ of the entire length of the cable for a given frequency is the summation of the propagation coefficients of each section. Hence,

$$\gamma_N(T) = \sum_{i=0}^n [\alpha_i(T_i) + j\beta_i(T_i)] \quad (8)$$

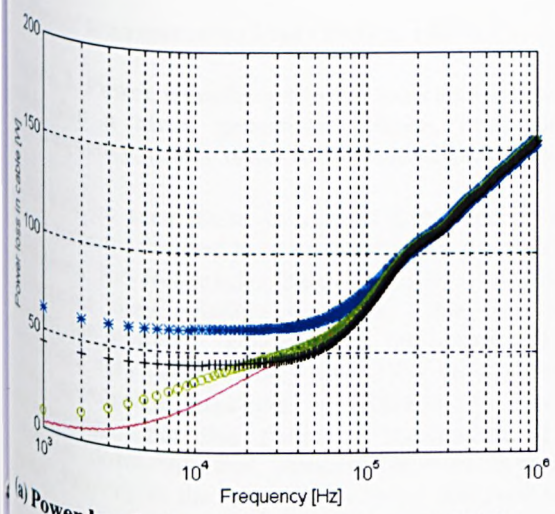
From this, Z_S and Z_T (as defined above in figure 1) for the entire transmission line are obtained as functions of the temperature profile of the cable, operational frequency, and cable length.

Since $Z_S = f(Z_0, Z_L)$ and $Z_T = f(Z_0, Z_G)$, it is possible to compute the power transferred to the load and power loss in the cable for a given generator voltage, temperature, frequency and cable length under different matching conditions, as shown below, where the respective curves are shown for:

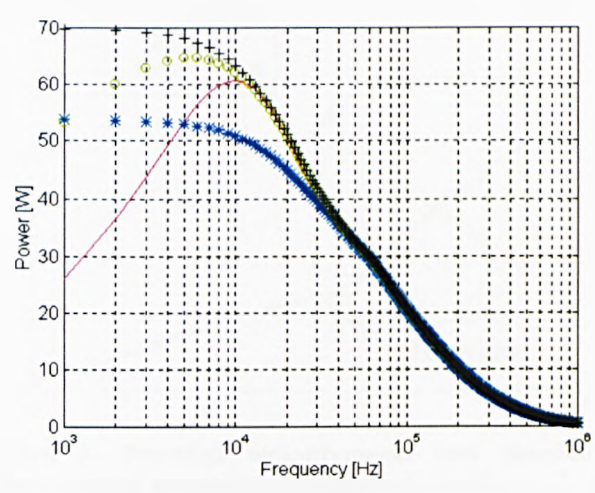
- $Z_G = Z_L = \text{Conjugate of } Z_0$ (---)
- $Z_G = Z_L = R_0$ (****)
- $Z_G = R_0, Z_L = \text{conjugate of } Z_0$ (oooo)
- $Z_G = R_0, Z_L = \text{conjugate of } Z_T$ (++++)



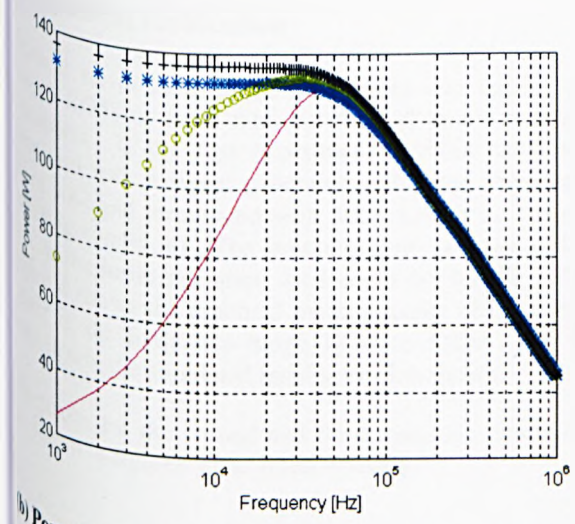
(c) Power loss in the cable, 2000m long, at 22°C



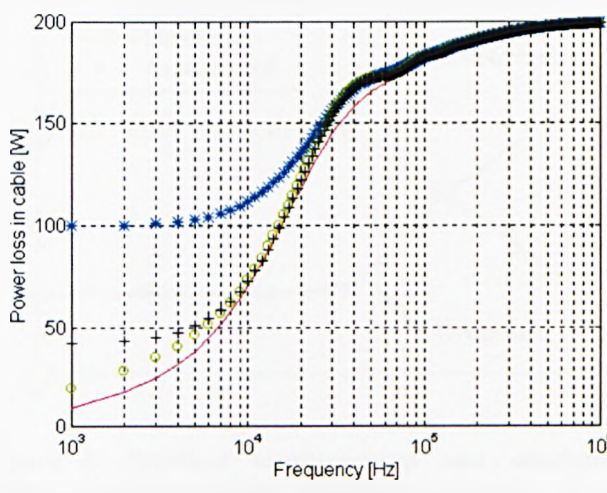
(a) Power loss in the cable, 500m long, at 22°C



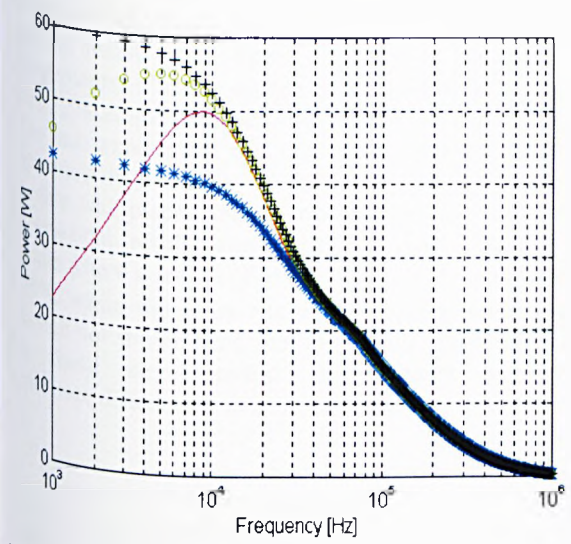
(d) Power transmitted to load (2000m, 22°C)



(b) Power transmitted to load, 500m cable at 22°C



(e) Power loss in the cable, 2000m long, at 100°C



(f) Power transmitted to load (2000m, 100⁰ C)
Figure 3. Power transferred to the load and loss in the cable for a given generator voltage, temperature and frequency, under different matching conditions.

As can be seen, there is a wide difference between power transmission and losses depending on the matching conditions for frequencies below ~50Khz. At higher frequencies they coincide since the cable impedance reaches the nominal characteristic impedance. These results are very useful as they now allow the designer to choose appropriate matching combinations to suit the applications. For this particular application of the ultrasonic down-hole tool, considerable improvement in power delivery to the transducer can be achieved using the matching conditions (4), where $Z_G=R_0$ and $Z_L=$ conjugate of Z_T , according to this investigation.

2.1. Practical verification

Practical verification of the simulations was carried out using a RG58 co-axial cable for the last three matching conditions. In the first experiment a 500m cable was connected with a signal generator with input impedance Z_G of 50Ω and terminated with 50Ω resistor Z_L (second matching condition). The generator emf was set at 44V rms, as the instrumentation used could not handle 200V. Figure 4 shows the practical measurements of the output power in the frequency range 1Khz to 1Mhz. On the same figure, the simulated results are also shown. The results for the second and third matching conditions are shown in figures 5 and 6 respectively.

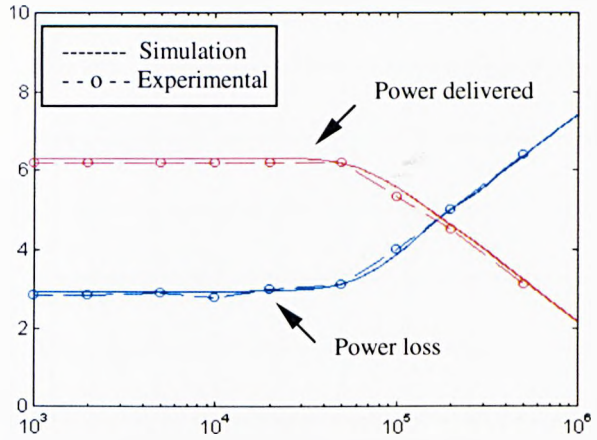


Figure 4. Practical measurements and simulated results (second matching condition $Z_G = Z_L = R_0$)

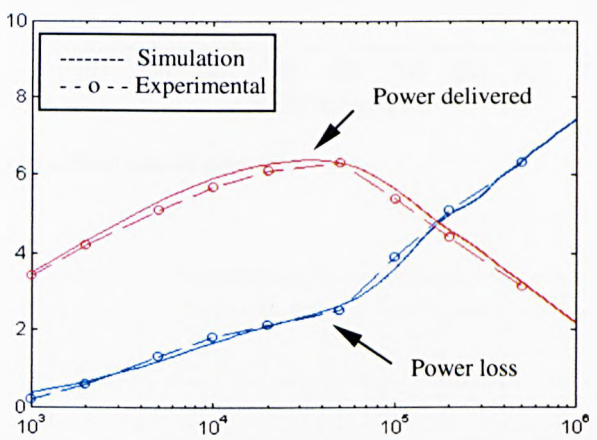


Figure 5. Practical measurements and simulated results (third matching condition $Z_G = R_0$, $Z_L =$ conjugate of Z_0)

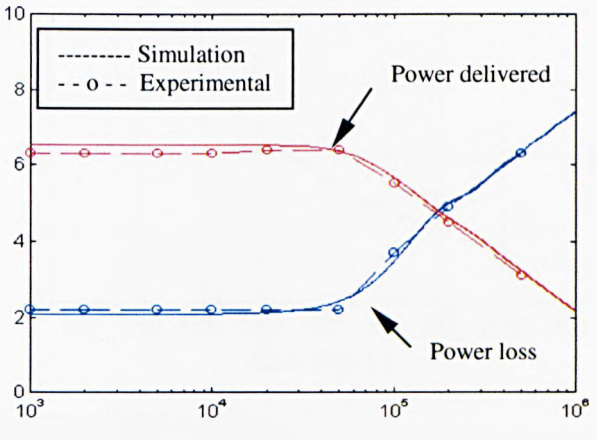


Figure 6. Practical measurements and simulated results (fourth matching condition $Z_G = R_0$, $Z_L =$ conjugate of Z_T)

As can be seen from the practical verification of the simulated results from figure 4, 5 and 6, the practical measurements closely agreed with the simulation to within 3.5% at all frequencies of interest.

The next experiment was concerned with the effect of temperature differentials. In this case a known length of the cable was placed inside an oven and the theoretical and practical results compared. Figure 7 shows an example where a length of 100m of the cable is subjected to 75°C while the other 400m at ambient temperature. Although not shown here, due to practical difficulties the tests could be extended to represent segmental temperature differences in a similar manner.

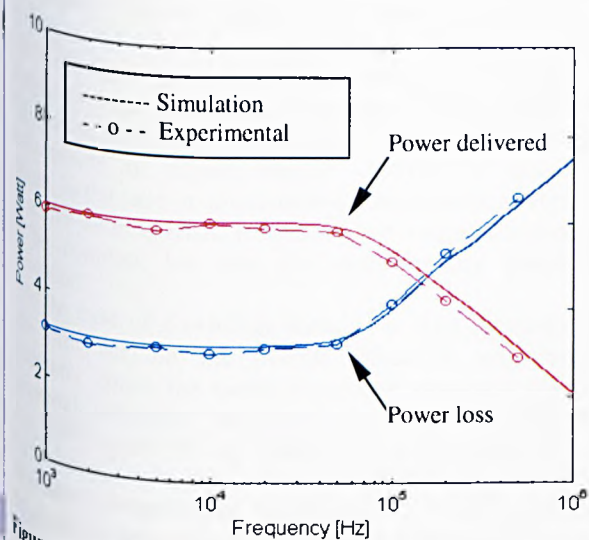
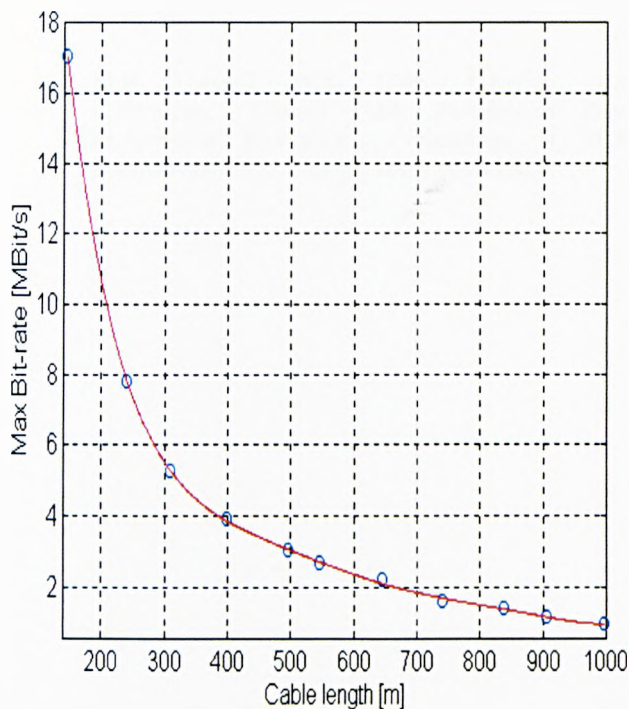


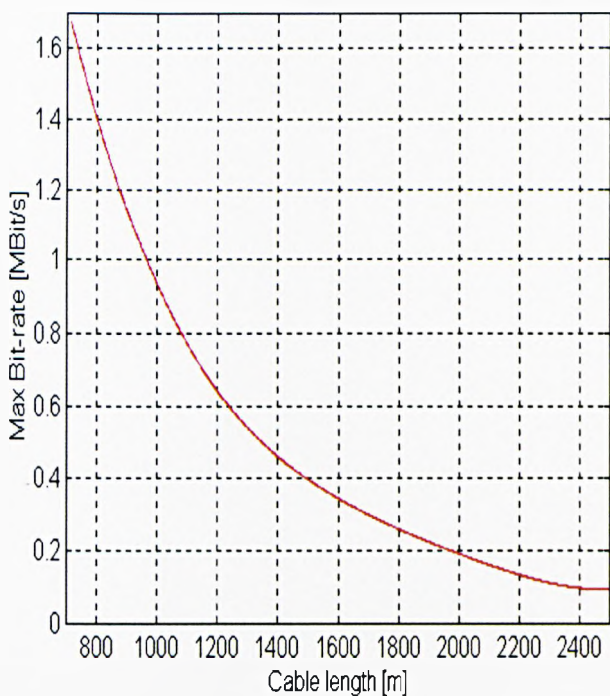
Figure 7. Cable subjected to temperature differentials. Simulated results compared with experimental results. (Second matching condition $Z_G = Z_L = R_0$)

3. Digital transmission

The simultaneous use of the cable for data transmission on a time-shared basis was then examined. Since the signal spectrum contain much higher frequencies than for the case of analogue drive signals, and optimisation of power is not essential, source and termination impedance of 50Ω were used. The maximum bit rates (limited by frequency dependent attenuation and inter-symbol interference) were then experimentally assessed for various cable lengths and temperatures. Figure 6(a) shows the results of this investigation for cable lengths up to 1000m, and figure 6(b) shows the extrapolated pattern for assessment of maximum bit rates for longer cable lengths. However, in this case, the termination impedance cannot be the same as that required for low frequency analogue signals, if maximum bit rates are required.



(a) Practical measurements



(b) Extrapolated results

Figure 6. Maximum bit rate over a given cable length

4. Conclusions

The operational requirements of communication cables used in the offshore environment are very different from those used for terrestrial telecommunications. Since the cost of these cables could be comparatively very high, extending their operational capabilities should allow new cost-effective solutions to be found, and increase the range of activities supported.

In this study it has been shown that the conventional method of matching cables, e.g. by the use of purely resistive source and load impedance equal to the cable characteristic impedance, does not necessarily give optimal performance when using long coaxial cables for transmission of low to medium frequencies. The characteristic impedance of the cable is a function of frequency and temperature, and the determination of appropriate termination impedance is necessary if optimal transmission of signals below ~100Khz is required. Hence, in the case of simultaneous transmission of signals on a time-sharing basis, it is not only the signals that need to be coupled, but also the compensating matching networks.

In the case of down-hole tools, it is also necessary to take into account the overall effect of temperature gradients. Since the model developed can cater for the changes in temperature, an interesting possibility would be to monitor the temperature as the tool advances into the seabed, in order to generate the dependent transmission coefficients of the network. Automatic compensation of termination impedance could then be carried out. This work is in progress.

Acknowledgement

Authors wish to express their gratitude to Dr Richard W. Keatch, Keatch Chem, Aberdeen, for sponsoring this work. Thanks are also due to Mr Bill Black and the technical and secretarial staff of the University.

References

1. G. Berthelsen: "Communication Cables in the Offshore Environments", Electrical Communication, 1st Quarter 1994, pp 60-65.

2. H. Mokhtari, A. Nyeck, C. Roussey, A. Roussey: "Finite difference method and Pspice simulation applied to the coaxial cable in a linear temperature gradient", IEE PROCEEDINGS-A, Vol. 139, No. 1, January 1992, pp 39-41.

3. M.D. Carangi, W.Y. Chen, K.Kerpez, and C.F.Valenti: "Coaxial Cable Distribution Plant Performance Simulation", Proceedings of SPIE International, 1995, Volume 2609, pp 215-226.

DYNAMIC IMPEDANCE MATCHING OF TRANSMISSION CABLES FOR DOWNHOLE TOOLS

Y. Qureshi, G.P.P Gunarathne, K. Christidis

INTRODUCTION

Transmission cables for down-hole applications are required to carry analogue and digital signals over long distances^[1]. This study concentrates on the optimisation of power transfer from the topside location to an ultrasonic down-hole tool system^[2] via co-axial cables. The cable is to carry high power sinusoidal drive signals in the frequency range 10Khz - 80Khz (supplied by a 200V rms generator), digital signals up to 10Mhz for imaging applications, and DC power transmission for operation of the tool and data acquisition boards.

The main constraint on the transmission cable is that temperature gradients between topside and down-hole locations may be very large, e.g. in excess of 150°C, affecting the transmission parameters and hence the performance of the cables^[3]. Other types of transmission media (e.g. fibre optics and single wire) are costly for long distances and require various sub-systems^[4,5]. Some work has been reported on the analysis of cables for down-hole applications, but their scope is limited to specific applications under restricted conditions, such as for very low frequency, high frequency or low power applications^[6,7]. Analysis of the cable using finite difference techniques to investigate the optimal conditions for transmission of different signals using a single co-axial line, has been reported^[8]. The main objective of this work is based on this model to investigate the power transfer improvement by dynamic impedance matching of the cable, as it passes through various temperature zones into down-hole petroleum pipelines. The ultrasonic transducer is being used for dissolution enhancement of scales.

FINITE DIFFERENCE METHOD

The mathematical model developed in the previous study is based on the primary constants of the transmission line at any given temperature. These parameters are denoted as R_c , L , C , G ; where, R_c is the resistance, L is the inductance, C is the capacitance, and G is the conductance, per unit length under given operational conditions. Although not explicitly shown here, the temperature and frequency effects have been introduced in to the primary constants R_c , L , C , G through dependent parameters to form the following relationships^[8]:

$$R_{c(t)} = \left[\frac{1}{\pi_i^2 - \pi(r_i - \delta)^2} + \frac{1}{\pi_s^2 - \pi(r_s - \delta)^2} \right] i \cdot \rho_{(t)} \quad (1)$$

$$L_{(t)} = (R_{c(t)} / \omega) + [\mu_{(t)} \ln(r_o/r_i) / 2\pi] \quad (2)$$

$$C_{(t)} = 2\pi\epsilon_{(t)} / \ln(r_o/r_i) \quad (3)$$

$$G_{(t)} = \omega C_{(t)} \psi \quad (4)$$

where, $\rho(t)$ = conductor resistivity at $t^\circ\text{C}$, l = cable length, r_s = outer conductor external radius, r_i = inner conductor radius, r_o = outer conductor internal radius, δ = skin depth, $\epsilon(t)$ = permittivity of the insulation material at $t^\circ\text{C}$, $\mu(t)$ = permeability of the insulation material at $t^\circ\text{C}$, $\psi = \tan\theta$, θ = loss angle.

Hence the combined effect of temperature and frequency was taken into account unlike in the case of conventional models^[8]. Figure 1 shows the basic schematic of the transmission cable system used in the model.

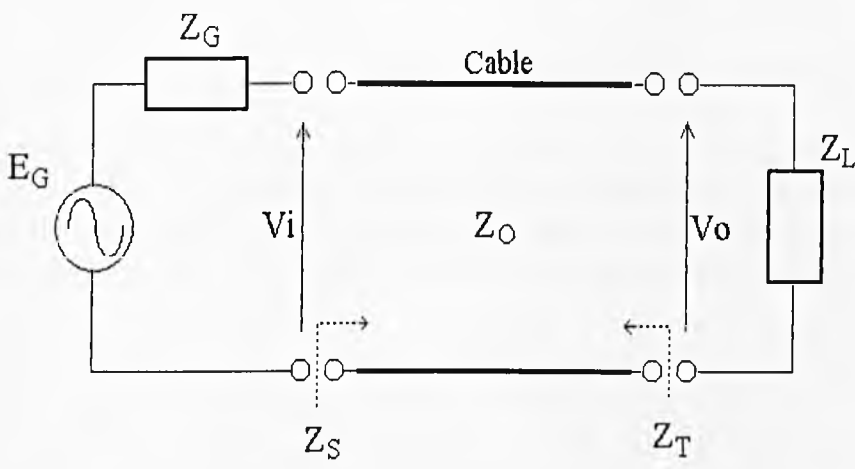


Figure 1. Schematic of a transmission system

Where Z_S is the impedance as seen at the input of the cable, Z_T is the impedance as seen at the output of the cable, Z_0 is the cable characteristic impedance and Z_L is the load impedance.

The characteristic impedance Z_0 of the cable may be written as:

$$Z_0 = \sqrt{\frac{R + j\omega L}{G + j\omega C}} \quad (5)$$

$$= \sqrt{\frac{RG + \omega^2 LC}{G^2 + \omega^2 C^2} + j \frac{\omega(LG - RC)}{G^2 + \omega^2 C^2}}$$

The impedances Z_T and Z_S are obtained using the standard relationship that: $Z_S = f(Z_0, Z_L)$ and $Z_T = f(Z_0, Z_G)$. Hence Z_T changes along the length of the cable if the temperature does not remain constant.

The complete cable system is considered to be a cascade of a finite number of small segments as shown in Figure 2, where the length of a segment is chosen to be small enough, so that the

temperature over that segment could be regarded as practically constant. However over the entire length of the cable the temperature is not constant in the pipeline.

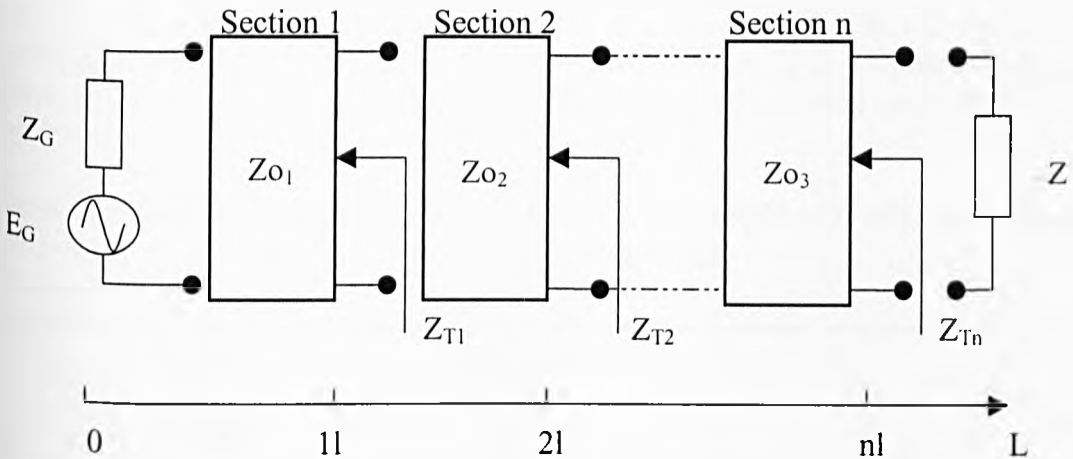


Figure 2: A long coaxial cable divided into n finite sections

Using the above model, the primary parameters were then defined in an array of $4 \times n$ elements, where n representing the number of segments in the finite element model. The temperature effect for each segment is introduced into each primary constant to generate a new $4 \times n$ array of the form as shown below. So for each different temperature section new coefficients are generated in the following matrix.

$$\begin{bmatrix} R_{c1} & R_{c2} & \dots & R_{cn} \\ L_1 & L_2 & \dots & L_n \\ C_1 & C_2 & \dots & C_n \\ G_1 & G_2 & \dots & G_n \end{bmatrix} f \begin{pmatrix} T_1 \\ T_2 \\ \vdots \\ T_n \end{pmatrix} \Rightarrow \begin{bmatrix} R_{c1}(T_1) & R_{c2}(T_2) & \dots & R_{cn}(T_n) \\ L_1(T_1) & L_2(T_2) & \dots & L_n(T_n) \\ C_1(T_1) & C_2(T_2) & \dots & C_n(T_n) \\ G_1(T_1) & G_2(T_2) & \dots & G_n(T_n) \end{bmatrix}$$

Experimentation and simulated results from the model has shown that a good matching condition for maximum power delivery to the load at low frequencies, occurs when Z_L is equal to the conjugate of $Z_T^{[8]}$. For a 2km cable at 100°C the power output at 1Khz is increased by approx. 40% with this matching condition, compared to matching with the nominal characteristic impedance of the cable. The effect on power output due to incremental temperature changes along the cable has still to be studied. When the cable parameters change with temperature, Z_T needs to be calculated whenever a new temperature zone is detected by the ultrasonic down-hole tool. An automatic tap-changing compensation network could then present the modified load impedance to the terminating end of the cable.

GENERATION OF DYNAMIC IMPEDANCES

The next stage of investigation was to determine whether a significant improvement occurs in power output if the cable termination impedance were to be dynamically adjusted to take into account the temperature zones. The existing model is not required to calculate Z_T continuously as the cable advances into the pipeline. Thus, an 'incremental length' is initially defined in the modified model. This is the length after which the temperature is logged by the down-hole tool, and the point when the new terminating impedance, Z_T is calculated. To calculate this impedance all the primary parameters, Z_o and the Z_T values for the length of the cable at previous temperatures are recalculated. This is illustrated in Figure 2 as Z_T is calculated iteratively. This process continues until the down-hole tool reaches its final destination.

For example consider a 100m cable that is connected to an ultrasonic power transducer in a down-hole tool. When lowered into the pipeline and the logging interval set at 2m say, the model calculates the required Z_T for the complete cable at any location within the pipeline, taking into account the sections outside the pipeline at ambient temperature. This process ensures that the model is updated automatically by dynamically calculating the terminating impedance at any required interval.

The model calculates the impedance Z_T and presents it in a graphical display, along with the relevant input data as shown in Figure 3 with some typical parameters.

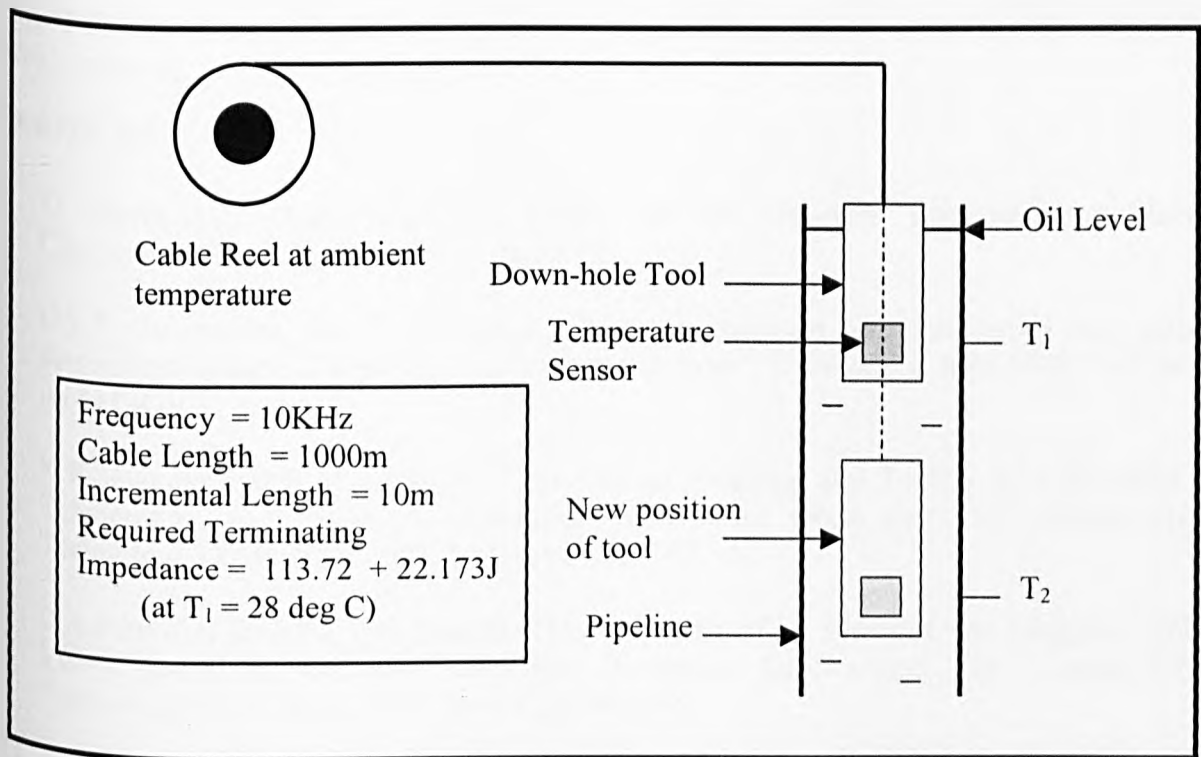


Figure 3: Graphical display of dynamic impedance matching model

SIMULATION RESULTS OF POWER OUTPUT WITH MATCHED CABLE

Using the model it is possible to show the effect of dynamically matching the cable through the temperature zones. The worst case situation is when the complete cable is at the highest temperature in the pipe. The model was used to predict the power output when a 1km cable was subjected to 100°C . It was found that when the cable was dynamically matched with the conjugate of Z_T , the power output increased marginally (but not significantly), compared to the case when matched with the Z_T for 25°C .

DISCUSSION

The above simulation results indicate that with dynamically matching the cable the power output increases by approx. 0.3%. Hence there seems no advantage in matching the cable in this way. However, the total termination impedance required is the combined impedance of the transducer and the supplementary matching network to provide the overall termination impedance required for optimal matching. The impedance of the transducer could change very considerably with temperature due to its temperature dependant electro-mechanical properties.

CONCLUSIONS

The operational requirements of communication cables used in the offshore environment are very different from those used for terrestrial telecommunications. Using the matching condition where the load termination, Z_L equals the conjugate of Z_T , maximum power is transferred to the load. In order to evaluate the effect of varying temperature gradients on the cable, the model has been successfully used. A software-based system would update the matrix coefficients and termination impedance when required. From this study it is found that the cable terminating impedance Z_T is not required to be dynamically matched as the cable advances into the pipeline, although the transducer parameters need to be compensated for optimal matching. This work is in progress. Once fully developed the model can be applied to other power transfer applications where the temperature is constantly varying.

REFERENCES

- [1] G. Berthelsen: "Communication Cables in the Offshore Environments", Electrical Communication, 1st Quarter 1994, pp 60-65.
- [2] G.P.P Gunarathne and R.W Keatch: "Novel techniques for monitoring and enhancing dissolution of mineral deposits in petroleum pipelines", Ultrasonics, June 1996, Vol. 34, pp 411-419.
- [3] K.P.Seymour and R.MacAndrew: "The Design, Drilling, and Testing of a Deviated High-Temperature, High Pressure Exploration Well in the North Sea", 25th Annual Offshore Technology Conference, 1993, Vol. 4, pp 733-740.
- [4] C.A.Peters, C.C.Cobb, P.K Schultz: "Development of an Electro-Opto Logging Cable and Video System for Offshore and Other Downhole Applications", 26th Annual Offshore Technology Conference, 1994, Vol. 4, pp 885-892.
- [5] O.J.Pinho, F.,Robert Eisemberg and D.S Sampaio: "Production Subsea Installations Control an Supervision Electronic Systems Development", 25th Annual Offshore Technology Conference, 1993, Vole 3, pp 455-460.
- [6] H.Mokhtari, A.Nyeck, C.Roussey, A.Roussey: "Finite difference method and Pspice simulation applied to the coaxial cable in a linear temperature gradient", IEE Proceedings-A, Vol. 139, No 1, January 1992, pp 39-42.
- [7] M.D Carangi, W.Y. Chen, K.Kerpez, and C.F.Valenti: "Coaxial Cable Distribution Plant Performance Simulation", Proceedings of SPIE International, 1995, Vol. 2609, pp215-226.
- [8] G.P.P Gunarathne, K.Christidis, Y.Qureshi, A.J Miller and N.D Deans: "Analysis and Optimisation of Transmission Characteristics of Cables for Down-hole Tools and Data Acquisition Systems, IEE Instrumentation & Measurements Technology Conference, May 1999, Venice, Italy.

Compensation of High Power Ultrasonic Transducers for Optimum Power Transmission

Y. Qureshi, G.P.P. Gunarathne and K. Christidis

School of Electronic and Electrical Engineering, The Robert Gordon University,
Schoolhill, Aberdeen, UK

Tel.: 01224-262443

Fax.: 01224-262444

E-mail: g.p.gunarathne@eee.rgu.ac.uk

Abstract

Ultrasonic power transducers are widely used for cleaning operations and in medical treatment. Often they are required to operate over a wide temperature range, which causes their electromechanical properties to change, and the resonance condition to drift, causing loss of efficiency. Conventional methods of regaining loss of efficiency due to drift is to dynamically maintain the drive voltage and current waveforms in phase. However, the generation of 'silent spots' in the case of transmission into confined spaces due to nodal regions is a problem in this case. In this project, an alternative technique has been investigated which is particularly suitable for transmission into confined spaces (such as in the case of cleaning pipelines), where the static nodes are to be avoided. Instead of sensing the phase of voltage and current waveforms, the approach taken here is to sense the actual power output using an elemental transducer bonded to the insonifying power transducer to dynamically optimise the power output. In doing so a degree of frequency modulation is also provided at the same time to eliminate static nodes. In this paper, the general performance characteristics of the sandwich transducers with respect to the temperature and a description of the control mechanism to optimise power output will be presented. Although the techniques developed were specifically meant for high power, low frequency transducers, they may be applied to NDT transducers, where the power output is a primary concern.

1. Introduction

It is widely known that ultrasonic irradiation could be used to aid cleaning operations. Often, these operations require elevated temperature to be effective and consequently the transducers are required to operate over a range of temperatures.

The output acoustic power of sandwich ultrasonic transducers radiating into liquid media varies with temperature due to the changes in their electro-mechanical properties^(1,2). This causes the transducer acoustic efficiency to decrease with increasing temperature. Also, the series resonance frequency of the transducer changes⁽¹⁻⁴⁾, further decreasing the power

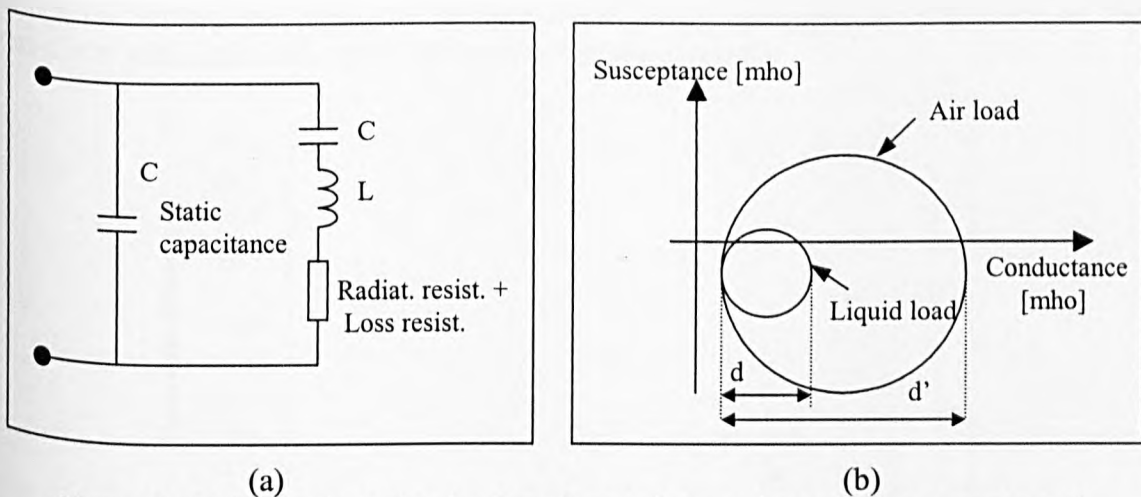
output unless the drive frequency is also changed accordingly. Previous work in the area of frequency control has tended to focus on the measurement of phase between the current and voltage waveforms applied.⁽³⁻⁵⁾ This technique often make use of a Phase Locked Loop (PLL) device whereby the voltage across and the current through the transducer are brought in phase. However, from our experiments performed in a water-filled pipe section, it was observed that the condition of resonance was difficult to detect in this way due to the reflections within the pipe and air bubbles forming on the surface of the transducer.

In recent years, the use of ultrasonic sandwich power transducers for dissolution enhancement of scales in petroleum pipelines were investigated.⁽⁶⁻⁸⁾ In this application the transducers were subjected to even higher temperatures ($\sim 85^{\circ}\text{C}$). However, a rapid decline in performance of the transducers used became apparent, particularly around 70°C approximately. Further investigations revealed that the centre frequency of the transducer drifts considerably requiring frequency tracking compensation to minimise further decline in power output of the transducer. Also, another problem observed in the case of transmission into confined spaces, such as pipelines was the generation of static nodes. To address both requirements at the same time, a novel technique based on sensing the actual power output from the transducer while introducing a degree of frequency modulation was proposed.⁽⁸⁾ In order to achieve this objective, a systematic study to obtain the transducer drift characteristics and to determine the parameters of the control and modulation system was undertaken in this project.

2. Variation of the transducer efficiency with temperature

2.1 Radiation efficiency

A simplified circuit of an ultrasonic transducer near resonance frequency is shown in Figure 1 together with a circle plot showing the variation of susceptance versus conductance of the transducer near resonance.



With reference to Figure 1(b), the radiation efficiency of the transducer (η) may be defined as⁽⁹⁾:

$$\eta = \frac{d' - d}{d'} \quad (1)$$

In order to carry out the efficiency tests under simulated practical conditions, a purpose built test rig, consisting of an extended S-shape plastic pipe section (Figure 2) was designed. The desired temperatures were achieved using a heated water circulation system. The transducer itself was immersed in a column of oil to prevent air bubbles forming on the surface of the transducer.

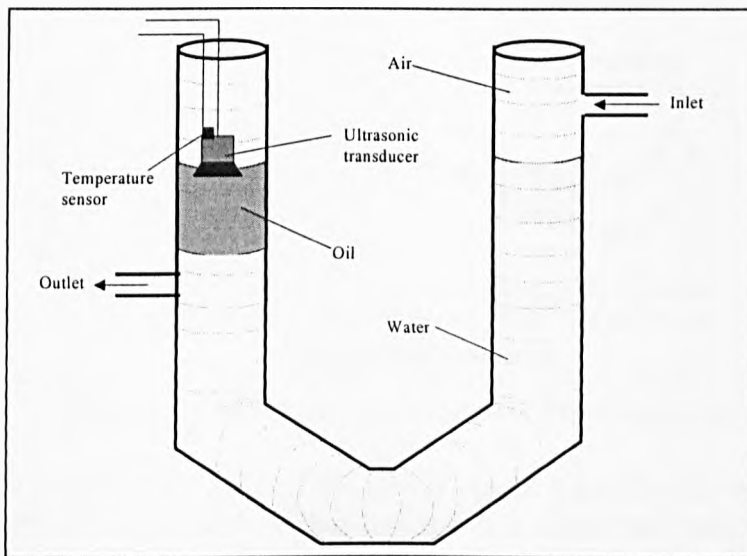


Figure 2. Test rig section for transmission efficiency measurements with dimensions

The transmission efficiency of the transducers were assessed at different temperatures using the equation 1. A large number of measurements were carried out to obtain average values at each temperature as the data scatter was found to be high; particularly at higher temperatures. Despite the data scatter (which was found to be mainly due to reflections within the pipe) the general trend of the decrease in efficiency of the transducer with increasing temperature was clearly observed.

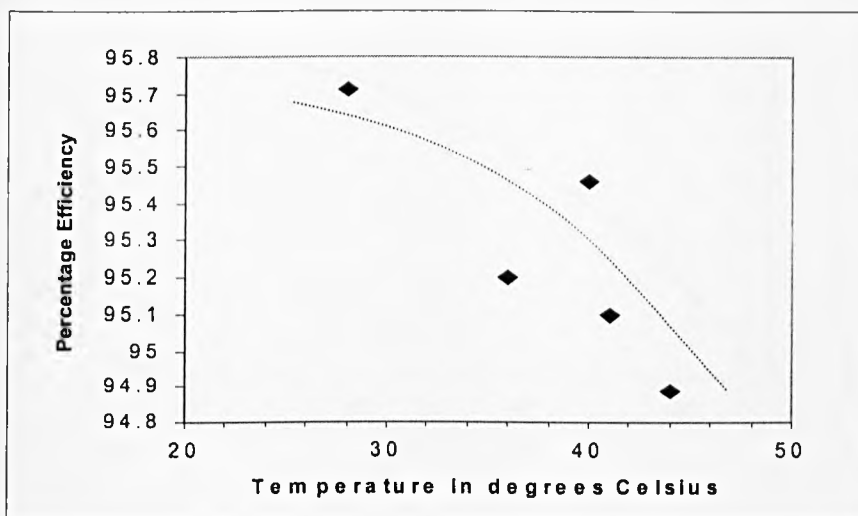


Figure 3. Transducer efficiency change with temperature: fully dipped in oil

Since it was difficult to obtain closely repeatable results for efficiency versus temperature in this way due to the problems of reflections, a different approach was then tried. In this method an elemental wide-band transducer was bonded to the power transducer and the pick up voltage was measured as a function of the temperature. The results of this test is shown in Figure 4. Curve (a) shows the variation of pick up voltage at optimal frequency setting for each temperature, while curve (b) shows the variation if frequency adjustments were not used.

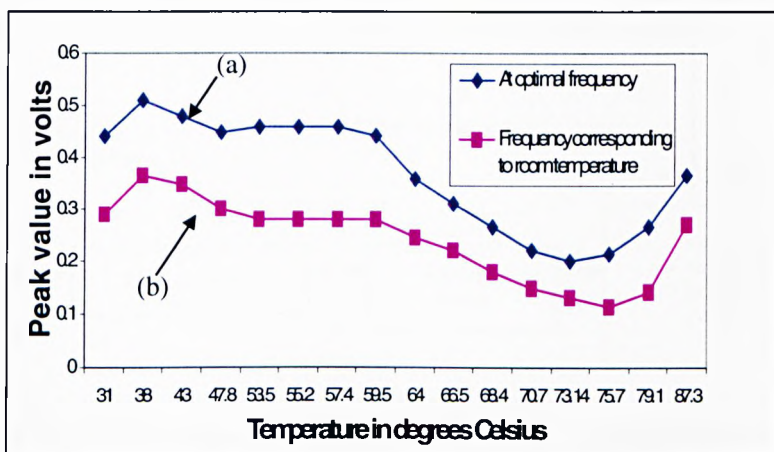


Figure 4. Transducer vibration characteristics in air

From Figure 4, it can be shown that the power output from the above transducer could drop to a value as low as 28% within the above temperature range, if no frequency compensation is applied.

2.2 Variation of resonance frequency with temperature

Since frequency drift has a profound effect on power, the extent of the drift was then measured. The results obtained from these measurements for an 80KHz sandwich transducer are shown in Figure 5.

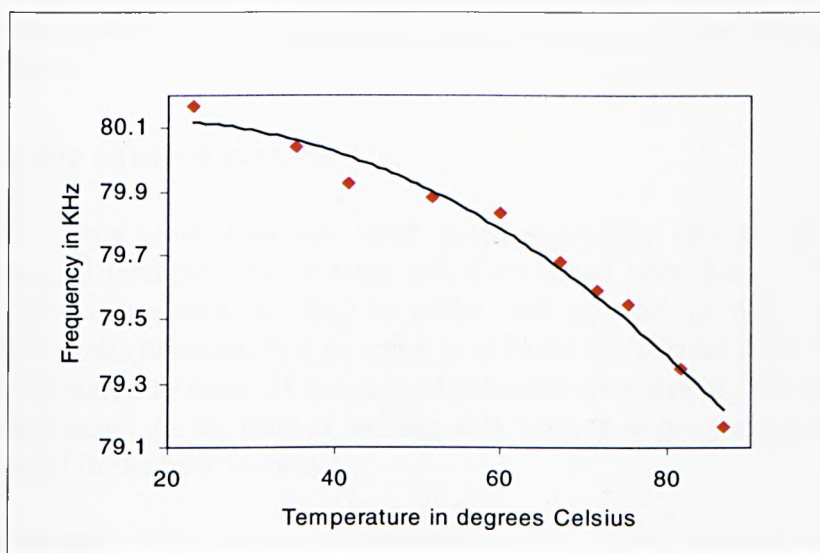


Figure 5. Variation of resonance frequency with temperature (radiation in air)

3. A new design approach for the frequency compensation

For optimum efficiency the frequency of the drive signal must be equal to the transducer resonance frequency. The new compensation scheme proposed to achieve this objective is schematically shown in Figure 6.

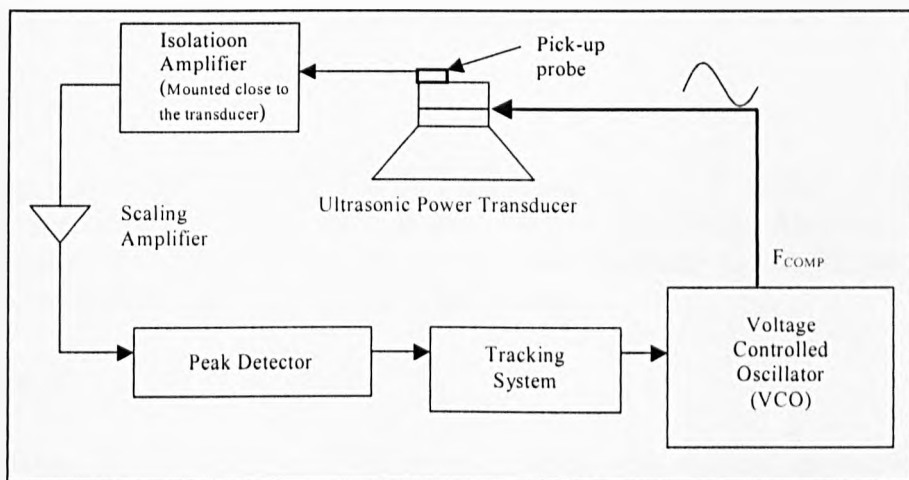


Figure 6. Block diagram of resonance frequency compensation system

The elemental wideband probe bonded to the power transducer detects the actual physical vibration. The probe will produce the maximum signal when the power transducer is driven at its resonance frequency. The output of the probe is appropriately scaled, rectified before the peak value is detected. The detected peak signal is then presented to a tracking system, whose function is to appropriately alter the input voltage presented to a voltage controlled oscillator (VCO) to change the output frequency until the power transducer produces its maximum output. A degree of frequency modulation (chirp) may also be introduced at this stage in one of many ways, for example by appropriately adjusting the delay within the system. The tracking system is designed to compare the present peak value with a previous peak while the system slightly drifts in and out of the resonance frequency at any temperature due to the induced frequency modulation. In this way both temperature compensation for optimal output and elimination of static nodes may be achieved.

4. Testing the control system

Components of the control system were tested separately and found to provide the necessary control features. The system was then tested open-loop and changes in the drive frequency in response to drop in probe pick up voltage was clearly observed. However, it became apparent that in order to achieve the correct close-loop behaviour, further modifications to some of the control elements (particularly the tracking system) would be necessary. At the time of writing, this work is in progress, which is expected to be completed in the near future.

5. Conclusions

It was found that the power transfer efficiency of ultrasonic sandwich transducers decreases considerably in a non-linear fashion with increase in temperature. Also it was

found that the resonance frequency drifts causing further profound reduction in power output, if the drive frequency was not adjusted to follow the drift. In order to address the latter aspect, a novel frequency control scheme has been proposed which is expected to be particularly useful in applications requiring transmission of ultrasound into confined spaces. Further tests and modifications to the system in order to evaluate its performance in practical applications is in progress.

Acknowledgements

The support extended by Prof. N. D. Deans and Dr. A. J. Miller of the school of Electronic and Electrical Eng. of the Robert Gordon University, Aberdeen, is gratefully acknowledged. Authors also wish to express their gratitude to Dr. Richard W. Keatch, UDD Ltd, for supporting this project at various stages.

References

1. M Martin, R Ceres, et al, 'Ultrasonic ranging gets thermal correction', *Sensor Review*, Vol 9, No 3, pp153-155, July 1989.
2. T Freire Bastos, J M Martin, et al, 'Ultrasonic signal variations caused by thermal disturbances', *Sensors and Actuators A*, Vol 44, No 2, pp 131-135, August 1994.
3. A Ramos-Fernandez, F Montoya-Vitini and J A Gallego-Juarez, 'Automatic system for dynamic control of resonance in high power and high Q ultrasonic transducers', *Ultrasonics*, Vol. 23, pp151-156, July 1985.
4. Jun-ichi Ishikawa, Yoko Mizutani, et al, 'High-Frequency Drive-Power and Frequency Control for Ultrasonic Transducer Operating at 3MHz', *IEEE Industry Applications Society*, 32nd Annual Meeting, New Orleans, Louisiana, U.S.A, October 5-9, pp 900-905, 1997.
5. Kiyoshi Ikeda, 'Ultrasonic Liquid-Concentration Sensor with Temperature Compensation, Proceedings of the 1998 IEEE International Frequency Control Symposium', Pasadena, CA, U.S.A, 27-29 May, pp 652-659, 1998.
6. G P P Gunarathne and R W Keach, 'Novel techniques for monitoring and enhancing dissolution of mineral deposits in petroleum pipelines', *Ultrasonics*, Vol. 34, pp 411-419, 1996.
7. R W Keatch and G P P Gunarathne, 'Novel techniques for quantification and enhancement of chemical dissolution of oil field mineral scale deposits', presented at the 8th International Symposium of oil field chemists, Gello, Norway, March 2-5, 1996.
8. Gunarathne G.P.P., Confidential laboratory and consultancy reports, 1994-1998.
9. G L Gooberman, *Ultrasonics: Theory and Application*, English Universities Press Ltd, pp 67-69, 1968.

Development of a Synthetic A-scan Technique for Ultrasonic Testing of Pipelines

G.P.P Gunaratne and Y.Qureshi
School of Engineering, The Robert Gordon University, Aberdeen, AB10 1FR, UK

Abstract - Multiple boundary echoes are often seen in ultrasonic testing of materials. Although these echoes can be a problem in many situations, they can also be used to advantage e.g. in identifying disbands of laminates or properties of materials beneath the test surface, such as scale deposits in pipelines. However, that requires echo comparison with signals from reference acoustic targets or templates. This is an exhaustive process, particularly when testing non-planar materials such as pipelines. In this paper, a new approach to synthesise reference signals using numerical modelling and computation is presented as an alternative method. The results of signal synthesis have been verified by experiment. Although the techniques described are specifically related to testing of pipelines, they can be extended to other general applications in Non-Destructive Testing of materials.

Keywords - ultrasonics, A-scan, NDT, scales

1. INTRODUCTION

Quantitative ultrasonic testing of targets often requires comparison of signal features with respect to standard reference samples, such as that given in the American Society for Testing of Materials (ASTM) [1]. For test objects with non-planar surface profiles, such as in pipelines, making standard reference samples to be used as acoustic templates is very difficult, since the object profiles and target dimensions are unlimited. A proposed solution to this problem is to artificially generate the acoustic signatures given the necessary parameters. In this regard, some work has been reported by Birchak and Serabian [2] where an empirical solution to pulse-echo ultrasonic inspection has been proposed. However, this solution caters for compensation of signal amplitude only, with an uncertainty of at least $\pm 2.5\text{dB}$. Also, it does not cater for changes to other important signal features, e.g. changes in the frequency domain. Hence this method is not applicable for high precision work where greater accuracy and fine details are required. The approach proposed in this work is to construct reference signals by a process of numerical computation using fundamental properties of acoustic waves and boundary transmission characteristics. Although the work described is mainly related to the inspection of petroleum pipelines for scale deposits, the underlying principles could be extended for general applications in Non-Destructive Testing (NDT) and measurement.

1.1 Petroleum pipeline scales

Predicting the location of scale deposits from exterior surface of pipelines using ultrasound measurements has been demonstrated previously [3]. Figure 1 shows a typical test configuration, where a transducer is placed on the top-side (outer surface) of a pipeline. The probe, once excited receives a series of multiple echoes of diminishing amplitudes due to reverberations of sound within the pipe-wall.

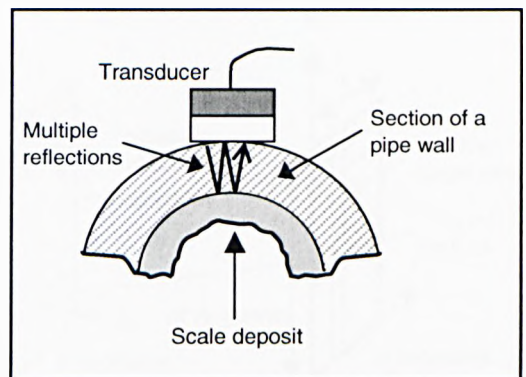


Figure 1: Top-side scale detection

The amplitude and frequency spectra of these multiple echoes generated within the pipe-wall of scaled pipes are compared with that of scale-free samples of the same dimensions. Figure 2(a) and (b) show an example of this, where the coefficients A-D refers to certain specific features of the signal.

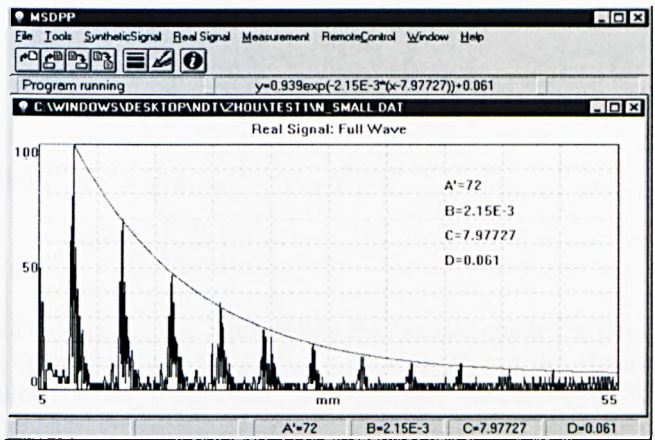


Figure 2(a): A-scan features of a clean pipe (B-decay coefficient)

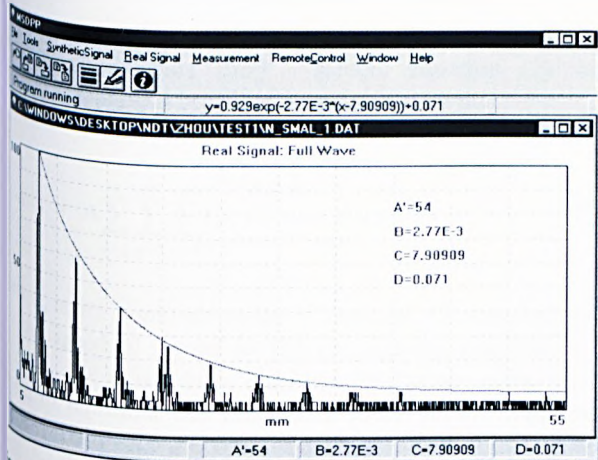


Figure 2(b): A-scan features of a pipe with a scale deposit forming beneath the pipe wall

However as stated before, it is practically impossible to obtain the reference scans for scale-free pipes in all cases, since tubings can be manufactured to any dimensions. Hence, the primary objective of this work was to artificially generate reference signals, given the pipe dimensions and other relevant parameters.

It has been previously shown that multiple reflections induced within a planar, layered material can be synthesised using boundary transmission and reflection coefficients for acoustic waves emitted by a probe at normal incidence [4]. However, in the present case the surfaces are cylindrical, and unlike in the case of planar surfaces, a flat-faced transducer produces a line contact along the diameter of the probe, with a variable couplant gap thickness at all other areas. Hence the above method can not be used. In order to overcome these problems a numerical model based on Huygens Green function [5] for synthesis of acoustic signals, taking into account the test object dimensions, has been proposed.

The process of signal synthesis involved two main steps: firstly to generate and validate the radiation pressure field of a transmitting transducer, and secondly to compute the received echoes after reflection from the target; in this case the cylindrical internal surface of the pipeline. This paper presents the work carried out and results obtained on the first of the above two main tasks, and synthesis of the 1st echo for a plane target. Extension of this work for cylindrical targets is in progress.

2. THEORY

Computation of radiation pressure field

A transducer of a finite size, where all points on its surface oscillate with the same amplitude and phase, can be considered as being composed of an infinite number of point sources (finite number of small sources in practice). The contribution of a small element of the transducer surface (Δs)

to the acoustic pressure P at a given point, for continuous emission, is given by Huygens Green function [5], such that

$$P = A \frac{\exp(-jkr)}{r} \Delta s \quad (1)$$

where: A is a constant

$k = 2\pi/\lambda$; λ is the wavelength in the medium

r = distance to the point from the elementary source

Figure 3 shows the geometry of a finite rectangular transducer of dimensions ($a \times b$), representing a matrix of ($n \times m$) elementary sources. The receiver (target) area is defined by the dimensions ($a_r \times b_r$), that represents a matrix of ($n_r \times m_r$) elementary receptors.

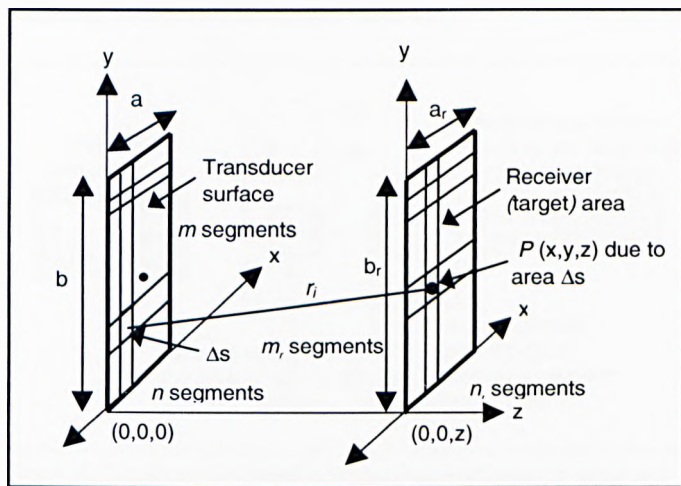


Figure 3: Geometry of a rectangular transducer with dimensions ($a \times b$) and elements ($n \times m$) and receiver area with dimensions ($a_r \times b_r$) giving ($n_r \times m_r$) elements

With reference to Fig 3, the pressure at point $P(x,y,z)$ due to continuous excitation at a single frequency can then be written as

$$P(x,y,z) = A \sum_{v=1}^{m_r} \sum_{u=1}^{n_r} \frac{\exp j(-\frac{2\pi}{\lambda} r_i)}{r_i} \Delta s \quad (2)$$

where: $r_i = \sqrt{(x - x_u)^2 + (y - y_v)^2 + z^2}$

$$\Delta s = \left(\frac{ab}{mn} \right)$$

and $u = 1, 2, 3 \dots n_r$, representing the element number in the x -direction and $v = 1, 2, 3 \dots m_r$, representing the element number in the y -direction. In the present case however, the excitation signal is a broadband pulse containing a spectrum of frequency components. Although the number of frequency components is infinite, it is known that a broadband pulse

could be represented by a limited number of dominant frequency components [6,7]. Hence, equation (2) was extended to represent broadband emission such that

$$P(x,y,z) = A \sum_{s=1}^w \sum_{v=1}^m \sum_{u=1}^n C_{s,v,u} \frac{\exp j(-\frac{2\pi f_s}{c} r_i)}{r_i} \Delta s \quad (3)$$

where $C_{s,v,u}$ is the amplitude of the s^{th} frequency component (f_s), c is the speed of sound in the propagating medium, $s = 1, 2, 3, 4, \dots, w$; w is a finite number of frequency components chosen to represent the broadband pulse in the frequency domain. To obtain the time domain pressure signal at any point in the transducer field, the Inverse Fast Fourier Transform (IFFT) was used, such that:

$$P_{(t)}(x,y,z) = (\text{IFFT} [P(x,y,z)]) \quad (4)$$

3.2. Determination of effective target area

It is known that transmitted signals spread-out in the medium due to diffraction. Therefore, when computing signals reflected back from a target, the effective target area must be known. Hence, the mathematical model represented by eq (3) and (4) was then extended, in such a way to obtain the total pulse pressure amplitude over gradually increasing target width, so that the effective target area could be determined, such that

$$P_{(t)}(x,y,z) = A \sum_{s=1}^w \sum_{q=1}^m \sum_{p=1}^n \sum_{v=1}^m \sum_{u=1}^n C_{s,q,p,v,u} \frac{\exp j(-\frac{2\pi f_s}{c} r_i)}{r_i} \Delta s \quad (5)$$

where $p = 1, 2, 3, \dots, n$, representing the element number in the x-direction and $q = 1, 2, 3, \dots, m$, representing the element number in the y-direction.

3.3. Computation of the 1st reflected echo - theoretical modelling

To compute the 1st reflected echo after reflection from a plane target, the reflector is now considered as a transmitter in the reverse direction. Hence if $P_R(x,y,z)$ is the pressure amplitude at the reflector, then the received pressure amplitude at the transmitting transducer after reflection from the target could be modelled as:

$$P_{T1}(x,y,z) = A \sum_{s=1}^w \sum_{v=1}^m \sum_{u=1}^n C_{s,v,u} |P_R(x,y,z)| \cdot R \cdot \left[\frac{\exp j(-\frac{2\pi f_s}{c} r_i + \phi)}{r_i} \right] \Delta s \quad (6)$$

where $R = (Z_1 - Z_2)/(Z_1 + Z_2)$ is the reflection coefficient at normal incidence, Z_1 and Z_2 are the acoustic impedances of the two media and $\phi = \angle P_R(x,y,z)$.

3. EXPERIMENTAL VERIFICATION OF THE MODEL: MEASUREMENT APPROACH

Figure 4 shows the practical measurement system used. A 5Mhz broadband circular probe was masked using a thin, acoustically non-transmissive substance to define a rectangular aperture (2mm x 12mm). This aperture size was chosen in order to limit the maximum wedge-gap to within 1/10th of the wavelength of sound for the maximum test surface curvature of interest. The masked transducer was then placed in oil ($c=1450$ m/s). Also, a small circular aperture was made on an identical transducer, again by masking, to form an elementary receiver.

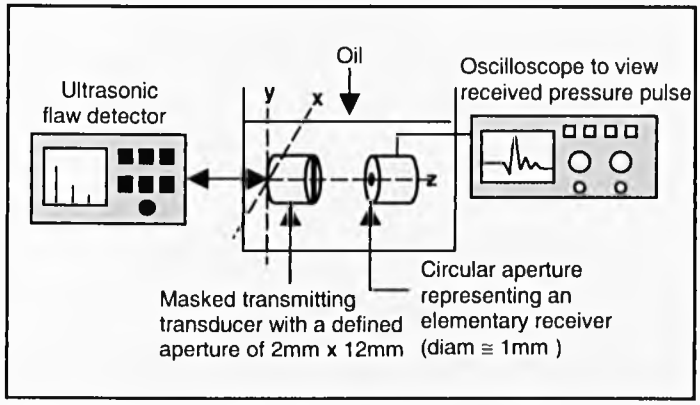


Figure 4: Practical measurement system for verification of simulated pressure field

It should be mentioned that an ideal source/receiver combination cannot be obtained in this way due to the finite size, masking thickness and bandwidth limitation of the receiver. However for observing general agreement of trends between theoretical predictions and practical measurements, this arrangement was found to be adequate.

The received signal by this point receiver was then examined at different co-ordinates in the transmitter field. The same set-up was used for estimating the effective target area, by replacing the circular aperture of the receiving transducer with a rectangular aperture, and then increasing the size of the aperture until no further significant increase in signal amplitude was observed. In this way the effective target area was estimated for comparison with that estimated by simulation.

Having obtained the effective target area, the next step was to measure the 1st received echo for validating the simulated response. Since the initial simulations were carried out with a plane reflector, a plane steel target was placed at a distance of 13mm in place of the above point receiver, and the received

4. RESULTS

4.1 Radiation field profile

Figure 5(a) and 5(b) show the computed signal for an experimental receptor area of the target on the central axis, and practical measurement for a target separation of $z = 13\text{mm}$. The general agreement of the simulated and practical measurement can be clearly seen from Figs 5(a) and 5(b).

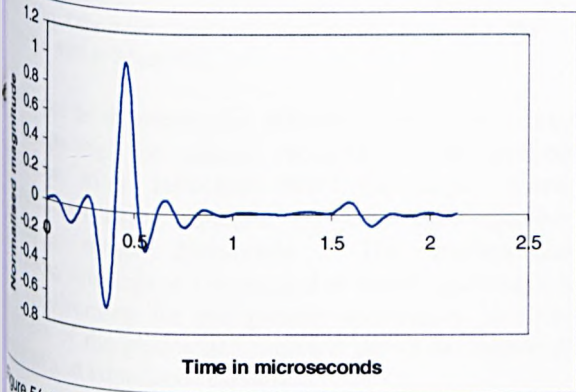


Figure 5(a): Simulated pulse received by a point receiver at centre using a 300 point IFFT



Figure 5(b): Results from practical measurement system
Vertical axis = 5mV/div Horizontal axis = 0.5µs/div

Experiments were then conducted to examine the general features of the pressure field, for example the sensitivity to co-ordinate changes. This was done by repeating the above measurements for a range of co-ordinates and also for small variations around fixed co-ordinates. An example of these measurements is shown in Figures 6(a) and 6(b). As can be seen the theoretical and practical results agree favourably.

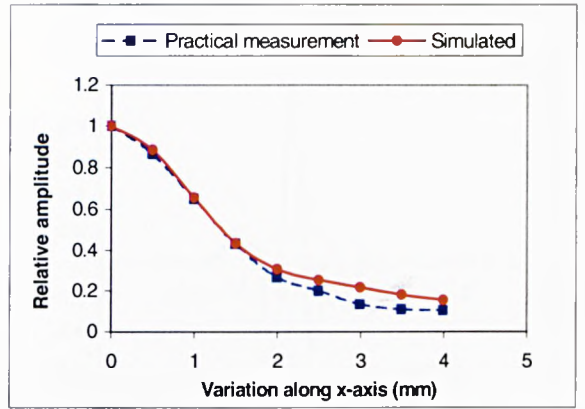


Figure 6(a): Pulse amplitude variation along x-axis. Starting co-ordinate (0,0,13mm)

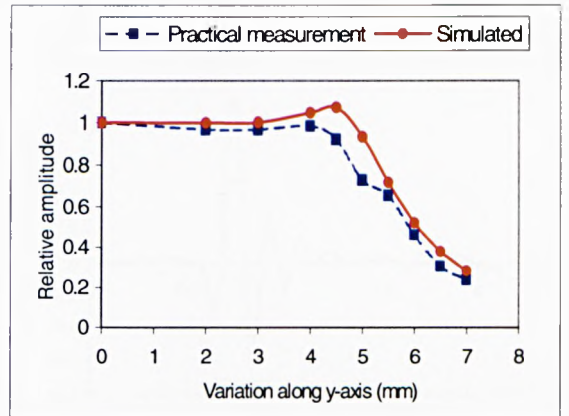


Figure 6(b): Pulse amplitude variation along y-axis. Starting co-ordinate (0,0,13mm)

4.2 Effective Reflector Area

Figures 7(a) and 7(b) show an example of the computed response and the actual received pulse at a distance of 13mm along the central axis when the point receiver was replaced by a target (receiver) area identical to that of the transmitter (2mm x 12mm). The agreement between the theoretical model and practical results can be clearly seen.

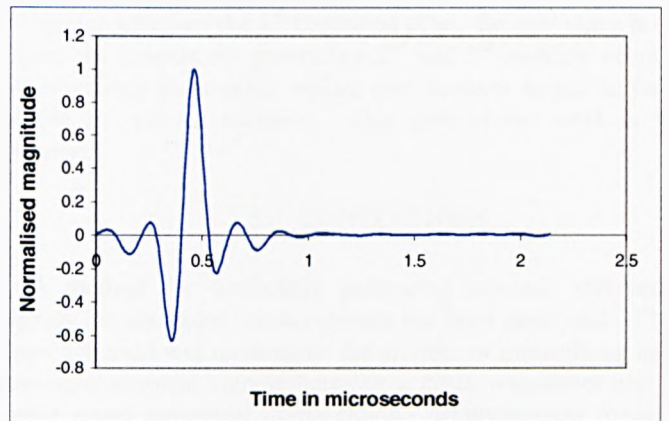


Figure 7(a): Simulated pulse using a 300 point IFFT



Figure 7(b): Observed pulse waveform Vertical axis = 0.1V/div
Horizontal axis = 0.5μs/div

In order to determine the effective target area as required for computing the signals received by the transmitting transducer after reflection from the target, numerical computations using equation (5) were then repeated for increasing target dimensions. The transmitter/target separation was kept at 15mm, as that would represent a worst case requirement for the present application in terms of thickness of the pipe-wall. Figure 8 shows the results of the practical and simulated responses.

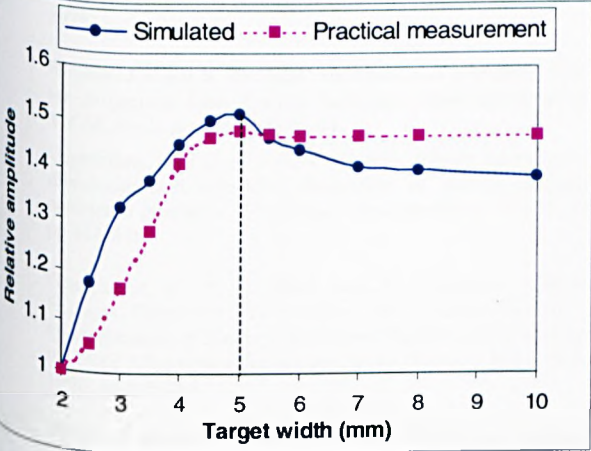


Figure 8: Variation of relative pulse amplitude with target width ($z = 15\text{mm}$)

As can be seen from above that there is little change in signal amplitude above 5mm target width. Therefore, for the present case, a reflector width of 5mm was considered to be adequate for the synthesis of reflected signals.

1st reflected echo from a planar reflector

Figures 9(a) and 9(b) show the results obtained from simulation and practical measurement.

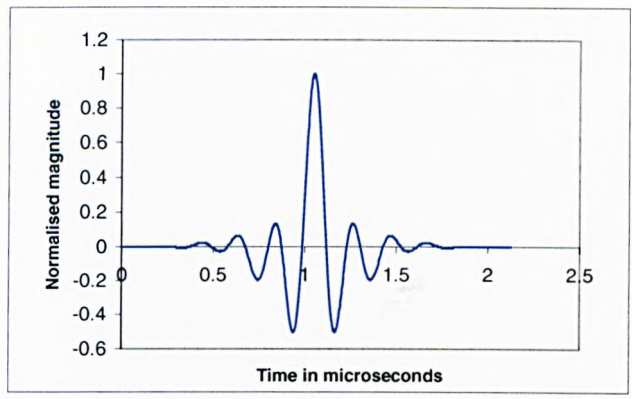


Figure 9(a): Simulated 1st echo after reflection from a plane target ($z = 13\text{mm}$)

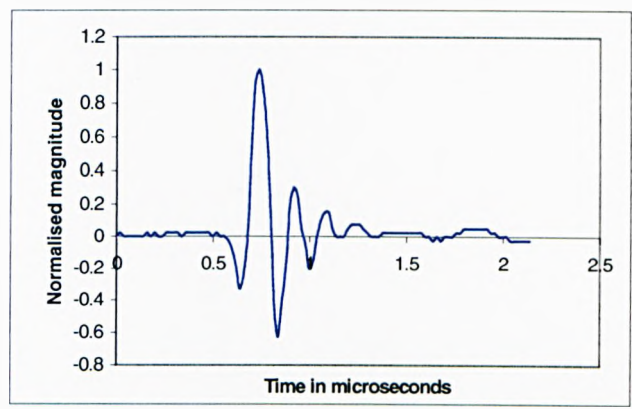


Figure 9(b): Practical measurement of 1st echo after reflection from a plane steel reflector in oil ($z = 13\text{mm}$)

Although the leading edge of the pulses are somewhat different, (perhaps due to non-idealities in both the experimental system and the theoretical modelling) the general agreement can be seen. Since the ultimate aim is to obtain relative 'peak' amplitudes between received multiple echoes rather than exact comparison of waveforms, it is considered that further improvement in terms of pulse shape was not necessary at this stage.

Having obtained the 1st computed echo, the next stage is to repeat the process for generating 2nd and 3rd multiple echoes by extending the model, taking into account target surface profile i.e. curved surfaces. This part of the work is in progress.

5. CONCLUSIONS

A method for artificially generating acoustic reference signals for ultrasonic measurements has been described. The approach used was to simulate the process of transmitting and receiving acoustic signals between a given transducer and a target using numerical computation. Mathematical models required for this purpose, representing the radiation pressure

field from a narrow rectangular transducer has been successfully developed and experimentally verified.

This model was further extended to compute the received signal amplitude by a plane reflector at a given location, to allow the determination of the effective reflector area as required for signal synthesis by computation. The 1st reflected echo was then modelled and generated. Based on the agreement of the results obtained between theoretical and practical investigations, it is expected that the final objective of generating the first three reference echoes for pipeline inspection would be completed in the near future.

ACKNOWLEDGEMENTS

The support extended by the School of Engineering at The Robert Gordon University, is gratefully appreciated. Special thanks are also due to the technical staff and in particular to Mr Martin Johnstone and Mr Bill Black for providing unserved support.

6. REFERENCES

ASTM Recommended Practices A388-71, A418-64(69), E114-74 and E164-74, *1975 Annual Book of ASTM standards*, Parts 4 and 11, Philadelphia: American Society of Testing and Materials, 1975.

Birchak, J.R and S. Serabian: 'Calibration of Ultrasonic Systems for Inspection from Curved Surfaces', *Materials Evaluation*, Vol.36, No.1, Jan 1978, pp.39-44.

Gunarathne, G.P.P and R.W Keatch: 'Novel techniques for monitoring and enhancing dissolution of mineral deposits in petroleum pipelines', *Ultrasonics Sonochemistry*, Vol.34, 1996, pp.411-419.

Gunarathne, G.P.P; Q. Zhou, and K. Christidis: 'Ultrasonic Feature Extraction Techniques for Characterisation and Quantification of Scales in Petroleum Pipelines', *Proceedings of the IEEE Ultrasonics Symposium*, Japan (Sendai), Vol.1, October 1998, pp.859-864.

Marini, J and J. Rivenez: 'Acoustical fields from rectangular ultrasonic transducers for non-destructive testing and medical diagnosis', *Ultrasonics*, No12, November 1974, pp.251-256.

El Amrani, et al: 'Numerical computation of the acoustic field passing through a plane interface: Application of new phased array transducers', *Ultrasonics International Conference Proceedings*, 1993, pp.197-200.

Christidis, K: 'Characterisation and monitoring of mineral deposits in down-hole petroleum pipelines', PhD Thesis, The Robert Gordon University, October 2000.

A Novel Technique for Dynamic Alignment of Ultrasonic Transducers in Real-time Non-destructive Testing

G.P.P Gunarathne and Y.Qureshi

School of Engineering, The Robert Gordon University, Aberdeen, AB10 1FR, UK

Abstract – Ultrasonic non-contact inspection methods require the correct alignment of test probes before return signals (echoes) are required. However, for critical remote applications, such as pipeline inspection, there are no accurate means of achieving this objective, and hence the accuracy and full potential of ultrasonic inspection is not realised. In this paper, a novel sensing technique to detect angular misalignment of a test probe with a view to ensure automatic alignment of the probe with the target is presented. The technique is based on analysing the waveform features of the received signals. In this regard, a theoretical formulation concerning the applicability of the method is first reported, followed by a detailed practical study. The technique could be employed for automatic alignment of the test probes in remote ultrasonic inspection.

Keywords – NDT, ultrasound, pipeline inspection

1. INTRODUCTION

An important requirement in quantitative ultrasonic testing is the correct alignment of test probes with respect to the target. For example, in bond testing or testing of laminates, the probe needs to be aligned normal to the surface of the test object so that the equations for normal boundary reflection coefficients could be applied [1]. Another very important application is in pipeline inspection, where the transducers are mounted on a 'pig' or at the end of a tool, which travels inside the pipeline. This requires constant alignment of the transducers if accurate assessment of the integrity of the pipe is to be made or to detect the presence of scale formation [2]. Large errors due to misalignment between transmitter and reflector are encountered in other applications such as ultrasonic ranging [3].

In localised test systems alignment may be carried out manually at the start of a test, but it is impossible in the case of remote applications such as in pipeline inspection. However, present inspection systems do not have reliable means of ensuring correct alignment of transducers and therefore the degree of certainty of test results are adversely affected.

This paper presents a study on the development of a novel technique for remote alignment of transducers by analysing the waveform features of the signals received by the test probe itself. Although specific reference has been made for the case of pipelines, the technique is applicable to general

inspection systems in ultrasonic Non-destructive Testing (NDT) which requires remote probe alignment.

2. PREVIOUS WORK

Pederson and Orofino [4,5] have modelled the effect of target angular mis-orientation on the spectrum of the received ultrasonic signals by deriving an Angle-dependent, Spectral Distortion (ASD) function. However the ASD function is transducer specific and the work published so far only deals with planar targets. For applications of pulse-echo measurements inside fluid-filled pipes, some work has also been reported by Stanke et al. [6] emphasising the effects of the amplitude changes of received waveforms due to transducer misalignment. However, this work only gives results for the lateral displacement of the transducer with respect to the pipe, and not on the radial angular misalignment along a given radial line.

3. PRESENT OBJECTIVES

In contrast to the methods described above, the emphasis of the present work is to develop a general sensing technique which can be applied to both planar and non-planar uniform targets. The work reported here is mainly based on a practical study since it was initially thought that generalised rules can be derived from such a study. However, it was found from this study that generalised rules to predict the suitability of test parameters, such as probe-target distance and probe aperture etc. which would give good sensitivity in detecting probe alignment can not be formulated in this way. Hence a theoretical approach was also developed to enable the assessment of suitability of test parameters without having to determine this by laborious practical measurements.

4. APPROACH

If a probe is aligned normal to a target, then the signals received should have the maximum amplitude compared to the case if the probe was not in normal alignment. Similarly, if the probe was scanned by a few degrees either side of the normal position, then it should not only give a drop in amplitude, but also the waveform shape should change as illustrated in Fig 1.

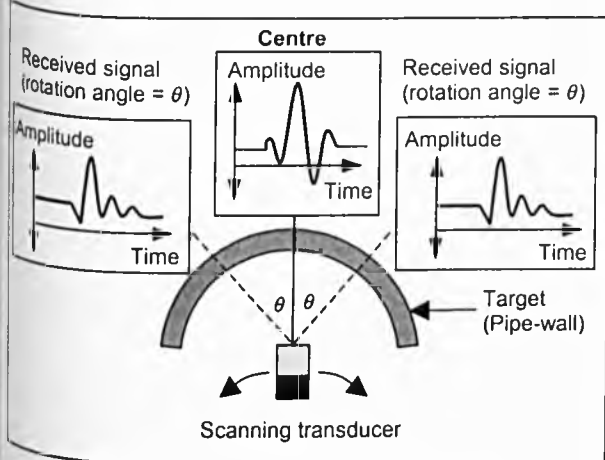


Fig. 1. Detecting angular misalignment of the probe

5.1 Basic modeling approach

The first step was to model the radiation field produced by the probe (strip-line transducer in this case) and hence obtain the pressure amplitude at the reflector using Huygens Green function [8]. Figure 2 shows the geometry of a finite rectangular transducer of dimensions ($a \times b$), representing a matrix of ($n \times m$) elementary sources. The receiver (target) area is defined by the dimensions ($a_r \times b_r$), that represents a matrix of ($n_r \times m_r$) elementary receptors.

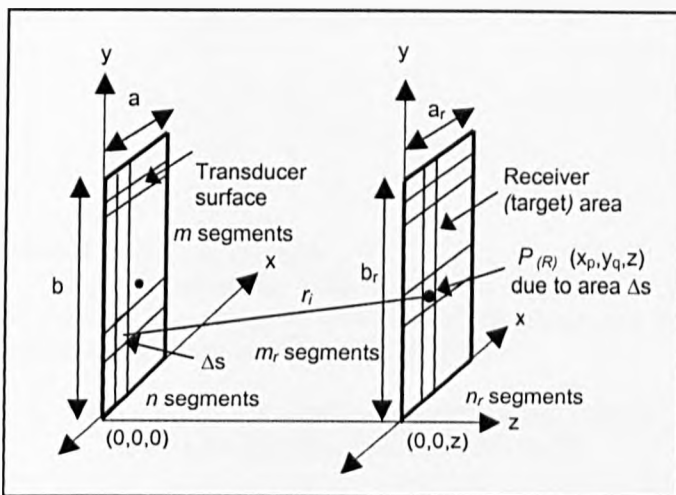


Fig.2. Geometry of a rectangular transducer with dimensions ($a \times b$) with elements ($n \times m$), and receiver area with dimensions ($a_r \times b_r$) giving ($n_r \times m_r$) elements.

For the case of a finite broadband pulse, it has been shown that the acoustic pressure spectrum $P_{s(R)}(x_p, y_q, z)$ at the point (x_p, y_q, z) on the target could be written as [7]

$$P_{s(R)}(x_p, y_q, z) = A \sum_{v=1}^m \sum_{u=1}^n C_s \frac{\exp j(-\frac{2\pi f_s}{c} r_i)}{r_i} \Delta s \quad (1.1)$$

where, A is a constant,

$k = 2\pi/\lambda$; λ is the acoustic wavelength in the medium,

$$r_i = \sqrt{(x_p - x_u)^2 + (y_q - y_v)^2 + z^2},$$

$\Delta s = \left(\frac{ab}{mn}\right)$ - surface area of an elementary source

and $u = 1, 2, 3 \dots n$, representing the element number in the x -direction and $v = 1, 2, 3 \dots m$, representing the element number in the y -direction on the transducer surface. Similarly $p = 1, 2, 3 \dots n_r$, represents the element number in the x -direction and $q = 1, 2, 3 \dots m_r$, representing the element number in the y -direction on the surface of the target. C_s is the amplitude of the s^{th} frequency component (f_s) of the emitted pulse and c is

Therefore, the two properties of interest are: optimal wave shape and maximum amplitude of signals. It can be understood that if the angular displacement about the central position is equal, as shown in Fig. 1., then the waveforms on either side would be identical. However, the amplitude of the signals will be less than that at the normal. It is found by experiment that the latter property is much easier and accurate to use in the present application, since amplitude changes are easier to monitor than waveshape changes.

However, to use this approach the detectable limits, i.e. the rotation angle that gives a detectable change in signal amplitude above noise levels, need to be known. In practice there are a number of factors that effect the detectable angular resolution such as probe aperture, pipe diameter, and probe/target separation. Hence the suitability of a particular combination of these parameters should be assessed before the technique could be applied to a given test situation.

One approach to determine this would be to carry out experimental measurements. The other approach is to develop a theoretical model that would predict the response for a given combination of parameters. Both approaches have been tried as detailed in the following sections.

THEORETICAL DETERMINATION OF ANGULAR RESOLUTION (AT NORMAL INCIDENCE)

In a previous publication we have developed a model for a 10 MHz strip-line broadband transducer that synthesises the multiple echoes generated in plane steel objects [7]. Due to its flexibility, this model was extended to compute the 1st received echo from a plane target in oil at normal and oblique incidence relative to the probe. The detectable angular resolution can be determined using this model, given the probe aperture and target dimensions. Although only plane targets were modeled here as an example, the approach can be easily extended to other shapes such as cylindrical targets.

speed of sound in the propagating medium ($s = 1, 2, 3, 4, \dots$), v is a finite number of frequency components chosen to represent the broadband pulse in the frequency domain)

To compute the 1st reflected echo from the plane reflector at normal incidence, the above process was repeated by considering the target as a transmitter in the reverse direction. Hence if $P_{s(R)}(x_p, y_q, z)$ is the pressure amplitude at a point at the reflector, then the total received pressure amplitude $P_{s(EI)}$ (1st echo) at the transmitting transducer after reflection from the target could be modeled as

$$P_{s(EI)} = A \sum_{v=1}^m \sum_{u=1}^n C_s \left| P_{s(R)}(x_p, y_q, z) \right| \cdot R \cdot \left[\frac{\exp - j \left(\frac{2\pi f_s}{c} r_i + \phi \right)}{r_i} \right] \Delta s \quad (1.2)$$

where $R = (Z_1 - Z_2)/(Z_1 + Z_2)$ is the reflection coefficient at normal incidence, Z_1 and Z_2 are the acoustic impedances of the two media and $\phi = \angle P_{s(R)}(x_p, y_q, z)$.

2. Modeling the effect of probe/target orientation

Having derived a mathematical model that would mathematically determine the reflected signal from the target, the next step was to model the effect of target/probe orientation as given below.

An angled, plane reflector can be considered as a projection of the normal plane with each of the elementary areas projected by an amount (δ_R) as shown in Fig. 3. below.

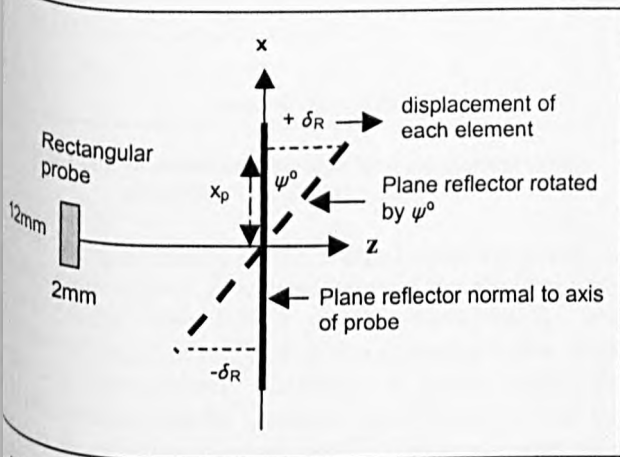


Fig. 3. Angular orientation of a plane reflector in the x-z plane

From Fig. 3. the projection distance δ_R due to a reflector at oblique incidence can be obtained such that

$$|\delta_R| = x_p \tan \psi^\circ \quad (1.3)$$

where, x_p is x-co-ordinate of the pth element (or point) along the x-axis, and ψ is the relative angular orientation of the reflector with respect to the probe.

Hence if $P_{s(R\psi)}(x_p, y_q, z)$ is the pressure amplitude at the point (x_p, y_q, z) at the reflector, then the 1st echo pressure amplitude $P_{s(EI\psi)}$ after reflection from the angled plane reflector can be expressed as

$$P_{s(EI\psi)} = A \sum_{v=1}^m \sum_{u=1}^n C_s \left| P_{s(R\psi)}[x_p, y_q, (z \pm \delta_R)] \right| \cdot R \cdot \left[\frac{\exp - j \left(\frac{2\pi f_s}{c} r_i + \phi_A \right)}{r_i} \right] \Delta s \quad (1.4)$$

where $\phi_A = \angle P_{s(R\psi)}(x_p, y_q, z)$.

Using this model the relative pressure amplitude as a function of the deviation from normal incidence can be obtained as demonstrated in the results section.

6. PRACTICAL EXAMINATION OF DETECTABLE ANGULAR RESOLUTION - APPROACH

The basic configuration used for the experimental investigation of the detectable limits of the transducer alignment is shown in Fig. 4. The reflector shown in Fig 4 represents a cylindrical section of a pipeline. The same arrangement was used for plane targets, except in this case the transducer was masked to define an aperture of 2mm x 12mm in order to be consistent with the theoretical model. A rotatable arm was used to adjust the angle of rotation of the 5MHz broadband transducer, immersed in oil, to an accuracy of within $\pm 0.5^\circ$. Pulse waveforms received by the flaw detector were transferred to a PC.

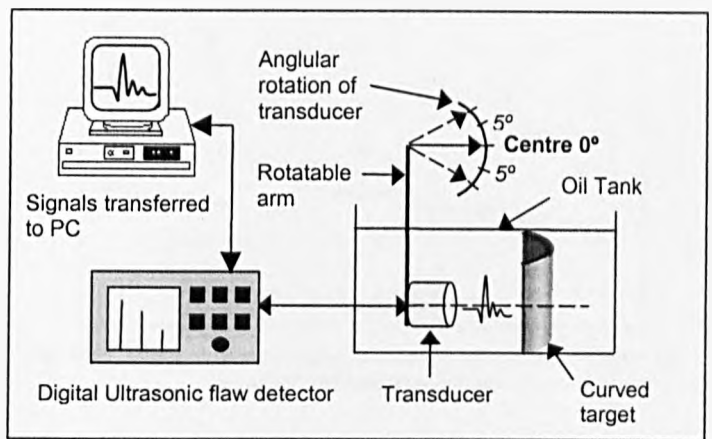


Fig.4. Experimental configuration to investigate detectable limits for transducer positional symmetry

In the case of cylindrical reflectors, the detectability of angular misalignment using the 1st received pulse was investigated for three diameters, and in each case for probe distances in the range of 6.5 to 20.5mm. For the targets the combination of test parameters included the range of probe/target distance and the angular displacement with respect to the target.

7. RESULTS

Verification of model

The 1st echo amplitude after reflection from a plane steel reflector was computed for various rotation angles at a probe distance $z = 6.5\text{mm}$ using eqⁿ (1.4) (This distance was used as previously pre-fixed for detection of scales in oil pipelines). The practical variation of the detectability was obtained using the measurement system of Fig 4, but with the circular probe replaced by the 2mm x 12mm rectangular probe obtained by masking the circular probe. Also, a plane steel reflector was used. The computed and practical results of the relative amplitude variation with probe rotation angles are shown in Fig. 5.

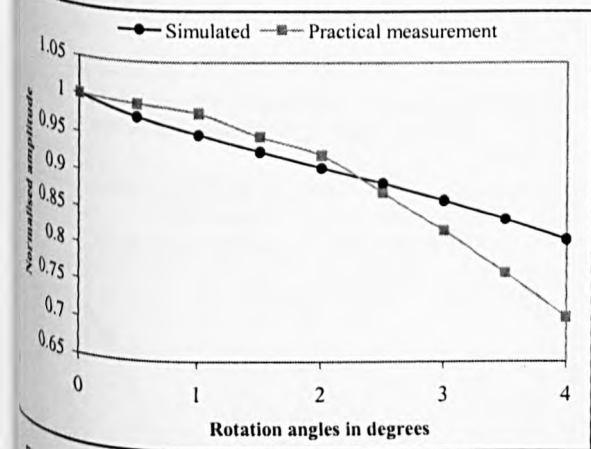


Fig. 5. Relative amplitude variations for a plane target in oil probe/target separation = 6.5mm

Given the non-ideality of the masked aperture, it can be seen that there is good agreement between the simulated and practical results within 0-3° of angular displacement. The maximum deviation of received echo amplitudes in this range is only 5% approximately. However at greater angles the deviation between results increases, most likely due to the variation in effective aperture width at oblique angles as a function of the finite thickness of the mask. In any case, for practical applications, detection of accuracy within 3° is well adequate. These results show that it is very much feasible to study the effect of probe angular movement with respect to

the target, to determine the suitability of a particular probe-target combination.

Having verified that a modelling approach could be used to determine the effect of probe/target misalignment, a practical study was then carried out to observe whether generalised rules with respect to test parameters such as probe aperture, probe/target separation and target curvature could be derived. The results of this study are given below.

7.2 Effect of curvature on the angular resolution

Figures 6(a) & (b) show results for the variation of echo amplitudes for three cylindrical reflectors of diameter 13.4, 11.6 and 8.8cm, and for a plane reflector respectively. The probe/target separation was kept at 6.5mm. The diameter of the probe used was 12.7mm and the probe frequency was 5MHz.

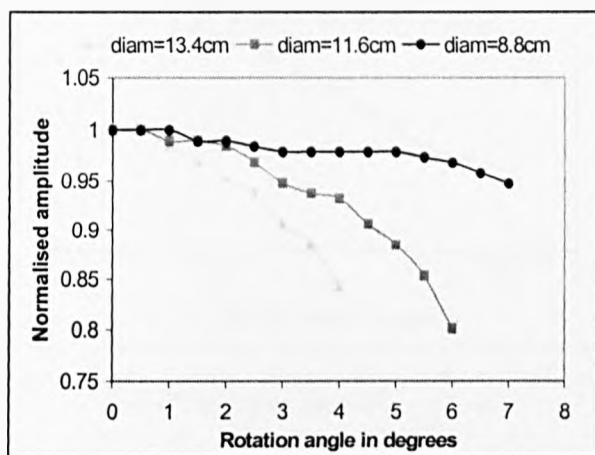


Fig. 6(a). Variation of echo signal amplitude for three cylindrical reflectors - target/probe separation = 6.5mm

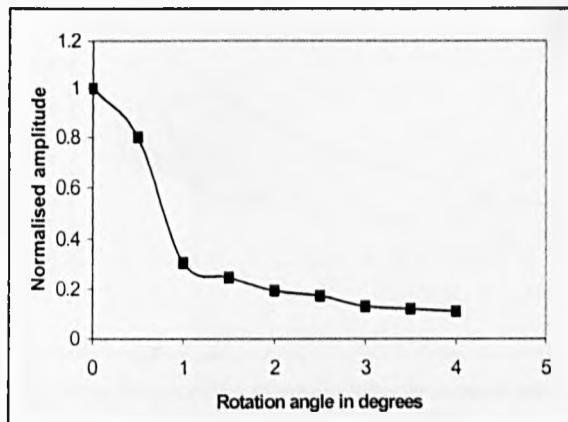


Fig. 6(b). Variation of echo signal amplitude for a plane reflector target/probe separation = 6.5mm

From Fig 6(a) it can be seen that the smallest resolvable angle for the 8.8cm diameter reflector is about 5.5°, while that for the 13.4cm diameter is less than 1°. The result therefore

in this case, the angular resolution increases with increase in target diameter. For the plane reflecting surface (diameter $\rightarrow \infty$) it is noticeable from Fig 6(b) that the angular resolution is even higher, being nearer 0.25° - a result consistent with observation from Fig 6(a).

Effect of probe/target distance on angular resolution

Figure 7(a) shows representative results for the angular resolution when using the cylindrical target with 11.6cm diameter, for various target/probe distances. Figure 7(b) shows the result for the case of the planar reflector.

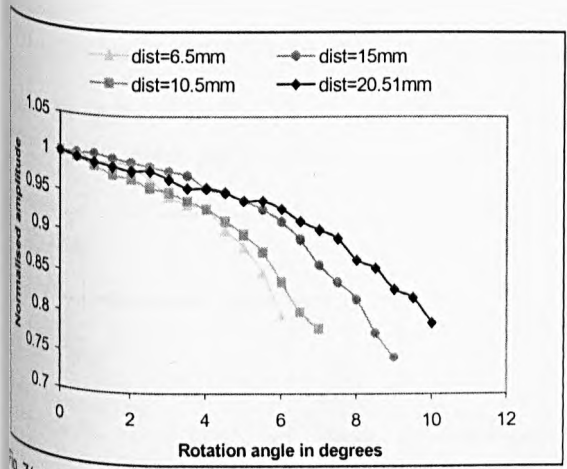


Fig 7(a). Variation of echo signal amplitude with distance for a cylindrical reflector of 11.6cm diameter

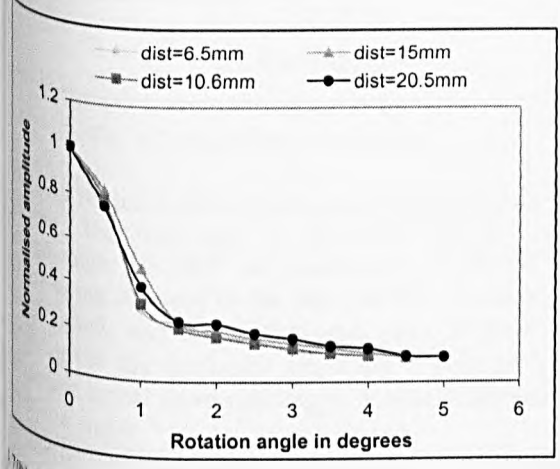


Fig 7(b). Variation of echo signal amplitude with distance for a plane reflector

From the above measurements it can be observed that as probe/target distance increases, the detectable angular resolution at normal incidence also increases for the 11.6cm cylindrical target. However, Fig. 7(b) shows that for a plane reflector, there is virtually no change in the angular resolution with distance within the above range. This

indicates that as the diameter increases the variation of angular resolution with distance diminishes.

7.4 Effect of probe aperture on angular resolution

Since there is the effect of focussing signals back to the probe aperture area in the case of cylindrical targets, the next step was to examine the effect of angular resolution on the size of the probe aperture. Sample results were obtained for angular resolution with the probe previously used (5MHz, 12.7mm aperture) and that for a smaller probe (5MHz, 7mm aperture). Figure 8(a) shows the results for an 8.8cm diameter target and Figure 8(b) shows that for a plane target.

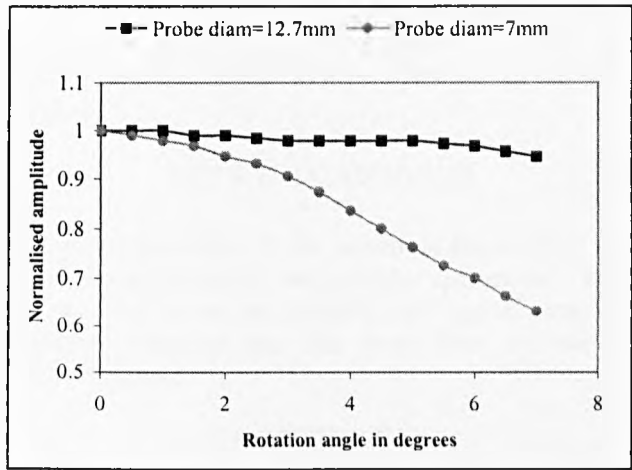


Fig. 8(a). Angular resolution measurements - reflector diameter = 8.8cm, target/probe separation = 6.5mm

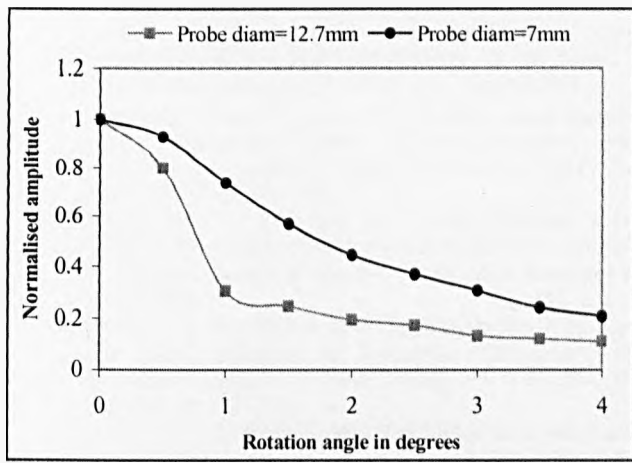


Fig. 8(b). Angular resolution measurements for a plane reflector - target/probe separation = 10.6mm

It can be observed from the above measurements that the sample results obtained for a small diameter target, as in Fig. 8(a), indicate that the use of a smaller probe aperture can give better detectability of probe alignment compared to that using a larger probe aperture, under the conditions specified.

areas for the plane target in Fig. 8(b), it is the opposite. Hence for the intermediate curvatures, it is not possible to know what would be the best option using a right set of rules. Thus, one of the general conclusions that can be derived from the above practical study is that the detectable angular resolution at normal incidence with respect to probe misalignment is a function of a number of variables including target diameter, probe diameter and probe/target separation. Hence, a modelling approach as demonstrated earlier in Section 5 would be very appropriate to determine in advance, whether a particular combination of parameters would yield good results.

PRACTICAL APPLICATION OF THE TECHNIQUE

Figure 9 shows a method under development for implementing the technique described.

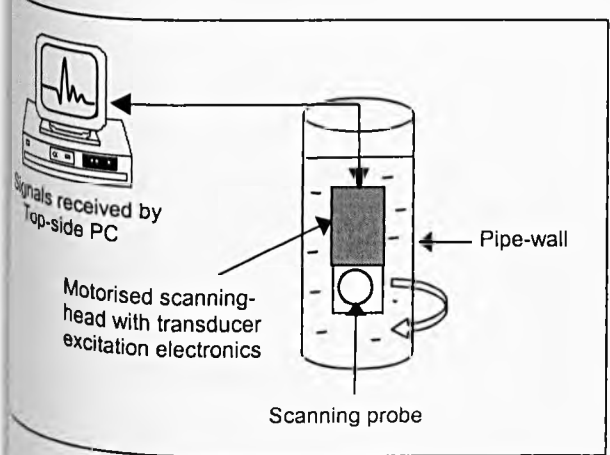


Fig. 9. Dynamic alignment of probe

According to this scheme, when an ultrasonic test is to be carried out, the transducer is scanned through a predetermined angle (or 360° as appropriate) while the echo signals are being received by the top-side PC. The computer processes the signals and detects the peak value of each. The signal that gives the maximum amplitude is selected as the ultrasonic signal corresponding to normal incidence with respect to the target.

An alternative approach to implement the proposed technique, particularly suitable in the case of pipeline testing using 'pigs' or tools, is to incorporate a microcontroller-based feedback control system. This would dynamically align the transducers as the 'pig' or tools advances through the pipeline during inspection. This work is in progress.

9. CONCLUSIONS

In remote ultrasonic NDT, an important aspect is the correct alignment of the transducers with respect to the

targets. In this regard, a new sensing technique based on examining the return echo amplitudes has been developed.

It was also found that the degree of detectability of misalignment is dependent on a number of parameters such as probe aperture, probe/target separation and target curvature. Therefore, prior to the technique being applied to a given test situation, the suitability of the combination of the above parameters should be ascertained. In this respect, a theoretical approach to pre-determine the degree of detectability of probe/target misalignment for a given combination of test parameters has also been developed and verified for the case of plane targets. Although the model was presently used for plane targets only, it could be readily extended to other cases, such as cylindrical targets.

The next stage of the work is to use this sensing technique for automatic alignment of the ultrasonic test probes using a motorised feedback control system. This part of the work is in progress.

ACKNOWLEDGEMENTS

The support extended by the School of Engineering at The Robert Gordon University, is gratefully appreciated. Special thanks are also due to the technical staff and in particular to Mr Martin Johnstone and Mr Steve Pirie for providing unreserved support.

REFERENCES

- [1] Birks, A.S and Green R.E Jr.: 'Nondestructive Testing Handbook - Second Edition', Volume 7: Ultrasonic Testing, American Society for Nondestructive Testing, ISBN 0-931403-04-9, 1991, pp. 48-50, p. 390
- [2] Christidis, K: 'Characterisation and monitoring of mineral deposits in down-hole petroleum pipelines', *D.Phil Thesis*, The Robert Gordon University, Aberdeen, UK, October 2000.
- [3] Lamancusa, J.S and Figueora, J.F: 'Ranging errors caused by angular misalignment between ultrasonic transducer pairs', *Journal of the Acoustical Society of America*, Vol.87, No.3 March 1990, pp. 1327-1335
- [4] Orofino, D.P and Pederson, P.C: 'Angle-dependant spectral distortion for an infinite planar fluid-fluid interface', *Journal of the Acoustical Society of America*, Vol.92, No.5, November 1992, pp.2883-2889.
- [5] Pederson, P.C and Orofino, D.P: 'Modeling of Received Signals from Finite Reflectors in Pulse-Echo Ultrasound', *IEEE Ultrasonics Symposium*, Cannes, France, Nov 1-4, 1994, Vol.2 Part2 of 3, pp.1177-1181
- [6] Stanke, F.E et al: 'Experimental verification of a mathematical model for internal ultrasonic inspection of pipes', *Journal of the Acoustical Society of America*, Vol.88, No.1, July 1990, pp.525-534.
- [7] Gunaratne, G.P.P and Qureshi, Y: 'Development of a Synthetic A-scan Technique for Ultrasonic Testing of Pipelines', *Proceedings of the IEEE Instrumentation & Measurement Technology Conference*, 21-23rd May 2002, Anchorage, AK, USA, Vol.1 pp.547-552.
- [8] Marini, J and J. Rivenez: 'Acoustical fields from rectangular ultrasonic transducers for non-destructive testing and medical diagnosis', *Ultrasonics*, No.12, November 1974, pp.251-256.

List of Key Symbols

Chapter 2

P	Pressure at a given point
r	distance from an elementary source to a given point
k	wave number
Δs	finite elementary source size
n	number of elementary sources on transducer x-axis
m	number of elementary sources on transducer y-axis
u	element number in transducer x-axis
v	element number in transducer y-axis
f_s	frequency components for broadband pulse excitation
C_s	amplitude of the s^{th} frequency component
w	finite number of dominant frequency components
c	speed of sound in medium
r_i	distance from an elementary source to a point on the target area
n_r	number of elementary receptors in target x-axis
m_r	number of elementary receptors in target y-axis
p	target element number in x-direction
q	target element number in y-direction
$P_s (R1)$	pressure distribution at the target

Chapter 3

$P_s (E1)$	1 st received echo by transducer
ϕ	phase angle of each element at the target
$P_s (R2)$	pressure distribution at target after reflection from probe
ϕ_{E1}	phase angle of $P_s (E1)$
$P_s (E2)$	2 nd received echo by transducer
ϕ_{R2}	phase angle of $P_s (R2)$
$P_s (R3)$	pressure distribution at target after 2 nd reflection from probe
ϕ_{E2}	phase angle of $P_s (E2)$
$P_s (E3)$	3 rd received echo by transducer
ϕ_{R3}	phase angle of $P_s (R3)$
δ_τ	projection distance of elementary areas for a curved reflector
$P_s (E1C)$	1 st received echo by transducer - curved target
α	attenuation coefficient
R_T	reflection coefficient at transducer boundary
B	coefficient of decay of A-scan signals

Chapter 4

δ_R	projection distance of elementary areas - oblique incidence reflector
ψ_s	angular rotation of plane reflector
$P_s (RIA)$	pressure distribution at an angled plane reflector
$P_s (EIA)$	1 st received echo by transducer - angled plane reflector
ϕ_A	phase angle of each element at an angled plane reflector

Chapter 5

λ	wavelength in medium
G	transducer conductance
B	transducer susceptance
D_a	unloaded circle diameter
D_L	loaded circle diameter
R_L	loss resistance
R_R	radiation resistance
η	transducer efficiency

Chapter 6

Z_M	geometric mean impedance
W_2	power output for matched transducer
W_1	power output for unmatched transducer
λ_S	wavelength in spindle
λ_W	wavelength in water
d_1	separation distance of disks

Chapter 7

λ	electrical wavelength
Z_T	cable terminating impedance
Z_S	cable input impedance
Z_O	cable characteristic impedance
$R(t)$	distributed resistance per unit length
$L(t)$	distributed inductance per unit length
$C(t)$	distributed capacitance per unit length
$G(t)$	distributed conductance per unit length
r_i	inner conductor radius
θ_L	loss angle
l_{inc}	incremental length of cable
P_o	power output
Z_{TT}	transducer impedance

Appendix A

Calculations and Discussions for Theoretical Models in Chapters 2 to 4

A.1: Selection of transmitting transducer width

When a flat contact transducer of diameter w , is placed on a convex specimen surface, a couplant gap is created as shown below in Figure A1.1.

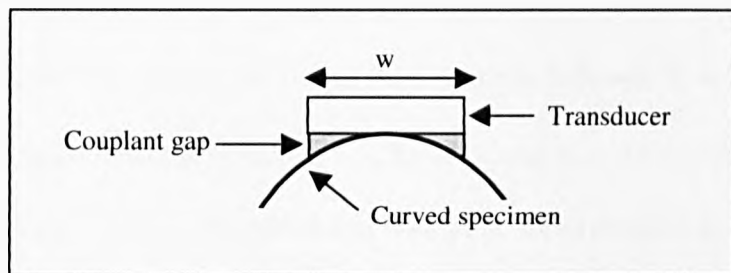


Figure A1.1: Flat transducer on a convex specimen surface

Previous work by Birchak and Serabian [35] has shown that the radius of curvature (specimen) which produces a couplant gap, that reduces the transmission at the transducer edge to half its transmission on a flat plate, is given by

$$R_C = 0.45 fw^2 Z_t / [v_c Z_c (1 + Z_t / Z_m)] \quad (A1.1)$$

where

f is the centre frequency of the transducer

v_c = velocity of sound in the coupling medium

Z_c = acoustic impedance of the couplant

Z_t = acoustic impedance of the transducer

Z_m = acoustic impedance of test specimen

Eqⁿ (A1.1) can be re-arranged to express the transducer width as a function of the curvature radius such that

$$w = \sqrt{\frac{R_C [v_c Z_c (1 + Z_t / Z_m)]}{0.45(fZ_t)}} \quad (\text{A1.2})$$

For the present case the parameters in eqⁿ A1.1 were as follows: $Z_t = 28$ Rayls, $Z_m = 47$ Rayls (acoustic impedance of steel), $Z_c = 1.3$ Rayls, and $v_c = 1450$ m/s. By substituting these values into eqⁿ (A1.2) the transducer width can be expressed as

$$w = \sqrt{\frac{R_C}{(4.189 \times 10^{-3})f}} \quad (\text{A1.3})$$

Eqⁿ (A1.3) was plotted for a range of curvature radiuses and for different transducer frequencies to select an appropriate width that would reduce the wedge effect. The results of this are shown in Figure A1.2.

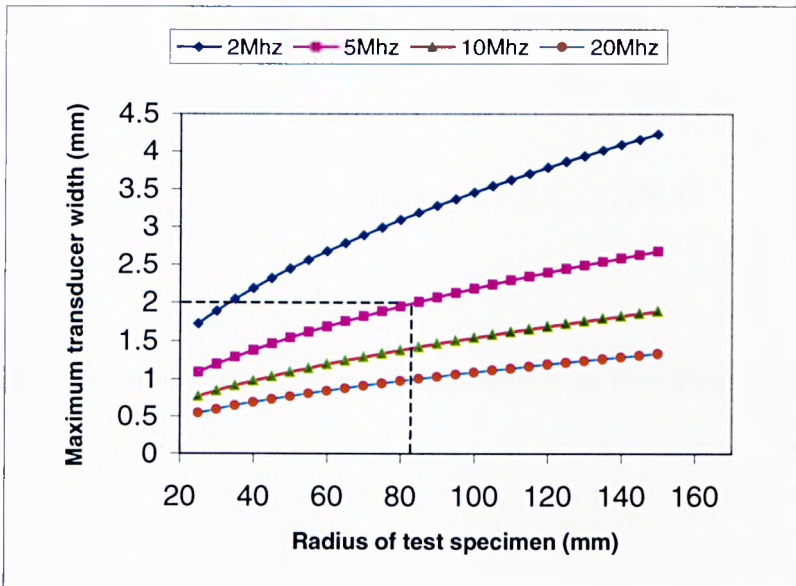


Figure A1.2: Variation of transducer width with convex test surface radius

For a 5Mhz transmitting transducer it can be seen from Figure A1.2 that a width of 2mm is appropriate for a curvature radius down to 85mm. This transducer width is therefore sufficient for the present investigation as the majority of pipe dimensions of interest are above this value.

A.2: Definition of Fourier Transforms

The Inverse Discrete Fourier Transform (IDFT) is readily obtainable from the Discrete Fourier Transform (DFT) with small modifications. This allows the time-domain signal to be obtained from the pressure frequency spectrum. Thus, if the N point DFT $F[n]$ of a signal $f[k]$ is defined as

$$F[n] = \sum_{k=0}^{N-1} f[k] e^{-j \frac{2\pi}{N} kn} \quad \text{for } n = 0, 1, 2, \dots, (N-1) \quad (\text{A2.1})$$

then the inverse DFT $f[k]$ is obtained from

$$f[k] = \frac{1}{N} \sum_{n=0}^{N-1} F[n] e^{j \frac{2\pi k}{N} n} \quad \text{for } k = 0, 1, 2, \dots, (N-1) \quad (\text{A2.2})$$

In MATLAB the above two functions are implemented as Fast Fourier Transforms i.e. FFT and IFFT.

A.3: Determining the Frequency Components for Broadband

Pulse Excitation

To obtain the frequency components as required for computation of the pressure distribution due to broadband pulse excitation using eqⁿ 2.4, a 5MHz transmission pulse was obtained by practical measurement [40]. This pulse is the actual signal received by a 5MHz broadband circular transducer after reflection from a plane aluminium reflector in oil. As the same transducer will be masked to produce a rectangle aperture, this transmission pulse could be used for the simulation without a significant error. The transmitted pulse is shown in Figure A3.2a.

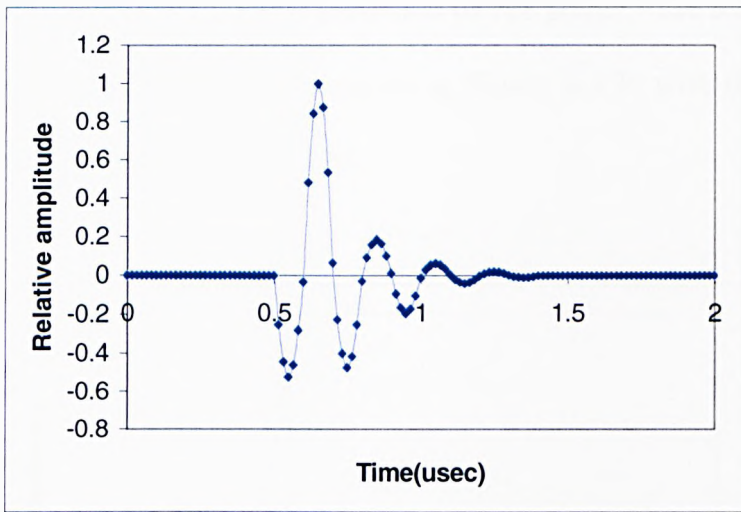


Figure A3.2a: 5MHz transmission pulse in time domain used for simulations

To obtain the frequency spectrum of this pulse a 128-point Fast Fourier Transform (FFT) was performed. The frequency spectrum produced is shown in Figure A3.2b.

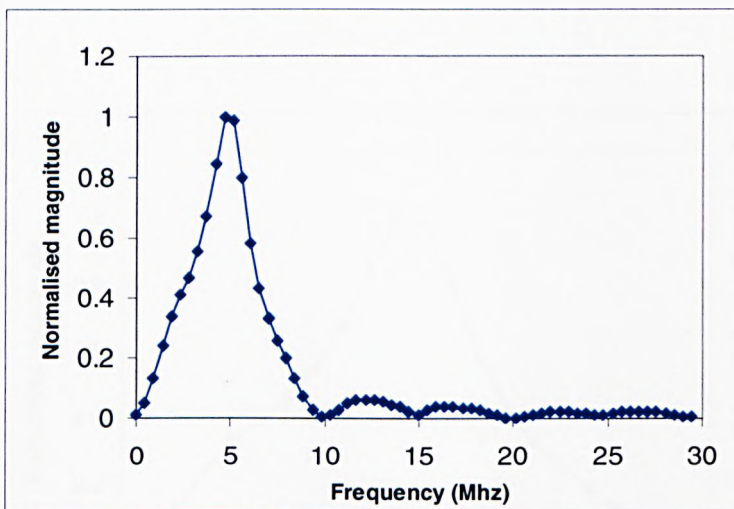


Figure A3.2b: 5MHz transmission pulse in frequency domain using a 128 point FFT

By taking the Inverse Fast Fourier Transform (IFFT) of the above frequency spectrum for gradual decrease in the number of samples, it was found that a minimum of 22 frequency components were sufficient to reconstruct the original time domain pulse (Fig A3.2a) without any significant loss of accuracy.

The IFFT itself was performed with a minimum of 128 points. The reconstructed pulse with the 22 frequency components is shown in Figure A3.2c with the corresponding frequency domain signal in Figure A3.2d.

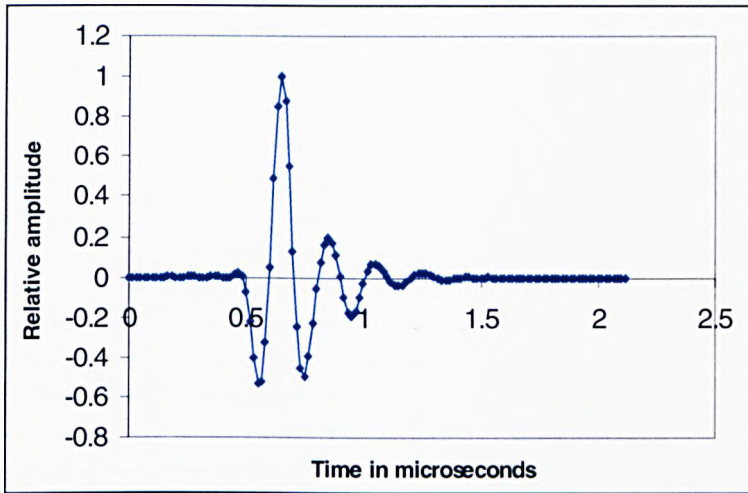


Figure A3.2c: Reconstructed time domain pulse with 22 frequency components using a 128-point IFFT

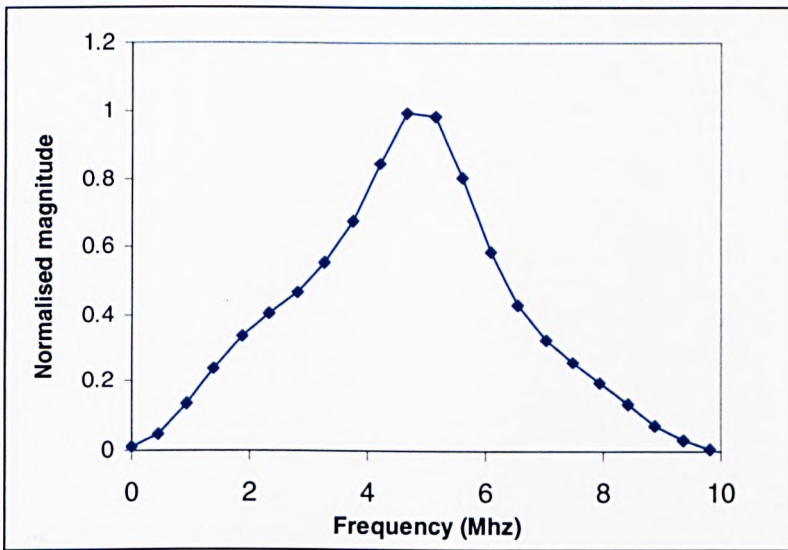


Figure A3.2d: Frequency spectrum of transmission pulse with 22 dominant frequency components

The actual values of the frequencies and corresponding magnitudes required for the simulations are shown in Table A3.1.

Table A3.1: Selected frequency components for broadband pulse excitation (5MHz)

Frequency (Mhz)	Normalised amplitude
0	0.0105
0.468	0.0478
0.936	0.1342
1.403	0.2388
1.871	0.3371
2.339	0.4066
2.807	0.468
3.275	0.5543
3.743	0.6734
4.21	0.8483
4.678	1
5.146	0.9877
5.614	0.8044
6.082	0.5855
6.549	0.4326
7.017	0.3298
7.485	0.2579
7.953	0.1995
8.421	0.1354
8.888	0.0748
9.356	0.029
9.824	0.0054

A.4: Discussion on Experimental Factors Effecting Theoretical and Practical Comparison of Radiation Pressure Field

1. Finite Receiver Size

In the model, the size of each receiving element (Δs) has dimensions equivalent to $<0.5\lambda$ approx. (0.125mm). However in the practical case it is extremely difficult to make a receiving element of this size. In fact, with the practical measurement system used a receiver element size of ~ 1 mm diameter was used. Hence, this could introduce a significant error, which may partly account for the difference in pulse shape.

2. Masking Thickness

Circular broadband transducers were masked to define the transmitting transducer aperture and the receiving element. The masking material used was polyethylene which had a thickness of ~ 1 mm (for adequate acoustic isolation but not excessively thick) on both transmitter and receiver. Particularly on the receiving element, reflections of sound energy can occur between the masked-aperture wall and transducer surface causing some distortion to the signals received.

Also at increasing angles, the projected aperture width is reduced due to the thickness of the mask, causing reduction in received amplitudes. This would likely to be the case for experimental results in the verification of models in Chapter 4.

3. Alignment Difficulties

In the experimental configuration of Figure 6 (Chapter 2), the position of the receiver transducer is fixed, and only the position of the transmitting transducer was variable in x, y and z-axes using vernier adjustments. This set-up lacked accurate angular orientation and hence accurate alignment was never achieved. In addition, due to non-idealities (1) and (2) explained previously, the process of alignment was difficult due to effects of signal distortion.

4. Attenuation Considerations

The intensity of an acoustic wave (P_x) after travelling a distance x, in an attenuating medium can be represented by

$$P_x = P_i \exp(-\alpha x) \quad (\text{A4.1})$$

where, P_i is the pressure amplitude at an initial distance and α is the attenuation coefficient in nepers/m (Np/m).

An expression for the attenuation coefficient can be obtained in Np/m or dB/m as follows

$$\alpha = \frac{1}{x} \ln \left(\frac{P_i}{P_x} \right) \text{Np} \quad (\text{A4.2})$$

$$\alpha = \frac{1}{x} 20 \log_{10} \left(\frac{P_i}{P_x} \right) \text{ dB.} \quad (\text{A4.3})$$

4.1 Practical Measurement of Attenuation Coefficient for the Present Work

Attenuation is also frequency dependent since the broadband excitation pulse has a range of frequencies. Ideally the effect on each component should be introduced into the model. However, this is tedious since different coefficients need to be firstly determined - e.g. by experiment, although coding would not be a significant problem. Therefore it was decided that an average (or gross) value for a given pulse waveform would be used. This was first obtained from published tables [41] and also confirmed by practical measurements (42 Np/m in oil).

A.5: Calculation of B-coefficients from Relative Echo Amplitudes

From the simulated and practical relative echo amplitudes the decay coefficient, B is calculated using the following two equations

$$y_2 = \exp^{(Bx)} \quad (\text{A5.1})$$

$$y_3 = \exp^{(B.2x)} \quad (\text{A5.2})$$

where y_2 and y_3 are the relative values of the 2nd and 3rd echoes respectively and x is the distance between transducer and reflector. For the present study the average value of the B-coefficient was used from the above two equations.

Appendix B

MATLAB Software Code and Program Structures

B.1: Computation of Radiation Pressure Field from a Rectangular Transducer - Broadband Pulse Excitation

```
/******  
*                                                                 *  
*      School of Engineering                                     *  
*                                                                 *  
*      The Robert Gordon University, Aberdeen                 *  
*                                                                 *  
*****  
*                                                                 *  
*      File name: strip1pf.m                                   *  
*      Author:   Yasser Qureshi                               *  
*      Created:  21/1/02                                       *  
*      Chapter:   2                                           *  
*                                                                 *  
*****  
*                                                                 *  
* Description: This program cycles through the 22 selected frequency components for *  
*              broadband excitation. It calls the program strip1atn.m for every frequency *  
*              compute the pressure pulse at a point P in the transducer field. It should be *  
*              mentioned that this program is common to all subsequent programs for *  
*              computing pressures, with the only change the program being called. *  
*              The following program codes could be improved by using vectors instead *  
*              of explicit loops, and by avoiding passing global variables in all the programs *  
*                                                                 *  
*****/  
clear all  
  
for i=1:22      % 22 frequency components from 5MHz broadband disc transducer  
i  
if i==1        % main loop counter  
f=0;          % frequency in Hz  
cnm=0.0105;   % normalised amplitude of each frequency component  
  
elseif i==2  
f=468000;  
cnm=0.0478;  
  
elseif i==3  
f=936000;  
cnm=0.1342;  
  
elseif i==4  
f=1403000;  
cnm=0.2388;
```

```
elseif i==5  
f=1871000;  
cnm=0.3371;
```

```
elseif i==6  
f=2339000;  
cnm=0.4066;
```

```
elseif i==7  
f=2807000;  
cnm=0.468;
```

```
elseif i==8  
f=3275000;  
cnm=0.5543;
```

```
elseif i==9  
f=3743000;  
cnm=0.6734;
```

```
elseif i==10  
f=4210000;  
cnm=0.8483;
```

```
elseif i==11  
f=4678000;  
cnm=1;
```

```
elseif i==12  
f=5146000;  
cnm=0.9877;
```

```
elseif i==13  
f=5614000;  
cnm=0.8044;
```

```
elseif i==14  
f=6082000;  
cnm=0.5855;
```

```
elseif i==15  
f=6549000;  
cnm=0.4326;
```

```
elseif i==16  
f=7017000;  
cnm=0.3298;
```

```
elseif i==17  
f=7485000;  
cnm=0.2579;
```

```
elseif i==18  
f=7953000;  
cnm=0.1995;
```

```
elseif i==19  
f=8421000;  
cnm=0.1354;
```

```

elseif i==20
    f=8888000;
    cnm=0.0748;

elseif i==21
    f=9356000;
    cnm=0.029;

elseif i==22
    f=9824000;
    cnm=0.0054;

end

strip1an; % calls program to calculate pressure field at a point P

press_freq(i)=final_pressure; % stores total pressure at point P in an array
end

% manipulate data for IFFT

press_all=flipud(rot90(press_freq))
save c:/matsim/bin/top_sims/any_press_all % saves pressure in file

inverse=ifft(press_all,300); % 300 point IFFT
load time3; % loads a 300 point time axis
plot(t_axis300,real(inverse),'k-') % plots real part of IFFT with time
xlabel('Time in microseconds'); % axes labels
ylabel('Real part of IFFT');
title(' Pressure at centre Z=9.6mm ');
maximum=max(real(inverse)) % finds peak value of pulse
minimum=min(real(inverse))
peak=maximum-minimum

/*****
*
* School of Engineering
*
* The Robert Gordon University, Aberdeen
*
*****/
*
* File name: strip1an.m
* Author: Yasser Qureshi
* Created: 21/1/02
* Chapter: 2
*
*****/
*
* Description: Computes the pressure field at a point P in the transducer field (medium is
* oil) - with added attenuation correction
*
*****/

a=2*10^(-3); % Transducer width-2mm
b=12*10^(-3); % Transducer length-12mm

```

```

n=15; % number of elements in x-axis
m=85; % number of elements in y-axis

ds=(a*b)/(m*n); % area of each element

f % frequency
cnm % amplitude of each component

lamda=1450/f; % c=1450 m/s for 5Mhz Transducer- transmitting in OIL
k=(2*pi)/lamda; % wave number
alpha=42.02; % atten coeff. Np/m

%Starting point Co-ordinate values w.r.t transducer origin
xu=0; % x-value
yv=0; % y-value

%Co-ordinates of a point P in the transducer field (eg. an edge/centre)
xp=((0.5*a)); % at centre of transducer
yq=((0.5*b));

z=10*10^(-3) % distance to reflector

vcount=1; % display counter
pxyz=0; % initialize pressure variable
for v=1:1:m % main loop along y-axis
    vcount;
    yv;

    for u=1:1:n % inner loop along x-axis
        xu;
        rpt1=((xp-xu)^2);
        rpt2=((yq-yv)^2);
        r=sqrt(rpt1+rpt2+(z^2)); % distance from transducer to point P

        p1=exp(-(j*k*r));
        p2=p1/r;
        p_new=(p2*ds); % pressure for each element ds
        p_atn=exp(-alpha*r); % attenuation effect
        p_pract=(p_new*p_atn); % pressure due to attenuation
        pxyz=p_pract+pxyz; % totalling pressure from previous elements

        xu=xu+(a/n); % increments along x-axis of transducer
    end % end of inner loop along x-axis

    xu=0; % reset to start of n elements on transducer x-axis
    yv=yv+(b/m); % moves to next row up (along y-axis) of m elements

    vcount=vcount+1; % counter for main loop
end % end of main loop along y-axis

% cnm=normalised frequency amplitude
final_pressure=(pxyz*cnm) % total pressure value at point P

```

B.2: Computation of Radiation Pressure Amplitude to Determine the Effective Target Area

```
/*
*
*      School of Engineering
*
*      The Robert Gordon University, Aberdeen
*
*****
*
*      File name:  striplpf.m
*      Author:    Yasser Qureshi
*      Created:   10/2/02
*      Chapter:   2
*
*****
*
* Description:   This program cycles through the 22 selected frequency components for
*                computing the pressure amplitude at the reflector. Calls stripref.m
*
*****/
```

```
clear all
```

```
for i=1:22      % 22 frequency components from 5MHz broadband disc transducer
```

```
i
```

```
if i==1        % loop counter
f=0;           % frequency
cnm=0.0105;    % normalised amplitude
```

```
elseif i==2
f=468000;
cnm=0.0478;
```

```
elseif i==3
f=936000;
cnm=0.1342;
```

```
elseif i==4
f=1403000;
cnm=0.2388;
```

```
elseif i==5
f=1871000;
cnm=0.3371;
```

```
elseif i==6
f=2339000;
cnm=0.4066;
```

```
elseif i==7
f=2807000;
cnm=0.468;
```

```
elseif i==8
f=3275000;
cnm=0.5543;

elseif i==9
f=3743000;
cnm=0.6734;

elseif i==10
f=4210000;
cnm=0.8483;

elseif i==11
f=4678000;
cnm=1;

elseif i==12
f=5146000;
cnm=0.9877;

elseif i==13
f=5614000;
cnm=0.8044;

elseif i==14
f=6082000;
cnm=0.5855;

elseif i==15
f=6549000;
cnm=0.4326;

elseif i==16
f=7017000;
cnm=0.3298;

elseif i==17
f=7485000;
cnm=0.2579;

elseif i==18
f=7953000;
cnm=0.1995;

elseif i==19
f=8421000;
cnm=0.1354;

elseif i==20
f=8888000;
cnm=0.0748;

elseif i==21
f=9356000;
cnm=0.029;

elseif i==22
f=9824000;
cnm=0.0054;
```

```

end

stripref; % calls program to compute pressure over a defined reflector area

press_freq(i)=press_total; % stores total pressure at reflector in an array
end

% manipulate data for IFFT

press_all=flipud(rot90(press_freq))
save c:/matsim/bin/refw10mm press_all % saves pressure in a file

inverse=ifft(press_all,300); % 300 point IFFT

load time3; % loads a 300 point time axis
plot(t_axis300,real(inverse),'k-') % plots real part of IFFT with time
xlabel('Time in microseconds'); % axes labels
ylabel('Real part of IFFT');
title(' Pressure received by a plane reflector at Z=13mm');
maximum=max(real(inverse)) % peak value of pulse
minimum=min(real(inverse))
peak=maximum-minimum

/*****
*
* School of Engineering
*
* The Robert Gordon University, Aberdeen
*
*****/
*
* File name: stripref.m
* Author: Yasser Qureshi
* Created: 28/1/02
* Chapter: 2
*****/
*
* Description: This program defines a target width and controls the xp and yq increment -
* the x and y co-ordinates in the reflector plane. The pressure at the effective
* reflector is then computed by calling strip1trf.m.
*****/

rw=5*10^(-3); % variable reflector area width-5mm
rl=12*10^(-3); % Reflector area length

nr=38; % increased number of elements in x-axis of reflector
mr=85; % number of elements in y-axis of reflector

xp=-0.0015; % xp co-ordinates of starting point at the reflector (w=5mm)
yq=0; % yq co-ordinates of starting point at the reflector
z=15*10^(-3); % distance to reflector

press_total=0; % initialise pressure variable - total pressure at reflector

for q=1:1:mr % main loop along y-axis of reflector
q
for p=1:1:nr % inner loop along x-axis of reflector

```

```

q
p
strip1trf          % calls program to calculate pressure at a point (xp,yq,z)
xp=xp+(rw/nr);    % increments xp along reflector x-axis
end                % end of inner loop along x-axis

xp=-0.0015;       % resets xp co-ordinate at end of array
yq=yq+(rl/mr);   % increments yq along reflector y-axis

end                % end of main loop along y-axis

press_total        % total pressure at reflector

/*****
*
*          School of Engineering
*
*          The Robert Gordon University, Aberdeen
*
*****
*
*          File name:  strip1trf.m
*          Author:    Yasser Qureshi
*          Created:   21/1/02
*          Chapter:   2
*
*****
*
* Description:  Computes the pressure amplitude over a given reflector area
*
*****/

a=2*10^(-3);      % Transducer width-2mm
b=12*10^(-3);     % Transducer length-12mm

n=15;             % number of elements in x-axis
m=85;            % number of elements in y-axis

ds=(a*b)/(m*n);  % area of each element

f                % frequency
cnm              % normalised amplitude

lamda=1450/f;    % 5MHz Transducer- transmitting in OIL
k=(2*pi)/lamda; % wave number

%Starting point Co-ordinate values w.r.t transducer

xu=0;            %x-value
yv=0;            % y-value

vcount=1;        % display counter
pxyz=0;          % initialise pressure
for v=1:1:m       % main loop along y-axis
vcount;
yv;

```

```

for u=1:1:n                % inner loop along x-axis
    xu;
    rpt1=((xp-xu)^2);
    rpt2=((yq-yv)^2);
    r=sqrt(rpt1+rpt2+(z^2)); % distance from transducer to a point P

    p1=exp(-(j*k*r));
    p2=p1/r;
    p_new=(p2*ds);        % pressure for each element ds

    % p_atn=exp(-alpha*r); % attenuation effect
    %p_pract=(p_new*p_atn); % pressure due to attenuation
    %pxyz=p_pract+pxyz;   % totalling pressure from previous elements

    pxyz=p_new+pxyz;     % totalling pressure from previous elements

    xu=xu+(a/n);        % increments along x-axis

end                        % end of inner loop along x-axis

xu=0;                    % reset to start of n elements on transducer
yv=yv+(b/m);            % moves to next row up (along y-axis) of m elements

vcount=vcount+1;       % counter for main loop
end                      % end of main loop along y-axis

%cnm=normalised frequency amplitude
final_pressure=pxyz*cnm; % total pressure value from all transmitting elements

press_total=final_pressure+press_total % running total of pressures at reflector

```

B.3: Program Structure for Computing the 1st, 2nd and 3rd, Reflected Echoes

This section details the MATLAB M-files program structure for computing the reflected echoes. For every reflected echo there is a total of four M-files that are used: a main program calling three other M-files. To reduce the computation time the pressure distribution on the transmitter/receiver areas was calculated using the symmetrical nature of the surfaces. This therefore required calculation for only a quarter of the effective areas.

System block diagrams showing the operation of these programs are now discussed in the following sections with **sample** programs in section B.4.

It should be mentioned that the programs listed for computing the multiple echoes are only for propagation into steel. The same programs were used for propagation into oil but with changes to the medium velocity and attenuation figure.

1st reflected echo from a plane target

M-files: *freqs1.m, cntrl1.m, recvrst.m, echo1qst.m*

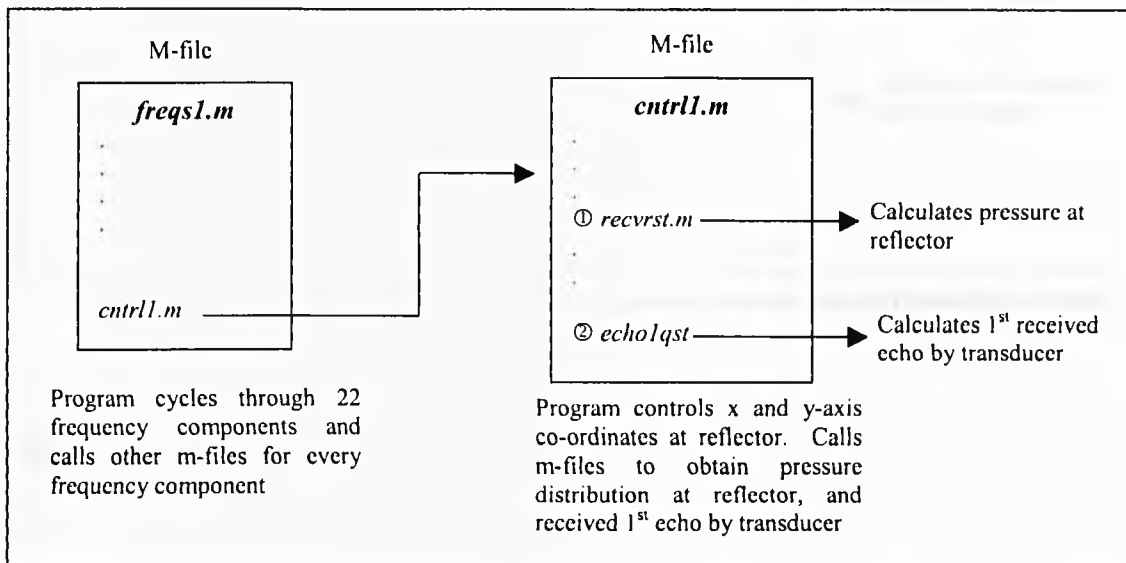


Figure B3.1: Program calls for 1st echo computation

2nd reflected echo from a plane target

To compute the 2nd reflected echo it is firstly required to re-calculate the 1st echo pressure distribution at the transmitter, with the width $w = 7\text{mm}$.

The pressure distributions (at each frequency) at the transmitter due to this effective area are stored in a file. The 2nd reflected echo is then calculated from an *effective* reflector area width of 10mm.

Step 1: Calculation of 1st echo received by a transducer width of 7mm

M-files: *freqs1.m, cntrl1a.m, recvr1st.m, echo1wqst.m*

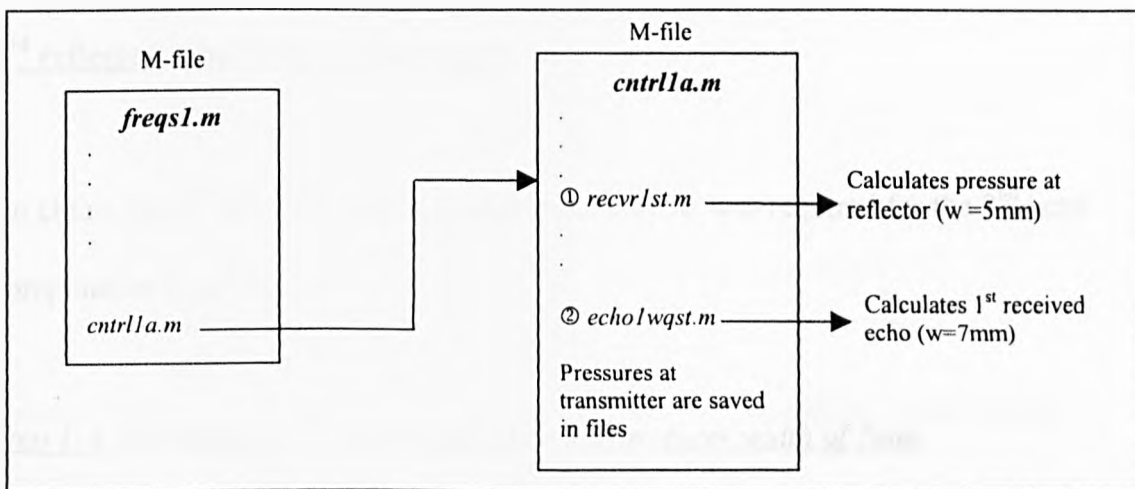


Figure B3.2: Program calls for 1st echo computation with increased transmitter width

Step 2: Calculation of 2nd reflected echo

M-files: *freqs2.m, cntrl2.m, recv2qst.m, echo2qst.m*

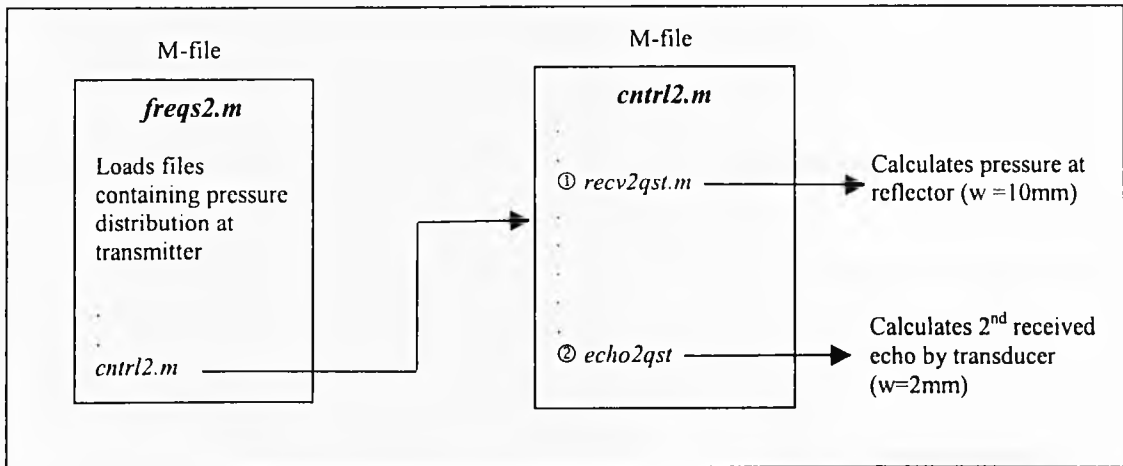


Figure B3.3: Program calls for 2nd echo computation

3rd reflected echo from a plane target

To obtain the 3rd reflected echo a similar procedure as was required for the 2nd echo computation is needed.

Step 1: Calculation of 2nd echo received by a transducer width of 7mm

M-files: *freqs2.m, cntrl2a.m, recv2qst.m, echo2wqst.m*

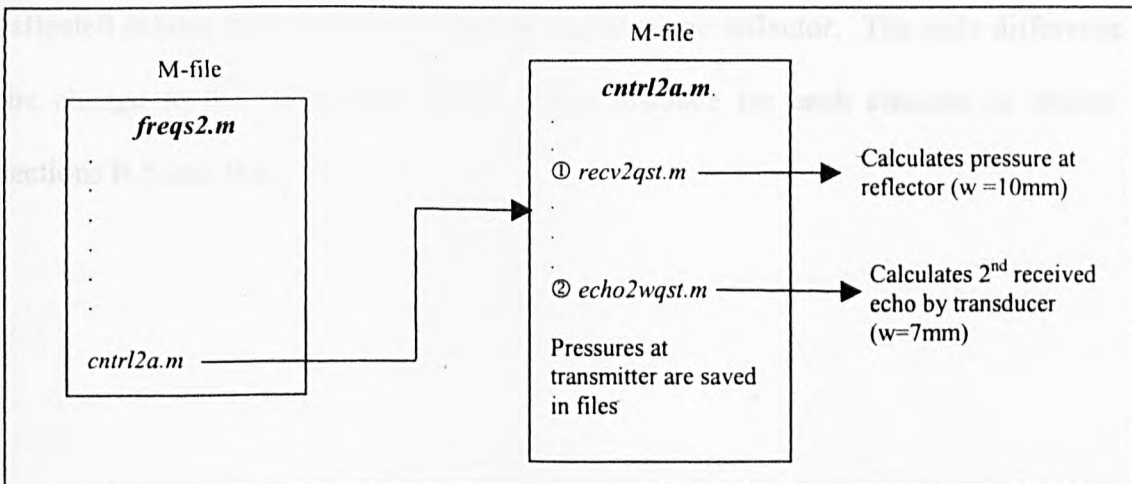


Figure B3.4: Program calls for 1st echo computation with increased transmitter width

Step 2: Calculation of 3rd reflected echo

M-files: *freqs3.m, cntrl3.m, recv3qst.m, echo3qst.m*

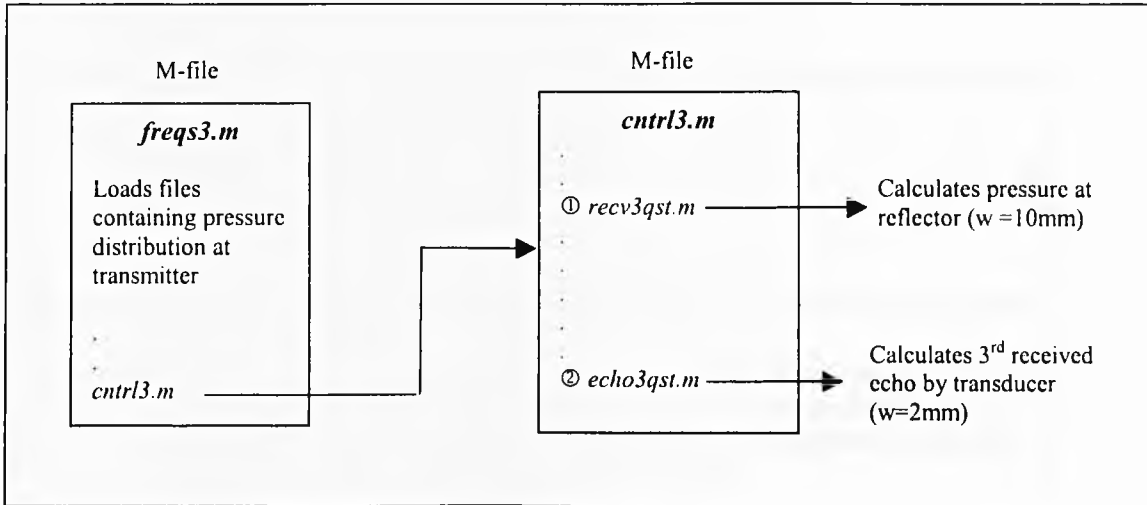


Figure B3.5: Program calls for 3rd echo computation

Computing the reflected echoes from a curved reflector and an angled plane reflector

The same procedure as described in the above sections is used for computing the reflected echoes from a curved reflector/angled plane reflector. The only difference is the change to the calculation of the z-axis distance for each element as shown in sections B.5 and B.6.

B.4: Computation of 1st Reflected Echo - Plane Target

```

/*****
*
*          School of Engineering
*
*          The Robert Gordon University, Aberdeen
*
*****
*
*          File name:   cntrl1.m
*          Author:     Yasser Qureshi
*          Created:    25/4/02
*          Chapter:    3
*
*****
*
* Description:   This program controls x and y co-ordinates at the reflector to calculate the
*               pressure at the reflector. Also uses symmetry of pressure distribution to
*               calculate pressure at reflector and at transducer. This program is called by
*               freqs1.m (same as striplpf.m so not listed here)
*
*****/

rw=5*10^(-3);           % Reflector area width-5mm
rl=12*10^(-3);         % Reflector area length

nr=40;                 % number of elements in x-axis of reflector
mr=86;                 % number of elements in y-axis of reflector

xp=-0.0015;           % co-ordinates of starting point on reflector
yq=0;
z=6.5*10^(-3);        % thickness of steel block

press_total=0;         % initialising pressures
press_total2=0;
el_total=0;
rev_total=0;

for q=1:1:(mr/2)       % outer loop along y-axis of reflector
q
  for p=1:1:(nr/2)     % inner loop along x-axis of reflector
  p
    recvrst           % calls program to calculate pressure at reflector
    xp=xp+(rw/nr);    % increments xp co-ordinate
  end                 % end of inner loop along x-axis

  xp=-0.0015;         % resets xp
  yq=yq+(rl/mr);      % increments yq co-ordinate
end                   % end of outer loop along y-axis

% subroutine mirrors quarter of array on reflector to obtain complete distribution

x_count=(nr/2);       % column counter for x-axis
y_count=(mr/2);       % row counter for y-axis

```

```

for col=1:1:(nr/2)
final_pressure(:,((nr/2)+col))=final_pressure(:,x_count);
x_count=((nr/2)-col);
final_pressure2=final_pressure;
end

for row=1:1:(mr/2)
final_pressure2(((mr/2)+row),:)=final_pressure2(y_count,:);
y_count=((mr/2)-row);
finalp_all=final_pressure2;
end

press_total2=(press_total)*4;           % total pressure at reflector

echo1qst                               % calls program to calculate 1st echo

% subroutine mirrors quarter of array on transmitter to obtain complete distribution

xt_count=(n/2);                         %column counter for x-axis
yt_count=(m/2);                         %row counter for y-axis

```

```

for col=1:1:(n/2)
recv_pressure(:,((n/2)+col))=recv_pressure(:,xt_count);
xt_count=((n/2)-col);
recv_pressure2=recv_pressure;
end

for row=1:1:(m/2)
recv_pressure2(((m/2)+row),:)=recv_pressure2(yt_count,:);
yt_count=((m/2)-row);
first=recv_pressure2;
end

```

```

e1_total=(rev_total)*4;                 % total 1st echo pressure amplitude at transducer

```

```

/*****
*
*      School of Engineering
*
*      The Robert Gordon University, Aberdeen
*
*****
*
*      File name:   recvrst.m
*      Author:     Yasser Qureshi
*      Created:    25/4/02
*      Chapter:    3
*****
*
* Description:    This program calculates the pressure distribution at the reflector.
*                It is called by cntrl1.m.
*****/

```

```

a=2*10(-3);           % Transducer width-2mm
b=12*10(-3);         % Transducer length-12mm

```

```

n=16;                % number of elements in x-axis
m=86;                % number of elements in y-axis

A1=1000              % constant in steel - A
ds=(a*b)/(m*n);     % area of each element

f
cnm

lamda=5960/f;        % 5MHz Transducer- transmitting in STEEL
k=(2*pi)/lamda;     % wave number
alpha=2.47;         % approx. atten coeff. np/m in steel

%Starting point Co-ordinate values w.r.t transducer

xu=0;                % x-value
yv=0;                % y-value

vcount=1;           % display counter
pxyz=0;
for v=1:1:m          % main loop along y-axis of transducer
vcount;
yv;
for u=1:1:n          % inner loop along x-axis of transducer
xu;
rpt1=((xp-xu)^2);
rpt2=((yq-yv)^2);
r=sqrt(rpt1+rpt2+(z^2)); % distance from transducer to point P

p1=exp(-(j*k*r));
p2=p1/r;

p_new=(p2*ds);      % pressure for each element ds
p_atn=exp(-alpha*r); % attn effects with transmission
p_pract=(p_new*p_atn);

pxyz=p_pract+pxyz; % totalling pressure from previous elements

xu=xu+(a/n);        % increments along x-axis of transducer

end                  % end of inner loop along x-axis

xu=0;                % reset to start at begining of n elements on transducer
yv=yv+(b/m);        % moves to next row up (along y-axis) of m elements

vcount=vcount+1;    % counter for main loop
end                  % end of main loop along y-axis

%cnm=normalised frequency amplitude
final_pressure(q,p)=A1*(pxyz*cnm); % pressure at every element at reflector is stored in array

press_total=final_pressure(q,p)+press_total; % total of pressure for all receiving elements

```

```

/*****
*
*      School of Engineering
*
*      The Robert Gordon University, Aberdeen
*
*****/
*
*      File name:   echo1qst.m
*      Author:     Yasser Qureshi
*      Created:    3/5/02
*      Chapter:    3
*
*****/
*
* Description:    This program calculates the 1st received echo from a plane target
*                It is called by cntrl1.m
*****/

dsr=(rw*rl)/(mr*nr);      % ds on reflector area w=5mm

RC=0.9458333;            % Reflection coefficient between steel(mild)/oil

% Symbol `t` represents calculation on transmitter surface

xp=-0.0015;              % starting co-ordinates at reflector w=5mm
yq=0;

xu=0;                    % starting co-ordinates at transmitter
yv=0;

for out=1:1:(m/2)        % along 1/2 y-axis of transmitter

    for in=1:1:(n/2)      % along 1/2 x-axis of transmitter

% Starting Co-ordinate values on reflector w.r.t transducer origin

pxyzt=0;                % pressure recieved by transmitter elements
for vt=1:1:mr           % outer loop along y-axis of reflector
yv;
    for ut=1:1:nr        % inner loop along x-axis of reflector

        return_press=finalp_all(vt,ut);      % pressure at each element at reflector
        mag_ret=abs(return_press);           % magnitude of return pressure
        phi=angle(return_press);            % angle of pressure in RADIANS

        rtpt1=((xu-xp)^2);
        rtpt2=((yv-yq)^2);
        rt=sqrt(rtpt1+rtpt2+(z^2));          % distance from transducer to point P

        p1t=exp(-(j*((k*rt)+phi)));
        p2t=p1t/rt;
        p_new=(p2t*dsr);                    % pressure for each element dsr

        p_new2=(p_new*RC*mag_ret);          % final calculation of pressure
        p_atnt=exp(-alpha*rt);             % attn when reflecting back to transmitter
        p_practt=(p_new2*p_atnt);
    end
end

```

```

pxyzt1=p_practt+pxyzt1;          % totalling pressure from previous elements on transducer

xp=xp+(rw/nr);                   % increments along x-axis of reflector

end                               % end of inner ut loop along x-axis
xp=-0.0015;                       % reset to start at begining of n elements on reflector
yq=yq+(rl/mr);                   % moves to next row up (along y-axis) of m elements on reflectors

end                               % end of outer vt loop along y-axis

%cnm=normalised frequency amplitude for each component
testp=A1*(pxyzt1*cnm);
recv_pressure(out,in)=testp;      % stores returned pressure values on transmitter in an array

rev_total=recv_pressure(out,in)+rev_total; % total of pressures on transducer

xu=xu+(a/n);                      %moves to next element on transmitter
xp=-0.0015;                       % resets to reflector start position
yq=0;

end                               % end of 'in' loop along 1/2 of x-axis of reflector

xu=0;

yv=yv+(b/m);                     % increments along y-axis of transmitter
end                               % end of 'out' loop along 1/2 of y-axis of reflector

```

B.5: Computation of 1st Reflected Echo from a Curved Reflector

```

*****
*
*      School of Engineering
*
*      The Robert Gordon University, Aberdeen
*
*****
*
*      File name:   recvrstc.m
*      Author:     Yasser Qureshi
*      Created:    25/7/02
*      Chapter:    3
*
*****
*
* Description:    This program calculates the pressure distribution at the curved reflector.
*                It is called by cntrl1.m.
*                Note: an almost identical change is also required in the 1st echo program
*                echo1qst.m for the z-axis distance calculation of each element transmitting
*                back to the probe.
*
*****/

a=2*10^(-3);          % Transducer width-2mm
b=12*10^(-3);        % Transducer length-12mm

diameter=5.4*10^(-2); % inernal diameter of curvature or pipe in cm
radius=(diameter/2); % internal radius of reflector in cm

```

```

n=16;           % new number of elements in x-axis
m=86;           % new number of elements in y-axis

A1=1000         % constant in steel - A
ds=(a*b)/(m*n); % area of each element

lamda=5960/f;   % 5MHz Transducer- transmitting in STEEL
k=(2*pi)/lamda; % wave number
alpha=2.47;     % approx. atten coeff. np/m in steel

%Starting point Co-ordinate values w.r.t transducer

xu=0;  % x-value
yv=0;  % y-value

% Implementing curvature effect

xc=xp-0.001;   % correction variable along x-axis- i.e. 1mm offset
cv1=asin(xc/radius); % first part of equation
cv2=(cos(cv1)*radius); % second part
deltat=radius-cv2; % this is deviation from plane reflector
zm=z+deltat;   % this is new z distance for every element

vcount=1;      % display counter
pxyz=0;
for v=1:1:m     % main loop along y-axis of transducer
vcount;
yv;
  for u=1:1:n    % inner loop along x-axis of transducer
  xu;
  rpt1=((xp-xu)^2);
  rpt2=((yq-yv)^2);
  r=sqrt(rpt1+rpt2+(zm^2)); % distance from transducer to point P with curvature

  p1=exp(-j*k*r);
  p2=p1/r;
  p_new=(p2*ds); % pressure for each element ds
  p_atn=exp(-alpha*r); % attn effects with transmission
  p_pract=(p_new*p_atn);
  %p_pract=p_new;
  pxyz=p_pract+pxyz; % totalling pressure from previous elements

  xu=xu+(a/n); % increments along x-axis of transducer
end % end of inner loop along x-axis of transducer

xu=0; % reset to start of n element on transducer
yv=yv+(b/m); % moves to next row up (along y-axis) of m elements of transducer

vcount=vcount+1; % counter for main loop
end % end of main loop along y-axis of transducer

%cnm=normalised frequency amplitude
final_pressure(q,p)=A1*(pxyz*cnm); % pressure at every element at reflector is stored in array

press_total=final_pressure(q,p)+press_total; % total of pressure for all receiving elements

```

B.6: Computation of 1st Reflected Echo from an Angled Reflector

```

*****
*
* School of Engineering
*
* The Robert Gordon University, Aberdeen
*
*****
*
* File name:   recvrsta.m
* Author:     Yasser Qureshi
* Created:    10/9/02
* Chapter:    4
*
*****
*
* Description: This program calculates the pressure distribution at an angled plane
* reflector. It is called by cntrl1.m.
* Note: an almost identical change is also required in the 1st echo program
* echo1qst.m for the z-axis distance calculation of each element transmitting
* back to probe.
*****/

phi = 0.0349;           % rotation angle of plane reflector in radians = 2 deg

a=2*10^(-3);           % Transducer width-2mm
b=12*10^(-3);          % Transducer length-12mm

n=16;                  % number of elements in x-axis
m=86;                  % number of elements in y-axis

A1=3163                % constant in oil
ds=(a*b)/(m*n);       % area of each element

%f=frequency
f
cnm

lamda=1450/f;          % 5MHz Transducer- transmitting in oil
k=(2*pi)/lamda;       % wave number
alpha=42.02;           % atten coeff. np/m in oil

%Starting point Co-ordinate values w.r.t transducer

xu=0;   % x-value
yv=0;   % y-value

%Implementing the reflector angle with respect to probe

xc=xp-0.001;           % correction variable along x-axis- 1mm offset
deltar=xc*tan(theta); % projection from normal incident reflector

if(xc<0)                % subtract deltar on one side of reflector
zm=z+deltar;           % this is new z distance for every element
elseif(xc=0)           % at centre there is no displacement
zm=z;

```

```

elseif(xc>0)          % add deltar on other side of reflector
    zm=z+deltar;
end

vcount=1;            % display counter
pxyz=0;
for v=1:1:m          % main loop along y-axis of transducer
vcount;
yv;
    for u=1:1:n      % inner loop along x-axis of transducer
        xu;
        rpt1=((xp-xu)^2);
        rpt2=((yq-yv)^2);
        r=sqrt(rpt1+rpt2+(zm^2));    % distance from transducer to point P with angled reflector

        p1=exp(-(j*k*r));
        p2=p1/r;
        p_new=(p2*ds);    % pressure for each element ds
        p_atn=exp(-alpha*r);    % attn effects with transmission
        p_pract=(p_new*p_atn);
        %p_pract=p_new;
        pxyz=p_pract+pxyz;    % totalling pressure from previous elements

        xu=xu+(a/n);    % increments along x-axis of transducer
    end                % end of inner loop along x-axis

    xu=0;    % reset to start of n elements on transducer
    yv=yv+(b/m);    % moves to next row up (along y-axis) of m elements on transducer

vcount=vcount+1;    % counter for main loop
end                % end of main loop along y-axis

%cnm=normalised frequency amplitude
final_pressure(q,p)=A1*(pxyz*cnm);    % pressure at every element at reflector is stored in array

press_total=final_pressure(q,p)+press_total; %total of pressure for all receiving elements

```

B.7: Plotting of Circle Diagram for Efficiency of Transducers

```

*****
*
*      School of Engineering
*
*      The Robert Gordon University, Aberdeen
*
*****
*
*      File name:   circle.m
*      Author:     Konstantinos Christidis/Yasser Qureshi
*      Created:    3/2/98
*      Chapter:    5/6
*
*****
*
* Description:    This program generates two arrays (admittance values and frequency
*                points) after entering the data from practical measurement. The program
*                then plots a circle in the admittance plane.
*
*****/

```

clear all

r=2.71; % small resistor value in series with transducer (in ohms)
vi=8; % input voltage in volts (peak-peak)

f(1)=70.788; % frequency - these measurements are for an 80Khz sandwich transducer
vra(1)=0.04; % Voltage across resistor 'r' in volts
vrb(1)=82.8; % Phase angle of voltage across 'r' w.r.t vi (degrees)

f(2)=73.;
vra(2)=0.045;
vrb(2)=79.2;

f(3)=75.127;
vra(3)=0.05;
vrb(3)=72;

f(4)=75.490;
vra(4)=0.05;
vrb(4)=68.4;

f(5)=75.890;
vra(5)=0.05;
vrb(5)=64.8;

f(6)=76.558;
vra(6)=0.05;
vrb(6)=61.2;

f(7)=77.022;
vra(7)=0.05;
vrb(7)=57.6;

f(8)=77.921;
vra(8)=0.05;
vrb(8)=50.4;

f(9)=78.538;
vra(9)=0.05;
vrb(9)=41.4;

f(10)=79.164;
vra(10)=0.04;
vrb(10)=41.4;

f(11)=80.032;
vra(11)=0.035;
vrb(11)=36;

f(12)=81.020;
vra(12)=0.03;
vrb(12)=36;

f(13)=82.314;
vra(13)=0.02;
vrb(13)=43.2;

```
f(14)=83.563;
vra(14)=0.02;
vrb(14)=50.4;
```

```
f(15)=84.397;
vra(15)=0.02;
vrb(15)=61.2;
```

```
% manipulating data to plot points in admittance plane
```

```
vrb=vrb/180;
vrb=vrb*pi; % convert angle to radians

vr=vra.*(cos(vrb)+i*sin(vrb)); % convert voltage to polar form

ii=vr/r; % complex current through transducer
z=vi./ii; % transducer impedance
y=1./z; % transducer admittance

G=real(y); % tranducer conductance
B=imag(y); % transducer susceptance

whitebg
plot(G,B,'or') % plots circle in admittance plane
%plot(G,B,'or',G,B,'b-')
xlabel('G') % axes labels
ylabel('B')
%axis([-0.0012 0.0012 -0.0012 0.0012]) % option to set scale of axes
grid

for i=1:17 % labels frequency points on plot
    datatxt = sprintf('%3.0f', i);
    x=G(i);
    y=B(i);
    text(x,y, datatxt)
end
```

B.8: Dynamic Impedance Matching of Cable

```
*****
*
* School of Engineering
*
* The Robert Gordon University, Aberdeen
*
*****
*
* File name: cab1sl6.m
* Author: Yasser Qureshi/Konstantinos Christidis
* Created: 23/3/99
* Chapter: 7
*****
*
* Description: This program generates the dynamic co-axial cable terminating impedance
* as the cable passes through temperature zones (dummy values used). The
* user enters the cable length and incremental length.
*****/
```

%*** Input parameters

EG=200; % Generator voltage in volts
f = 10000; % frequency
ZG=50; % Generator impedance in ohms
length = 500; % Cable length in m
load temp.dat % loads dummy tool-temperature file

sprintf('AUTOMATIC CABLE IMPEDANCE MATCHING PROGRAM')

n=input('Enter full cable length in m: ');

incr=input('Enter increment length in m: ');

sprintf('NOTE:length1 = cable length at 22 deg C and length2 = cable length at respective measured temps')

T =temp(1) % read first temp value from tool memory file

k=0; % initialisation of various counter variables

a=0;

m=0;

b=n;

p=0;

q=0;

z=0;

looper=n/incr; % number of times calculation of impedances is required

for count=1:looper % main overall program counter for 'n' sections of cable

length1 = (n-(a+k)) % length in m at 22 deg C

T=temp(1)

ZG=50;

count

%*** Cable Characteristics

ri=(0.9/2)*10⁽⁻³⁾; % Internal conductor diameter

ro=(2.95/2)*10⁽⁻³⁾; % Insulated material diameter

rs=(3.6/2)*10⁽⁻³⁾; % Outer conductor diameter

a1 = pi*(ri²); % Inner conductor sectional area

a2 = pi*((rs²)-(ro²)); % Outer conductor sectional area

%*** Materials characteristics

loss = 0.0002; % PE dielectric loss tangent

mi = 1.2566*10⁽⁻⁶⁾; % Cu permeability

rho20 = 2.458*10⁽⁻⁸⁾; % SnCu measured practically

ar = 0.0001604; % SnCu resistance temp coef

ac = 0.0535*10⁽⁻¹²⁾; % PE insulated material temp

%*** Primary Parameters Calculations

rat1=(1/a1)+(1/a2); % length/area rate

rho = ((rho20*rat1)+((T-22)*ar))/rat1; % rho temp adj.

skin = sqrt(rho/(pi*f*mi)); % Skin depth

omega = 2*pi*f; % omega calculation

*** Cable Parameters at 20 deg temperature

```
C22 = 101*10^(-12);           % Capacitance is 101pF per meter
C = C22 - ((T-22)*ac);
L1 = C*(50^2);               % Inductance is 237.5nH per meter
G = loss*C*omega;           % Conductance calculation per m.
```

% Resistance calculation per m.

```
if ri - skin > 0
    a1 = pi*((ri^2)-((ri-skin)^2));
else
    a1 = pi*(ri^2);
end
if rs-ro-skin > 0
    a2 = pi*((rs^2)-((rs-skin)^2));
else
    a2 = pi*((rs^2)-(ro^2));
end
R = rho*((1/a1)+(1/a2));
L = L1 + R/omega;
```

***** Attenuation and phase shift calculation *****

```
part1=(sqrt((R^2+((omega^2)*L^2))*(G^2+((omega^2)*C^2)))/2);
part2=((R*G)-((omega^2)*L*C))/2;
atten = sqrt(part1+part2);
phase = sqrt(part1-part2);
```

Zo = sqrt((R+(j*omega*L))/(G+(j*omega*C))); %cable characteristic impedance

*/ ***Required cable termination impedance Zt1, for first temperature section***** /

```
ZG
pa1 = (ZG+Zo)*(exp((atten*length1) + j*(phase*length1)));
pa2 = (ZG-Zo)*(exp(-((atten*length1) + j*(phase*length1))));
pa3 = pa1 + pa2;
pa4 = pa1 - pa2;
pa5 = pa3 / pa4;
```

```
Zt = Zo * pa5
MagZt = abs(Zt);
angleZt = angle(Zt);
conjugate=conj(Zt);
```

*****main terminating impedance calculation loop*****

```
if length1 < (n-q)           % main loop for impedance calculations for sections at temperature
    length2 = incr;         % length of cable incremented into pipe - incremental length
    v=(n-length1)/incr;
    for s=1:v               % loop for calculating impedances when a new temperature value is recorded
        length2
```

```

T=temp(2+z)                % second section temperature
z=z+1;

%*** Primary Parameters Calculations (repeated for 2nd and later sections at temp)

rat1=(1/a1)+(1/a2);        % length/area rate
rho = ((rho20*rat1)+((T-22)*ar))/rat1; % rho temp adj.
skin = sqrt(rho/(pi*f*mi)); % Skin depth
omega = 2*pi*f;            % omega calculation

%*** Cable Parameters at 20 deg temperature

C22 = 101*10-12;          % Capacitance is 101pF per meter
C = C22 - ((T-22)*ac);
L1 = C*(502);            % Inductance is 237.5nH per meter
G = loss*C*omega;        % Conductance calculation per m.

% Resistance calculation per m.

if ri - skin > 0
    a1 = pi*((ri2)-((ri-skin)2));
else
    a1 = pi*(ri2);
end
if rs-ro-skin > 0
    a2 = pi*((rs2)-((rs-skin)2));
else
    a2 = pi*((rs2)-(ro2));
end
R = rho*((1/a1)+(1/a2));
L = L1 + R/omega;

%***** Attenuation and phase shift calculation *****

part1=(sqrt((R2+((omega2)*L2))*(G2+((omega2)*C2))))/2;
part2=((((R*G)-((omega2)*L*C)))/2;

atten = sqrt(part1+part2);
phase = sqrt(part1-part2);

Zo = sqrt((R+(j*omega*L))/(G+(j*omega*C))); %cable characteristic impedance

%/ **Required termination impedance Zt2, for second temperature section***** /

ZG=Zt                %previous temp section Zt value is now the new ZG for the next section
pa1 = (ZG+Zo)*(exp((atten*incr) + j*(phase*incr)));
pa2 = (ZG-Zo)*(exp(-((atten*incr) + j*(phase*incr))));
pa3 = pa1 + pa2;
pa4 = pa1 - pa2;
pa5 = pa3 / pa4;

Zt = Zo * pa5
MagZt = abs(Zt);
angleZt = angle(Zt);
Zt_conj=conj(Zt);

```

```
    end          % end of 'for' loop for calculating impedance when a new temperature is recorded
end            % end of 'if' main loop for terminating impedance calculations
if length1 < n
    z=0;
end

k=k+incr;    % increment a by one
m=m-incr;    % decrement b by one

if count > 2
    q=q+1;
end

end          % end of main overall program counter for n sections of cable
```

Appendix C

Practical Measurements for Verification of Theoretical Models in Chapters 2 - 4

C.1: Practical Measurements and Theoretical Investigation of the Sensitivity to Co-ordinate Changes for a Point Source Receiver

Table 1(a): Variation of normalised pulse amplitude along x-axis at centre (x, y, z = 0,0,13mm)

Co-ordinate variation	x + 0.5mm	x + 1mm	x + 1.5mm	x + 2mm	x + 2.5mm	x + 3mm	x + 3.5mm
Simulation	0.8837	0.6558	0.4334	0.3067	0.2528	0.2161	0.1793
Practical measurement	0.8667	0.65	0.4333	0.2667	0.2	0.1333	0.1083

Co-ordinate variation	x + 4mm
Simulation	0.154
Practical measurement	0.1033

Table 1(b): Variation of normalised pulse amplitude along x-axis at (x, y, z = 0, ± 1mm,13mm)

Co-ordinate variation	x + 0.5mm	x + 1mm	x + 1.5mm	x + 2mm	x + 2.5mm	x + 3mm	x + 3.5mm
Simulation	0.8836	0.6558	0.4334	0.3067	0.2529	0.2163	0.1794
Practical measurement	0.9833	0.8093	0.5667	0.3473	0.2333	0.16	0.1333

Co-ordinate variation	x + 4mm
Simulation	0.1548
Practical measurement	0.1133

Table 1(c): Variation of normalised pulse amplitude along y-axis at centre (x, y, z = 0,0,13mm)

Co-ordinate variation	y + 2mm	y + 3mm	y + 4mm	y + 4.5mm	y + 5mm	y + 5.5mm	y + 6mm
Simulation	0.9992	1.0021	1.0472	1.0722	0.9335	0.7184	0.523
Practical measurement	0.9688	0.9688	0.9844	0.9219	0.7294	0.6562	0.4612

Co-ordinate variation	y + 6.5mm	y + 7mm
Simulation	0.3796	0.282
Practical measurement	0.3062	0.2375

Table 1(d): Variation of normalised pulse amplitude along x-axis at centre (x, y, z = 0,0,9.12mm)

Co-ordinate variation	x + 0.5mm	x + 1mm	x + 1.5mm	x + 2mm	x + 2.5mm
Simulated	0.7969	0.4937	0.3351	0.2251	0.1873
Practical measurement	0.8837	0.4884	0.314	0.1581	0.1023

Table 1(e): Variation of normalised pulse amplitude along y-axis at centre (x, y, z = 0,0,9.12mm)

Co-ordinate variation	y + 1mm	y + 2mm	y + 3mm	y + 4mm	y + 5mm	y + 6mm	y + 7mm
Simulation	1.001	1.0094	0.9992	0.9933	1.0054	0.5264	0.2602
Practical measurement	0.9651	0.9535	0.9302	0.9535	0.6977	0.3721	0.1558

Table 1(f): Variation of normalised pulse amplitude as z-axis distance is increased from 9.25mm along central axis (with attenuation correction)

Co-ordinate variation	z = 10.42mm	z = 11.98mm	z = 13.54mm	z = 14.19mm	z = 15.76mm
Simulated	0.9051	0.7999	0.71168	0.6788	0.6053
Practical measurement	0.9269	0.8306	0.7641	0.7226	0.6312

Co-ordinate variation	z = 16.53mm	z = 17.44mm	z = 18.88mm	z = 19.78mm	z = 20.69mm
Simulated	0.5713	0.5363	0.4877	0.4595	0.433
Practical measurement	0.6229	0.5731	0.5316	0.515	0.4983

Co-ordinate variation	z = 21.86mm	z = 22.38mm	z = 24.21mm	z = 25.12mm	z = 29.99mm
Simulated	0.4018	0.3876	0.3453	0.3262	0.244
Practical measurement	0.4651	0.4319	0.3987	0.39	0.299

C.2: Practical Measurements and Theoretical Investigation of

Sensitivity to Co-ordinate Changes for the Case when the Target

Area is Equal to Transmitting Transducer (2mm x 12mm)

Table 1(a): Variation of normalised pulse amplitude along x-axis at centre (x, y, z = 0,0,13.5mm)

Co-ordinate variation	x + 0.5mm	x + 1mm	x + 1.5mm	x + 2mm	x + 2.5mm	x + 3mm	x + 4mm
Simulation	0.9091	0.7078	0.5	0.3247	0.2013	0.1494	0.0974
Practical measurement	0.9818	0.8509	0.6182	0.3636	0.2327	0.1382	0.0764

Table 1(b): Variation of normalised pulse amplitude along y-axis at centre (x, y, z = 0,0,13.5mm)

Co-ordinate variation	y + 1mm	y + 2mm	y + 3mm	y + 4mm	y + 5mm	y + 6mm	y + 7mm
Simulated	0.9675	0.8766	0.7857	0.7013	0.6104	0.526	0.4351
Practical measurement	0.963	0.8333	0.7963	0.7222	0.6667	0.5833	0.477

Co-ordinate variation	y + 8mm	y + 9mm
Simulated	0.3506	0.2597
Practical measurement	0.3815	0.2704

Table 1(c): Variation of normalised pulse amplitude as z-axis distance is increased from 11.98mm along central axis (*with attenuation correction*)

Co-ordinate variation	z = 12.76mm	z = 13.54mm	z = 14.71mm	z = 15.62mm	z = 16.53mm
Simulated	0.9479	0.9062	0.8438	0.7917	0.75
Practical measurement	0.9492	0.9153	0.8814	0.8475	0.8136

Co-ordinate variation	z = 17.57mm	z = 18.74mm	z = 19.65mm
Simulated	0.7083	0.6562	0.6146
Practical measurement	0.7458	0.6958	0.6695

C.3: Practical Measurements and Simulated Results for Relative Amplitudes of Reflected echoes (plane reflector in oil)

Table 1(a): Practical gain measurements for first, second and third reflected echoes from plane steel target in oil (z=18mm). Screen height is 79.5% for all echoes.

1 st echo gain (dBs)	2 nd echo gain (dBs)	3 rd echo gain (dBs)
53.4	68.6	82.4
53.4	68.6	82.7
53.3	68.4	82.2
53.1	68.2	82.2
53.4	68.55	82.9
53.4	68.5	82.0
53.4	68.7	82.3
53.4	68.6	82.4

Mean 1 st echo gain (dBs)	Mean 2 nd echo gain (dBs)	Mean 3 rd echo gain (dBs)
53.35	68.519	82.3875

Difference from 1 st echo (dBs)	Difference from 1 st echo (dBs)	Difference from 1 st echo (dBs)
0	-15.169	-29.0375

Table 1(b): Practical gain measurements for first, second and third reflected echoes from plane steel target in oil ($z=12.95\text{mm}$). Screen height is 79.5% for all echoes

1 st echo gain (dBs)	2 nd echo gain (dBs)	3 rd echo gain (dBs)
50.2	63.2	74.5
50.1	62.7	73.9
50.2	63.4	74.8
50.2	63.1	74.3
50.3	62.8	74.5
50.2	63.1	74.4

Mean 1 st echo gain (dBs)	Mean 2 nd echo gain (dBs)	Mean 3 rd echo gain (dBs)
50.2	63.05	74.4

Difference from 1 st echo (dBs)	Difference from 1 st echo (dBs)	Difference from 1 st echo (dBs)
0	-12.85	-24.2

The normalised amplitudes V_{Norm} in the case of Tables 1(a)-(b) were obtained using the following relationship

$$\text{Gain (dBs)} = 20 \log_{10} V_{Norm} \quad (\text{C3.1})$$

Hence the normalised value is given by

$$V_{Norm} = 10^{(\text{dBs}/20)} \quad (\text{C3.2})$$

Tables 2(a)-(b): Normalised reflected echo amplitudes from a plane reflector in oil from simulated and practical data

(a)

$z = 13\text{mm}$	Practical measurement	Simulated
1 st echo	1	1
2 nd echo	0.22777	0.2035
3 rd echo	0.06166	0.04467

(b)

z = 18mm	Practical measurement	Simulated
1 st echo	1	1
2 nd echo	0.1744	0.1344
3 rd echo	0.035328	0.0195

C.4: Practical Measurements and Simulated Results for Relative Amplitudes of Reflected Echoes in Steel Block (immersed in oil)

Table 1(a): Practical measurements of % screen height (SH) of reflected echoes in steel block (z = 10.28mm).

Gain (dBs)	1st echo (%SH)	2nd echo (%SH)	3rd echo (%SH)
33.2	95.5	41	22.5
33.3	95	41.5	23
33.0	95	41	22.5
33.6	95	41	23
33.7	95	41.5	23
33.7	95	41.5	23

Mean 1st echo (%SH)	Mean 2nd echo (%SH)	Mean 3rd echo (%SH)
95.08	41.25	22.833

Table 1(b): Practical measurements of % screen height (SH) of reflected echoes in steel block (z = 7.517mm).

Gain (dBs)	1st echo (%SH)	2nd echo (%SH)	3rd echo (%SH)
31.6	95	39	20
32.2	95	39.5	20.5
31.9	95.5	39.5	20.5
31.8	95.5	39.5	20
31.7	95.5	39.5	20
32	95	39.5	20

Mean 1 st echo (%SH)	Mean 2 nd echo (%SH)	Mean 3 rd echo (%SH)
95.25	39.417	20.167

Table 1(c): Practical measurements of % screen height (SH) of reflected echoes in steel block ($z = 6.473\text{mm}$).

Gain (dBs)	1 st echo (%SH)	2 nd echo (%SH)	3 rd echo (%SH)
31.3	95.5	37.5	18.5
31.3	95.5	37.5	18.5
31.8	96	38.5	19
31.7	96	38.5	19
30.8	95.5	37.5	18.5
30.9	96	38.5	19

Mean 1 st echo (%SH)	Mean 2 nd echo (%SH)	Mean 3 rd echo (%SH)
95.75	38	18.75

Table 1(d): Practical measurements of % screen height (SH) of reflected echoes in steel block ($z = 5.024\text{mm}$).

Gain (dBs)	1 st echo (%SH)	2 nd echo (%SH)	3 rd echo (%SH)
30.4	96	38	16.5
30.4	95.5	38.5	16.5
30.5	96	39	16.5
30.6	96	38.5	16.5
30.7	95.5	39	16.5
30.7	95.5	39	16.5

Mean 1 st echo (%SH)	Mean 2 nd echo (%SH)	Mean 3 rd echo (%SH)
95.75	38.67	16.5

Tables 2(a)-(d): Normalised reflected echo amplitudes in steel from simulated and practical data

(a)

z = 10mm	Practical measurement	Simulated
1 st echo	1	1
2 nd echo	0.43383	0.43357
3 rd echo	0.24015	0.23167

(b)

z = 7.5mm	Practical measurement	Simulated
1 st echo	1	1
2 nd echo	0.41382	0.39125
3 rd echo	0.21173	0.19467

(c)

z = 6.5mm	Practical measurement	Simulated
1 st echo	1	1
2 nd echo	0.3969	0.3852
3 rd echo	0.19582	0.19213

(d)

z = 5mm	Practical measurement	Simulated
1 st echo	1	1
2 nd echo	0.4038	0.38
3 rd echo	0.188	0.1956

C.5: Simulated Results for Relative Amplitudes of Reflected Echoes from a Curved Steel Target

z = 5mm	Diam=12.5cm	Diam=5.4cm
1 st echo	1	1
2 nd echo	0.3783	0.38422
3 rd echo	-	-

Note that for a corresponding plane steel reflector the relative 2nd echo amplitude is 0.38

C.6: Practical Measurements and Simulated Results for Relative

Amplitudes of 1st echo from an Angled Reflector - Probe

Aperture 2mm x 12mm

Table 1: Normalised pulse amplitude variations of simulated and practical results for an angled steel plane reflector (in oil) $z = 6.5\text{mm}$

Angular rotation of probe/reflector	Practical measurement	Simulated
0°	1	1
0.5°	0.994	0.977
1°	0.982	0.954
1.5°	0.952	0.932
2°	0.928	0.911
2.5°	0.877	0.8897
3°	0.825	0.8667
3.5°	0.768	0.841
4°	0.709	0.813

Appendix D

Investigation of Received Echo Pulse-shapes (Chaps 2-3)

The computed received echo pulse waveshapes in sections 3.5.1 were found to be somewhat different to the practical echoes. The computed echo signal was displayed by MATLAB as a symmetrical pulse as shown in the results section. To investigate this discrepancy in results a series of investigations, focussing on the implementation of the mathematical model were carried out. The aim of this being, to identify the source of the problem in the mathematical computation process.

Problem Description

The received echoes by the finite rectangular transducer have been modelled in the same way as that for the pulse at the reflector. All of the elements on the reflector surface act as transmitters in the reverse direction. Thus, by summing the pressure contribution of each element on the reflector surface, taking into account of the phase of each element (eqⁿ 3.1) the 1st received echo can be obtained. An example of the computed pulse from MATLAB after performing the IFFT is shown in Figure D.1.

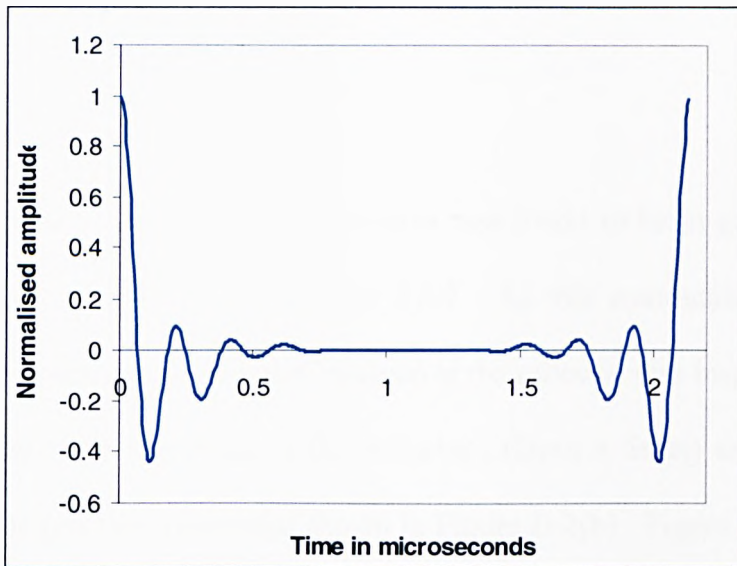


Fig. D.1: Computed received echo pulse from after reflection from a plane target in oil

As can be seen from Figure D.1 the pulse waveshape is split and symmetrical in the MATLAB display window. Further investigation into the phase spectrum of the above pulse showed that the phase elements all had a value of zero i.e. a null phase spectrum for the computed response. To investigate why this was the case a series of tests were performed on the mathematical model as detailed below.

Tests Performed on the Mathematical Model

Test 1

The MATLAB program code for the 1st echo was thoroughly checked for any errors. A possible error could have been the numerical precision used for the pressure calculations. This was confirmed to have no effect on the calculation even with double precision formatting of the pressure calculations.

Test 2

The computed pulse over a given reflector area was found to be in good agreement with the practical pulse in Chap.2 section 2.6.2. As this computation gave good results the phase spectrum of the pulse received at the reflector was inspected. Figure D.2(a) shows the computed pulse at the reflector (12mm x 5mm) at a distance of $z=13\text{mm}$ with the practical pulse also shown in Figure D.2(b). Figure D.3 shows the corresponding phase spectrum of this pulse at the reflector.

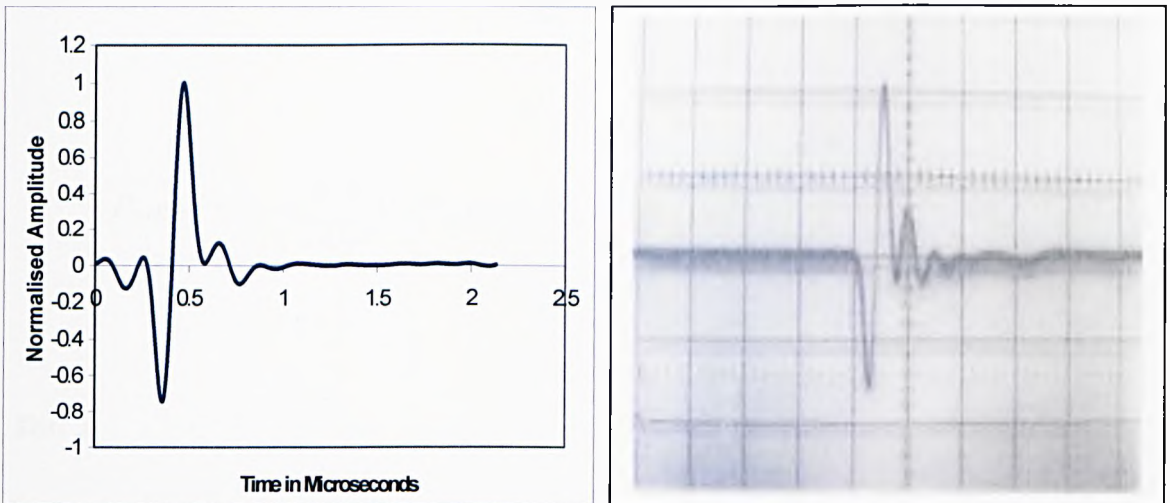


Figure D.2 (a): Received pulse over a target area of (5mm x 12mm) $z=13\text{mm}$

Figure D.2 (b): Measured pulse by practical measurement system. Vertical axis = 0.1V/div
Horizontal axis = 0.5 μs /div

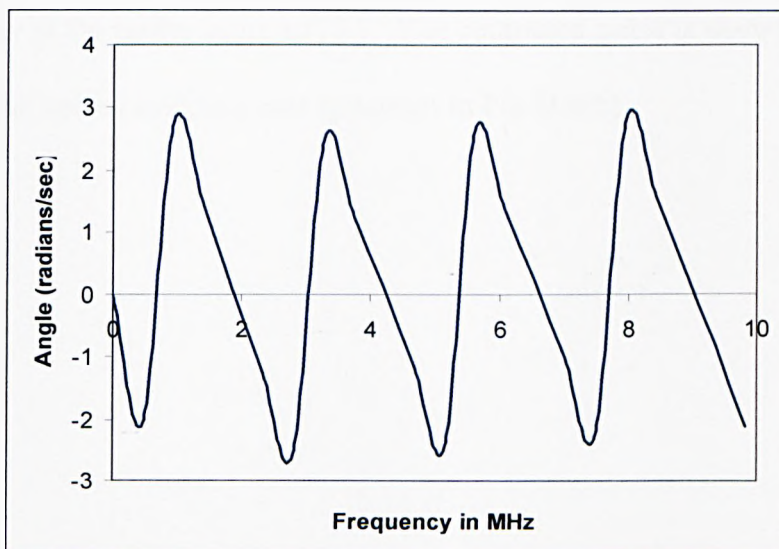


Figure D.3: Phase spectrum of pulse over a target area of (5mm x 12mm) $z=13\text{mm}$

From Figure D.3 it can be observed that the computed pulse at the reflector does have a continuous phase component. A closer inspection of the pressure distribution matrix over the target area showed that all the elements (40 x 86) had phase values associated with them as expected, some of which were verified by manual calculations. Thus there seems to be no discrepancy with the pressure distribution at the target with regard to the phase values for each of the elements.

It is these phase values of each element that were used to compute the 1st received echo, using eqⁿ 3.1 as given below

$$P_{s(EI)} = A \sum_{v=1}^m \sum_{u=1}^n C_s \left| P_{s(RI)}(x_p, y_q, z) \right| \cdot R \cdot \left[\frac{\exp - j \left(\frac{2\pi f_s}{c} r_i + \phi \right)}{r_i} \right] \Delta s \quad (D.1)$$

Test 3

The 1st received echo by the transducer was computed again but for a **single** element receiving only at the centre using eqⁿ 3.1. The computed pulse is shown below in Fig D.4(a) with the corresponding phase spectrum in Fig D.4(b).

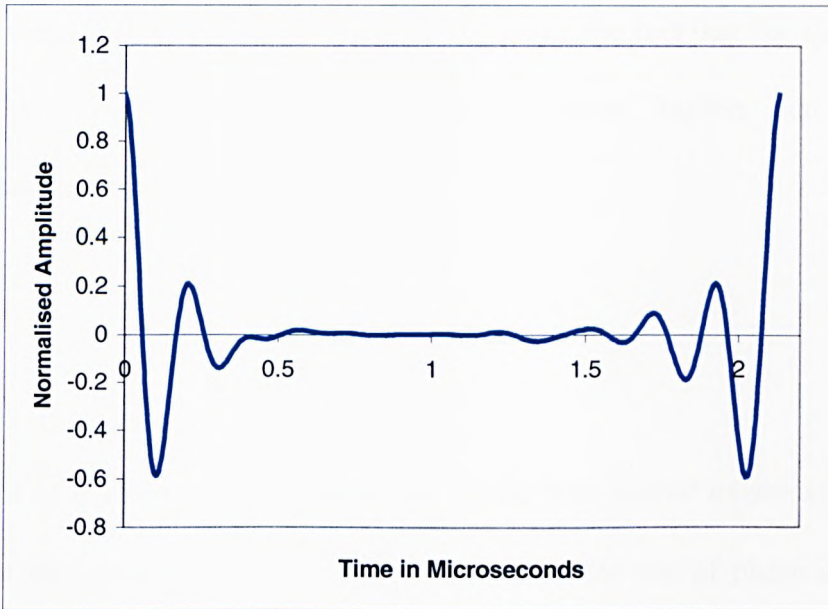


Figure D.4(a): Simulated 1st echo in steel for a single element $z = 6.5\text{mm}$

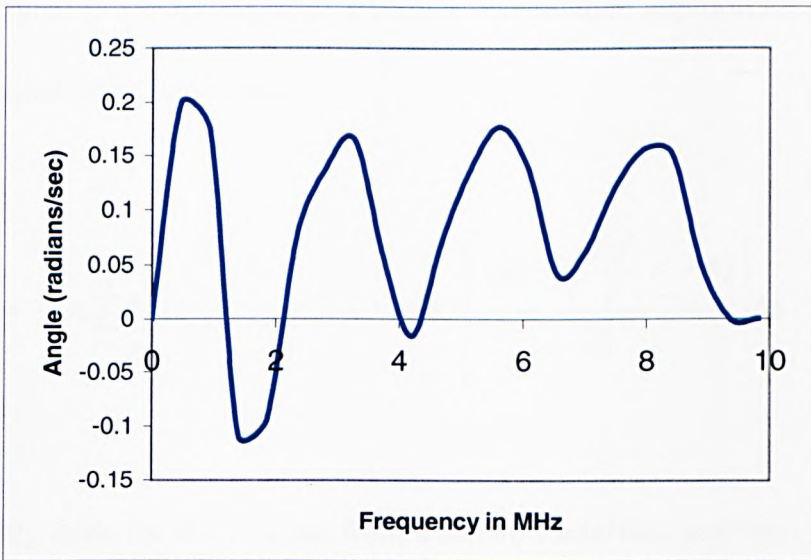


Figure D.4(b): Phase spectrum for a single element receiving in steel $z = 6.5\text{mm}$

For the single element receiving on the transducer surface at the centre, the computed pulse remains split in the MATLAB window, but it still appears closely symmetrical. The computation was also repeated for a single element offset from the centre ($x+3\text{mm}$, $y+2\text{mm}$, $z=6.5\text{mm}$) that also showed a degree of symmetry implying an error in re-construction. It is also noted that although the phase spectrum for the

single receiving element does show a sinusoidal trend, the fact that the spectrum does not intersect 0 radians/sec in a symmetrical manner implies that there is a computational error.

Test 4

On the basis of the above observations, the model was further examined and it was thought that this problem is very likely to be due to the use of phase angle ϕ as a positive quantity. But upon examination it appeared that the phase angle ϕ w.r.t transmitted signal is always lagging. Hence it was thought appropriate to invert the sign of ϕ in equation D.1 such that

$$P_{s(El)} = A \sum_{v=1}^m \sum_{u=1}^n C_s |P_{s(Rl)}(x_p, y_q, z)| \cdot R \cdot \left[\frac{\exp - j\left(\frac{2\pi f_s}{c} r_i - \phi\right)}{r_i} \right] \Delta s \quad (D.2)$$

This was firstly done for the 1st echo from a steel/oil interface and then repeated for the 2nd echo. Figures D.5(a) and D.5(b) show the simulated and practical results for the 1st received echo. Figures D.6 (a) and D.6(b) shows the simulated and practical results for the 2nd echo pulse with a negative phase being used in eqⁿ (3.1) and (3.4).

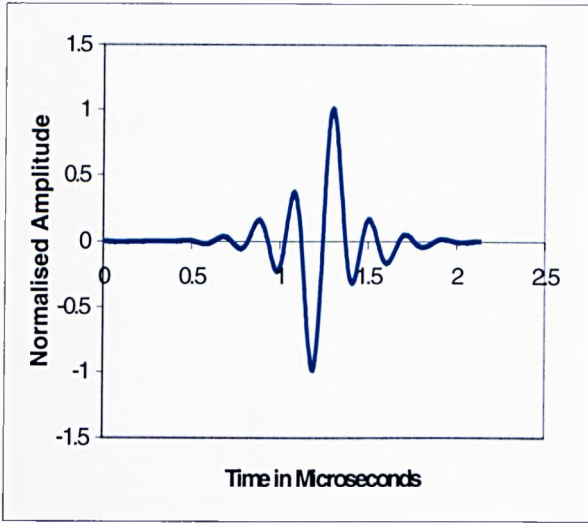


Figure D.5(a): Simulated 1st echo in steel with phase reversed ($z=10\text{mm}$)

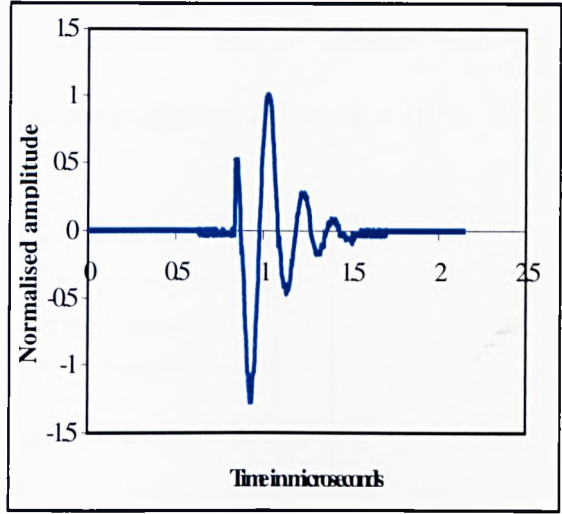


Figure D.5(b): Practical measurement of 1st reflected echo in steel ($z=10\text{mm}$)

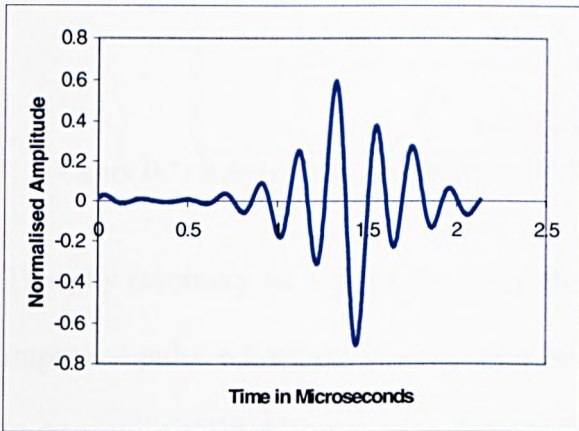


Figure D.6(a): Simulated 2nd echo in steel with phase reversed ($z=10\text{mm}$)

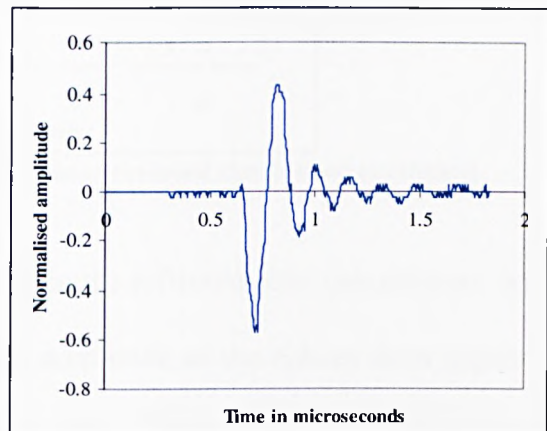


Figure D.6(b): Practical measurement of 2nd echo in steel ($z=10\text{mm}$).

As can be seen from the above results the simulated and practical echo pulses are much closer in shape compared to the previous computation. By inverting the phase angle in the mathematical model the echo waveforms now give a closer representation of the practical signals (Chap 3 sections 3.5.1/3.5.2).

However the relative amplitudes from the above results for the simulated 2nd and 3rd echoes echo (w.r.t 1st echo) was found to be somewhat different to the practical

measured amplitudes as recorded in Appendix C, section C.4. Figure D.7 below shows a plot of the relative amplitudes for the 1st, 2nd and 3rd echoes with the modified model and the corresponding practical measurements (Note: $A = 10^3$).

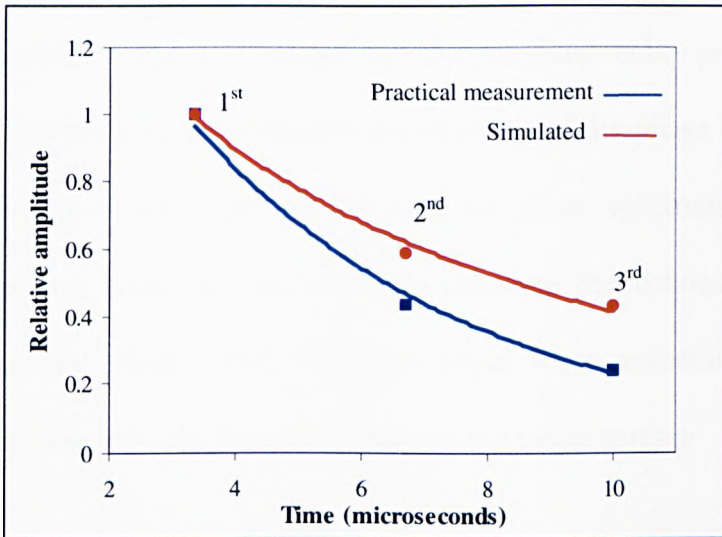


Figure D.7: Relative echo amplitudes in steel with phase reversed simulations ($z=10\text{mm}$)

Thus, by reversing the sign of the phase element in the reflected echo calculations, an improved pulse waveform is achievable but the amplitude of the echoes does appear to be significantly different from the practical pulses. This could be due to the fact that there is a scaling factor required between the simulated relative echo amplitudes from the model with phase inversion, and the practical echo amplitudes as previously shown in Chap 3, section 3.5.2. For example, for the case of Figure D.7, a scaling factor of 0.73 would be required for the simulated 2nd echo and a factor of 0.56 for the 3rd echo.

However, if a second set of results were to be computed, it is possible to observe the scaling factors (i.e. if they are the same). If this was the case, then the technique of synthesised echoes may be used as references. This step is proposed as a future work.

Conclusions from Test Results

The aim of the above tests on the mathematical model for the echo computations was to identify the problem that causes the echo to be displayed incorrectly in MATLAB. It can be concluded that the reason for the received echo pulse shape being symmetrical is because of the erroneous computation of the phase component of the pulse. To investigate why this was the case the phase spectrum on the reflector surface was plotted (used by the model to calculate the echoes) to confirm the expected sinusoidal trend. This was also noted when inspecting the complete pressure distribution (40 x 86 elements) array on the target surface.

The phase spectrum for the 1st echo with a single element receiving showed the error in the mathematical model. It shows that the received phase spectrum does not intersect the x-axis in a sinusoidal manner. Thus when the pressures of each element on the transmitter are totalled the resultant phase becomes zero giving an incorrect 1st echo pulse.

However when the phase angle was reversed for the reflected echoes, in the mathematical model on the basis of phase retardation w.r.t reference, the pulse waveshapes gave a good representation of the practical signals in terms of pulse shape as shown in Figure D.5(a). The relative amplitudes were also found to be different in comparison with the practical results. This implies that a scaling factor is required between simulated and practical results. The magnitude of this scaling

factor need to be further confirmed by repeating the process for at least a second set of simulated results. A possible explanation of the effect of phase inversion on the 1st echo computation could be as follows.

At the point of the first transmission from the transmitter to the reflector the initial phase values have been set to 0 radians/sec. When the elements on the reflector surface receive a pressure wave as given by Huygens Green Function there is a *phase lag* taking place (w.r.t to initial phase at transmitter) due to the propagation delay in the medium. The equation for the 1st echo shows the phase value of each element on the reflector being added to the distance between each respective element on transmitter and reflector surface i.e. a *phase advance*. This method of simulation is therefore incorrect because in actual fact, for each travel between transmitter and reflector there is a phase delay taking place that is not being accounted for in eqⁿ D.1 in the case of reflected echoes. Therefore when the phase is reversed as shown in eqⁿ D.2 a proper phase lag is being implemented between each respective element on the transmitter and receiver surfaces. This is why the echo pulse waveforms appear to be similar to the practical signals when the phase element is reversed as shown by eqⁿ D.2.

Appendix E

Data for Dynamic Impedance Matching of Cable

E.1: Simulated Tool Temperature Profile

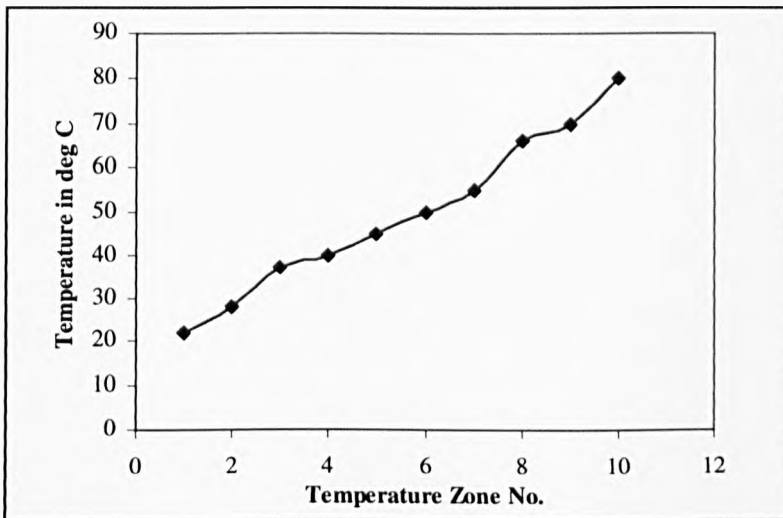


Figure E.1: Simulated tool temperature profile to test the cable model for dynamic impedance matching